



Osman, Hafiiz (2018) *Ultrasonic disinfection using large area compact radial mode resonators*. PhD thesis.

<https://theses.gla.ac.uk/30592/>

Copyright and moral rights for this work are retained by the author

A copy can be downloaded for personal non-commercial research or study, without prior permission or charge

This work cannot be reproduced or quoted extensively from without first obtaining permission in writing from the author

The content must not be changed in any way or sold commercially in any format or medium without the formal permission of the author

When referring to this work, full bibliographic details including the author, title, awarding institution and date of the thesis must be given

Enlighten: Theses

<https://theses.gla.ac.uk/>
research-enlighten@glasgow.ac.uk

Ultrasonic Disinfection using Large Area Compact Radial Mode Resonators



Hafiz Osman

(B.Eng, M.Eng)

Submitted in fulfilment of the requirements for the degree of
Doctor of Philosophy (PhD)

School of Engineering
College of Science and Engineering
University of Glasgow

March 2018

To my family.

Declaration

I declare that this thesis is a record of the original work carried out by myself under the supervision of Associate Professor Fannon Lim, and Professor Margaret Lucas in the School of Engineering at the University of Glasgow, United Kingdom, during the period of June 2014 to February 2018. The copyright of this thesis, therefore, belongs to the author under the terms of the United Kingdom Copyright acts. The due acknowledgement must always be made of the use of any material contained in, or derived from, this thesis. The thesis has not been presented elsewhere in consideration for a higher degree.

Abstract

Ultrasonic water treatment is based on the ability of an ultrasonic device to induce cavitation in the liquid, generating physical and chemical effects that can be used for biological inactivation. Effective treatment requires the ultrasonic device to generate intense cavitation field in a large treatment volume. Most conventional ultrasonic radiators fulfil only the first of these two requirements, rendering such devices highly unsuitable for use in high-volume, high-flow liquid processes. The present research investigates the design and performance of a new type of radial resonator in terms of their electromechanical characteristics, nonlinear behaviour, and their ability to treat synthetic ballast water with lower power consumption and short treatment times.

The radial resonators were designed using finite element (FE) modelling, and the best designs related to their predicted modal behaviour and vibration uniformity were selected for fabrication and experimental evaluation. Experimental modal analysis (EMA) of the radial resonators showed excellent correlation with the FE models, deviating by only 0.3% at the tuned mode. Impedance analysis showed that the mechanical quality factor of the radial resonators are 28–165% higher than the commercial high-gain probe, but their coupling coefficients are 40–45% lower.

Harmonic response characterisation (HRC) revealed shifts in the resonance frequencies at elevated excitation voltages. Duffing-like behaviour were observed in all resonators. RP-1 exhibited the Duffing-like behaviour to a far greater extent compared to the RPS-16 and RPST-16 multiple orifice resonators, indicating the influence of geometric parameters on the overall stiffness of the structure.

Finally, experiments with *Artemia* nauplii and *Daphnia* sp. showed excellent biological inactivation capability of the radial resonators. Comparison with previous studies showed that 90% reduction in *Artemia* nauplii can be achieved with up to 33% less energy and using just one radial resonator compared to the dozens of conventional resonators used in precedent investigations.

The present research have successfully demonstrated the use of FE modeling, EMA, and HRC to develop, validate, and characterise a new type of radial resonator. Experimental analysis showed that the radial resonators exhibited promising electrical, mechanical, and acoustical characteristics that has the potential to be cost-efficient, scalable, and a viable alternative water treatment method.

Acknowledgement

Foremost, I express my sincerest gratitude to Mr. Simon Kuik for initiating this programme and encouraging me to take up the challenge. I also express my sincere appreciation to Mr. Prakash and Mr. Chew Tee Tank for rendering support whenever sought, often without question. Thank you all, for extending this rare opportunity to me, and granting me full autonomy in the conduct of the research.

I am most grateful to my supervisor Dr Fannon Lim, for his guidance and support throughout my PhD career, helping me overcome numerous challenges, being a good company, and cheering me on to the finish line. Most of all, thank you for your friendship.

I consider myself very fortunate to be under the supervision of Professor Margaret Lucas, whom through our correspondences, showed immense knowledge and wisdom. Thank you for seeing the value of my research, and inspiring me to be a better researcher.

A special acknowledgement to Dr Andrew Mathieson and Dr Andrew Feeney for showing me the ‘ropes’ in transducer design and characterisation in Glasgow. Without their guidance, the ultrasonics test station would not have been built successfully in Singapore.

I am grateful to all those with whom I have had the pleasure to work during this research and other related projects. This thesis becomes a reality with the kind support and help from many individuals, and I would like to extend my sincere thanks to all of them.

This research would not have been possible without the support of the Singapore Economic Development Board (EDB) and Sembcorp Marine Repairs and Upgrades Pte. Ltd. through the Industrial Postgraduate Programme (IPP) grant number COY-15-IPP/140002

Hafiz Osman

Singapore, March 2018

Contents

Declaration	iii
Abstract	iv
Acknowledgement.....	v
Contents	vi
List of Figures	xi
List of Tables	xvi
List of Symbols.....	xviii
Abbreviations	xx
<i>Chapter 1</i> Introduction.....	1
1.1 Ultrasonic disinfection of ballast water	1
1.2 Ultrasonic disinfection – the conventional approach.....	3
1.3 Ultrasonic disinfection using a radial resonator	4
1.3.1 Previous work.....	4
1.3.2 Effect of mode shape on cavity pressure	4
1.3.3 Effect of cavity diameter on cavity pressure	6
1.4 Research objectives.....	7
1.5 Scope of work	7
1.6 Thesis organisation.....	7
<i>Chapter 2</i> Review of Literature.....	9
2.1 Mechanisms of ultrasonic disinfection	9
2.1.1 Cellular resonance.....	9
2.1.2 Mechanical cell disruption	10
2.1.3 Free radical attack	11
2.2 Efficacy of ultrasonic treatment on marine organisms	12
2.2.1 Effect on zooplankton.....	12
2.2.2 Effect on phytoplankton.....	14
2.2.3 Effect on bacteria	17

2.3	Assessment of current US radiator designs	18
2.3.1	Limitations of conventional resonators.....	18
2.3.2	Large area mono-directional radiators.....	19
2.3.3	Ring radiators.....	20
2.3.4	Tubular radiators	21
2.3.5	Corrugated cylindrical radiators.....	22
2.4	Assessment of current US reactor designs.....	23
2.4.1	Conventional batch reactors and baths.....	23
2.4.2	Flow-through reactors	24
2.5	Performance challenges in the operating environment	26
2.5.1	Operational variability	26
2.5.2	Water loading effects.....	26
2.5.3	Acoustic impedance matching	28
2.5.4	Variability of marine water constituents.....	28
2.5.5	Nonlinear dynamic behaviour of ultrasonic devices	29
2.6	Conclusion	30
<i>Chapter 3</i>	<i>Piezoelectric Transducer Modeling.....</i>	<i>31</i>
3.1	Fundamental equations	31
3.1.1	Equations of motion	31
3.1.2	Modal and harmonic response	31
3.2	Piezoelectric transduction.....	32
3.2.1	Theoretical background	32
3.2.2	Constitutive relations	32
3.2.3	Stiffness and compliance.....	34
3.2.4	Piezoelectric coefficients	35
3.2.5	Dielectric coefficients.....	36
3.3	FE modelling parameters	36
3.3.1	Geometry and meshing.....	36
3.3.2	Contact definitions, support, and loads.....	37
3.3.3	Piezoelectric model set-up	38
3.3.4	Modal analysis & harmonic response simulation.....	41
3.4	Conclusion	41

<i>Chapter 4</i>	Modelling & Analysis of Radial Resonators	42
4.1	Design objectives	42
4.1.1	Basic construction	43
4.1.2	Parts and materials	45
4.2	Finite element (FE) design approach	50
4.2.1	Mesh convergence	51
4.2.2	FE data extraction	53
4.3	Design of RP-, RPS-, and RPST-type radial resonators.....	53
4.3.1	Determination of a basic radial resonator design (RP-type).....	53
4.3.2	Modifications incorporating secondary orifices (RPS-type)	54
4.3.3	Modifications incorporating tertiary orifices (RPST-type)	59
4.4	Analysis of radial resonator designs	61
4.4.1	Modal solutions	61
4.4.2	Harmonic response simulation.....	65
4.5	Conclusion	69
<i>Chapter 5</i>	Experimental Analysis.....	70
5.1	Radial resonator assembly	70
5.1.1	Design selection	70
5.1.2	Exciter section assembly.....	70
5.1.3	Emitter section and final assembly	71
5.2	Preload characteristics.....	73
5.2.1	Preloading the radial resonators.....	73
5.2.2	Impedance analysis (IA) of preload characteristics	75
5.3	Experimental Modal Analysis (EMA)	77
5.3.1	Experimental set-up	77
5.3.2	Laser Doppler Vibrometry (LDV).....	78
5.3.3	Data acquisition and signal processing.....	79
5.3.4	Modal parameter extraction	81
5.4	Resonance and mode shape extraction	83
5.4.1	Comparison of FE and EMA results	83
5.4.2	Comparison of FE and IA results.....	86

5.4.3	Correlation between electrical and mechanical resonances	89
5.5	Electromechanical parameters	90
5.5.1	Resonator equivalent circuit	90
5.5.2	Electromechanical coupling coefficient	92
5.5.3	Mechanical quality factor	93
5.5.4	Comparison of electromechanical parameters	93
5.6	Conclusion	99
<i>Chapter 6</i>	<i>Harmonic Response Characterisation</i>	100
6.1	Harmonic response characterisation (HRC)	100
6.1.1	Experimental set-up	100
6.1.2	Measurement procedures and data processing	102
6.1.3	Ultrasonic driver circuit	103
6.2	Harmonic response of Alloy Steel-bolted resonators	107
6.2.1	Voltage responses	107
6.2.2	Harmonic response at different excitation	108
6.2.3	Displacement, output power, and amplification factor (AF)	110
6.2.4	Frequency shift	112
6.2.5	Skewness of vibration response curve	113
6.3	Beryllium Copper as preload bolt	118
6.3.1	Selection criteria	118
6.3.2	Impedance analysis of C17200-bolted radial resonators	119
6.4	Harmonic response of Beryllium Copper-bolted resonators	124
6.4.1	Harmonic response at different excitation levels	124
6.4.2	Displacement and amplification factor (AF)	125
6.4.3	Frequency shift	127
6.4.4	Skewness	128
6.5	Current vs. vibrational amplitude	130
6.6	Conclusion	131
<i>Chapter 7</i>	<i>Inactivation of Zooplankton</i>	133
7.1	Experimental set-up and procedures	133
7.1.1	Equipment and apparatus	133

7.1.2	Breeding and harvesting of test organisms.....	134
7.1.3	Experimental procedures	134
7.2	Driving of water-loaded resonators.....	136
7.2.1	Transmission cable impedance consideration	136
7.2.2	Compensation of capacitive reactance.....	137
7.3	Calorimetric measurement of ultrasonic energy density.....	141
7.4	Evaluation of US treatment efficacy	144
7.5	Flow-through reactor scale-up design.....	151
7.6	Conclusion	154
<i>Chapter 8</i>	<i>Conclusions</i>	155
8.1	Summary and main contributions	155
8.2	Recommendations for future work	157
	References.....	160
	Achievements	173

List of Figures

Figure 1.1 Ballast water treatment methods.	2
Figure 1.2 Ultrasonic water treatment using multiple horns operating below saturation [34,35]...	3
Figure 1.3 Contour plot of cavity pressure field by three radial modes of vibration R0 (top), R1(middle), and R3 (bottom) alongside graphs showing pressure distribution across the cavity [40].	5
Figure 1.4 R0 mode cavity pressure for various orifice diameters [40].	6
Figure 2.1 Barbell-shaped horns [111,113].	20
Figure 2.2 Radial mode ring radiator.	21
Figure 2.3 Tubular radiators: (a) conventional [120,122]; (b) cup-shaped [123]; (c) barbell- coupled [124].	22
Figure 2.4 Multiple-stepped horn variants; (a) Rawson [116]; (b) Peshkovsky et al. [111]; (c) Wei et al. [125].	23
Figure 2.5 Resonant cavities: (a) multiple-transducer arrangement [134]; (b) single transducer arrangement with a closed end [136]; (c) single transducer arrangement with open ends [137].	24
Figure 2.6 Flow-through reactor configurations: (a) longitudinal radiators in linear array [20]; (b) multi-stepped radiator in spiral cross-flow [22]; (c) serial ring radiators [141].....	26
Figure 3.1 Contact definitions, supports, and loads in FE model.	37
Figure 4.1 Radial resonator basic construction.....	43
Figure 4.2 Possible flange positions in PZT transducer.	49
Figure 4.3 Approach to multiple orifice radial resonator design.	51
Figure 4.4 Graph of mesh independence for the RPS-16 emitter.	51
Figure 4.5 FE mesh for radial resonator designs.	52
Figure 4.6 FE model data extraction point and paths for (a) vibrational amplitude and phase response; (b) vibrational velocity along at the outer circumference (OC) and primary orifice circumference (PC).	53
Figure 4.7 RPS resonator geometric parameters.	54
Figure 4.8 RPS resonator design chart.	55

Figure 4.9 CSOF contributions from the primary orifice and the secondary orifices; Number above the bar chart indicates the total CSOF (top), and the %S-CSOF (bottom).	57
Figure 4.10 Influence of secondary orifice quantity on emitter mass and circumferential radiating area.	57
Figure 4.11 RPST resonator geometric parameters.	59
Figure 4.12 RPST resonator design chart.....	60
Figure 4.13 Normalised deformation contours of RP1 emitter modes (10–25 kHz).	61
Figure 4.14 Normalised deformation contours of RP1 resonator modes (10–25 kHz).	62
Figure 4.15 Relative mass, radiating surface area, and area-to-mass ratio of radial resonators...	64
Figure 4.16 Simulated response of RP-1 resonator.	65
Figure 4.17 Simulated velocity response of radial resonators; mode superposition (closed markers); full solution (open markers); hybrid solution (line).	66
Figure 4.18 Simulated velocity profiles of radial resonators along the outer circumference (OC), and along the primary orifice circumference (PC).	67
Figure 4.19 Comparison of vibrational uniformity of RPS resonators (no. of measurement points = 100).	68
Figure 4.20 Vibrational uniformity of RPST resonators (no. of measurement points = 100).....	68
Figure 5.1 Exciter section components.	71
Figure 5.2 Exciter section assembly steps.....	71
Figure 5.3 Fabricated RP-1 radial resonator.	72
Figure 5.4 Fabricated RPS-16 multiple-orifice radial resonator.	72
Figure 5.5 Fabricated RPST-16 multiple-orifice radial resonator.	72
Figure 5.6 Effect of preloading on PZT.	73
Figure 5.7 Transducer preloading tools and equipment: (a) radial resonator; (b) torquing clamps; (c) torque wrench; (d) bench vise; (e) multimeter; (f) perforated foam support; (g) test leads; (h) test fixture; and (i) impedance analyser.....	74
Figure 5.8 Evolution of Z_m and f_m with pre-stress (RP-1).	76
Figure 5.9 Evolution of Z_m and f_m with pre-stress (RPS-16).....	76
Figure 5.10 Evolution of Z_m and f_m with pre-stress (RPST-16).	76
Figure 5.11 EMA schematic.....	77
Figure 5.12 Sensor head and laser beams; top view (left); side view (right).....	78
Figure 5.13 EMA measurement points for radial resonators.	82
Figure 5.14 FRFs from 48 DOF measurement points per device obtained from EMA.	83
Figure 5.15 Radial modes of RP-1 – EMA (top), FE (bottom).	85

Figure 5.16 Radial modes of RPS-16 – EMA (top), FE (bottom).....	85
Figure 5.17 Radial modes of RPST-16 – EMA (top), FE (bottom).....	86
Figure 5.18 Measured broadband admittance (top) and phase angle (bottom) spectra of RP-1.	87
Figure 5.19 Measured broadband admittance (top) and phase angle (bottom) spectra of RPS-16.	87
Figure 5.20 Measured broadband admittance (top) and phase angle (bottom) spectra of RPST- 16.	87
Figure 5.21 Correlation of IA and EMA measured resonances.....	89
Figure 5.22 Equivalent circuit model of an unloaded piezoelectric resonator [221,222].	90
Figure 5.23. Impedance-phase angle spectra of RP-1 from IA (line) and EC model (dash).....	94
Figure 5.24. Impedance-phase angle spectra of RPS-16 from IA (line) and EC model (dash).....	94
Figure 5.25. Impedance-phase angle spectra of RPST-16 from IA (line) and EC model (dash)..	95
Figure 5.26. Impedance-phase angle spectra of P25 from IA (line) and EC model (dash).....	95
Figure 5.27. ‘Stretching’ of the impedance and phase response spectra.	98
Figure 6.1 HRC schematic.	101
Figure 6.2 HRC measurement points on (a) RP-1; (b) RPS-16; (c) RPST-16; and (d) P25.	102
Figure 6.3 HRC equipment: (a) 4-channel DAQ; (b) power amplifier; (c) PC with MATLAB and DAQ software; (d) 4-channel oscilloscope with signal generator; (e) laser signal processor; (f) sensor head; (g) translation stage; (h) resonator fixture; (i) breadboard; (j) lab-jack...	103
Figure 6.4 Block diagram of ultrasonic generator circuit for driving air-loaded resonators, highlighting the input and output impedances of interconnecting devices ($Z_s = Z_{in} = Z_{out} = 50 \Omega$).....	104
Figure 6.5. V_R (RMS) vs. Z_R at different V_s (peak-to-peak).....	106
Figure 6.6. I_R (RMS) vs. Z_R at different V_s (peak-to-peak).....	106
Figure 6.7. P_R (RMS) vs. Z_R at different V_s (peak-to-peak).....	106
Figure 6.8. Profile of resonator voltages at different PA input signal levels (P25 for comparison).	107
Figure 6.9. Vibration response of A574-bolted radial resonators (P25 for comparison).....	108
Figure 6.10. Input and output responses of A574-bolted radial resonators (P25 for comparison).	111
Figure 6.11. Δf vs. V_R (RMS) of A574-bolted resonators (P25 for comparison).....	112
Figure 6.12. Δf vs. I_R (RMS) of A574-bolted resonators (P25 for comparison).	113
Figure 6.13. Skewness direction.	114

Figure 6.14. 1 st skewness coefficients for A574-bolted radial resonators.	117
Figure 6.15. 2 nd skewness coefficients for A574-bolted radial resonators.....	117
Figure 6.16. Impedance-phase angle spectra of C17200-bolted RP-1 from IA (line) and EC model (short dash); Impedance-phase angle spectra of A574-bolted RP-1 from IA (long dash) plotted for comparison.....	120
Figure 6.17. Impedance-phase angle spectra of C17200-bolted RPS-16 from IA (line) and EC model (short dash); Impedance-phase angle spectra of A574-bolted RPS-16 from IA (long dash) plotted for comparison.....	120
Figure 6.18. Impedance-phase angle spectra of C17200-bolted RPST-16 from IA (line) and EC model (short dash); Impedance-phase angle spectra of A574-bolted RPST-16 from IA (long dash) plotted for comparison.....	121
Figure 6.19. Comparison of k_{eff} between A574- and C17200-bolted radial resonators.....	123
Figure 6.20. Comparison of Q_m between A574- and C17200-bolted radial resonators.	123
Figure 6.21. Normalised k_{eff} and Q_m of C17200-bolted radial resonators ($k_{\text{eff}} = Q_m = \mathbf{K} = 1$ for P25)	123
Figure 6.22. Vibration response of C17200-bolted radial resonators (P25 for comparison).	124
Figure 6.23. Input and output responses of C17200-bolted resonators (P25 for comparison)...	125
Figure 6.24. Comparison of output displacement amplitude of A574- and C17200-bolted radial resonators.....	126
Figure 6.25. Comparison of displacement gains of A574- and C17200-bolted radial resonators.	126
Figure 6.26. Δf vs. I_R (RMS) of C17200-bolted resonators (P25 for comparison).....	127
Figure 6.27. Comparison of 1 st skewness coefficients at 30 V.....	129
Figure 6.28. Comparison of 2 nd skewness coefficients at 30 V.....	129
Figure 6.29. Current vs. displacement amplitude.....	131
Figure 7.1. Mechanical set-up for inactivation experiments; RP-1, RPS-16, RPST-16 (left to right).....	133
Figure 7.2. <i>Artemia</i> sp. culture tank; Petri dish will cultured <i>Artemia</i> sp. nauplii; pre-sonication and post-sonication enumeration of <i>Artemia</i> nauplii (left to right).....	135
Figure 7.3. Process for cumulative exposure and discrete exposure inactivation experiments, ..	136
Figure 7.4 Block diagram of modified ultrasonic generator circuit for driving water-loaded resonators, highlighting the input and output impedances of interconnecting devices ($Z_s = Z_{\text{in}} = Z_{\text{out}} = 50 \Omega$).....	138
Figure 7.5. Effect of reactance compensation on the impedance-phase spectra of RP-1.	139
Figure 7.6. Effect of reactance compensation on the impedance-phase spectra of RPS-16.	139

Figure 7.7. Effect of reactance compensation on the impedance-phase spectra of RPST-16.....	139
Figure 7.8 Effect of reactance compensation inductors on resonator voltage and power.	140
Figure 7.9. Calorimetric test tank with insulation (left); reactance compensation inductors (right).	141
Figure 7.10. Schematic of experimental set-up for calorimetric analysis.	142
Figure 7.11. Example of calorimetric analysis using actual data from RPS-16.	143
Figure 7.12. Effect of cumulative ultrasound exposure on <i>Artemia</i> sp. survival for different resonators; actual survival (open markers); mean survival calculated from 3 samples (closed markers).	146
Figure 7.13. Effect of cumulative ultrasound energy density on <i>Artemia</i> sp. survival for different resonators; actual survival (open markers); mean survival calculated from 3 samples (closed markers).	146
Figure 7.14. Effect of discrete ultrasound exposures on <i>Artemia</i> sp. survival for different resonators; actual survival (open markers); mean survival calculated from 3 samples (bars).	146
Figure 7.15. Effect of ultrasonic power density on <i>Artemia</i> sp. survival; actual survival (open markers); mean survival calculate from 3 samples (bars).	149
Figure 7.16. Comparison of <i>Artemia</i> sp. and <i>Daphnia</i> sp. survival with ultrasound exposure; actual survival (open markers); mean survival calculated from 3 samples (closed markers).	149
Figure 7.17. Micrograph of <i>Artemia</i> sp. nauplii before (left) and after (right) sonication.	151
Figure 7.18. Micrograph of <i>Daphnia</i> sp. before (left) and after (right) sonication.	151
Figure 7.19. Simulated acoustic pressure contours; RP-1 (left); RPS-16 (middle); RPST-16 (right).	152
Figure 7.20. Flow-through reactor with two radial resonators; side view (left); flange view (right).	152
Figure 7.21. Serial (top) and parallel (bottom) arrangement of the flow-through US reactor. ..	153

List of Tables

Table 2.1 Ultrasonic inactivation of zooplankton.....	14
Table 2.2 Ultrasonic inactivation of phytoplankton.....	16
Table 2.3 Ultrasonic inactivation of bacteria.....	17
Table 2.4 Acoustic impedance of common transducer materials and pure water at 20 kHz.....	28
Table 3.1 NCE81 piezoceramic ring properties.....	40
Table 4.1 Mechanical properties of transducer parts [189–191].....	45
Table 4.2 Acoustic properties of transducer materials.....	46
Table 4.3 Dimensions of socket head cap screw used as a preload bolt [192].....	46
Table 4.4 Exciter section dimensions for two bolt lengths.....	47
Table 4.5 Piezoceramic classification according to U.S. military standard.....	48
Table 4.6 NCE81 piezoceramic ring measurements.....	49
Table 4.7 Comparison of RPS configurations.....	56
Table 4.8 Weightage of RPS designs based on geometric considerations.....	58
Table 4.9 Comparison of RPST configurations.....	60
Table 4.10 Comparison of RPS radial resonator design outcomes.....	63
Table 4.11 Comparison of RPST radial resonator design outcomes.....	63
Table 5.1 Torque calculation parameters.....	74
Table 5.2 Preloading steps.....	75
Table 5.3 EMA configuration and settings.....	80
Table 5.4 Frequency separation between R0 and adjacent modes.....	84
Table 5.5 Modal frequencies percentage error – FE vs. EMA.....	84
Table 5.6 Modal frequencies percentage error – FE vs. IA.....	88
Table 5.7 Measured (IA) characteristic frequencies and impedances.....	96
Table 5.8 Equivalent circuit parameters and figures of merit.....	96
Table 5.9 Simulated (EC) characteristic frequencies and impedances.....	97
Table 6.1 Calculation of relative acoustic output (A574-bolted resonators and P25) at 30 V excitation.....	109
Table 6.2 Displacement and amplification factor of A574-bolted resonators (P25 for comparison).	111

Table 6.3 Data for skewness coefficient calculation at $V_{in} = 30$ V (A574-bolted resonators)....	116
Table 6.4 Mechanical properties of preload bolt materials [191,248,249].	118
Table 6.5 Equivalent circuit parameters and figures of merit of C17200-bolted resonators.....	119
Table 6.6 Measured (IA) characteristic frequencies and impedances of C17200-bolted resonators.	122
Table 6.7 Displacement and amplification factor of C17200-bolted resonators.....	126
Table 6.8 Gradient of linear fit function for the graph of Δf vs. I_R (RMS).	128
Table 6.9 Data for skewness coefficient calculation at $V_R = 30$ V (C17200-bolted resonators).	128
Table 7.1 Calculation of reactance compensation inductance.	138
Table 7.2 Impedance and phase angle with reactance compensation inductors.	140
Table 7.3 Resonator output area and volume of orifices.	144
Table 7.4 Calculation of ultrasonic power density from calorimetric measurement data.....	144
Table 7.5 Comparison of ultrasonic inactivation performance with previous studies [48,90].	148

List of Symbols

Symbol	Description	Unit
A_{pp}	Peak-to-peak displacement	m
c	Sound velocity	m/s
C	Capacitance	F
d_{33}, d_{31}	Piezoelectric charge constants	m/V
D	Diameter	m
E	Young's modulus	N/m ²
f	Frequency	Hz
f_a	Motional anti-resonance frequency	Hz
f_m	Frequency at minimum impedance or maximum admittance	Hz
f_n	Frequency at maximum impedance or minimum admittance	Hz
f_p	Parallel resonance frequency, phase angle zero.	Hz
f_r	Motional resonance frequency	Hz
f_s	Series resonance frequency, phase angle zero	Hz
F	Force	N
G	Conductance	S or 1/Ω
I_{US}	Ultrasonic intensity	W/m ²
I	Current	A
I_R	Resonator/transducer input current	A
k_{33}, k_{31}, k_p, k_t	Piezoelectric coupling coefficients	-
k_{eff}	Effective coupling coefficient of piezoelectric transducers	-
P	Pressure	Pa
P_E	Electrical power	W
P_{US}	Ultrasonic power density	W/m ³
S	Surface area	m ²
t	Time	s
T	Torque	Nm
$\tan \delta$	Piezoelectric dissipation factor	-
u	Vibrational displacement	m
\dot{u}	Vibrational velocity	m/s

\ddot{u}	Vibrational acceleration	m/s^2
V	Voltage	V
V_R	Resonator/transducer input voltage	V
V_p	Velocity amplitude	m/s
w	Specific acoustic power	W/m^2
W	Total acoustic power	W
Y	Electrical admittance	S
Z	Electrical impedance	Ω
Z_m	Minimum electrical impedance	Ω
Z_n	Maximum electrical impedance	Ω
Z_{act}	Acoustic impedance	kg/s

Greek symbols

ϵ	Electric permittivity	F/m
λ	Wavelength	m
ρ	Density	kg/m^3
σ	Stress	N/m^2
θ	Phase angle	radians
ω	Angular frequency	radians/s

Subscripts

act	Acoustic
appl	Applied
calc	Calculated
loss	Loss
maj	Major
meas	Measured
p	Pitch
s	Static preload
pri,sec,tert	Primary, secondary, tertiary
x,y,z	Directions in Cartesian coordinate system
r, ϕ ,z	Directions in Cylindrical coordinate system
W	Water
V	Vessel

Abbreviations

BWMS	Ballast Water Management System
CSOF	Cross-section open fraction
DAQ	Data acquisition
DOF	Degree of Freedom
DUT	Device-under-test
EC	Equivalent circuit
EMA	Experimental Modal Analysis
FEM	Finite element modelling
FOM	Figure of Merit
HRC	Harmonic response characterisation
IA	Impedance Analysis
LDV	Laser Doppler Vibrometry
US	Ultrasonic
UV	Ultraviolet

Chapter 1

Introduction

1.1 Ultrasonic disinfection of ballast water

Marine vessels transport more than 80% of the world's commodities and exchange between 3 to 7 billion tonnes of ballast water annually [1]. Over 3000 species of microorganism are carried in ballast water on a daily average [2]. The introduction of invasive aquatic organisms through ballast water discharge poses a significant threat to marine ecology, economy, property and public health. Non-indigenous invasive species compete with native species for nourishment and space, induce new behavioural responses in the native species, and threaten biodiversity. The economic consequence of marine invasive species is estimated to cost around \$137 billion annually for the United States alone [3]. Meanwhile, the global impact of invasive species has been investigated in great detail by academia, environmentalists, and statutory bodies, and has resulted in the passing of a new regulation to manage ballast water discharge [4,5].

Ballast water management systems (BWMS) can be broadly categorised as mechanical, physical, or chemical systems as shown in Figure 1.1 [6,7]. Chemical-based systems capable of *in-situ* production of biocidal agents dominate the chemical category and are known industry-wide to be very effective against invasive species and more cost-effective for larger capacities compared to most physical treatment methods [8]. The performance of systems based on electrochemistry is known to be highly dependent on salinity and temperature [9]. Such systems require continuous monitoring of residual oxidant concentration not only to ensure sufficient dosage for effective treatment but also to safeguard the environment against excessive discharge of toxic effluents [8,10]. Ultraviolet (UV)-based disinfection constitutes around 35% of all type-approved systems to date and accounts for more than 70% of systems in the physical treatment category [11]. The proven reliability and safety track-record, and its environmentally-benign effluent contributed to the popularity of UV-based systems. However, UV-based systems suffer from delayed treatment effect, high dependence on water quality, and organism dose-response variability, all of which impose severe practical limitations on the system as a whole [12–14]. As a mitigation measure, UV systems are sized to deliver 3 to 5 times more UV dosage than necessary [15]. This brute force approach increases the physical size and power

consumption of the system substantially [16,17], making them less competitive and more challenging to implement especially in retrofit installations where space and power are limited [18].

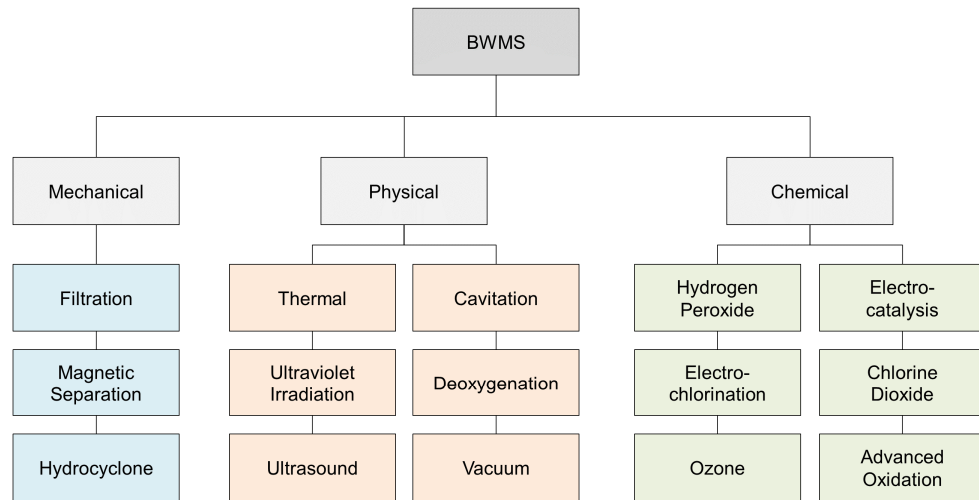


Figure 1.1 Ballast water treatment methods.

Ultrasonic (US) technology has the potential to overcome some of these challenges by augmenting existing treatment methods [19–21] or by operating independently as an alternative treatment method [22]. Since the mid-1900s, studies have demonstrated the ability of ultrasonic radiation to destroy microscopic organisms [23]. Despite the abundance of scientific literature and interest in the subject, the technology has found limited implementation in BWMS [24]. Although US technology appears promising in laboratory evaluations and small-scale tests, translation into a full-scale commercial system remains challenging. The present research focuses on the design of an ultrasonic resonator capable of generating high ultrasound power density and a well-distributed ultrasound field with the goal of applying the technology in a US-based or US-assisted BWMS. Realising this goal requires knowledge spanning the vibration characteristics of the ultrasound emitter, to the cavitation-inducing acoustic wave propagation, to the biological effects. This understanding is critical for the design of an optimised ballast water treatment solution, which presents unique challenges associated with organism diversity and the physicochemical characteristics of ballast water [25]. This review highlights the advances in the field of US-based and US-assisted disinfection technology and presents a forward-look towards the successful implementation of ultrasonic technology in ballast water treatment.

1.2 Ultrasonic disinfection – the conventional approach

Ultrasonic cavitation technology finds few implementation in large-scale treatment plants due to the inherent limitations of ultrasonic devices [26,27]. The application of ultrasound in ballast water treatment has been successfully demonstrated, but the power consumption required to implement such systems at the industrial scale would be immensely prohibitive [28,29]. Review of literature revealed that most studies in this area utilised standard off-the-shelf devices that are not suitable for the large-scale applications. In conventional reactors fitted with flat-tipped power ultrasonic probes, the cavitation zone is confined to a small volume near the tip of the device [30]. Although it is possible to slightly increase the cavitation zone by increasing the vibration amplitude [31], there is a limit beyond which the formation of a large air cushion below the radiating surface effectively shields the water body from the incoming acoustic energy [32,33]. The usual approach of deploying multiple devices operating below their saturation level (see Figure 1.2) partly overcome the said limitations [34]. Although this is a logical approach, the number of associated electronics and auxiliary devices required to support the operation of the multiplicity of transducers result in high capital and running costs, discouraging widespread implementation.

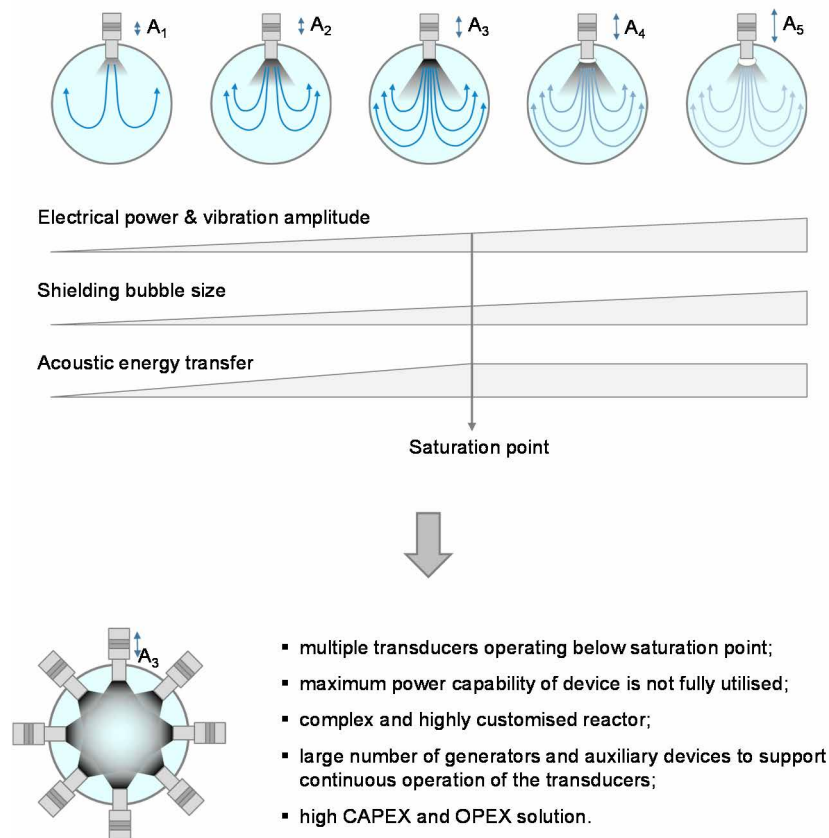


Figure 1.2 Ultrasonic water treatment using multiple horns operating below saturation [34,35].

There have been attempts to design resonators with larger radiating surface areas [36–38]. However, most of the investigated designs achieve a larger output area through scaling and mass addition. Structural mass is an important consideration in the design of an efficient resonator since the electrical energy required to excite the device scale accordingly its physical size. In addition, it is recommended to study the impact of structural damping, mechanical losses, and acoustic radiation impedance [39] on the behaviour of the resonator early in the design stage, especially if they will be applied in water and other liquids with densities much greater than air.

1.3 Ultrasonic disinfection using a radial resonator

1.3.1 Previous work

Hunter [40] investigated the effectiveness of a radial-mode ultrasonic resonator in the inactivation of *Escherichia coli* K12 and *Staphylococcus aureus* population. The research was based on the premise that the fundamental radial mode can concentrate acoustic power at the centre of the resonator cavity while also creating a well-distributed cavitation field across the entire cavity. Focusing the acoustic field in such manner produced high negative acoustic pressures with low driving amplitudes. Although the focus was on the fundamental radial mode (R0), the acoustic effects of R1 and R3 radial modes were also investigated.

1.3.2 Effect of mode shape on cavity pressure

Acoustic pressure distribution in the liquid-filled cavity was numerically determined using finite element simulation and the acoustic field generated by the three radial modes were compared. As shown in Figure 1.3, R1 and R3 modes produced maximum pressures close to the vibrating surface whereas the R0-tuned resonator generated maximum pressure at the centre of the cavity. Comparing the magnitudes of acoustic pressure generated from a 6 μm vibrational input amplitude, the R1-tuned resonator produced a maximum that was approximately three times the maximum pressure generated by the R0-tuned resonator. On the other hand, the R3 mode generated the lowest pressure at approximately 30% of the pressure generated by R0.

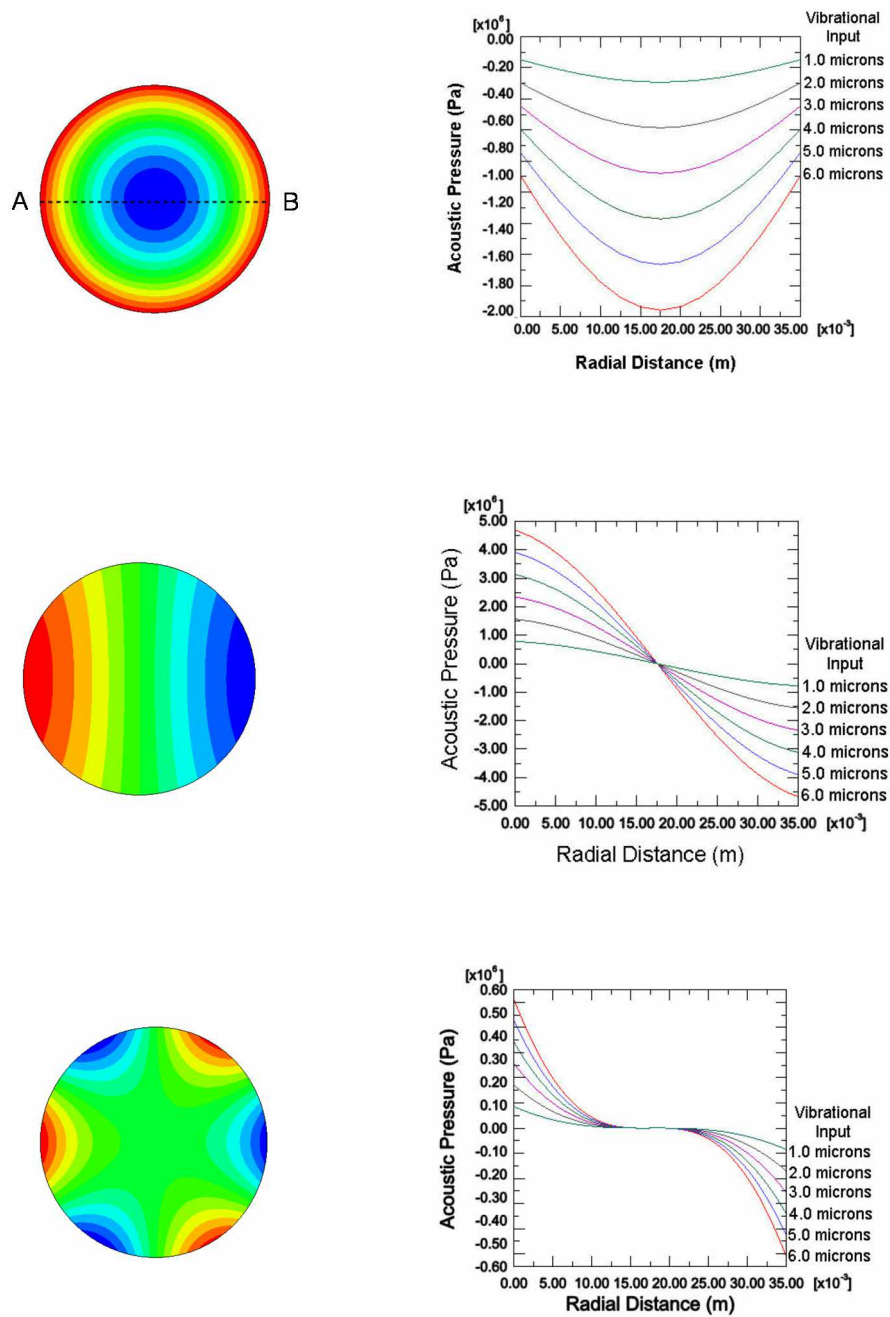


Figure 1.3 Contour plot of cavity pressure field by three radial modes of vibration R0 (top), R1(middle), and R3 (bottom) alongside graphs showing pressure distribution across the cavity [40].

These acoustic pressure predictions corroborated with the ultrasound-induced cavitation field captured by Sonochemiluminescence (SCL) experiments, and have good correlation with the *E. coli* and *S. aureus* inactivation rates. The study showed that the R0 resonator achieved higher inactivation rates than the R3 resonator; the R0 resonator achieved 3-log reductions in 4 minutes with ultrasonic power density of 2.6 W/cm^3 , while the R3 resonator achieved 2-log reductions within the same exposure time, but at 20% higher ultrasonic power density. These results indicate that cavitation distribution and pressure magnitude greatly influenced the inactivation kinetics.

Based on the above findings, it is apparent that the design of an ultrasonic disinfection system should aim towards achieving high negative pressures that are also well-distributed. Although Hunter’s work has shed new insight on the influence of vibrational modes on bacterial inactivation, the work was limited to comparing the biocidal efficacies of R0 and R3 modes only. It would have been interesting to see if the R1 mode, which was shown to generate the highest acoustic pressures, can induce biocidal effect that is greater than the R0 mode.

1.3.3 Effect of cavity diameter on cavity pressure

Cavitation intensity, which is a measure of ‘white cavitation noise’ [41], is often associated with the strength of ultrasound-induced pressure field [36,40]. In reality, the formation of cavitation bubbles is also influenced by the physicochemical properties of the medium such as the concentration of nucleation sites, impurities [42,43], and dissolved gases [44]. Although mathematical models for predicting ultrasonic cavitation have been refined and successfully applied [45], the use of pressure field as an indirect prediction of cavitation activity is computationally less expensive but acceptable if the emphasis is to investigate the geometric effects of the resonator. Using this approach, the influence of cavity diameter on the pressure fields generated can be evaluated relatively quickly. Figure 1.4 showed that smaller cavities produced more uniform but weaker acoustic fields than larger cavities. In flow-through applications, a small cavity results in higher head-loss and high fluid velocity. High head-loss is operationally undesirable because it increases the pumping pressure requirement, while high fluid velocity reduces the ultrasound exposure time. Studies have shown that inactivation of bacteria [46], phytoplankton [47], zooplankton [48] and other microscopic organisms [49] increases with the applied ultrasonic dose (J/m^2), which depends on the ultrasonic intensity (W/m^2) and exposure time (s) [29]. Thus, the design of any efficient ultrasonic treatment system should seek to maximise both ultrasound intensity and exposure time simultaneously.

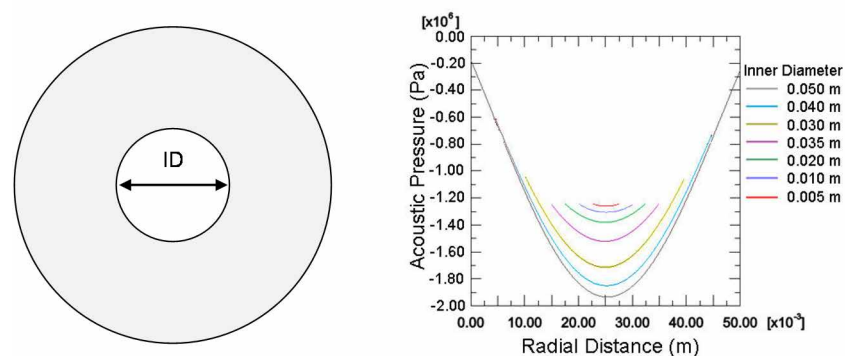


Figure 1.4 R0 mode cavity pressure for various orifice diameters [40].

1.4 Research objectives

The primary goal of this research is to design, build, and characterise a set of compact radial mode resonators that have a high output area-to-mass ratio compared to conventional probe-type devices. The resonators shall have the ability to generate a relatively well-distributed ultrasound field, at an adequate ultrasonic energy density to effect in a significant reduction in marine organism populations. It is envisioned that the achievement of the said objectives will lead to the scale-up design of an ultrasonic reactor that uses fewer resonators, consume less power, and is economically competitive with conventional ballast water treatment methods.

1.5 Scope of work

1. Finite element (FE) design of large-area compact radial resonators.
2. Analyse, select, and fabricate radial resonator designs.
3. Perform experimental modal analysis (EMA) to validate the FE models.
4. Perform impedance analysis (IA) to determine the electromechanical characteristics of the radial resonators under unloaded and water-loaded conditions.
5. Perform harmonic response characterisation (HRC) to determine the nonlinear behaviour of the radial resonators under unloaded conditions.
6. Perform calorimetric analysis to determine the ultrasonic power density applied in the inactivation experiments.
7. Perform inactivation experiments on model zooplankton species to benchmark the radial resonator treatment efficacy against previous studies.

1.6 Thesis organisation

The work contained within this thesis describes a programme of research into the design of a new-type of power ultrasonic resonators for ballast water treatment. The thesis is divided into 8 chapters.

Chapter 1 describes the problem of marine invasive species and the legislation introduced to curb the transport of destructive nonindigenous organisms in ship ballast water. Conventional ballast water treatment methods are discussed and their limitations are highlighted. Ultrasound is proposed as an alternative treatment method and the rationale for utilising a radial-mode ultrasonic resonator over a conventional probe-type device is presented.

Chapter 2 reviews the mechanisms of ultrasound-induced cellular destruction and how they relate to the inactivation of aquatic species of zooplankton, phytoplankton and bacteria. Ultrasonic

radiator and reactor designs from industrial, academic, and patent literature are discussed, highlighting their principal features, merits, and limitations. Finally, performance challenges related to the variability in the operation parameters, water loading effects, differences in the acoustic impedance between the radiator and the liquid, variability in marine water constituents, and the nonlinear electromechanical and dynamic behaviour of the ultrasonic devices are discussed.

Chapter 3 describes the finite element (FE) modeling approach to ultrasonic resonator design. The fundamental equations governing the electromechanical behaviour of the piezoelectric-based resonators are described, and the geometry, meshing scheme, and boundary conditions are defined for modal analysis and harmonic response computations.

Chapter 4 focuses on the radial resonator design features wherein the basic construction, parts, and materials are discussed to address the engineering design considerations. This is followed by FE modeling and analysis of a number of radial resonator designs with different orifice configurations. The influence of orifice parameters (size, position, and quantity) on the resonance frequencies, mode shapes, and vibrational uniformity are discussed.

Chapter 5 describes the fabrication, assembly, and characterisation of the selected radial resonators. The electromechanical characteristics of the resonators are measured and the equivalent circuit parameters describing the behaviour of each device are determined. Finally, results from experimental modal analysis (EMA) are discussed and comparison with the FE modeling results are made as a form of validation.

Chapter 6 focuses on the harmonic response of the radial resonators in terms of their vibrational amplitudes at different voltages and currents. Nonlinear behaviour in terms of frequency shifts, amplitude jumps, and hysteretic behaviour are also discussed. The effect of bolt material on the electromechanical characteristics, and dynamic behaviour of the resonators are also investigated.

Chapter 7 investigates the biological efficacy of the radial resonators using standard test organisms. The treatment efficacy of the resonators are benchmarked against a commercial probe-type device. Scale-up design for full-scale ballast water treatment application is also discussed.

Finally, Chapter 8 summarises the work carried out and the main contributions of the present research. Recommendations for future work are suggested to expand the present research towards industrial-scale implementation.

Chapter 2

Review of Literature

2.1 Mechanisms of ultrasonic disinfection

In any application of ultrasonic treatment of liquids, a complete understanding of the underlying mechanisms involved in the annihilation of biological cells is critical. Biocidal effects of ultrasound can proceed via several simultaneous mechanisms. Cell resonance can lead to its disruption, while sonically-induced cavitation can release energy and generate mechanical and sonochemical reactions that can have destructive effects [50]. Microbial inactivation through cellular resonance in the absence of cavitation is a direct effect of ultrasound, while sonochemical and physical effects associated with acoustically-induced cavitation are the indirect effects of ultrasound. The following sections discuss these mechanisms in more detail.

2.1.1 Cellular resonance

Several studies have reported the use of ultrasound to disrupt biological cells through cellular resonance [51–54]. This effect is achieved by matching the ultrasound frequency with the target cell resonance frequency to rupture the cell wall. The effect of cellular resonance have been investigated in a number of studies. One study reported that ultrasound exposure at specific frequencies could control the growth of cyanobacteria and other bloom-forming phytoplankton [52] by targeting the semi-permeable gas vacuoles found in the phytoplankton cells. The gas vacuole provide the algal cells the buoyancy necessary for securing light and nutrients near the surface of the water body [51]. With the destruction of the gas-vacuole, the cell loses its buoyancy and therefore its access to surface light and nutrients, thereby inhibiting photosynthetic activities necessary for cell multiplication [55]. Zhang et al. [51] showed that phytoplankton inactivation rate is around 400% greater at 1.3 MHz compared to 20 kHz, but no significant improvement was observed between 20 kHz and 150 kHz. This result indicates that the destruction of gas vacuole must be associated with its resonance at a frequency related to its lateral dimension via the Rayleigh-Plesset bubble activation equation [56]:

$$f_{\text{cell}} = \frac{1}{2\pi} \sqrt{\frac{1}{\rho r^2} \left[3\gamma \left(p_0 + \frac{2\sigma}{r} \right) - \frac{2\sigma}{\rho r} \right] - \left(\frac{2\mu}{\rho r^2} \right)^2}. \quad (2.1)$$

This equation relates the resonance frequency of a cell, f_{cell} (Hz), suspended in a liquid medium with gas vacuole radius r (m), having surface tension σ (N/m). The remaining terms are properties of the acoustic medium namely, the ratio of heat capacities of the gas at constant pressure γ , the ambient pressure p_0 (Pa) and the density ρ (kg/m^3) of the surrounding medium. There are other theoretical models for cellular resonance [57], but regardless of the model employed, inducing the destructive effects of cellular resonance on micron-sized biological cells requires sonication frequencies in the MHz range.

2.1.2 Mechanical cell disruption

Cells are susceptible to mechanical disruption when exposed to high-pressure shock-waves and high-shear turbulent flows generated by high-intensity ultrasound. Cavitation bubbles are generated when a liquid is irradiated with ultrasound waves at a pressure meeting the cavitation threshold. The cyclic expansion and compression of the liquid in the ultrasound field generates microscopic bubbles which undergo oscillatory growth through rectified diffusion over several cycles before its final implosion [58]. The number of cavitation bubbles depends on the density of pre-existing bubbles and nucleation sites, which comprise of solid impurities and microscopic crevices in the walls of the reaction vessel. During stable cavitation, vapour cavities form, grow, and collapse after many cycles. Meanwhile, a high-intensity ultrasound field promotes inertial cavitation bubbles that implode without oscillating [59]. In both cases, the gas cavities grow when the local static pressure falls below the vapour pressure and implode violently when the pressure recovers [60]. The asymmetric collapse of cavities near a solid surface produce high-speed liquid microjets with velocities in the order of 100 m/s [61], whereas the symmetric collapse away from a solid surface produce acoustic shock waves and turbulent eddies. In ultrasound-induced cavitation, the high-speed implosion of a microbubble result in the adiabatic compression of the gas cavity, which generates extreme localised pressure and temperature that have physicochemical consequences [62,63]. Although the cavitation event lasts only a few microseconds, the energy released can have destructive effects on zooplankton [48,64,65], algal cells [26,28,66], and bacteria [67–69].

Ultrasound power and frequency play a major role in the generation of a strong cavitation field. The average bubble size induced by an ultrasound field increases with applied power and decreases with increasing frequency. It has been shown that low-frequency ultrasound (around 20 kHz) generates bubbles that produce a stronger cavitation field than bubbles generated at higher

ultrasonic frequencies [70,71]. Meanwhile, high-frequency sonication tends to produce smaller bubbles (less than 10 μm in diameter [72]) in greater quantity, but the implosion effects are also weaker [73]. On the other hand, bubbles that are too large (a few cm in diameter) are not useful for inactivation [44]. Cavitation events release mechanical energy, creating shear forces and micro-jets capable of inflicting physical damage to water-borne microorganisms [50,74]. Shear forces from acoustic streaming arise from the dissipation of the acoustic standing wave in a fluid adjacent to a solid or between two oscillating bubbles [75]. In most cases of high-intensity sonication, the shear forces are due to both macroscopic acoustic streaming and micro-scale streaming. The latter occurs when the establishment of oscillating microbubbles leads to the formation of high velocity, cyclic eddy currents around the bubbles. Microstreaming is a characteristic of low-frequency sonication and becomes less prominent at higher frequencies [76].

The formation and ejection of high-velocity penetrative microjets due to the aspherical implosion of microbubbles near a solid surface is said to be another possible mechanism of cell destruction [77]. Cavitation shock waves have also been suggested as another mechanism for cellular disruption. The effects of cavitation shock waves have been demonstrated through the independent investigations of Furuta et al. [78] and Abe et al. [79] wherein the annihilation of *E. coli* and *Vibrio* sp. cells with shock wave pressures exceeding 200 MPa were reported. Although there have been numerous attempts to explain the mechanisms of ultrasonic inactivation, the minute time and length scales as well as the technical limitations in the conduct of experiments are obstacles to accurate observation of the inactivation pathways [80,81].

2.1.3 Free radical attack

Cavitation bubble implosion is known to produce active compounds that contribute to the overall efficacy of the ultrasonic treatment plant. The extreme localised temperature and pressure [62,63] generated during bubble implosion facilitates the pyrolytic formation of free radicals and other compounds with biocidal properties [67]. In water, the energy released from a cavitation event can cleave the molecular bonds of water vapour and other gaseous mixtures contained in the bubble, forming hydroxyl ($\text{OH}\cdot$) ions and free hydrogen ($\text{H}\cdot$) atoms [80,82]. The $\text{OH}\cdot$ radicals have been shown to attack the cell wall membranes and render the microorganism inviable. Further, the recombination of the $\text{OH}\cdot$ ions leads to the formation of hydrogen peroxide, a potent oxidising agent and biocide, which contributes to the overall treatment effect [71]. The concentration of $\text{OH}\cdot$ ions generated has been shown to correlate with the sonication frequency. High-frequency sonication generates more cavitation events and favours the generation of $\text{OH}\cdot$ ions compared to low-frequency sonication [51,83,84]. The frequency dependence of $\text{OH}\cdot$ genesis was shown to be related to the relative lifetimes of the cavitation bubbles and the radical species [81,85].

In the absence of a direct observation method, researchers have measured cavitation activity using hydroxyl ion scavengers such as t-butanol [71], potassium iodide (KI) [86], Rhodamine B [87], and other compounds [51,66]. These experiments indicate that the cell membrane integrity was compromised by the physical effects of cavitation, and increased the cell's exposure to oxidant penetration [67]. However, not all cases studied have involved physical rupture of the cell membrane. For example, Tang et al. [52] reported that the interaction between the cell membrane and the free radicals can also increase the cell's susceptibility to chemical oxidant penetration. Inhibition of photosynthetic activity follows, and lipid peroxidation is induced leading to a loss of the cell's vital functions. Although no single model exists to completely describe the microscopic free radical pathway of disinfection, at a global level, there is a consensus among the scientific community that cell inactivation rate increases with hydroxyl radical concentration [66,88].

2.2 Efficacy of ultrasonic treatment on marine organisms

Ballast water remains a highly challenging environment for any treatment technology due to the considerable variability in its physicochemical properties, dynamic shipboard operating conditions, and the diversity of organisms, to name but a few. The goal is to achieve effective and efficient application of ultrasound waves to eliminate invasive species in ballast water. Past research have investigated the efficacy of US treatment by exposing natural and cultured species of zooplankton, phytoplankton, and bacteria to ultrasound. The influence of ultrasound frequency, intensity, exposure time, organism sensitivity, and so on have been investigated. Most of these studies were performed in laboratory conditions, using synthetic marine water and conventional longitudinal-mode US devices having output areas between 1.26 cm² and 12.6 cm² [48,89]. Static experiments were carried out in 10–50 cm³ vessels [48,65], while flow-through experiments utilised reactor vessels between 12.4 cm³ and 2900 cm³ in volume [48,90]. Mortality rate was determined by enumerating the number of live cells before and after ultrasonic treatment. Direct enumeration was used for larger cells (i.e. zooplankton) or when there are only a handful of live cells remaining after sonication, while the serial dilution method with staining is used to estimate the number of viable phytoplankton and bacterial cells [91]. The following sections discuss some of the key findings related to US inactivation of marine invasive species.

2.2.1 Effect on zooplankton

Zooplanktons are small aquatic animals that are weak swimmers and whose size varies from 2 µm to several cm in length. The use of ultrasound to eliminate invasive zooplankton species from ballast water has been reported to be a viable approach. Studies have shown that the mechanisms

for zooplankton destruction are far less complicated than the suggested mechanisms involved in the destruction of bacteria and phytoplankton. Zooplanktons being multicellular organisms are physically larger [92] and more susceptible to dismemberment by the turbulent shear flow induced by high-intensity sonication. Holm et al. [48] reported that the ultrasonic energy density required for 90% reduction (i.e. decimal reduction energy density, DRED) in a zooplankton population was around one-tenth the DRED for phytoplankton and bacteria. Liquid microjets was suggested to have played a dominant role in the inactivation of larger organisms since the formation of destructive microjets requires an asymmetric bubble collapse near a surface much larger than the bubble diameter [50,93]. Although the fracture or total loss of non-vital body parts such as limbs or antlers may not always be immediately lethal, the survivability of a dismembered zooplankton can be severely impaired.

Holm et al. [48] reported that 19–20 kHz is most effective against zooplankton greater than 100 μm . Using *Artemia* sp., Rotifers (*Branchionus plicatilis* and *Branchionus calyciflorus*) and a Cladoceran (*Ceriodaphnia dubia*) as zooplankton surrogates, it was shown that 90% mortality rate could be achieved with less than 10 s exposure to 20 kHz ultrasound at an energy density of less than 20 J/cm^3 . Guo et al. [65] reported a similar outcome with barnacle cyprid (*Amphibalanus Amphitrite*). The study showed that sonication at 23 kHz was far more effective than 63 kHz or 102 kHz in inhibiting the growth barnacle cyprid. On the other hand, if the frequency is too low, the treatment effect becomes weaker resulting in increased sonication time and higher energy consumption. These results suggest that ultrasound frequency of around 20 kHz promotes the formation of liquid microjets [94] which leads to the inactivation of zooplankton [26].

Organism vulnerability to ultrasound exposure varies from taxa to taxa, and species to species. Even within the same species, specific life cycle stages are also more vulnerable than others. Gavand et al. [26] reported that cysts of *Artemia salina* are most resilient to ultrasound irradiation while the larvae are the most vulnerable. A particular experiment showed that 20 min of sonication destroyed most of the larvae but only 60% of the cysts. Another study showed that a zooplankton soup comprising Polychaete larvae (*Nereis virens*) and two copepod species (*Tisbe battagliai* and *Acartia tonsa*) subjected to 20 kHz ultrasound in an industrial-grade ultrasonic processor (UIP2000, Hielscher) achieved only up to 40% reduction in the zooplankton population [89,95,96]. Thus, it is important to evaluate the effectiveness of a treatment system using robust test organisms to ensure that the system is not under-designed.

The duration of exposure to the ultrasonic field and the field strength influence the rate at which the organisms are inactivated. Studies have shown that a longer sonication time and a higher field intensity can increase the mortality rate. However, the relationship between mortality and exposure time is nonlinear. Collings [28] showed that 20 s of ultrasound exposure resulted in 96.5%

reduction in *A. catanella* cysts population but their complete elimination required at least an additional 110 s of exposure, which is highly disproportionate. Table 2.1 summarises some of the previous studies on ultrasonic inactivation of zooplankton.

Table 2.1 Ultrasonic inactivation of zooplankton.

Organism	Treatment parameters	Key findings	Ref.
<i>Artemia</i> sp.; <i>Branchionus</i> sp.; <i>Ceriodaphnia</i> sp.	19 kHz, 6–19 J/cm ³ ; 3–9 s exposure; 12.4 cm ³ flow reactor; 3.19–22.75 cm ³ /s; Horn output 1.26 cm ² .	Sonication times for 90% mortality varies with species: <i>Branchionus</i> sp. (9 sec), <i>Artemia</i> sp. (4 sec), <i>Ceriodaphnia</i> sp. (3 sec).	[48]
<i>A. amphitrite</i> cyprid	23, 63, 102 kHz; 150 s exposure; 10 ml vessels.	Most effective cyprid growth inhibition at 23 kHz; the difference in cyprid growth inhibition between sonication at 63 Hz and 102 kHz is not significant.	[65]
<i>Artemia</i> sp. cysts, larvae, adult	1.4 kHz; 5 min exposure.	Mortality varies with life-cycle stage: lowest for cysts (15%), adult (45%) larvae (50%).	[26]
<i>N. virens</i> larvae; <i>T. battagliai</i> ; <i>A. tonsa</i>	20 kHz; 500–4000 W; 0.2–1.6 m ³ /hr; Horn output 12.6 cm ² .	Mortality below 40%.	[89,95,96]

2.2.2 Effect on phytoplankton

Phytoplankton are a diverse group of autotrophic water-borne organisms. Some common types are blue-green algae, red algae, brown algae, diatoms, and flagellates, each having different responses to ultrasonic treatment. The phytoplankton growth inhibition mechanism is known to comprise of simultaneous pathways that include free radical attack and disruption of gas vesicles induced by acoustic resonance [97]. Sunlight, temperature and nutrients which are present in abundance near the surface of a water body provide a phytoplankton with the ingredients for photosynthetic activity and growth. The destruction of the gas vesicles due to ultrasound exposure obstruct the phytoplankton cell's access to the photosynthetic ingredients near the surface. As a consequence, their growth and multiplication are severely inhibited [98]. Tang et al. [52] compared the effect of 1.7 MHz irradiation on gas vacuole-positive cyanobacterium and gas vacuole-negative cyanobacterium and observed that the growth inhibition effect is more significant in the former. This observation suggests that vesicle disruption by ultrasound is responsible for limiting the proliferation of gas vacuole-positive phytoplankton.

Phytoplankton growth inhibition is also dependent on the sonication frequency. While low-frequency sonication has been shown to be effective against zooplankton, it loses its potency when applied to phytoplankton. Hao et al. [99] demonstrated that sonication at 1.7 MHz eliminated more *Spirulina platensis* than sonication at 20 kHz. Yamamoto et al. [100] compared the effect of four sonication frequencies (20, 580, 864, and 1146 kHz) on *Chlamydomonas concordia* and *Dunaliella salina* cells and found that the rate of cell disruption increased with sonication frequency. On the other hand, Joyce et al. [47] reported that sonication at 580 kHz was most effective against *M. aeruginosa*. These observations suggest that the destruction of gas vesicles through bubble resonance played a major role in phytoplankton growth inhibition.

Ultrasonic inactivation of phytoplankton cells is a complex challenge which is dependent on various competing factors. The variability in phytoplankton sensitivity to ultrasound treatment may be attributed to the differences in the cell structure which influences the severity of cavitation damage. Holm et al. [48] subjected estuarine dinoflagellate (*Pfiesteria piscicida*), marine diatom (*Thalassiosira eccentrica*), and freshwater cyanobacteria (*Anabaena flos-aquae*) to a 19 kHz field and found that the responses of the organisms vary across species. Mortality rate was highest for diatom while the dinoflagellate was the most resistant to low-frequency sonication, even at elevated ultrasound intensities.

Although many investigations have been carried out to study the effects of ultrasound on phytoplankton, it is not possible to draw a conclusion regarding the most effective ultrasonic configuration for treating particular phenotypes due to the myriad of experimental configurations, devices, and frequencies used in the studies [98]. What is known is that decimal reduction of phytoplankton requires an exposure timescale of minutes compared to the timescale of seconds for zooplankton.

The assessment of ultrasonic efficacy has so far focused on ultrasonic intensity and ultrasonic energy density, taking into account the geometry and size of the sonication vessel. However, such global metrics do not adequately represent the real potential of the ultrasonic devices. Leclercq et al. [98] argued that the test configurations in most of these studies involved highly non-uniform ultrasound fields, which limit the treatment region to just a small fraction of the sonication volume. Thus, the contaminated water must be exposed to a US field for extended periods to allow for sufficient exposure in the treatment zone. Depending on the frequency, ultrasound intensity, and the target species, exposure times required to achieve at least a 1-log reduction in algal population can range from several minutes [28,48] to a significant fraction of an hour [100–102]. It is appreciated that more research is needed to improve the US treatment efficacy considerably. Table 2.2 summarises previous studies related to the US inactivation of phytoplankton.

Table 2.2 Ultrasonic inactivation of phytoplankton.

Organism	Treatment parameters	Key Findings	Ref.
<i>M. aeruginosa</i> ; <i>Synechococcus</i>	1.7 MHz; 0.6 W/cm ² ; 300 s exposure.	Reduced growth of gas vacuole-positive cyanobacterium (<i>M. aeruginosa</i>); Negligible effect on the growth of gas vacuole-negative cyanobacterium (<i>Synechococcus</i>).	[52]
<i>P. piscicida</i> ; <i>T. eccentric</i> ; <i>A. flos-aquae</i>	19 kHz; 31–109 J/cm ³ ; 120–600 s exposure; 100 cm ³ vessel; Horn output 1.26 cm ² .	Decimal reduction time (DRT) varies with species. <i>T. eccentric</i> (2.1–3.8 min), <i>A. flosaquae</i> (5.6–7.2 min), <i>P. piscicida</i> (8–10 min).	[48]
<i>A. catanella</i> cyst	20 kHz; 150–160 W; 20–130 s exposure; 20–120 cm ³ samples; Horn output 1.23 cm ² .	96.5% mortality with 20 sec sonication; 100% mortality requires at least 130 sec.	[28]
<i>Spirulina platensis</i>	20 kHz; 70 W; Horn output 4.5 cm ² . 1.7 MHz; 14 W; Horn output 2.7 cm ² . 300 s exposure; 800 cm ³ samples.	63% reduction in 1.7 MHz field; 50% reduction in 20 kHz field.	[99]
<i>M. aeruginosa</i>	20 kHz, 0.0178 W/cm ³ ; 40 kHz, 0.0213 W/cm ³ ; 580 kHz, 0.0018 W/cm ³ ; 864 kHz, 0.0042 W/cm ³ ; 1146 kHz, 0.0026 W/cm ³ ; 1800 s exposure; 200 cm ³ samples.	Order of effectiveness: 20 < 1146 < 864 < 580 kHz.	[47]
<i>C. concordia</i> ; <i>D. salina</i>	20, 580, 864, 1146 kHz; 3–60 W; 1800 s exposure; 400 cm ³ samples.	Order of effectiveness: 20 < 580 < 864 < 1146 kHz.	[100]
<i>M. aeruginosa</i> ; <i>A. flos-aquae</i> ; <i>S. subspicatus</i> ; <i>Melosira</i> sp.	20 kHz, 1.47 W/cm ³ ; 582 kHz, 1.32 W/cm ³ ; 862 kHz, 0.41 W/cm ³ ; 1144 kHz, 1.02 W/cm ³ ; 1500 cm ³ samples.	16% reduction in <i>M. aeruginosa</i> , 99% reduction in <i>A. flos-aquae</i> , at 862 kHz, 13.3 J/cm ³ ; 20% reduction in <i>S. subspicatus</i> at 862 kHz, 6.7 J/cm ³ ; 83% reduction in <i>Melosira</i> sp. at 20 kHz, 1.9 J/m ³ .	[102]
<i>T. pseudonana</i> ; <i>A. tamarensis</i>	20 kHz; 500–4000 W; 0.2–1.6 m ³ /h. Horn output 12.6 cm ² .	Up to 71 % reduction based on <i>chlorophyll a</i> concentration.	[89,95,96]

2.2.3 Effect on bacteria

Maritime regulations [5,103] place particular emphasis on eliminating pathogenic bacteria from unintended transport, specifically toxigenic *Vibrio cholerae*, *eschericia coli* and intestinal *enterococci*. Like other classes of organisms, bacterial inactivation is a frequency and intensity dependent process. Kumar et al. [104] compared the inactivation of *E. coli* suspension subjected 35 kHz and 130 kHz sonication and observed that the latter was more effective. Hua and Thompson [67] reported that 205 kHz was the most effective against *E. coli* compared to the other frequencies investigated (20, 358, 618, and 1071 kHz). It was further reported that the inactivation rates for *E. coli* and *Streptococcus* were better with 500kHz ultrasound compared with 20kHz [105]. Further, *Streptococcus mutans* was observed to be the more resilient of the two owing to its thicker cell wall [106]. These findings indicate that the most lethal frequency for bacterial inactivation lies between 130 kHz and 358 kHz. This frequency range promotes hydroxyl radical generation [67,71,105] and improves the transport of free radicals away from the cavitation bubbles and into the target cells [67]. Research have shown that bacterial mortality rates have a strong correlation with US intensity and exposure time [48,104,107]. This holds true for most of the bacterium species studied, but for certain bacteria such as *cobetia marina* and *enterococcus avium*, there exists a limit beyond which further increase in ultrasonic intensity do not lead to significant improvement in mortality [48]. Table 2.3 summarises previous work related to ultrasonic inactivation of bacteria.

Table 2.3 Ultrasonic inactivation of bacteria.

Organism	Treatment parameters	Key findings	Ref.
<i>C. marina</i> ; <i>E.coli</i> <i>E. avium</i> ; <i>V. cholera</i> <i>B. globigii</i>	19 kHz; 100 cm ³ vessel; Horn output 1.26 cm ² .	90% reduction: <i>C. marina</i> – 3.6 min, 23 W/cm ² ; <i>E.coli</i> – 1.4 min, 31 W/cm ² ; <i>E. avium</i> – 20.1 min, 16 W/cm ² ; <i>V. cholera</i> – 0.9 min, 31 W/cm ² ; <i>B. globigii</i> – 213 min, 23 W/cm ² .	[48]
<i>E.coli</i>	20 kHz; 4.6–74 W/cm ² ; 0.27–0.46 W/cm ³ ; 1000 cm ³ vessel; Horn output 1.08–30.7 cm ² .	Inactivation depends moderately on US intensity and power density.	[67]
<i>E. coli</i> <i>Streptococcus mutans</i>	20 kHz, 500 kHz; 0.02–0.28 W/cm ³ ; 50 cm ³ samples; 300–1500 s exposure.	500 kHz most effective; Inactivation rate increase with ultrasonic intensity.	[105]

Table 2.3 (continued).

Organism	Treatment parameters	Key findings	Ref.
<i>E. coli</i>	35 kHz, 130 kHz; 50 W/cm ² , 2500 W/cm ³ ; 100 cm ³ samples; 300–1800 s exposure.	<i>E. coli</i> removal rate increases with sonication frequency and sonication time.	[104]
<i>Mycobacterium</i> sp.	20 kHz; 0.058–0.411 W/cm ³ ; 120 min exposure. 612 kHz; 0.013–0.114 W/cm ³ ; 210 min exposure. 150–300 cm ³ samples; 500 cm ³ treatment vessel.	<i>Mycobacterium</i> sp. removal rate increases with ultrasonic power density, and sonication time; Higher removal rates at low sample volumes; US treatment at 20 kHz is more effective than at 612 kHz.	[108]

2.3 Assessment of current US radiator designs

2.3.1 Limitations of conventional resonators

Ultrasonic resonators are devices used for transforming mechanical vibrations to acoustic energy. The acoustic energy can be used to intensify chemical synthesis, extract biological compounds, disinfect water, and enhance other liquid processes. Ultrasonic horns are typically constructed from metals that have high fatigue strengths and low acoustic losses. The salient aspect of horn design is the resonance frequency and the determination of the correct resonance wavelength. The wavelength should usually be the integer multiple of the half wavelength of the horn. The resonance frequency of a horn that has a simple shape can be determined analytically, while finite element method is employed for more complex geometries. Ultrasonic devices are also increasingly being explored for adoption in new applications, driving the development of new and innovative designs.

Commercially available horns come in many shapes and sizes, but the most common are the probe-types, including catenoidal, exponential, conical, and stepped horns. These devices are most commonly used in static batch processes such as lysing, emulsification, and disinfection. Horns with broad and flat outputs are usually used for welding while horns with sharper outputs are more suitable for cutting.

Conventionally, high-amplitude directional ultrasonic devices have a correspondingly small application area. The inverse relationship between the amplification factor and the input-to-output area ratio imposes a limitation in the design of the probe-type device. In conventional horns, the output amplitude and the output area cannot be maximised simultaneously, limiting the amount of

acoustic power that can be transmitted. The ultrasound power P (W) radiated into the acoustic medium can be calculated from [109]:

$$P = \frac{2\pi^3 \rho f^4 S^2 A^2}{c}, \quad (2.2)$$

where ρ (kg/m³) is the density of the medium, c (m/s) is the speed of sound in the medium, f (Hz) is the vibrating frequency, A (m) is the vibration amplitude of the radiator output surface, and S (m²) is output surface area of the resonator.

Moussatov et al. [110] reported that a well-developed cavitation field begins to form with a specific acoustic power exceeding 8 W/cm². Using equation (2.2), a conventional probe device with 25 mm output diameter operating at 20 kHz would have to operate at an output amplitude of around 5 μ m in order to develop a cavitation field in water. Conventional mono-directional devices designed for low-frequency ultrasonic applications, can achieve amplitudes of that order, but their output diameters are usually less than 30 mm. Although the output diameter depends on the design frequency, material of the resonator, and the vibrational amplification required, the output diameter is typically less than $\lambda/4$. Conversely, block horns can have lateral output dimensions between $\lambda/4$ and $\lambda/2$ (typically between 50 mm and 150 mm for horns constructed from titanium-alloy), but have significantly lower vibrational amplitudes and amplification factors. Despite the known limitations of conventional probe-type devices, they are widely used in US inactivation studies including those works reviewed in Section 2.2. Moving forward, there is a need to focus the research towards new resonator designs that can achieve a high vibrational amplitude (50–100 μ m) over a large radiating surface area ($\gg 20$ cm²) to achieve a well-distributed cavitation field. The following sections review the various resonator designs found in industrial, academic, and patent literature, with the goal of assessing their usefulness in ballast water treatment application.

2.3.2 Large area mono-directional radiators

Large area mono-directional radiators are longitudinal mode devices with relatively flat and broad output faces. The barbell-shaped design of Peshkovsky et al. [111,112] has a low input-to-output face ratio (1:1) for a high amplification factor of 2 to 11. This is achieved through a unique five-section design comprising three cylindrical sections bridged by two translational sections as shown in Figure 2.1. The length of the translational section is related to the wave number and the ratio of diameters of the interconnecting cylindrical sections, and has the effect of reducing the dynamic stress in the structure. When compared to conventional probes of similar dimensions, the barbell horn exhibits a much more uniform stress distribution to enable operation at a relatively high vibrational amplitude without breaking. More recently, the barbell horn dynamic characteristics

were enhanced by adopting a catenoidal profile at the translational sections. This geometric modification permits a shorter translational section than would be allowed with a conical profile [113]. To put things to perspective, a typical industrial-grade horn having an output diameter of around 40 mm will operate at a maximum amplitude of around 25 μm . In contrast, a barbell horn having an output diameter of 65 mm is capable of operating at a maximum amplitude of around 100 μm . Relative to the conventional device, the barbell horn offers an increase in acoustic power output by a factor of 40, which is significant.

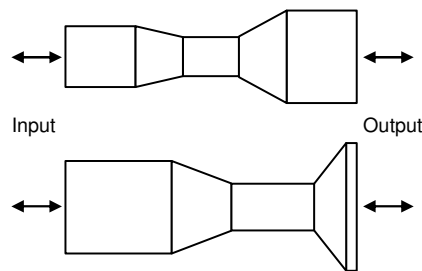


Figure 2.1 Barbell-shaped horns [111,113].

2.3.3 Ring radiators

Radial mode devices have been used since the 1970s [114] for wire drawing, but a thorough study on the effect of tool loading and parasitic modes on radial die performance was carried out only twenty years later [115]. Application of the radial design in water treatment soon followed [116] with the intention of overcoming the radiating area limitation of conventional probe-type devices [117]. In a radial-mode radiator (see Figure 2.2), acoustic waves are emitted via its circumferential surfaces, providing a radiating surface area that is at least 1-order of magnitude greater the radiating surface provided by a conventional probe-type device. The ability of a radial radiator to distribute the ultrasonic energy over a larger area enable the device to be operated at considerably high ultrasonic power density [118]. Also, the geometry of the radial-mode radiator encourages the dispersion of bubbles, minimising the effect of acoustic shielding arising from bubble coalescence.

The radial-mode device radiates ultrasonic energy from its outer circumferential surface when operated in a pure fundamental radial mode. Since acoustic pressure decays with increasing distance from the radiating surface, the shape and size of the US reactor must be carefully considered. Meanwhile, summation of wavefronts emitted from the internal circumference of the radial device generates very high acoustic pressure around the centre cavity [38]. Although the radial design appears simple, sizing for an industrial application requires detailed analysis of the design

requirements. Typically, an R0 mode tuned radiator will have its mean circumference equal to an integer multiple of its wavelength [27]. This implies that the cylindrical reactor must have an internal diameter of at least 100 mm in order to fit a Ti-alloy radiator tuned to 20 kHz [119]. If a larger reactor vessel is required, the radiator can be scaled-up accordingly (using the relationship between mean circumference and the wavelength), but its thickness should not exceed $\lambda/4$ to ensure a pure R0 mode operation.

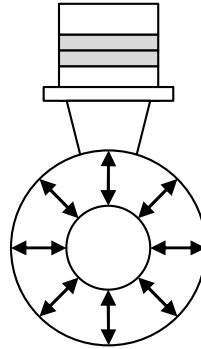


Figure 2.2 Radial mode ring radiator.

2.3.4 Tubular radiators

Tubular radiators are hollow cylindrical structures with axial length L_z (m) to mean diameter \bar{D} (m) aspect ratio equal to an integer multiple of $\pi/2$ [120,121]. The radial mode is achieved by coupling the tube with conventional longitudinal mode transducers at both ends as shown in Figure 2.3a. Foil erosion tests showed that tubular radiators can generate a cavitation field inside and around the tube. In practise, harnessing the acoustic energy from both sides of the circumference will require a relatively complex reactor design which will be very costly to build. Further, the thickness of the tubular radiator has been shown to influence the acoustic energy dispersion [122] and must therefore be carefully studied prior to implementation.

Most tubular radiators have constant internal and external diameters, but a conical profiled annulus has also been proposed as shown in Figure 2.3b [123]. This particular tubular resonator comprises a piezoelectric actuator section coupled to a cup-shaped radiator section which can hold liquids for ultrasonic processing. The radial vibration of the conical surface provides a relatively large area for acoustic transmission into the processing liquid. However, considerable fraction of the acoustic energy generated is also radiated out from the external surface, making such design highly inefficient. Figure 2.3c shows another iteration of the tubular radiator configuration which combines the cup-shaped design with a barbell horn [124] to achieve even higher radial displacement

amplitudes. Although the tubular resonators are conceptually interesting, they are difficult to scale-up and their use may be limited to laboratory-scale batch processes only.

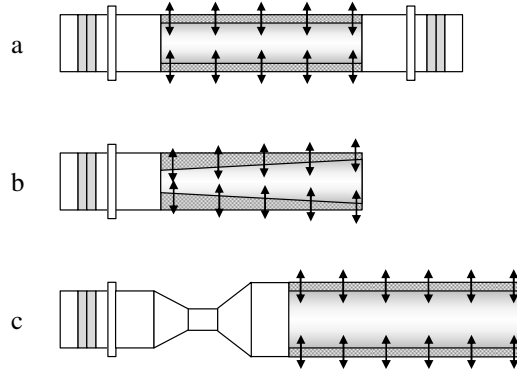


Figure 2.3 Tubular radiators: (a) conventional [120,122]; (b) cup-shaped [123]; (c) barbell-coupled [124].

2.3.5 Corrugated cylindrical radiators

Multiple-stepped radiators resemble ultrasonic probes (see Figure 2.4) except that their design is optimised for acoustic radiation in the radial direction. A multiple-stepped radiator follows the design principle of any longitudinal-mode device, wherein its axial length is an integer multiple of $\lambda/2$. In any longitudinal-mode device, the stress-wave propagates primarily in the axial direction, but a fraction of the vibrational energy is always transmitted radially due to Poisson's effect. The multiple-step design amplifies radial acoustic transmission through lateral diversion of the incoming axial stress-wave. The origin of the so-called multiple-stepped horn is not clear, but elements of its design principles can be found in embodiments of the Rawson [116] and Peshkovsky [111]. Rawson's design shown in Figure 2.4a consists of concentric cylindrical sections of diameters d_1 and d_2 , and a pitch of $n\lambda/2$. Meanwhile, Peshkovsky's design shown in Figure 2.4b provisioned an arbitrary number of cylinder diameters and pitches in a single device, allowing greater flexibility in the design.

More recently, Wei and colleagues [125] developed a multiple-stepped horn design which, unlike earlier versions, features abrupt changes in the cylindrical cross-sections and a variable pitch as illustrated in Figure 2.4c. A variation of the multiple-stepped horn design feature a conical tip instead of the usual flat profile to increase the effective range of the ultrasonic field radiating from the tip [126]. This multi-stepped design was reported to have achieved up to 165% higher energy efficiency and between 240% and 1500% more acoustic energy delivery compared to a conventional probe. Due to its impressive acoustic performance, multiple units of the multiple-stepped horn was deployed in a prototype ballast water treatment reactor [127].

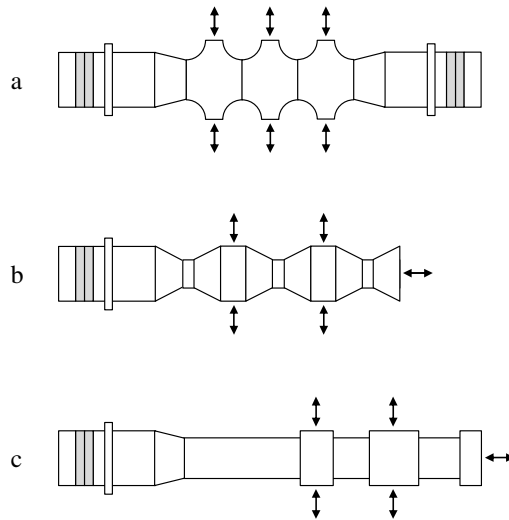


Figure 2.4 Multiple-stepped horn variants; (a) Rawson [116]; (b) Peshkovsky et al. [111]; (c) Wei et al. [125].

2.4 Assessment of current US reactor designs

Present ultrasonic technology is still too costly for ballast water treatment application. Although several US-based BWMS have been demonstrated in laboratory-scale and pilot-scale tests, scaling up for shipboard utilisation remain a significant challenge. Typical full-scale BWMS have treatment rated capacities of $120 \text{ m}^3/\text{h}$ to $3000 \text{ m}^3/\text{h}$, whereas US-based systems have only been tested at flow rates in the order of $1 \text{ m}^3/\text{h}$ [24,29,48]. When it comes to ballast water treatment, there is a significant gap between ultrasonic research and its industrial application. This technological gap is evident from the absence of US-based BWMS in the list of statutory-approved products. On a more positive note, there are successful BWMSs that use ultrasound as a secondary treatment process to augment a conventional physical or chemical treatment method [20]. Around five of such system exists at the time of writing. One of the US-augmented system uses ultrasound to enhance filtration [128], while another uses ultrasound to enhance its advanced electrolysis oxidation processes (AEOP) [129]. In both implementations, the role of ultrasound is quite rudimentary. Systems utilising ultrasound as the core treatment have been conceptualised, and some may have been piloted [130,131]. However, none have completed the test requirements necessary for statutory approval.

2.4.1 Conventional batch reactors and baths

In typical horn-type reactors, the cavitation intensity decreases exponentially away from the radiating surface and vanishes beyond a distance of a few centimetres. It is challenging to scale up such systems for large process volumes without deploying more devices and expending more energy to ensure the a good coverage in the treatment vessel [132]. An ultrasonic bath can provide good

acoustic field coverage and larger treatment volumes than a flow-through reactor, but an effective treatment require long processing time. An ultrasonic bath typically comprises of a rectangular tank and an array of transducers mounted at the bottom or at the side of the tank. Ultrasonic baths can be easily configured for multiple frequency operation to increase the cavitation activity [95]. However, ultrasonic baths are only suitable for batch processes up to a volume of 8 m³ [133]. In ballast water treatment application where ballast tank volumes range from 500 m³ to 1000 m³, more transducers may be deployed and operated over long periods to deliver the required ultrasonic dose. However, this solution would be too costly to implement and too difficult to maintain in a ship.

2.4.2 Flow-through reactors

The concept of a flow-through ultrasonic irradiation chamber for continuous processing is not a new idea. Numerous designs have been conceived, and many have been tested for their various intended applications. Many early designs feature a multitude of transducers mounted on the walls of a cylindrical or rectangular conduit as shown in Figure 2.5a. The tight coupling between the transducers and the conduit produces acoustic waves that treat the liquid contained within [134,135]. A rigorous analysis of the vibration characteristics of the resonant cavity is needed to ensure efficient transfer of the vibration energy to the liquid. Maximum energy transfer may be achieved by providing a conduit with an acoustic impedance similar to the vibrating element, and further imposing a conduit thickness of $\lambda / 4$ [134]. Another variation of the resonant cavity design exploits the Poisson deformation induced at the nodal circumference of a longitudinally vibrating transducer, which in turn induce radial vibrations in the tubular conduit (see Figure 2.5b) [136]. This arrangement can potentially reduce the number transducers required to agitate the liquid compared to the earlier designs [134,135]. However, since one end of the conduit is blocked by the transducer, another opening will be required to enable a continuous treatment process. In doing so, the vibration behaviour of the structure will be altered and a redesign must ensue for optimum performance. Alternatively, the circumferential positioning of the vibrating element as shown in Figure 2.5c automatically provides the preferred flow-through configuration.

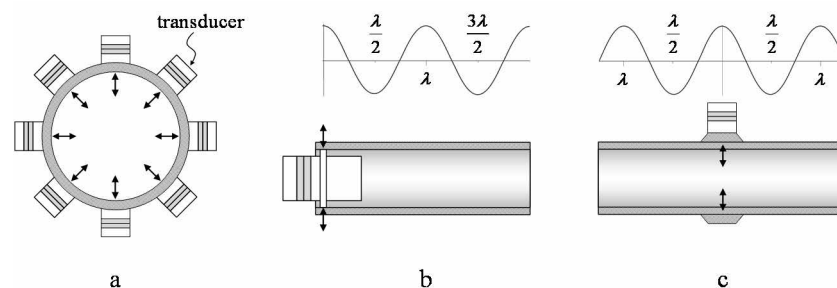


Figure 2.5 Resonant cavities: (a) multiple-transducer arrangement [134]; (b) single transducer arrangement with a closed end [136]; (c) single transducer arrangement with open ends [137].

Although the resonant cavity configurations shown in Figure 2.5b and Figure 2.5c are relatively less complex compared to designs that utilise multiple transducers to achieve a similar vibration profile, they may not be the most efficient. In both configurations, vibrational amplitude is highest nearer to the transducer resulting in an acoustic field that is not uniform.

Designs that decouple the vibration characteristics of the active element from the conduit are considered more robust due to their flexibility in adapting to a variety of conduit configurations. This can be achieved by having the ultrasound radiator in direct contact with the liquid. In early designs, the piezoelectric crystals are mounted directly into the liquid [138] to minimise transmission losses. However, the crystals are prone to failure due to its exposure to moisture, and high tensional stresses. Later designs incorporate backing materials to isolate the crystals from the wet medium, and to provide a preload force on the crystals for better dynamic performance [139,140].

A reactor can be configured with multiple transducers arranged in a regular pattern around the body of the reactor as shown in Figure 2.6a. The spacing between transducers need to be determined numerically through an optimisation process to ensure a good ultrasonic field distribution. Further, it is also possible to operate the transducers at different frequencies to achieve the synergistic treatment effects of a simultaneous low-frequency and high-frequency ultrasound irradiation [20].

Helical arrangement of the ultrasonic transducers may also be considered, but the choice of radiator is critical for a good ultrasound field coverage. Figure 2.6b illustrates an example of a flow-through reactor with a helical configuration, in which the use of multiple-stepped horns (refer to Section 2.3.4) provide a relatively good ultrasound field distribution in the reactor cross-section [22]. Similarly, the distance between radiators need to be determined carefully – too large spacing between probes results in dead regions which lack ultrasound exposure, while the too small spacing between probes results in an ineffective field such as a cancelling field.

A unique reactor configuration comprising of several piezoceramic rings enclosing a cylindrical conduit is shown in Figure 2.6c [141]. A notable feature of the design is the use of a pressurised fluid medium as a means of transferring the acoustic energy to the treatment fluid. Formation of cavitation bubbles in the transmission fluid is suppressed through hydraulic pressurisation to circumvent the eroding effects of cavitation. Motor oil or other electrically non-conducting fluids are used as the acoustic energy transfer medium so that the piezoceramic elements can be in direct contact with the transmission fluid. Although an interesting concept, the lack of backing material to keep the piezoceramics under compression limits the operation to vibrational amplitudes that will be too low to be of practical use in ballast water treatment.

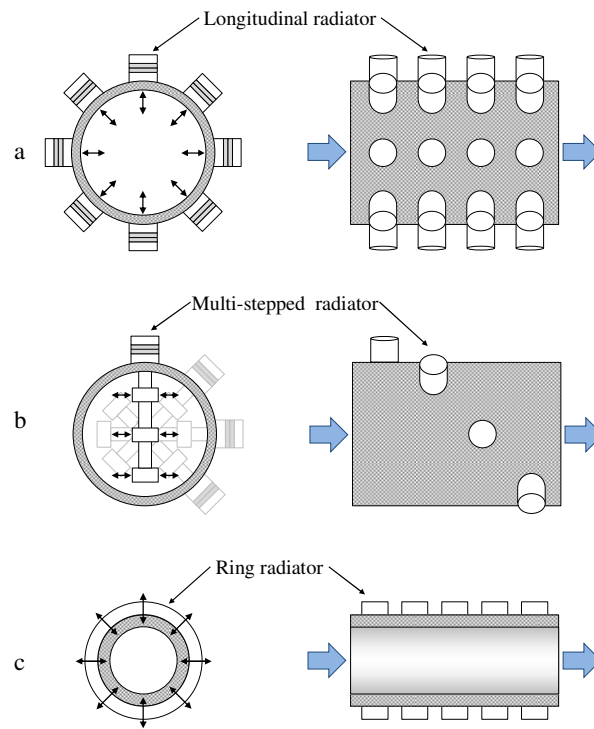


Figure 2.6 Flow-through reactor configurations: (a) longitudinal radiators in linear array [20]; (b) multi-stepped radiator in spiral cross-flow [22]; (c) serial ring radiators [141].

2.5 Performance challenges in the operating environment

2.5.1 Operational variability

Shipboard ballast water treatment equipment is expected to perform efficiently and reliably in the actual operating environment where the salinities, temperature, water quality, and organism diversity can vary considerably. Depending on the ship type and its trade route, water salinity can range from 0.1 ppt in freshwater lakes to 35 ppt in the coastal regions [142,143]. Meanwhile, seawater temperature can vary from 0 to 35 °C [144]. Ballast water pressure and flow rate can also deviate from the rated values, especially near the start and towards the end of a ballast water uptake or discharge operations. These operational variabilities add complexity to the ultrasonic system operation, making it extremely challenging to design a disinfection system that covers all installation and operation scenarios.

2.5.2 Water loading effects

The behaviour of a piezoelectric ultrasonic resonator subjected to water load can be markedly different from its behaviour at atmospheric pressure. Various studies have shown that the resonance frequencies of a radiator can shift when subjected to external loading [115,145,146]. The shift in

resonances between in-air and in-water measurements can vary between 10% and 25% depending on the vibrational mode, resonator geometry, and immersion depths [147–150]. Resonators with large radiating surfaces exhibit a more substantial shift in their resonance frequency [35]. To add further complication, the shifts of the resonance peaks are not always uniform [115] and changes in modal separation are highly unpredictable. This increases the risk of modal coupling if the change results in the non-tuned mode frequencies approaching the tuned mode frequency.

The change in resonance frequencies Δf can be estimated using Sauerbrey [151], Kanazawa and Gordon [152], or Hunt et al. [153] formulations, respectively,

$$\Delta f = \frac{-2f_o^2 \Delta m}{A \sqrt{\rho_q K_q}}, \quad (2.3)$$

$$\Delta f = -2f_o^{3/2} \sqrt{\frac{\eta_L \rho_L}{\pi \rho_q K_q}}, \text{ and} \quad (2.4)$$

$$\Delta f = \frac{-2f_o^2 h_L}{\sqrt{\rho_q K_q}} \left[\rho_L - \frac{K_L}{V_S^2} \right]. \quad (2.5)$$

These expressions relate Δf and the unloaded resonance frequency f_o (Hz) to the properties of the piezoelectric device and the acoustic medium represented by their density ρ (kg/m³), stiffness K (Pa), and viscosity η (Pa.s). The loading conditions were represented through the mass loading Δm (kg), acoustic wave radiating area A (m²), water column thickness h (m), and the acoustic shear wave velocity V_S (m/s). The subscripts q and L denote the properties associated with the piezoelectric material and the acoustic medium respectively.

In addition to resonance shift, water loading can dramatically alter the electromechanical impedance and quality factor of a piezoelectric resonator. Measurements performed on a conventional 25 mm ultrasonic probe showed more than 10-fold increase in the minimum impedance Z_m (Ω) and a corresponding 10-fold decrease in mechanical quality factor when the device is fully loaded [154].

Although water loading effect is often neglected during the initial design of an ultrasonic device, it is worthwhile to quantify its impact early in the design stage. Understanding the electromechanical behaviour of the ultrasonic device subjected to different water loading conditions can contribute to, for example, the design of more robust electronic circuitry that delivers the appropriate responses to changes in the operating environment and ensure consistent performance [148].

2.5.3 Acoustic impedance matching

The ultrasonic resonator radiating surface converts mechanical vibration to acoustic energy which propagates through the medium to produce the desired effects such as cavitation. However, the conversion is lossy due to the significant difference in the acoustic impedance of the radiating structure and the acoustic medium. As shown in Table 2.4, the acoustic impedance of common transducer materials is larger than the acoustic impedance of water (acoustic impedance is $Z_{ac} = \rho c = \sqrt{E\rho}$). Depending on the degree of impedance mismatch, a fraction of the vibration energy is reflected back to its source [41].

Table 2.4 Acoustic impedance of common transducer materials and pure water at 20 kHz.

Parameters	SS316L	AL7075	Ti-4-6	Water
Acoustic impedance (MRayl)	39.3	14.2	22.5	1.5

One way to overcome this is through the use of one or more impedance matching layers between the resonator and the medium. This matching layer would be a quarter-wave thick and have a characteristic impedance that is close to $\sqrt{Z_S Z_L}$ [155]. Assuming the acoustic medium is water, a characteristic acoustic impedance of 4 to 8 MRayl is necessary to maximise acoustic transmittance [112]. In reality, sourcing of materials with such impedances is not straightforward and would likely involve more than one layer of materials such as epoxy [156], glass [157], or a specially formulated mixture of epoxy and metal powder [158,159]. The characteristic impedance of seawater ranges between 1.4 MRayl and 1.6 MRayl for salinities in the range 0 to 40 ppt and temperatures of 0 to 30 °C [25]. Since the variation of seawater characteristic impedance is small, a matching layer designed for use at a particular salinity will also work at other salinities. Thus, what is more important in the matching layer design is the selection of materials and the application method for cost-effective implementation.

2.5.4 Variability of marine water constituents

Driving ultrasonic resonators at high vibrational amplitudes can generate intense cavitation fields, provided the population of pre-existing nuclei and nucleation sites [160,161], and concentration of dissolved gas [162,163] in the water are favourable. Ceccio et al. [42] showed that for similar flow conditions, there were significant differences in the size and population of cavitation bubbles between freshwater and seawater. In natural seawater, the presence of suspended solids and bubbles are potential nucleation sites from which cavitation bubbles can be induced. However, depending on the

source of the seawater, there can be significant variability in the concentration of dissolved gas, suspended solids, and other constituents [25,164,165].

Liu et al. [163] reported that the presence of excessive dissolved gas impedes the formation of cavitation bubbles and reduces cavitation intensity. This is because the high concentration of dissolved gas has the effect of increasing the nucleation rate so immensely that the bubbles coalesce soon after formation [44]. As a result, the cavitation bubbles become more voluminous and collapse with more subdued impact. Large bubbles also tend to form air pockets that block the acoustic energy from penetrating deeper into the medium [58].

Most laboratory-scale studies were performed under idealised conditions, and distilled water or artificial seawater are commonly employed for experimental repeatability. However, translational technologies must be tested in the actual operating environment because a ballast water treatment system is expected to deliver repeatable performance in non-ideal conditions.

2.5.5 Nonlinear dynamic behaviour of ultrasonic devices

Although the efficacy of ultrasonic disinfection has been demonstrated by various investigators [28,48,67], scaling up to industrial-level capacities is often hampered by the nonlinear vibration behaviour of the devices when operated at high power levels. Nonlinear dynamic behaviour may be associated with changes in material properties, the physical geometry of the resonant structure, or from nonlinear forces exerted on the structure [166]. Piezoceramics are known to respond to elevated stress with an increase in elastic compliance, which has the effect of shifting the resonance frequency. Operation at high amplitudes can generate excessive heat which can further amplify the nonlinear behaviour and contribute to mechanical and dielectric losses [167]. The nonlinear behaviour can bring about changes in resonance frequency, saturate the vibration response, and cause energy leakage to spurious modes [168,169]. All these leads to the deterioration of transducer performance and premature failures. Unintended operation in a non-tuned mode due to significant shifts in the resonance frequency can adversely affect the efficiency and reliability of the device.

The ultrasonic treatment unit is a highly-tuned system at every stage of its energy conversion chain. Slight variations in transducer characteristic can bring about significant changes to the electrical current supplied, and the performance of the system can be adversely affected [170]. Thus, it is always useful to identify nonlinear interacting modes early in the design stage through a combination of FE analysis and experimental modal analysis so that appropriate combination of design and operational measures can be meted out during actual deployment.

2.6 Conclusion

Successful ultrasonic treatment of ballast water requires a holistic understanding of the system boundaries and limitations. Various strategies to increase the efficacy of ultrasonic treatment have been discussed. This include adjustments to operational parameters (e.g. frequency, amplitude, power density), alteration of the process parameters (e.g. flow rate, pressure, sonication time), and enhancements in the design of the ultrasonic system (e.g. reactor configuration, new materials, new resonator designs, smarter electronics).

The use of high-power ultrasonic resonators is essential if significant mortality is expected and new resonator designs capable of producing intense cavitation fields that are also well distributed is desired. New resonator designs should overcome the radiating surface area limitation of conventional devices and must achieve the desired disinfection rate with considerably fewer devices, and with relatively low power consumption. Achieving these goals will reduce both capital and running costs of the ultrasonic treatment system, and promote its use in the marine industry.

More importantly, there is a need to elevate ultrasonic disinfection studies beyond the laboratory. Full-scale tests in the actual operating environment using organisms found in nature is critical for demonstrating the performance of the system.

Chapter 3

Piezoelectric Transducer Modeling

3.1 Fundamental equations

3.1.1 Equations of motion

Modal analysis is a technique to determine a structure's vibration characteristics and is the most fundamental of all dynamic analysis types. Designers of ultrasonic devices make use of finite element method to determine the natural frequencies and mode shapes, and to predict the dynamic response of a structure. Finite element vibration analysis requires that the motion of a structure be described in mathematical form as

$$[M]\{\ddot{u}\} + [C]\{\dot{u}\} + [K]\{u\} = \{F^a\}, \quad (3.1)$$

where M (kg), C (N.s/m), and K (N/m) are the mass, damping, and spring constants respectively.

3.1.2 Modal and harmonic response

Modal solutions are obtained by setting the resultant force F (N) and damping coefficients in equation (3.1) to zero and then solving for the eigenvalues and eigenvectors,

$$([K] - \omega^2 [M])\{u\} = 0, \quad (3.2)$$

where the eigenvalues ω_1^2 represent the square of the natural frequencies, and the corresponding eigenvectors u_1 represent the mode shapes.

Harmonic response analysis proceeds by first assuming that all points in the structure are moving at the same frequency, but not necessarily in phase. The displacement u (m), velocity \dot{u} (m/s), and acceleration \ddot{u} (m/s²) vectors may then be expressed as

$$\{u\} = \{u_{\max} e^{i\theta}\} e^{i\omega t}, \quad (3.3)$$

$$\{\dot{u}\} = \{\omega u_{\max} i e^{i\theta}\} e^{i\omega t}, \text{ and} \quad (3.4)$$

$$\{\ddot{u}\} = \{-\omega^2 u_{\max} e^{i\theta}\} e^{i\omega t}. \quad (3.5)$$

Substituting equations (3.3) to (3.5) into equation (3.1) gives

$$\left(-\omega^2 [M] + i\omega [C] + [K]\right)\{u_i\} = \{F_i\}. \quad (3.6)$$

The harmonic response is obtained by solving for u_i . The above equation assumes that the mass, damping, and spring coefficients are constants, implying a linear elastic behaviour.

3.2 Piezoelectric transduction

3.2.1 Theoretical background

The ability of piezoelectric material to function as actuators and transducers stems from its mechanical strain producing property when subjected to an electric field, or conversely, its ability to generate an electric charge when subjected to a mechanical strain. Finite element analysis is a powerful technique that can be employed to calculate the strain and electric field distribution in complex geometries. This technique accelerates the design process and significantly reduce the development time and costs related to prototyping and testing of piezoelectric transducers. Successful application of finite element technique in transducer design requires that the elastic, piezoelectric, and dielectric properties be completely defined to fully characterise the piezoelectric effect within a given material. These properties enable the finite element code to calculate the degrees of freedom (DOF) at each node of the structural domain. For a piezoelectric material, the DOFs are the three displacement components (u_1, u_2, u_3), and voltage.

3.2.2 Constitutive relations

Linear behaviour of a piezoelectric continuum can be described by two fundamental electromechanical constitutive relations in which the elastic, piezoelectric, and dielectric coefficients are assumed constant and independent of the applied mechanical stress and electric field. This linear assumption is valid for low mechanical stress levels and low electrical fields under quasi-static conditions (i.e. dynamic effects are not represented). In reality, the piezoelectric behaviour is often nonlinear, especially under high stresses or voltages. Also, hysteresis effects, electrical ageing, and electro-mechanical interactions also contribute to the nonlinear behaviour of the material.

The strain-charge form of the piezoelectric constitutive relation with tensors in Voigt notation is expressed as [171],

$$\boldsymbol{\varepsilon}_i = s_{ij}^E \boldsymbol{\sigma}_j + d_{ik} \mathbf{E}_k, \text{ and} \quad (3.7)$$

$$D_k = d_{ki} \boldsymbol{\sigma}_i + e_{kl}^{\sigma} \mathbf{E}_l, \quad (3.8)$$

where the indices $i, j = 1, 2, \dots, 6$, and $k, l = 1, 2, 3$. Equation (3.7), which relates the strain $\boldsymbol{\varepsilon}$ generated due to the application of electric field \mathbf{E} (V/m) is also referred to as the actuator equation. Meanwhile, equation (3.8), which relates the electrical charge generated due to applied stress $\boldsymbol{\sigma}$ (N/m²) is also known as the sensor equation. The piezoelectric constitutive relations can also be expressed in stress-charge form as,

$$\boldsymbol{\sigma}_i = c_{ij}^E \boldsymbol{\varepsilon}_j - d_{ik}^* \mathbf{E}_k, \text{ and} \quad (3.9)$$

$$D_k = d_{ki}^* \boldsymbol{\varepsilon}_i + e_{kl}^{\varepsilon} \mathbf{E}_l, \quad (3.10)$$

where the actuator equation now relates stress generated due to the application of an electric field, and the sensor equation gives the electric charge density produced by a strain. Expressing equations (3.7), (3.8), (3.9), and (3.10) in matrix form, the strain and stress vectors in standard engineering notation are

$$\boldsymbol{\varepsilon}_i = \begin{bmatrix} \boldsymbol{\varepsilon}_1 \\ \boldsymbol{\varepsilon}_2 \\ \boldsymbol{\varepsilon}_3 \\ \boldsymbol{\varepsilon}_4 \\ \boldsymbol{\varepsilon}_5 \\ \boldsymbol{\varepsilon}_6 \end{bmatrix} = \begin{bmatrix} \boldsymbol{\varepsilon}_{11} \\ \boldsymbol{\varepsilon}_{22} \\ \boldsymbol{\varepsilon}_{33} \\ \gamma_{23} \\ \gamma_{13} \\ \gamma_{12} \end{bmatrix}, \text{ and } \boldsymbol{\sigma}_j = \begin{bmatrix} \boldsymbol{\sigma}_1 \\ \boldsymbol{\sigma}_2 \\ \boldsymbol{\sigma}_3 \\ \boldsymbol{\sigma}_4 \\ \boldsymbol{\sigma}_5 \\ \boldsymbol{\sigma}_6 \end{bmatrix} = \begin{bmatrix} \boldsymbol{\sigma}_{11} \\ \boldsymbol{\sigma}_{22} \\ \boldsymbol{\sigma}_{33} \\ \tau_{23} \\ \tau_{13} \\ \tau_{12} \end{bmatrix}, \quad (3.11)$$

where $\boldsymbol{\varepsilon}_{11}$, $\boldsymbol{\varepsilon}_{22}$, and $\boldsymbol{\varepsilon}_{33}$ are normal strains along axes 1, 2, 3 respectively, and γ_{23} , γ_{13} , and γ_{12} are shear strains. Similarly, $\boldsymbol{\sigma}_{11}$, $\boldsymbol{\sigma}_{22}$, and $\boldsymbol{\sigma}_{33}$ are the normal stresses along axes 1, 2, 3 respectively, and τ_{23} , τ_{13} , and τ_{12} are the shear stresses.

The electric displacement field D (C/m²), and electric field vector \mathbf{E} (V/m), are given by

$$D_k = \begin{bmatrix} D_1 \\ D_2 \\ D_3 \end{bmatrix}, \text{ and } \mathbf{E}_i = \begin{bmatrix} \mathbf{E}_1 \\ \mathbf{E}_2 \\ \mathbf{E}_3 \end{bmatrix}. \quad (3.12)$$

The electrical charge generated by the piezoelectric material due to applied stress can be calculated by multiplying D from equation (3.8) by the cross-section area of the device. In a piezoelectric transducer assembly, measuring the electrical charge generated can provide an estimate of the preload applied to the piezoelectric material.

The following sections describe the elastic, piezoelectric, and dielectric property of the piezoelectric material, through the elasticity matrices, s^E and c^E , the piezoelectric matrices, d and d^* , and dielectric permittivity ϵ , respectively.

3.2.3 Stiffness and compliance

The elastic properties of a piezoelectric material are defined by the compliance matrix s^E (m^2/N), or the stiffness matrix c^E (N/m^2), depending on which form of the constitutive relations is used. The compliance and stiffness matrices, each having 36 coefficients are reduced to just 6 by isotropic symmetry in the plane orthogonal to the poling direction ($s_{ij}^E = s_{ji}^E$ and $c_{ij}^E = c_{ji}^E$), several elements being equal ($s_{22}^E = s_{11}^E$, $s_{23}^E = s_{13}^E$, $s_{44}^E = s_{55}^E$), and several others are zero, due to the property of the piezoelectric material:

$$\begin{bmatrix} s^E \end{bmatrix} = \begin{bmatrix} s_{11}^E & s_{12}^E & s_{13}^E & s_{14}^E & s_{15}^E & s_{16}^E \\ s_{21}^E & s_{22}^E & s_{23}^E & s_{24}^E & s_{25}^E & s_{26}^E \\ s_{31}^E & s_{32}^E & s_{33}^E & s_{34}^E & s_{35}^E & s_{36}^E \\ s_{41}^E & s_{42}^E & s_{43}^E & s_{44}^E & s_{45}^E & s_{46}^E \\ s_{51}^E & s_{52}^E & s_{53}^E & s_{54}^E & s_{55}^E & s_{56}^E \\ s_{61}^E & s_{62}^E & s_{63}^E & s_{64}^E & s_{65}^E & s_{66}^E \end{bmatrix} = \begin{bmatrix} s_{11}^E & s_{12}^E & s_{13}^E & 0 & 0 & 0 \\ s_{12}^E & s_{11}^E & s_{13}^E & 0 & 0 & 0 \\ s_{13}^E & s_{13}^E & s_{33}^E & 0 & 0 & 0 \\ 0 & 0 & 0 & s_{44}^E & 0 & 0 \\ 0 & 0 & 0 & 0 & s_{44}^E & 0 \\ 0 & 0 & 0 & 0 & 0 & s_{66}^E \end{bmatrix} \quad (3.13)$$

$$\begin{bmatrix} c^E \end{bmatrix} = \begin{bmatrix} c_{11}^E & c_{12}^E & c_{13}^E & c_{14}^E & c_{15}^E & c_{16}^E \\ c_{21}^E & c_{22}^E & c_{23}^E & c_{24}^E & c_{25}^E & c_{26}^E \\ c_{31}^E & c_{32}^E & c_{33}^E & c_{34}^E & c_{35}^E & c_{36}^E \\ c_{41}^E & c_{42}^E & c_{43}^E & c_{44}^E & c_{45}^E & c_{46}^E \\ c_{51}^E & c_{52}^E & c_{53}^E & c_{54}^E & c_{55}^E & c_{56}^E \\ c_{61}^E & c_{62}^E & c_{63}^E & c_{64}^E & c_{65}^E & c_{66}^E \end{bmatrix} = \begin{bmatrix} c_{11}^E & c_{12}^E & c_{13}^E & 0 & 0 & 0 \\ c_{12}^E & c_{11}^E & c_{13}^E & 0 & 0 & 0 \\ c_{13}^E & c_{13}^E & c_{33}^E & 0 & 0 & 0 \\ 0 & 0 & 0 & c_{44}^E & 0 & 0 \\ 0 & 0 & 0 & 0 & c_{44}^E & 0 \\ 0 & 0 & 0 & 0 & 0 & c_{66}^E \end{bmatrix} \quad (3.14)$$

where s^E and c^E are the matrix inverse of each other

$$\begin{bmatrix} c^E \end{bmatrix} = \begin{bmatrix} s^E \end{bmatrix}^{-1}, \text{ and } \begin{bmatrix} s^E \end{bmatrix} = \begin{bmatrix} c^E \end{bmatrix}^{-1}. \quad (3.15)$$

3.2.4 Piezoelectric coefficients

The piezoelectric coefficient matrices d and d^* represent electromechanical coupling in the piezoelectric material. Matrix d (m/V or C/N) defines mechanical strain produced per unit electric field at constant stress and is also known as the charge constant matrix. Meanwhile, matrix d^* (N/Vm or C/m²) relates the mechanical stress to the electric field at constant strain and is used when the stress-charge form of constitutive relation is applied. The piezoelectric strain coefficient matrix d and the piezoelectric stress coefficient matrix d^* are expressed as,

$$[d] = \begin{bmatrix} d_{11} & d_{21} & d_{31} \\ d_{12} & d_{22} & d_{32} \\ d_{13} & d_{23} & d_{33} \\ d_{14} & d_{24} & d_{34} \\ d_{15} & d_{25} & d_{35} \\ d_{16} & d_{26} & d_{36} \end{bmatrix}, \text{ and } [d^*] = \begin{bmatrix} d_{11}^* & d_{21}^* & d_{31}^* \\ d_{12}^* & d_{22}^* & d_{32}^* \\ d_{13}^* & d_{23}^* & d_{33}^* \\ d_{14}^* & d_{24}^* & d_{34}^* \\ d_{15}^* & d_{25}^* & d_{35}^* \\ d_{16}^* & d_{26}^* & d_{36}^* \end{bmatrix}, \quad (3.16)$$

where the matrices are related to each other by

$$[d^*] = [c^E][d], \text{ and } [d] = [s^E][d^*]. \quad (3.17)$$

The coefficients d_{31} , d_{32} , and d_{33} define strain in the 1-axis, 2-axis, and 3-axis due to the electric field \mathbb{E}_3 along the 3-axis. Coefficients d_{24} and d_{15} define shear strains in the planes 2-3 and 1-3 due to the field \mathbb{E}_2 and \mathbb{E}_1 , respectively. Transverse isotropy in a piezoceramic result in $d_{31} = d_{32}$ and $d_{24} = d_{15}$. The selected piezoceramic is poled along the 3-axis, and electrodes are mounted on the 1-2 planes giving rise to an electric field \mathbb{E}_3 ($\mathbb{E}_1 = \mathbb{E}_2 = 0$). Shear stress is assumed to be absent in the 1-2 plane. The piezoelectric coefficient matrices in (3.16) are then simplified to

$$[d] = \begin{bmatrix} 0 & 0 & d_{31} \\ 0 & 0 & d_{32} \\ 0 & 0 & d_{33} \\ 0 & d_{15} & 0 \\ d_{15} & 0 & 0 \\ 0 & 0 & 0 \end{bmatrix}, \text{ and } [d^*] = \begin{bmatrix} 0 & 0 & d_{31}^* \\ 0 & 0 & d_{32}^* \\ 0 & 0 & d_{33}^* \\ 0 & d_{15}^* & 0 \\ d_{15}^* & 0 & 0 \\ 0 & 0 & 0 \end{bmatrix}. \quad (3.18)$$

3.2.5 Dielectric coefficients

Dielectric property of the piezoelectric material is defined by the electric permittivity matrices ϵ^E (F/m), and ϵ^σ (F/m), evaluated at constant strain (clamped) and constant stress (mechanically-free) respectively. These quantities are expressed as

$$\begin{bmatrix} \epsilon^E \end{bmatrix} = \begin{bmatrix} \epsilon_{11}^E & 0 & 0 \\ 0 & \epsilon_{11}^E & 0 \\ 0 & 0 & \epsilon_{33}^E \end{bmatrix}, \text{ and } \begin{bmatrix} \epsilon^\sigma \end{bmatrix} = \begin{bmatrix} \epsilon_{11}^\sigma & 0 & 0 \\ 0 & \epsilon_{11}^\sigma & 0 \\ 0 & 0 & \epsilon_{33}^\sigma \end{bmatrix}, \quad (3.19)$$

where $\epsilon_{11}^E = \epsilon_{22}^E$ and $\epsilon_{11}^\sigma = \epsilon_{22}^\sigma$ have been applied due to isotropic symmetry in the directions orthogonal to the direction of the applied electric field \mathbb{E}_3 . Cross-permittivity terms are zeros ($\epsilon_{ij} = 0$, for $i \neq j$) since most piezoelectric materials produce electric displacement only along the same axis as the applied electric field. It is noted that the electric permittivity of a piezoceramic is higher when mechanically-free than when it is clamped such that

$$\epsilon_{ii}^\sigma > \epsilon_{ii}^E, \text{ and} \quad (3.20)$$

$$\begin{bmatrix} \epsilon^E \end{bmatrix} = \begin{bmatrix} \epsilon^\sigma \end{bmatrix} - \begin{bmatrix} d \end{bmatrix}^T \begin{bmatrix} s^E \end{bmatrix}^{-1} \begin{bmatrix} d \end{bmatrix}. \quad (3.21)$$

3.3 FE modelling parameters

3.3.1 Geometry and meshing

A commercial finite element code (ANSYS 15.0) was used to carry out the computations for free vibration analysis enabling the extraction of mode shapes and corresponding modal frequencies for each design. The resonator design was determined iteratively through finite element method. The outer diameter and axial length of the radial resonators were kept equal for all cases considered, while specific parameters related to the orifice dimensions and positions were varied.

Candidate designs were then selected and further analysed to predict their dynamic response. The resonator designs were analysed by providing an excitation force at the input face of the resonator. The displacement and phase response of the structures were then extracted, and the excited modes in the frequency range of interest were identified.

Hexahedral meshing scheme was used where feasible. Otherwise, a dense tetrahedral mesh was implemented to obtain reasonably accurate results [172] (refer to section 5.4 for validation of the FE model). The resonator assembly is grouped into multibody parts to enable application of shared topology function to allow a continuous mesh across common regions where bodies touch.

A mesh convergence study was performed to determine the suitable mesh density required for mesh-independent results. A global damping ratio of 0.3%, a value derived from experimental modal analysis, was applied to all simulation cases.

3.3.2 Contact definitions, support, and loads

The FE geometry was organised such that two faces in continuous contact share the same mesh topology with mesh ‘imprints’ at the contact surfaces. The bolt and resonator body are grouped as separate parts so that the contact regions between the bolt surfaces and members of the resonator can be defined separately to allow for more control over the contact behaviour. Figure 3.1 illustrates that positions of the contact regions, support, and loads. Frictional contact with a friction coefficient of 0.15 was applied to the contact regions A, B, and C [173,174], while bonded contact was applied to contact region D to simulate thread engagement [173].

It is known that the physical and mechanical properties of the preload bolt and the degree of preloading can influence the modal behaviour and dynamic characteristics of a piezoelectric transducer [175,176]. This effect is accounted for by applying bolt preload of 30 kN to the bolt shaft and solving for displacements and stresses under static condition. The static structural solution was then used as the initial condition from which the modal solutions were computed. To simulate the structure’s response to periodic excitation, a fixed support boundary was applied at the base of the nodal flange, and a sinusoidal voltage was applied to the electrodes.

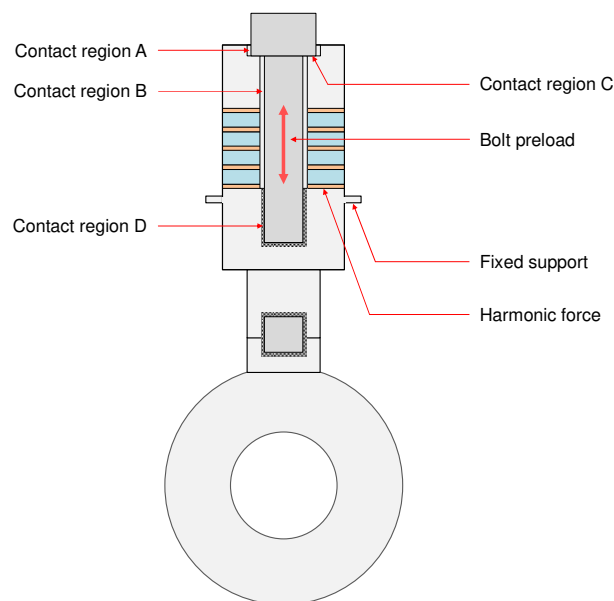


Figure 3.1 Contact definitions, supports, and loads in FE model.

3.3.3 Piezoelectric model set-up

3.3.3.1 Piezoceramic material constants

At this point, it is important to note that the manufacturer's data and usual conventions for specifying the mechanical vectors in Voigt notation take the form as shown in equation (3.11). This form differs from the convention used by the ANSYS finite element code in which the shear elements in the strain and stress vectors appear in a different order [177]:

$$\boldsymbol{\varepsilon}_i = \begin{bmatrix} \varepsilon_1 \\ \varepsilon_2 \\ \varepsilon_3 \\ \varepsilon_4 \\ \varepsilon_5 \\ \varepsilon_6 \end{bmatrix} = \begin{bmatrix} \varepsilon_{11} \\ \varepsilon_{22} \\ \varepsilon_{33} \\ \gamma_{12} \\ \gamma_{23} \\ \gamma_{13} \end{bmatrix}, \text{ and } \boldsymbol{\sigma}_j = \begin{bmatrix} \sigma_1 \\ \sigma_2 \\ \sigma_3 \\ \sigma_4 \\ \sigma_5 \\ \sigma_6 \end{bmatrix} = \begin{bmatrix} \sigma_{11} \\ \sigma_{22} \\ \sigma_{33} \\ \tau_{12} \\ \tau_{23} \\ \tau_{13} \end{bmatrix}. \quad (3.22)$$

Hence, it is necessary that the appropriate vectors and matrices in the constitutive equations be converted to a form that is recognised by the finite element code so that a reasonably representative model describing the piezoelectric material behaviour can be generated. Conversion to ANSYS format require the shifting of certain rows in the elasticity and electric permittivity matrices: move row 4 to row 5, row 5 to row 6, and row 6 to row 4. The resulting matrices are

$$\begin{bmatrix} s^E \\ \end{bmatrix} = \begin{bmatrix} s_{11}^E & s_{12}^E & s_{13}^E & 0 & 0 & 0 \\ s_{12}^E & s_{11}^E & s_{13}^E & 0 & 0 & 0 \\ s_{13}^E & s_{13}^E & s_{33}^E & 0 & 0 & 0 \\ 0 & 0 & 0 & s_{66}^E & 0 & 0 \\ 0 & 0 & 0 & 0 & s_{44}^E & 0 \\ 0 & 0 & 0 & 0 & 0 & s_{44}^E \end{bmatrix}, \quad \begin{bmatrix} d \\ \end{bmatrix} = \begin{bmatrix} 0 & 0 & d_{31} \\ 0 & 0 & d_{31} \\ 0 & 0 & d_{33} \\ 0 & 0 & 0 \\ 0 & d_{15} & 0 \\ d_{15} & 0 & 0 \end{bmatrix}. \quad (3.23)$$

Finally, the strain-charge equation in ANSYS format is given by,

$$\begin{bmatrix} \varepsilon_1 \\ \varepsilon_2 \\ \varepsilon_3 \\ \varepsilon_4 \\ \varepsilon_5 \\ \varepsilon_6 \end{bmatrix} = \begin{bmatrix} s_{11}^E & s_{12}^E & s_{13}^E & 0 & 0 & 0 \\ s_{12}^E & s_{11}^E & s_{13}^E & 0 & 0 & 0 \\ s_{13}^E & s_{13}^E & s_{33}^E & 0 & 0 & 0 \\ 0 & 0 & 0 & s_{66}^E & 0 & 0 \\ 0 & 0 & 0 & 0 & s_{44}^E & 0 \\ 0 & 0 & 0 & 0 & 0 & s_{44}^E \end{bmatrix} \begin{bmatrix} \sigma_1 \\ \sigma_2 \\ \sigma_3 \\ \sigma_4 \\ \sigma_5 \\ \sigma_6 \end{bmatrix} + \begin{bmatrix} 0 & 0 & d_{31} \\ 0 & 0 & d_{31} \\ 0 & 0 & d_{33} \\ 0 & 0 & 0 \\ 0 & d_{15} & 0 \\ d_{15} & 0 & 0 \end{bmatrix} \begin{bmatrix} \mathbb{E}_1 \\ \mathbb{E}_2 \\ \mathbb{E}_3 \end{bmatrix}, \text{ and} \quad (3.24)$$

$$\begin{bmatrix} D_1 \\ D_2 \\ D_3 \end{bmatrix} = \begin{bmatrix} 0 & 0 & d_{31} \\ 0 & 0 & d_{31} \\ 0 & 0 & d_{33} \\ 0 & 0 & 0 \\ 0 & d_{15} & 0 \\ d_{15} & 0 & 0 \end{bmatrix}^T \begin{bmatrix} \sigma_1 \\ \sigma_2 \\ \sigma_3 \\ \sigma_4 \\ \sigma_5 \\ \sigma_6 \end{bmatrix} + \begin{bmatrix} \epsilon_{11}^\sigma & 0 & 0 \\ 0 & \epsilon_{11}^\sigma & 0 \\ 0 & 0 & \epsilon_{33}^\sigma \end{bmatrix} \begin{bmatrix} \mathbb{E}_1 \\ \mathbb{E}_2 \\ \mathbb{E}_3 \end{bmatrix}, \quad (3.25)$$

where elements of the compliance matrix can be expressed in terms of Young's modulus E (Pa), shear modulus G (Pa), and Poisson's ratio ν such that,

$$s_{11}^E = \frac{1}{E_1} = \frac{1}{E_2}, \quad (3.26)$$

$$s_{12}^E = -\frac{\nu_{12}}{E_1}, \quad (3.27)$$

$$s_{13}^E = -\frac{\nu_{31}}{E_3}, \quad (3.28)$$

$$s_{33}^E = \frac{1}{E_3}, \quad (3.29)$$

$$s_{44}^E = \frac{1}{G_{23}} = \frac{1}{G_{13}}, \quad (3.30)$$

$$s_{66}^E = \frac{1}{G_{12}} = \frac{2(1+\nu_{12})}{E_1} = 2(s_{11}^E - s_{12}^E), \quad (3.31)$$

$$G_{12} = \frac{1}{s_{66}^E} = \frac{1}{2(s_{11}^E - s_{12}^E)}, \quad (3.32)$$

$$\nu_{12} = \frac{s_{12}^E}{s_{11}^E}, \text{ and} \quad (3.33)$$

$$\nu_{23} = -\frac{s_{13}^E}{s_{33}^E} = \nu_{13}. \quad (3.34)$$

In power ultrasonics applications, a Navy Type III piezoelectric material is used due to its high mechanical quality factor. The present study utilises Navy Type III equivalent NCE81 (Noliac, Denmark) piezoceramic rings. Table 3.1 provides the material data for NCE81 [178] formatted to ANSYS convention for use as input parameters in the FE model.

Table 3.1 NCE81 piezoceramic ring properties.

	Symbol	Unit	Value	Reference
Compliance coefficients	s_{11}^E	m^2/N	15.70×10^{-12}	Manuf. data
	s_{12}^E	m^2/N	-7.77×10^{-12}	Manuf. data
	s_{13}^E	m^2/N	-9.76×10^{-12}	Manuf. data
	s_{33}^E	m^2/N	16.74×10^{-12}	Manuf. data
	s_{44}^E	m^2/N	36.42×10^{-12}	Manuf. data
	s_{66}^E	m^2/N	44.12×10^{-12}	Manuf. data
Stiffness coefficients	c_{11}^E	N/m^2	-12.36×10^{10}	Eqn. (3.15)
	c_{12}^E	N/m^2	-16.62×10^{10}	Eqn. (3.15)
	c_{13}^E	N/m^2	-16.90×10^{10}	Eqn. (3.15)
	c_{33}^E	N/m^2	-13.73×10^{10}	Eqn. (3.15)
	c_{44}^E	N/m^2	2.75×10^{10}	Eqn. (3.15)
	c_{66}^E	N/m^2	2.27×10^{10}	Eqn. (3.15)
Piezoelectric coefficients	d_{31}	C/N	-1.00×10^{-10}	Manuf. data
	d_{33}	C/N	2.55×10^{-10}	Manuf. data
	d_{15}	C/N	3.80×10^{-10}	Manuf. data
	d_{31}^*	C/m^2	-14.11	Eqn. (3.17)
	d_{33}^*	C/m^2	-1.21	Eqn. (3.17)
	d_{15}^*	C/m^2	10.43	Eqn. (3.17)
Dielectric coefficients	$\epsilon_{11}^\sigma / \epsilon_0$	-	1060	Manuf. data
	$\epsilon_{33}^\sigma / \epsilon_0$	-	1020	Manuf. data
	$\epsilon_{11}^\epsilon / \epsilon_0$	-	612	Eqn. (3.21)
	$\epsilon_{33}^\epsilon / \epsilon_0$	-	736	Eqn. (3.21)
	ϵ_0	F/m	8.85×10^{-12}	Manuf. data
Young's modulus	E_1	Pa	6.37×10^{10}	Eqn. (3.26)
	E_2	Pa	6.37×10^{10}	Eqn. (3.26)
	E_3	Pa	5.97×10^{10}	Eqn. (3.28)
Shear modulus	G_{12}	Pa	2.27×10^{10}	Eqn. (3.32)
	G_{23}	Pa	2.75×10^{10}	Eqn. (3.30)
	G_{13}	Pa	2.75×10^{10}	Eqn. (3.30)
Poisson's ratio	ν_{12}	-	-0.49	Eqn. (3.33)
	ν_{23}	-	0.58	Eqn. (3.34)
	ν_{13}	-	0.58	Eqn. (3.34)
Density	ρ	kg/m^3	7730	Manuf. data

3.3.4 Modal analysis & harmonic response simulation

On completion of the FE model set-up, modal analysis was performed to determine the possible natural frequencies and the associated mode shapes. Modal analysis was executed using the Block Lanczos method which is suitable for large symmetric eigenvalue problems [177]. The modal sweep was carried out between 10 kHz and 25 kHz.

A sinusoidal excitation voltage was applied, and the harmonic response was computed using the hybrid method [179] which combines the solution obtained from the mode-superposition method, and the direct solution of the simultaneous equations of motion [173]. The benefit of implementing the hybrid method is that the vibrational response is solved at an even frequency interval while also enabling response calculation at the modal frequencies. The simulated response was recorded over a frequency range of 18 kHz to 22 kHz, with the objective of identifying parasitic modes within the 4 kHz band surrounding the 20 kHz operating frequency.

3.4 Conclusion

Finite element (FE) is a powerful technique that has become the de facto tool for transducer designers due to its ability to solve complex 3-dimensional Eigenvalue-problems [109]. In the past, 1-dimensional analytical methods are prevalent but the designs are limited to simple geometries, and the design iteration can be very tedious and expensive. The FE technique has shortened the design cycle and enabled the designers to produce innovative and non-conventional 3-dimensional designs.

In this chapter, the equations governing the dynamic and electrical behaviour of a piezoelectric transducer have been described. This include the equations of motion, the piezoelectric constitutive equations, and matrices describing the elastic and dielectric properties of the piezoelectric element. In addition, the modification of the standard piezoelectric matrices to ANSYS format, the contact definitions, supports, and loads used in the FE model were also described.

Chapter 4

Modelling & Analysis of Radial Resonators

4.1 Design objectives

Chapter 1 introduced the basic radial resonator that is essentially a thick-walled cylinder with axial length less than $\lambda / 4$ and proportioned such that it vibrates in the fundamental radial mode (R0) at the design frequency. When the resonator is operated in an acoustic medium such as water, acoustic field radiates from its circumferential surface outwards into the medium. From its inner circumference, the inward propagation of the acoustic field and the summing of wavefronts produce intense pressure field near the centre of its cylindrical cavity [27,40].

The radial resonator offers a much larger output surface area than a conventional longitudinal-mode device. This feature in itself offers several advantages but most notably, the ability of a single resonator to generate and transmit considerably high ultrasonic energy into the acoustic medium, maximising the operation of the piezoceramic element. Previous results have also shown that high power densities can be achieved with relatively low vibrational amplitudes, keeping the US resonator operation well below the ‘bubble shielding’ regime.

Considering the benefits offered by a radial resonator, it is of interest to investigate if the basic radial-mode design can be modified to enhance its electrical, dynamic, and acoustic performance. An incremental improvement in these aspects would hopefully translate to a more potent biological inactivation technology for ballast water treatment. In the present study, the objective is to design a radial resonator having the following features:

1. relatively compact resonator with a large area-to-mass ratio;
2. tuned mode (R0) that is well-isolated from adjacent modes;
3. provides a relatively uniform vibrational profile across its output surface;
4. exhibit excellent electromechanical characteristics;
5. ability to generate a strong and uniform acoustic field;
6. affect high organism inactivation rate with lower power consumption.

4.1.1 Basic construction

A radial resonator comprises a Langevin-type transducer [180] mechanically coupled to a radial-type horn. These two sections are henceforth referred to as the exciter section and emitter section respectively (see Figure 4.1). The exciter section is designed to operate in the first longitudinal mode (L1) while the emitter section is designed to operate in the fundamental radial mode (R0).

The R0 mode is identified by the radial displacement of the cylinder thickness in the absence of circumferential and axial displacement. Consequently, the R0 mode has no nodal diameter and no node circles due to the in-phase displacement of the inner and outer circumferences of the cylinder. In simple terms, the R0 mode is identified by the expansion and contraction of the mean diameter, with negligible change in the thickness of the cylinder [181]. In contrast, radial thickness modes are characterised by the presence of one or more node circles, a consequence of expansion and contraction of cylinder thickness, with nearly constant mean diameter [181]. Thickness modes, which are also referred to as radial breathing modes [121,182], are not excited in the frequency range of interest.

In designing the radial resonators, the exciter and emitter sections were designed and analysed separately using finite element (FE) technique to obtain geometric models that vibrate in the desired modes. The FE models of the exciter and emitter sections were then coupled, and further analyses were carried out to investigate the coupled behaviour. Although the exciter and emitter sections were individually tuned, the coupled assembly required further analysis to identify the shifts in the resonance frequencies, and to also predict the possible excitation of parasitic modes induced by the coupling. Shifts in frequency arising from the coupling were compensated by fine-tuning the device. Meanwhile parasitic modes were suppressed through systematic design adjustments [183,184].

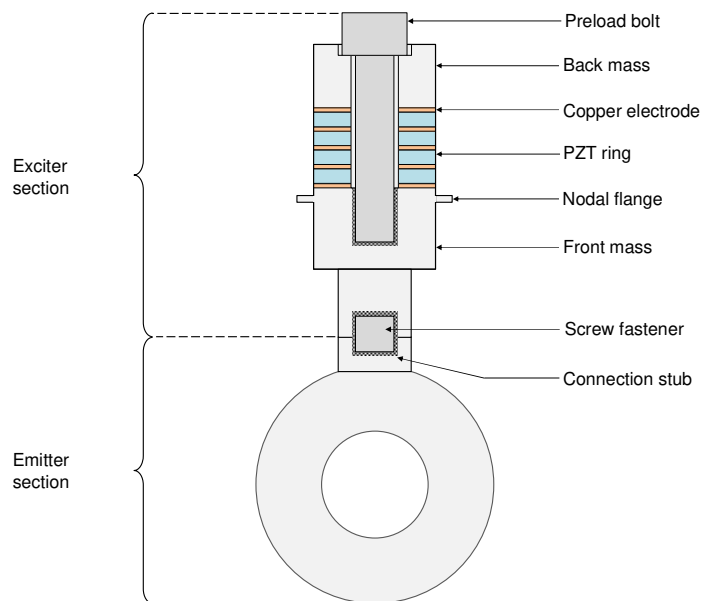


Figure 4.1 Radial resonator basic construction.

As shown in Figure 4.1, the basic construction of the exciter section comprises a piezoceramic (PZT) stack clamped between two metallic end-masses. An alloy steel (ASTM A574) preload bolt runs through the back-mass, PZT-stack, and the front-mass to provide the compressive force to hold the transducer assembly together while keeping the PZT-stack under compressive stress throughout the vibration cycle. The back-mass, which has a through-hole for the preload bolt, was machined from a solid stainless steel (SS316L) piece. The front-mass was machined from aluminium-alloy (Al-7075-T6) and has a threaded hole along its axis. The exciter was assembled by clamping the PZT-stack between the back-mass and the front-mass, and fixated into position by the bolt. The preload bolt acts as a stiff spring under tension, exerting a compressive axial force on the PZTs.

The exciter section was designed as a half-wave longitudinal transducer with cross-section diameter kept smaller than $\lambda / 4$ to avoid lateral coupling which can polarise the axial displacement in some other directions [185]. The lengths of the back-mass and front-mass were approximated by dividing the exciter section into two quarter-wave segments wherein the back-mass and the PZT-stack form one segment, and the front-mass form the other segment. The length of the front-mass L_f (m) with an exponential profile can be approximated using [186],

$$L_f = \frac{c_f}{4\pi f} \sqrt{(2\pi)^2 + (\ln n)^2}, \quad (4.1)$$

where f (Hz) is the design frequency, and n is the ratio of the small-end radius to the large-end radius. The speed of sound propagation in the front-mass c_f (m/s) can be calculated using the modulus of elasticity E (Pa), and the density ρ (kg/m³) of the material:

$$c_f = \sqrt{\frac{E}{\rho}}. \quad (4.2)$$

Assuming one-dimensional sinusoidal plane-wave propagation in the axial direction, the axial length of the back-mass L_b (m), was approximated as [187]

$$\frac{Z_b}{Z_{\text{PZT}}} \tan\left(2\pi f \cdot \frac{L_b}{c_b}\right) \tan\left(2\pi f \cdot \frac{L_{\text{PZT}}}{c_{\text{PZT}}}\right) = 1, \quad (4.3)$$

where the acoustic impedance is $Z = \rho c$, and L_{PZT} (m) is the axial length of the PZT-stack.

These empirical formulations provide the initial dimensions of the exciter. Further adjustments were made with the aid of FE modelling technique to arrive at the final design.

4.1.2 Parts and materials

The exciter section comprises of a 4-element PZT stack, a stainless steel back-mass, an aluminium alloy front-mass, and a preload bolt. A nodal flange forms part of the exciter front-mass for support and mounting purposes. The exciter section was designed such that nodal plane is located below the PZT stack as a provision for securing an enclosure over the active elements of the transducer. This configuration enables water-tight isolation between the dry section (the PZT stack and everything above it) and the wetted section (everything below the PZT stack) of the resonator.

4.1.2.1 Front and back-mass

The choice of metallic material for the front and back mass depends on the intended application. In general, the end-masses should have an acoustic impedance that is intermediate between the acoustic impedance of the PZT and the acoustic load. Effective acoustic energy transmission between the back-mass and the front-mass is achieved when [155]

$$Z_{\text{PZT}} = \sqrt{Z_{\text{b}}Z_{\text{f}}}. \quad (4.4)$$

Here the PZT-stack acts as an impedance matching interface between two dissimilar materials. Typically, the back-mass should have a higher acoustic impedance than the PZT and the front-mass so that the acoustic energy is preferentially directed forward. On the other hand, the front-mass should be constructed of a material with relatively low acoustic impedance. Thus, stainless steel (SS316L) was selected as the back-mass material, and either titanium alloy (Ti-Al6-4V) or aluminium alloy (Al-7075-T6) can be used for the front-mass. Ti-alloys have high tensile strength and are suitable for high power applications where the structure can be subjected to high displacements and stresses. They are also chemical resistant and less susceptible to cavitation damage, making them ideal for water processing. However, Ti-alloys are not only intrinsically costly, but also more expensive to machine compared to aluminium and steel [188]. This study utilised Al-alloy to keep costs low, but the commercial version may be constructed from Ti-alloy without tuning since the speed of sound propagation is similar in both materials. The mechanical and acoustical properties of the transducer parts are provided in Table 4.1 and Table 4.2.

Table 4.1 Mechanical properties of transducer parts [189–191].

	Unit	SS316L	Al-7075-T6	Ti-Al6-4V
Density	kg/m ³	8000	2810	4430
Young's Modulus	GPa	193	72	114
Poisson Ratio	-	0.25	0.33	0.34
Tensile strength, ultimate	MPa	558	572	950
Tensile strength, yield	MPa	290	503	880

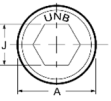
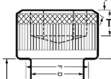
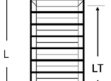
Table 4.2 Acoustic properties of transducer materials.

Section	Material	c (m/s)	λ (mm)	Z_o (MRayl)
Back-mass	SS316L	4912	245	39.3
Font-mass	Al-7075-T6	5051	253	14.2
	Ti-Al6-4V	5073	254	22.5
PZT stack	NCE81	2779	139	21.5

4.1.2.2 Preload bolt

A socket head cap screw (SHCP) fastener constructed according to ANSI/ASME B18.3 standard, and material conforming to ASTM A574 specification for alloy steel was selected due to its high tensile strength (maximum of 1300 MPa) [192]. A 12.7 mm screw was chosen taking into consideration the internal diameter of the PZT-stack (15 mm), the clearance required to avoid electrical arching with the copper electrodes, and the distribution of tension load across the width of the bolt shaft. The thread engagement length was selected taking into consideration the static pre-stress and the dynamic load to avoid thread damage. At the same time, the bolt should be as short as possible so that bolt modes are placed far from the tuned mode. A 12 mm screw having approximately 8 threads per cm (equivalent to $\frac{1}{2}$ - 20 UNF) was selected to meet the dimensional constraints and strength requirement. The dimensions of the SHCP are provided in Table 4.3.

Table 4.3 Dimensions of socket head cap screw used as a preload bolt [192].

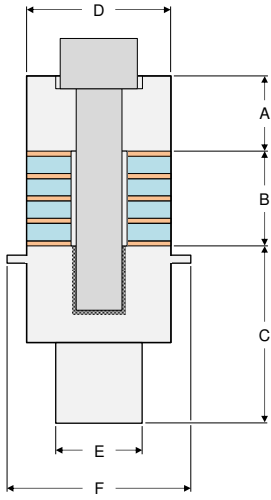
Dimensions		mm
	Nominal size	12
	Pitch	1.27
	Body diameter (D)	12.7
	Head diameter (A)	19.05
	Head height (H)	12.7
	Hex socket size (J)	9.525
	Key engagement (T)	6.223
	Nominal length (L)	50.8 / 57.15
	Thread length (LT)	38.1

4.1.2.3 Preload bolt length

Screw shaft lengths of 50.8 mm and 57.2 mm were considered as a reasonable compromise between maximising the thread engagement length and minimising the overall bolt length. Using FE modelling, it was determined that the use of a 57.2 mm bolt placed the tuned mode frequency at a slightly higher frequency than the assembly that utilised a 50.8 mm bolt. Tuning the two cases to approximately 20 kHz resulted in less than 3 mm difference in the length of the front-mass as

shown in Table 4.4. Due to this marginal difference, the 12.7 x 57.2 mm bolt was selected in consideration of thread wear resistance. Henceforth, all FE models and actual prototypes were constructed using the 12.7 x 57.2 mm bolt as an integral component.

Table 4.4 Exciter section dimensions for two bolt lengths.

Dimensions (mm)	Case 1	Case 2
		
Preload bolt	12.7 x 50.8	12.7 x 57.2
Back-mass		
Length (A)	14	14
Diameter (D)	38	38
PZT stack		
Length (B)	20.5	20.5
Outer diameter (D)	38	38
Inner diameter	15	15
Front-mass		
Length (C)	65.5	68
Diameter, PZT side (D)	38	38
Diameter, emitter side (E)	28	28
Flange diameter (F)	60	60

4.1.2.4 PZT-stack

The actuating property of the ultrasonic transducer is provided by the piezoceramic rings which deforms in the poling direction when a voltage is applied. Piezoceramics based on lead zirconate titanate (PZT) are common in many power ultrasonics applications due to its strong piezoelectric effect, high coupling factors and compliance[193]. PZTs with different properties can be manufactured by varying the additives and composition of the piezoceramic material so that its properties can be manipulated for a wide range of transducer applications.

The United States military standard [194] defines six categories of PZTs according to their properties and applications (see Table 4.5). The PZT-8 variety (a Navy Type III equivalent material) is most suitable for high power ultrasonics applications due to its strength, and superior mechanical, electrical, and piezoelectric properties. PZT-8 provides a piezoelectric coefficient that is between 2 and 4 times that of the other ceramics like barium titanate, lead niobate, and sodium-potassium niobate [193], and has a mechanical quality factor of around 1000, which is at least 4 times higher than can be provided by other conventional ceramics [193]. A material with a high mechanical Q is desirable because a narrow bandwidth and strong response are needed in power ultrasonics applications. A PZT-8 material has a moderately-high Curie temperature of around 300 °C, and should always be operated below this temperature to avoid depoling which would cause the material to lose its piezoelectric property. Also, the high dynamic tensile strength of up to 50 MPa, and the

high electric field limit of up to 1000 V/mm enable high amplitude operation [195,196]. PZT-8 devices can be sourced from various manufacturers, but their properties can vary due to variations in the doping compound, compositions, and manufacturing processes. Properties can also vary from batch to batch. Therefore, it is important to use only the latest data from the manufacturer.

Table 4.5 Piezoceramic classification according to U.S. military standard.

Type	Definition	Commercial materials
Navy Type I	Recommended for medium to high power acoustic applications; resistant to depoling at high voltage or high mechanical stress;	PZT-4 (MorganTech) NCE40, NCE41, NCE46 (Noliac) PIC181, PIC141, PIC300 (PI) Sonox P4
Navy Type II	High charge sensitivity, permittivity and time stability; not suitable for high voltage; susceptible to dielectric heating; more suitable for passive devices such as hydrophones.	PZT-5A (MorganTech) NCE51, NCE53 (Noliac) PIC151, PIC155, PIC255 (PI)
Navy Type III	Suitable for high power, high voltage applications; able to withstand high stresses; lower losses; reduced field dependency of electric and mechanical losses; high electro-mechanical quality factor.	PZT-8 (MorganTech) NCE80, NCE81 (Noliac) Sonox P8 (CeramTec)
Navy Type VI	High permittivity, coupling and piezoelectric constants, but lower time stability; suitable for applications requiring fine movement control and sensitive receiver; low Curie temperature.	PZT-5H (MorganTech) NCE55 (Noliac) PIC153 (PI)

In the present research, the piezoceramic rings (NCE81, Noliac) used in the construction of the resonators were individually measured to ensure that there are no significant deviations in their piezoelectric properties. The parameters were defined and measured according to the IEEE standards [197,198]. In the present research, three radial resonator prototypes were fabricated and assembled. Twelve PZT rings were used in total, with each resonator comprising of four NCE81 PZT rings. The series resonance frequency f_s , parallel resonance frequency f_p , electrical impedance Z , and the capacitance C of each PZT were measured using an impedance analyser. The loss tangent $\tan \delta$, coupling coefficient k_{eff} , and the mechanical quality factor Q_m were calculated using the equivalent circuit parameters derived from the impedance-phase spectra. PZT characterisation procedures are given in [199]. Table 4.6 provides the characterisation data of the twelve PZTs used in this study.

Table 4.6 NCE81 piezoceramic ring measurements.

No.	f_s (kHz)	f_p / f_s	$ Z $ (Ω)	C_{33}^T (pF)	$\tan \delta$	ϵ_{3R}	k_{eff}	Q_m
1	43.42	1.074	18	1647	1.3×10^{-3}	972	0.365	930
2	43.40	1.072	17	1617	1.4×10^{-3}	955	0.360	1028
3	43.45	1.071	16	1632	1.4×10^{-3}	964	0.358	1095
4	43.53	1.075	16	1610	1.4×10^{-3}	951	0.367	1054
5	43.48	1.077	15	1623	1.4×10^{-3}	958	0.371	1091
6	43.40	1.076	17	1623	1.4×10^{-3}	958	0.369	976
7	43.45	1.076	15	1618	1.4×10^{-3}	955	0.369	1108
8	43.47	1.075	16	1615	1.4×10^{-3}	954	0.367	1053
9	43.41	1.076	17	1622	1.4×10^{-3}	965	0.369	1086
10	43.46	1.071	16	1630	1.4×10^{-3}	964	0.367	1043
11	43.42	1.073	18	1615	1.4×10^{-3}	962	0.372	1071
12	43.44	1.075	15	1625	1.4×10^{-3}	962	0.359	995
Mean	43.44	1.074	16	1623	1.39×10^{-3}	960	0.366	1041
Std. Dev.	0.04	1.96	1.03	9.44	2.76×10^{-5}	5.66	0.004	48.40
% Dev.	0.08	0.18	6.29	0.58	1.99	0.59	1.22	4.65

4.1.2.5 Mounting and support

Provisions for support and mounting of the resonators were considered during the design process. A small nodal flange can be incorporated at the nodal plane without significant impact on the modal behaviour of the device. The nodal plane can be engineered to a position that is most favoured by the designer. In particular, two nodal plane positions were considered for the exciter section – in the middle of the piezoceramic stack, or in the front-mass below the piezoceramic stack. These two possibilities are illustrated in Figure 4.2.

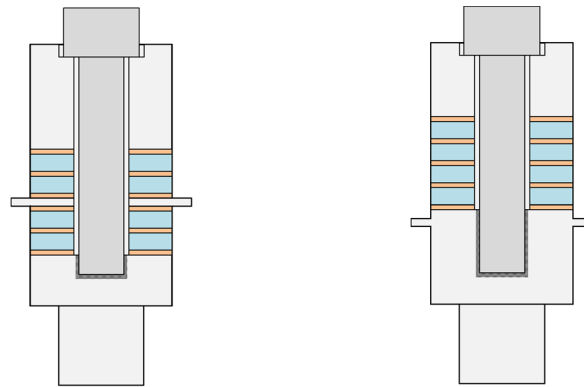


Figure 4.2 Possible flange positions in PZT transducer.

Engineering and practical considerations necessitate locating the nodal plane away from the piezoceramic stack. This is because piezoceramics have low tensile strength and can mechanically fail under excessive tension. The nodal plane is a region of high stress, and shifting the nodal plane away from the piezo-stack mitigates this risk. In addition, the nodal flange reduces the nodal stress by spreading the tensile forces over a larger surface area. Positioning the nodal plane in the front-mass allows the nodal flange to be machined as part of the structure as a single piece. However, a disadvantage of this approach is that the forces exerted by each PZT to effect in a displacement are not equal. Thus, the stresses exerted on the PZTs are not distributed equally and the failure of the transducer depends on the member that is subjected to the highest stress.

Positioning the nodal flange in the front-mass is straight-forward due to the geometric bias between the end-masses. The front-mass tends to be longer and has lower acoustic impedance than the back-mass to direct most of the vibrational energy forward. Meanwhile, the air-coupled back-mass has significantly lower useful vibrational output. Having the flange in the front-mass enable the mounting an enclosure around the PZT stack, which has the following practical benefits:

1. Protects the user from accidental contact with the live electrodes;
2. Provides a safe surface for handheld operation;
3. Protects the PZTs from contacting with water during operation.

4.2 Finite element (FE) design approach

This section addresses the first three objectives for radial resonator design as described in section 4.1. Figure 4.3 illustrates the step-wise design approach adopted in the design of a large area compact radial resonator that incorporates multiple orifices as a principal feature. Using Hunter's [27] radial horn as a starting point, the step-wise modifications proceeded as follows:

1. Resize the radial resonator to an OD of 100 mm and tune to approximately 20 kHz. Designs conceived from this step are referred to as the RP-type radial resonator.
2. Redesign the radial resonator with the inclusion of secondary orifices keeping the OD unchanged; investigate various orifice configurations and tune to approximately 20 kHz. Designs conceived from this step are referred to as the RPS-type radial resonators.
3. (a) Redesign the radial resonator with the inclusion of tertiary orifices keeping the OD unchanged; (b) add 'orifice-links' to obtain R0 mode at approximately 20 kHz. Designs conceived from this step are referred to as the RPST-type radial resonators.
4. Perform FE harmonic response analysis to predict vibrational uniformity and identify the presence of parasitic modes.

The radial resonators were named according to their orifice configurations for easy reference. The RP-type design has one ‘primary’ orifice in the centre; the RPS-type design is identified by the presence of a ‘secondary’ layer of orifices, in addition to the ‘primary’ orifice; finally, the RPST-type design has in addition a ‘tertiary’ layer of orifices, and ‘orifice-links’ connecting its ‘secondary’ orifices to its ‘primary’ orifice. The RP-type, RPS-type, and RPST-type (with orifice-links) designs will be studied in more detail in the sections that follow.

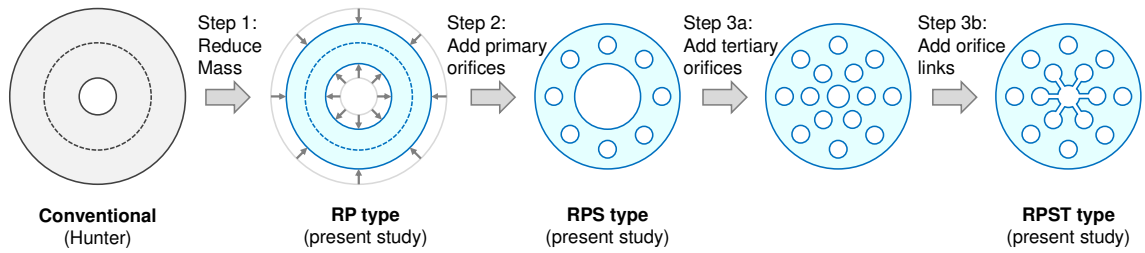


Figure 4.3 Approach to multiple orifice radial resonator design.

4.2.1 Mesh convergence

Mesh sensitivity analysis was carried out to determine the appropriate mesh density required for mesh-independent results. Figure 4.4 shows that mesh convergence was achieved for the first four radial modes with approximately 22,000 elements for the RPS-16 emitter section. Similar convergence behaviour was also observed for the RP and the RPST configurations. Mesh size similar to or smaller than the converged dimensions was applied to the complete radial resonator assembly. This approach generated approximately 200,000 mesh elements for the complete resonator model. The final mesh for the RP-1, RPS-type and RPST-type resonators are shown in Figure 4.5.

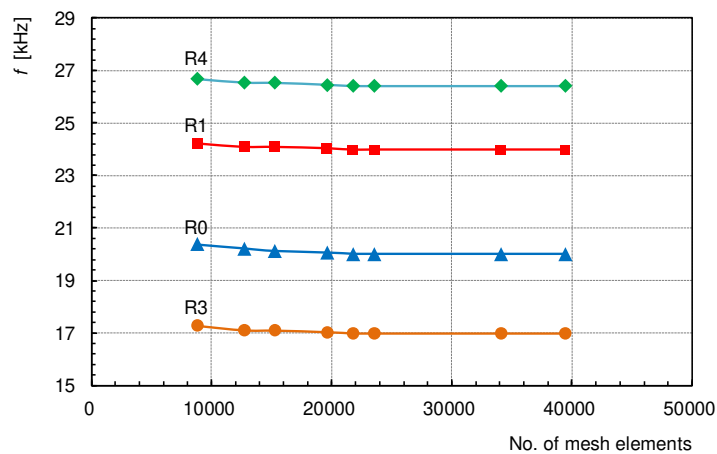
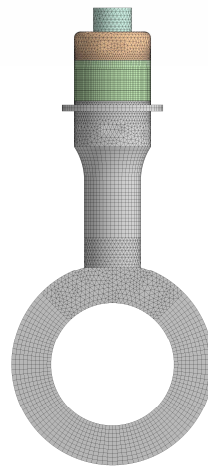
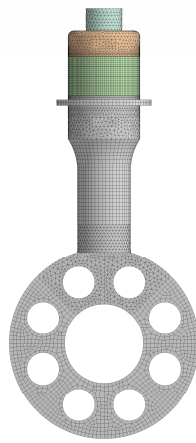


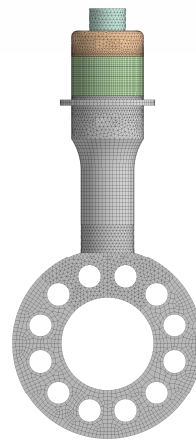
Figure 4.4 Graph of mesh independence for the RPS-16 emitter.



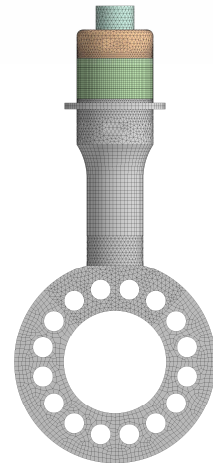
RP-1
190,698 elements



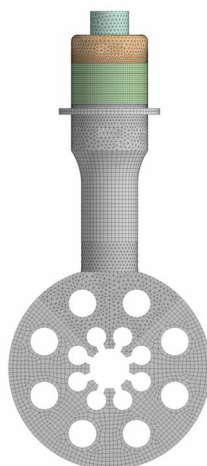
RPS-8
188,241 elements



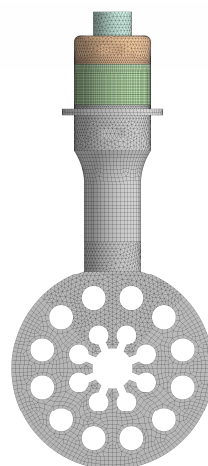
RPS-12
187,338 elements



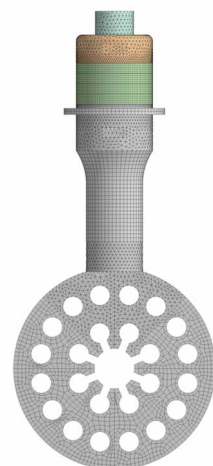
RPS-16
185,597 elements



RPST-8
192,827 elements



RPST-12
205,051 elements



RPST-16
189,532 elements

Figure 4.5 FE mesh for radial resonator designs.

4.2.2 FE data extraction

The velocity amplitude and phase as a function of frequency were extracted from a point located at 6 o'clock position of the emitter section outer circumference as shown in Figure 4.6a to identify the modes that will likely be excited when a harmonic force is applied. Radial vibration velocity \dot{u}_r (m/s) as a function of angular position ϕ (degrees) was extracted from the paths shown in Figure 4.6b to provide a quantitative measure of vibrational uniformity. Vibrational uniformity is important if a radial resonator is to radiate acoustic energy uniformly across its radiating surface. This ensures the organisms in the water are well-exposed to the ultrasound field, especially when the radial resonators are used in a cylindrical flow-through ultrasonic treatment chamber.

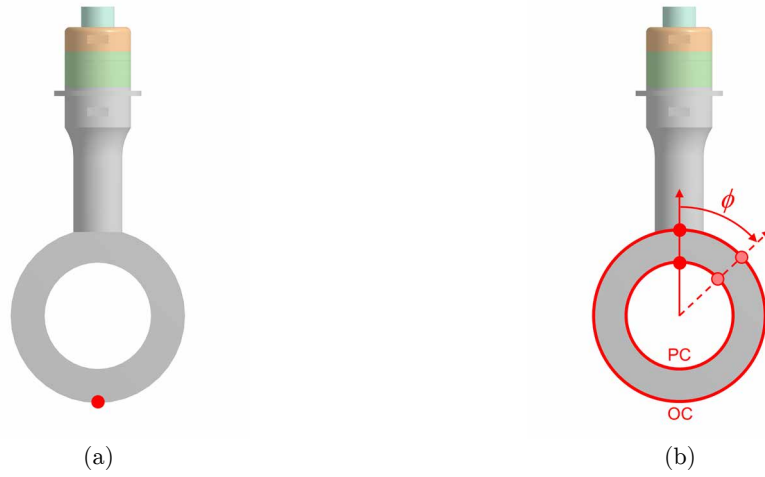


Figure 4.6 FE model data extraction point and paths for (a) vibrational amplitude and phase response; (b) vibrational velocity along at the outer circumference (OC) and primary orifice circumference (PC).

4.3 Design of RP-, RPS-, and RPST-type radial resonators

4.3.1 Determination of a basic radial resonator design (RP-type)

The basic radial resonator is a thick cylinder tuned to vibrate in the fundamental radial mode (R0) at the design frequency. The RP-type resonator follows the same design equations for thick-walled cylinders operating in the radial mode. The diameter of the resonator is calculated by forming an equality between the number of complete wavelengths $n\lambda$ and the mean circumference [115]:

$$\frac{\pi}{2}(D_{\text{ext}} + D_{\text{pri}}) = n\lambda. \quad (4.5)$$

The external diameter was set to $D_{\text{ext}} = 100$ mm, and the number of wavelengths was set to $n = 1$ to keep the physical size of the device relatively compact. Emitter thickness was set to $H = 30$ mm, deliberately smaller than $\lambda/4$ so that most of the vibration is oriented in the radial direction. Using the mechanical properties of Al-7075-T6 (see Table 4.1) and operating frequency of 20 kHz, the calculated wavelength is $\lambda = 253$ mm. Substituting these parameters into equation (4.5) gives the dimension of the primary orifice of $D_{\text{pri}} = 60.8$ mm.

An FE model was constructed based on the calculated geometrical parameters and the known material properties. The curved top of the emitter was flattened forming a 30 mm wide flat at the 12 o'clock position to facilitate mechanical coupling with the exciter section. FE modal computations yielded an R0 mode at a frequency of 20376 Hz. This deviation from hand-calculations was attributed to the structural modification involving the flat. The model was subsequently tuned by adjusting the inner diameter of the emitter. The final configuration was obtained with an inner diameter of 63.5 mm and the R0 mode occurring at 19999 Hz.

4.3.2 Modifications incorporating secondary orifices (RPS-type)

Structural modifications to the basic radial resonator design were carried out by introducing orifices without changing the general shape and overall dimensions of the device. The objective is to investigate how such modification influences the electromechanical characteristics of the device. Figure 4.7 shows the geometric parameters considered for the multiple-orifice radial resonator design.

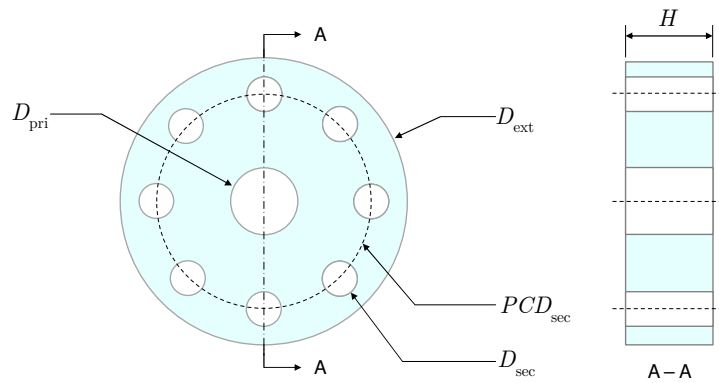


Figure 4.7 RPS resonator geometric parameters.

Variations in the orifice parameters can result in an infinite number of multiple orifice resonator configurations. By constraining the external dimensions and the tuning frequency, the possible configurations were limited to just a few. As before, the external diameter, D_{ext} , and emitter height, H , are kept constant at 100 mm and 30 mm respectively.

The RPS resonator feature a secondary layer of orifices distributed circumferentially and positioned at equidistant from the primary orifice. The primary orifice is a central orifice, common to all radial resonator designs considered, differing only in diameter. A parametric study was carried out to investigate the effect of primary orifice diameter D_{pri} , secondary orifice diameter D_{sec} , number of secondary orifices N_{sec} , and the radial position of the secondary orifice PCD_{sec} , on the R0 mode frequency. Figure 4.8 shows that PCD_{sec} vary proportionally with the resonance frequency while D_{pri} and D_{sec} vary inversely with the resonance frequency.

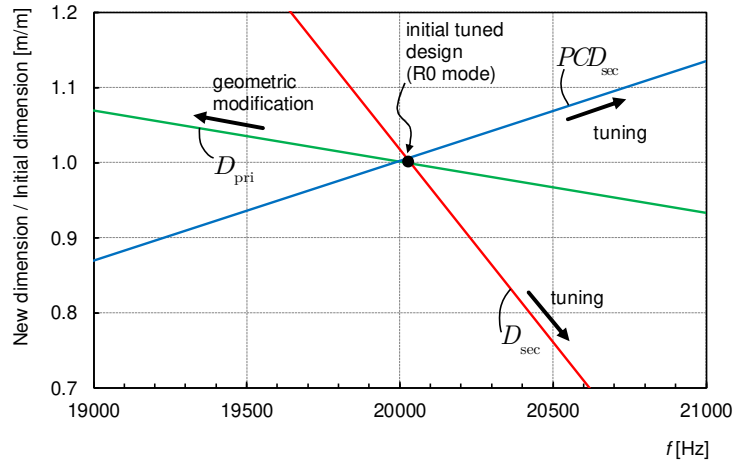
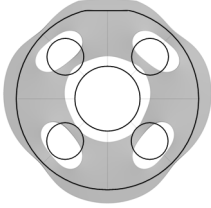
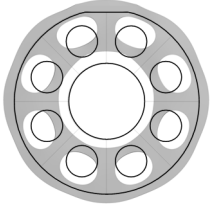
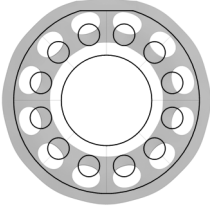
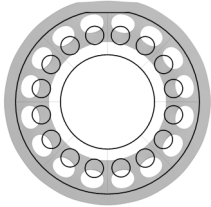
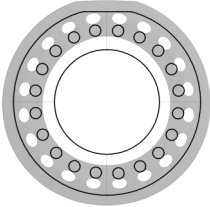
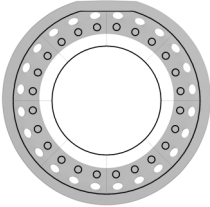


Figure 4.8 RPS resonator design chart.

By setting a different number of secondary orifices and then tuning the orifice parameters according to Figure 4.8, six RPS emitter section configurations were derived. The number of secondary orifices considered are: 4, 8, 12, 16, 20, and 24 through RPS-4, RPS-8, RPS-12, RPS-16, RPS-20, and RPS-24 designs respectively. Table 4.7 provides the orifice parameters of the six RPS designs, showing the deformed and undeformed (wireframe) shapes, and the number of mesh elements used in the finite element model. The RPS designs were all tuned to 20 kHz (within $\pm 0.01\%$). All designs exhibit strong in-phase radial displacements of the outer circumference and the primary orifice boundaries that are characteristic of the R0 mode. The boundaries of the secondary orifices do not intersect with any nodal lines and deform coherently with the structure. The vibration of the secondary orifices is a combination of rigid-body radial motion and an R2-like deformation, and is expected to generate high acoustic pressures suitable for biological cell inactivation.

Table 4.7 Comparison of RPS configurations.

Parameters	Emitter sections		
R0 mode	RPS-4	RPS-8	RPS-12
			
Pri. orifice dia. (mm)	35.5	41.5	48.5
Sec. orifice dia. (mm)	20	17	12
Sec. orifice PCD (mm)	65.2	69.6	73
No. of sec. orifices	4	8	12
Res. Freq. (Hz)	20005	19998	20003
Mesh elements	20,985	47,124	44,163
R0 mode	RPS-16	RPS-20	RPS-24
			
Pri. orifice dia. (mm)	51.0	56.0	58.7
Sec. orifice dia. (mm)	10	6	4
Sec. orifice PCD (mm)	73	77	80
No. of sec. orifices	16	20	24
Res. Freq. (Hz)	20017	19985	20022
Mesh elements	41,960	70,112	88,842

FE modal analysis of the six RPS designs showed that there is virtually no limit to the number of orifices that can be incorporated in the emitter, except that the orifices will have to get smaller to accommodate a higher number. Practically, orifices that are too small present a number of disadvantages such as low machinability, high susceptibility to choking, and high pressure drop. Further, water will preferentially flow through the larger primary orifice (the path of least resistance) making the smaller orifices redundant in the treatment process. The optimum orifice diameter may be determined qualitatively by considering the total cross-section open fraction (CSOF) of the emitter section and the percentage of this CSOF contributed by the secondary orifices (i.e. the %S-CSOF). Total CSOF is an important consideration because it influences the ultrasound dose delivered to the water – a low CSOF result in a high pressure drop and a shorter US field contact time. The %S-CSOF is an important consideration when evaluating the multiple-orifice designs. Assuming comparable acoustic pressures are generated within all orifices, %S-CSOF should be close to 50% so that the flow velocity through all the orifices are approximately equal. However, since a higher acoustic pressure is expected in the smaller orifices [40], a more uniform ultrasonic dose

(defined as the product of US intensity and exposure time) delivery may be achieved with %S-CSOF slightly below 50%. In Figure 4.9, it is shown that the total CSOF peaked at 16 secondary orifices (CSOF of 0.422) although this is only marginally more than the 8 and 12 orifices designs (CSOF of 0.405 and 0.410 respectively). Interestingly, RPS-4 has the lowest CSOF (0.287) despite having the largest secondary orifices. Meanwhile, the %S-CSOF are highest for the RPS-4 and RPS-8 designs (56% and 57% respectively) and lowest for the RPS-20 and RPS-24 designs (19% and 10% respectively). The %S-CSOF of the RPS-20 and RPS-24 designs are 50–80% lower than the %S-CSOF of the other four designs. Thus, a significant fraction of the flow will not go through the secondary orifices of the RPS-20 and RPS-24 designs.

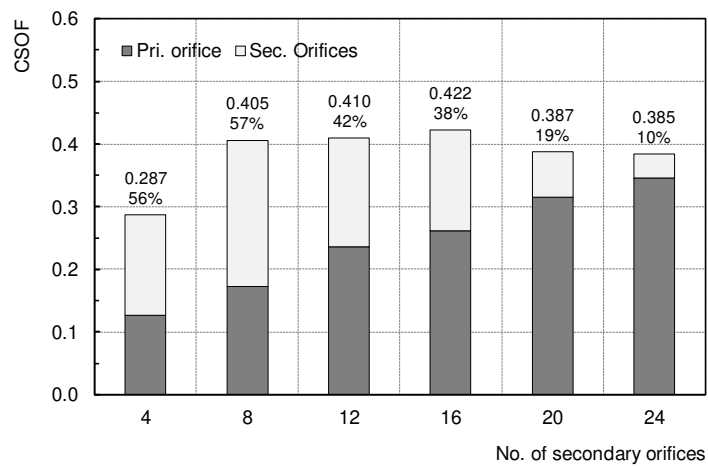


Figure 4.9 CSOF contributions from the primary orifice and the secondary orifices; Number above the bar chart indicates the total CSOF (top), and the %S-CSOF (bottom).

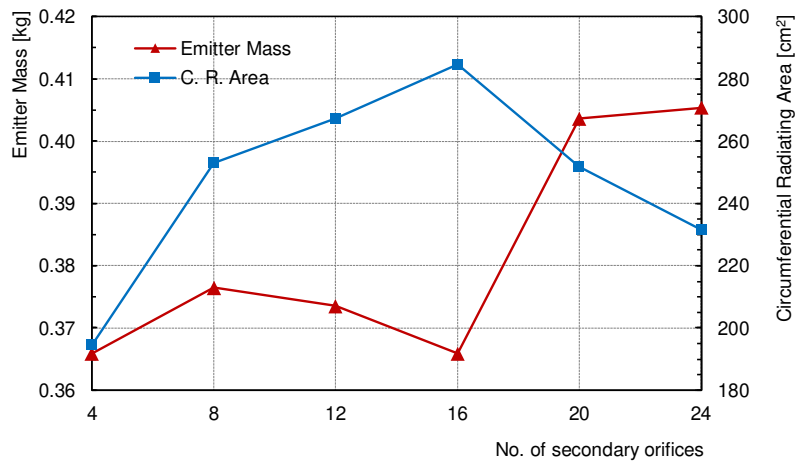


Figure 4.10 Influence of secondary orifice quantity on emitter mass and circumferential radiating area.

The mass of the emitter and the circumferential radiating area (which includes the external circumference, the primary orifice circumference, and the circumferences of the secondary orifices) must also be considered when evaluating the RPS designs. Since the objective is to design a large-area compact radial mode resonator, it is desirable to select a design that has the maximum circumferential radiating area and the smallest mass simultaneously. Figure 4.10 shows that the RPS-16 design provides the largest circumferential radiating area (285 cm²) and the lowest mass (0.37 kg) among the six RPS designs.

Table 4.8 provides the weightage of the RPS designs in terms of their CSOF, %S-CSOF, circumferential radiating surface area, and mass. The categorical weightage ranges from 1 to 6, with the more meritorious design in a category given the higher weightage. Based on geometric considerations alone, two designs stand out for being the most undesirable in terms of the discussed metrics. In addition to having the lowest CSOF and %S-CSOF, the RPS-20 and RPS-24 designs are also the heaviest at 404 g and 405 g respectively. In addition, their radiating surface areas are also among the lowest (252 cm² and 232 cm² respectively). In total, the RPS-20 and RPS-24 designs scored 6 and 10 points respectively, making these two designs the most unlikely candidates for a large-area compact resonator. Meanwhile, RPS-4 is one of the lighter design at 366 g. However, its circumferential radiating surface area (195 cm²) and CSOF is also the lowest. More importantly, what makes RPS-4 the weakest design of the lot is its highly non-uniform vibrational profile as indicated by the mode shape shown in Table 4.7.

Taking into account all the geometric factors, the designs comprising of 4, 20, and 24 secondary orifices present the most unfavourable design out of the six designs explored. Thus, the RPS-4, RPS-20, and RPS-24 designs will be excluded from further analysis.

Table 4.8 Weightage of RPS designs based on geometric considerations.

Designs	CSOF	%S-CSOF	C. R. Area	Mass	Total Points
RPS-4	1	5	1	5	12
RPS-8	4	6	4	3	17
RPS-12	5	4	5	4	18
RPS-16	6	3	6	6	21
RPS-20	3	2	3	2	10
RPS-24	2	1	2	1	6

4.3.3 Modifications incorporating tertiary orifices (RPST-type)

Following the approach described in section 4.3.2, the design of RPST resonators involve simultaneous adjustments to the primary, secondary, and tertiary orifice parameters (D_{pri} , D_{sec} , N_{sec} , PCD_{sec} , D_{trt} , N_{trt} , and PCD_{trt}) with D_{ext} , and H remain unchanged. The presence of tertiary orifices provides additional tuning parameter, giving rise to a higher number of design iterations. Figure 4.11 illustrates the geometric parameters of an RPST-type multiple orifice radial resonator.

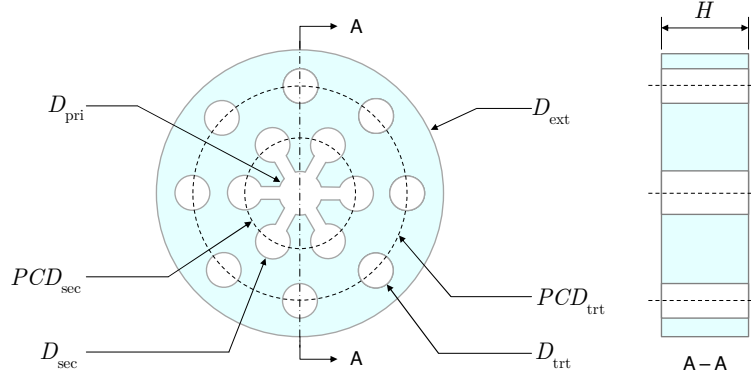


Figure 4.11 RPST resonator geometric parameters.

Interestingly, the addition of both secondary and tertiary orifices do not yield R0 mode as one of the eigensolutions. Instead, this configuration favoured a more complex modal behaviour that is not of interest. Through trial-and-error, it was discovered that the R0 mode could be excited if the secondary orifice layer in the RPST configuration is accompanied by the addition of another geometric feature known as the ‘orifice-link’. The orifice-links form channels between the primary orifice and the secondary orifices to form a symmetrical flower-like pattern that strongly induces the radial vibration of the structure. It is as though the linked primary and secondary orifices behave as one large patterned central orifice that promotes R0 mode deformation similar to the primary orifice of the RP and RPS designs.

The tuning parameters of the RPST design and its effect on the R0 mode frequency are shown in Figure 4.12. Iterative modal analysis solutions showed that D_{trt} is inversely proportional to the R0 mode frequency while PCD_{trt} varies linearly with the R0 mode frequency. The remaining orifice parameters do not have a linear relationship with the R0 mode frequency and have to be determined iteratively. Three RPST designs were conceived, each having one primary orifice and eight secondary orifices, but different quantities of tertiary orifices. The orifice parameters are provided in Table 4.9.

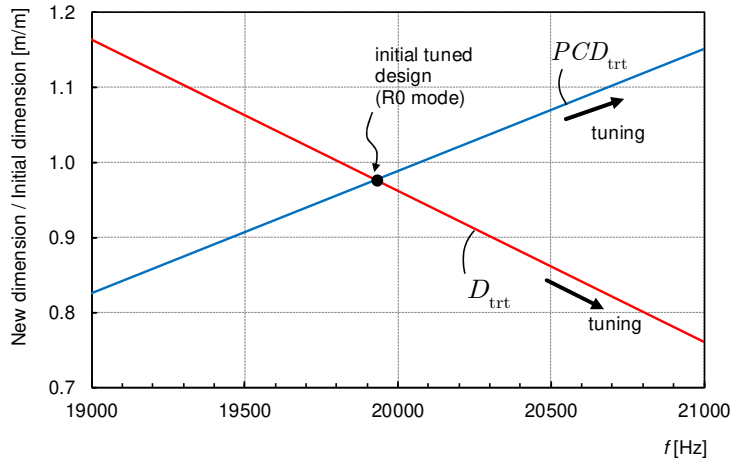
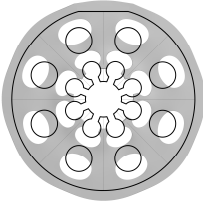
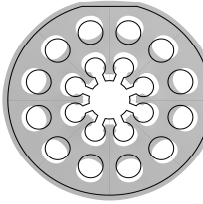
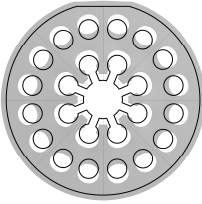


Figure 4.12 RPST resonator design chart.

As shown, the outer circumference and the primary orifice boundaries exhibit strong in-phase radial displacements that are characteristic of the R0 mode. Similar to the RPS designs, the boundaries of the secondary and tertiary orifices do not intersect with any nodal lines, and they deform coherently with structure. The secondary and tertiary orifices exhibit a combination of both rigid-body radial motion and an R2-like deformation induced by the motion of the inner and outer circumferences. The finger-like structures are not constrained circumferentially and provides additional degrees of freedom that can potentially manifest as parasitic resonances.

Table 4.9 Comparison of RPST configurations.

Parameters	RPST-8	RPST-12	RPST-16
Emitter section			
Pri. orifice dia. (mm)	20	20	20
Sec. orifice dia. (mm)	10	10	10
Sec. orifice PCD (mm)	34	36	38
No. of sec. orifices	8	8	8
Trt. orifice dia. (mm)	14	12	10
Trt. orifice PCD (mm)	70	72	74
No. of trt. orifices	8	12	16
Res. Freq. (Hz)	20007	19996	19986
Mesh elements	37,660	30,760	32,780

4.4 Analysis of radial resonator designs

4.4.1 Modal solutions

FE modal analysis was performed with frequency sweep between 10 kHz to 25 kHz, revealing eight possible modes of the RP-1 emitter section as shown in Figure 4.13. R3, R3*, and R0 appear to be the only radial modes that have no axial variations (the asterisk indicates an axisymmetric mode). The axial mode order is indicated by the numeric digit following the comma. For pure radial modes, only the radial mode order is indicated. The R3,1 and R3,1* are radial modes with one nodal plane in the axial direction, while the remaining modes can be classified following the definition of Lucas [115]. This research focuses only on pure radial modes.

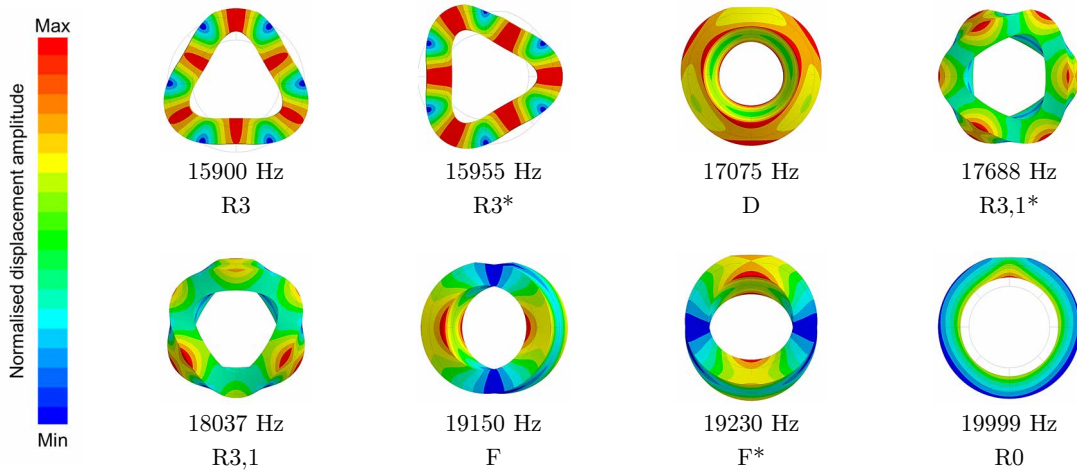


Figure 4.13 Normalised deformation contours of RP1 emitter modes (10–25 kHz).

Additionally, FE modal analysis was also performed on the mechanically-coupled exciter-emitter model to predict the shifts in resonances and to identify potential parasitic modes. As shown in Figure 4.14, the number of possible modes for the exciter-emitter geometry is significantly more diverse than the modes from the emitter section alone (Figure 4.13). Modal vibrations of the coupled geometry are a convolution of exciter modes, emitter modes, bolt modes, and flange modes, resulting in complex deformations that can be challenging to classify accurately. Coupled modes in which the exciter modes and the emitter modes can be distinguished were named while others were labelled as ‘complex’ and were not subjected to further scrutiny. The exciter section, which is primarily a longitudinal transducer, will have the following basic modes: longitudinal (L), bending (B), and torsional (T) [200–202]. Meanwhile, the basic emitter modes are radial (R), axial (A), torsional (W), face (F), and diameter (D) [115,121,203]. The numbers following the modal abbreviation indicate the mode order defined by the number of nodal lines or planes.

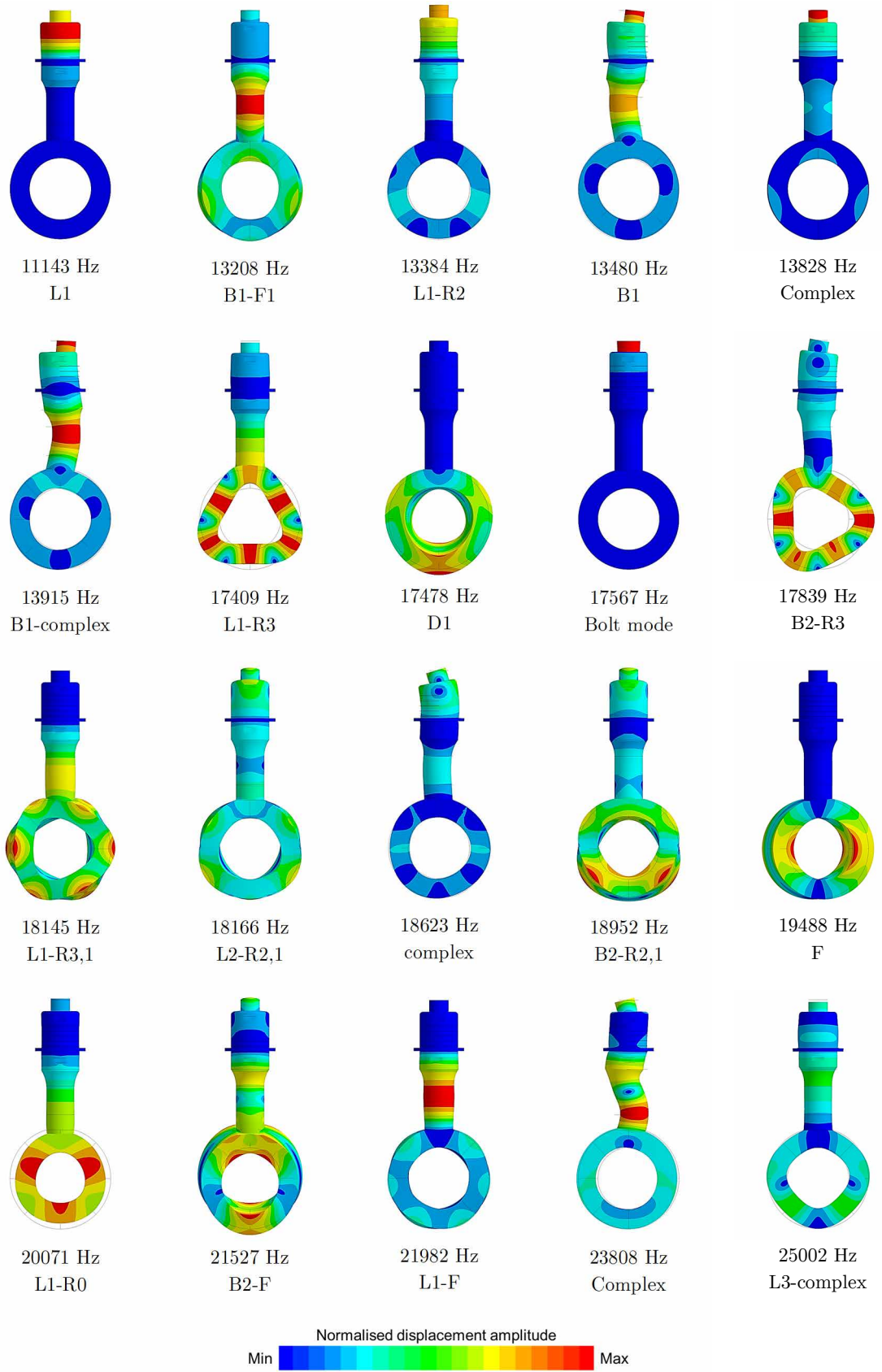


Figure 4.14 Normalised deformation contours of RP1 resonator modes (10–25 kHz).

Similarly, FE modal analyses were executed for the RPS and RPST resonator models comprising both exciter and emitter sections. Table 4.10 and Table 4.11 showed that the RPS and RPST resonators exhibited clear L1 mode in the respective exciter sections. The R0 modes are less obvious because the non-uniform deformations can be mistaken to be higher order radial modes. However, this is not the case since the circumferential boundaries of the emitter face displace primarily in the radial direction. Also, each element along the outer circumference and along the primary orifice circumference displaces in-phase, albeit at varying amplitudes. These are characteristics of a pure R0 mode. The coupling of the exciter and emitter sections also result in a slight reduction (around 1%) in the R0 frequency, which is not significant.

Table 4.10 Comparison of RPS radial resonator design outcomes.

Parameters	RPS-8	RPS-12	RPS-16
Mechanically-coupled exciter and emitter sections			
Mesh elements	188,241	187,338	185,597
Res. freq. (Hz)	19,762	19,769	19,742
Δ R0 freq. (Hz)	-236	-234	-275

Table 4.11 Comparison of RPST radial resonator design outcomes.

Parameters	RPST-8	RPST-12	RPST-16
Mechanically-coupled exciter and emitter sections			
Mesh elements	192,827	205,051	189,532
Res. freq. (Hz)	19,838	19,736	19,740
Δ R0 freq. (Hz)	-169	-260	-246

Modal analysis predicted 0.8–1.4% downshift in the R0 resonance frequency when compared to the emitter-only model. This shift is considered insignificant, and if tuning is desired, the most practical approach would be to carefully grind off the output end of the exciter section without making any adjustments to the emitter section. The mode shapes of the RPS and RPST models exhibited R0 modes that are deviating from the axisymmetric R0 vibration of the RP-1 design. Increasing the number of outer orifices (i.e. secondary orifices for the RPS-type, and tertiary orifices for the RPST-type) appear to correct this behaviour, encouraging a more axisymmetric deformation.

The multiple-orifice resonators (RPS and RPST designs) were designed with the objective of increasing the radiating surface area while keeping the mass and physical size of the device relatively unchanged. Here, a vibrating surface is considered radiating only if it is vibrating in a direction that is principally orthogonal to the surface. For a radial resonator operating in the R0 mode, the external circumferential surface and the primary orifice circumferential surface are the main areas from which the acoustic fields are radiated. Acoustic radiation from the faces of the emitter is neglected because their displacements are small compared to the circumferential surfaces.

The ratios of mass, radiating area, and radiating area per unit mass of the multiple-orifice devices to that of RP-1 are plotted in Figure 4.15. Here, it is shown that the goal of designing resonators with relatively large output area relative to its mass has been achieved. Compared to RP-1, the RPS configurations have 5–7% smaller masses but offer radiating surface areas that are 77–92% greater. Meanwhile, the RPST configurations are 10–13% heavier than RP-1, but the 118–160% increase in output area more than compensate the marginally larger mass. In terms of radiating surface area per unit mass (i.e. the area-to-mass ratio), the RPS and RPST multiple-orifice devices offered improvements of 85–107% and 95–130% respectively, over the RP-1 device.

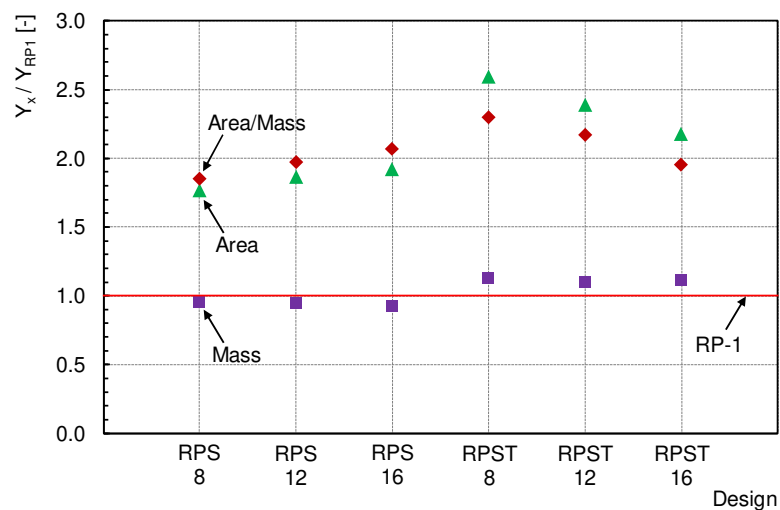


Figure 4.15 Relative mass, radiating surface area, and area-to-mass ratio of radial resonators.

4.4.2 Harmonic response simulation

Applying an excitation voltage and fixed support at the base of the flange constrain the model resulting in a condition that favours certain modes while suppressing others. A similar response behaviour was also observed when a sinusoidal force was applied to the input face of the emitter-only model. As shown in Figure 4.16, the normalised velocity response for RP-1 showed that the emitter-only model excites 2 modes out of the possible 5, while the exciter-emitter model excites 4 modes out of 20 modes in the same frequency range. It is apparent that low-order longitudinal and radial modes were favoured over torsional, flexural, and other complex modes. Although the device was designed for L1R0 mode operation, simulation results showed that the neighbouring modes can have a response magnitude that is similar to the tuned mode. Fortunately, untuned mode excitations are unlikely since the frequency of the tuned mode is separated from the frequencies of adjacent modes by more than 1500 Hz [204].

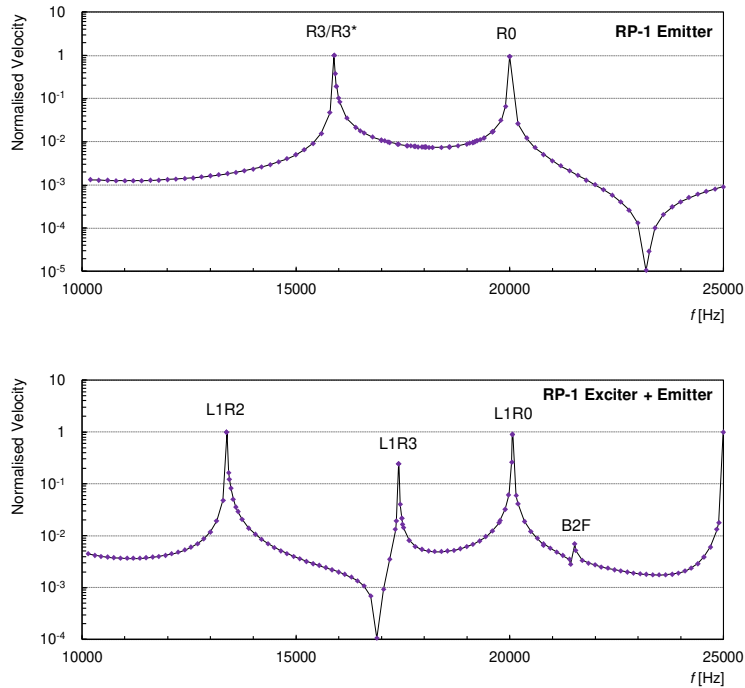


Figure 4.16 Simulated response of RP-1 resonator.

Subjecting the RPS and RPST models to the same excitation voltage and constraints as RP-1 yielded the response shown in Figure 4.17. Comparing the three RPS designs, the probability of modal coupling is highest for RPS-8 followed by RPS-12 due to the presence of adjacent modes within 1500 Hz of the tuned mode. The RPST-8 design presents the highest risk for modal coupling since its L1R0 mode is just 830 Hz away from an adjacent mode. Based on the simulated response

alone, RPS-16 is deemed as a more favourable configuration compared to RPS-8 and RPS-12. On the other hand, both RPST-12 and RPST-16 exhibited sufficient modal separation.

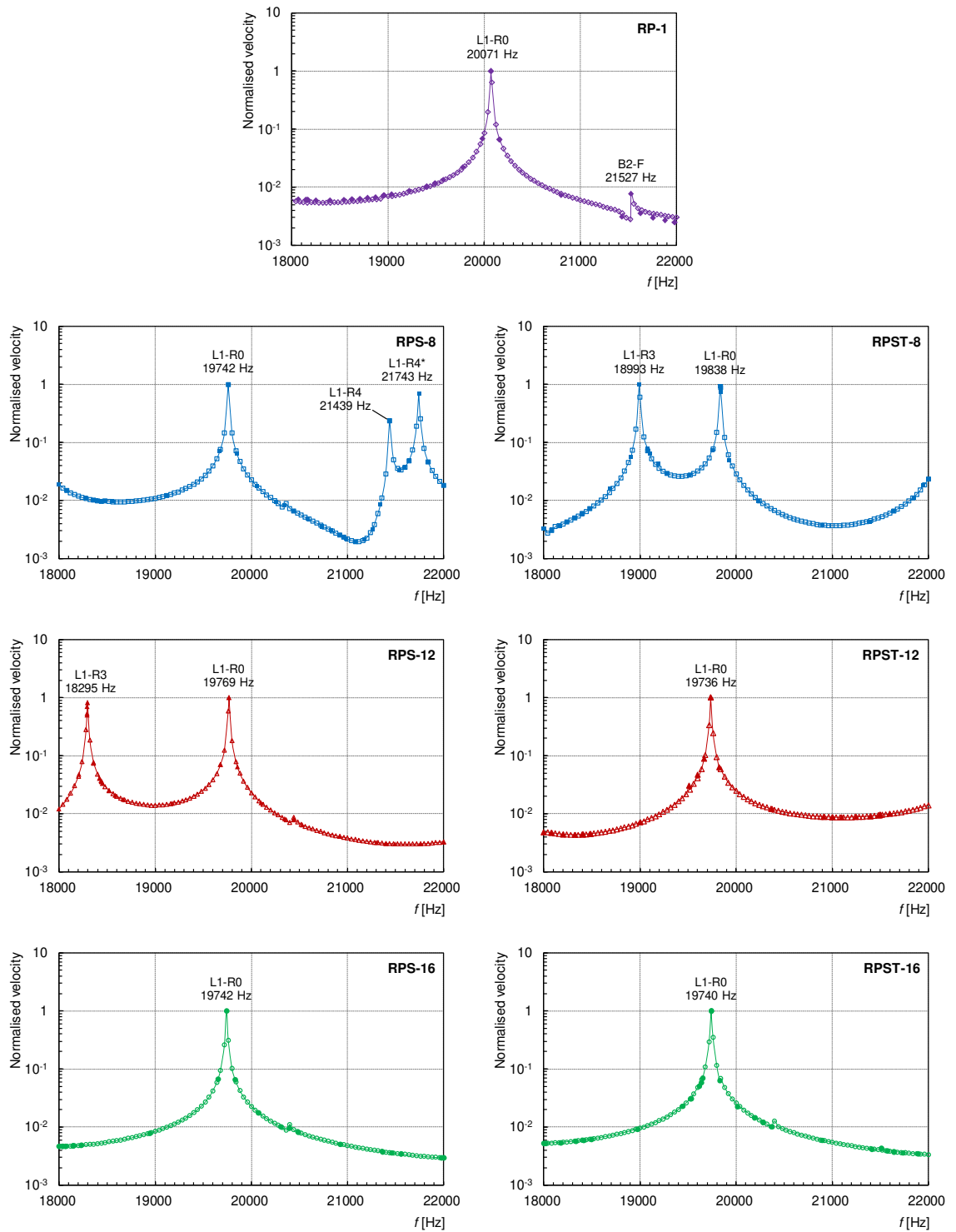


Figure 4.17 Simulated velocity response of radial resonators; mode superposition (closed markers); full solution (open markers); hybrid solution (line).

Radial velocities along the outer circumference and the primary orifice circumference were plotted as a function of angular position as shown in Figure 4.18. To generate a uniform pressure

field, the vibrational amplitudes along the radiating surface should be uniform. The radial resonators exhibited large differences between the velocity peaks and troughs indicating non-uniform displacement. Generally, the RPS and RPST configurations have less uniform vibrational amplitudes compared to RP-1. However, simulation results showed that vibration non-uniformity can be minimised by increasing the number of outer orifices.

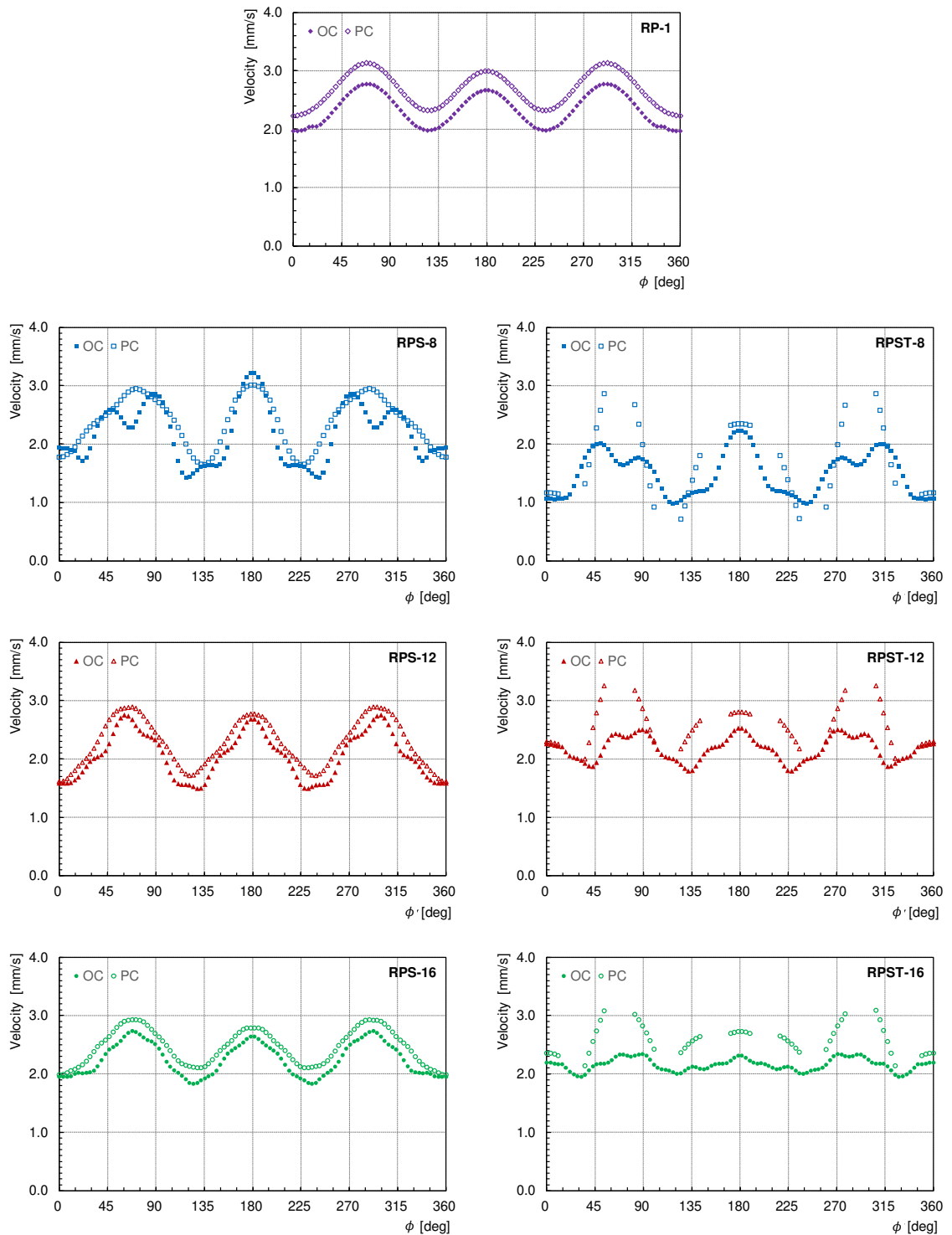


Figure 4.18 Simulated velocity profiles of radial resonators along the outer circumference (OC), and along the primary orifice circumference (PC).

Vibration uniformity is more clearly represented in the box and whisker charts of Figure 4.19 and Figure 4.20, in which the minimum, maximum, mean, 1st quartile, and 3rd quartile radial velocities extracted from data points around the circumferences of the resonators are represented. It should be noted that the data represented are deterministic, and based on one simulation run for each device. Here, it is observed that RPS-16 has the highest average radial velocity and the smallest standard deviation among the RPS-designs for both outer circumference and primary orifice circumference. Comparing the RPST designs, RPST-8 has the lowest average radial velocity, while RPST-12 and RPST-16 exhibited similar velocities at the outer circumference and the primary orifice circumference. However, RPST-16 configuration has the most uniform vibrational amplitude followed by RPST-12 as indicated by the length of the whiskers in the chart.

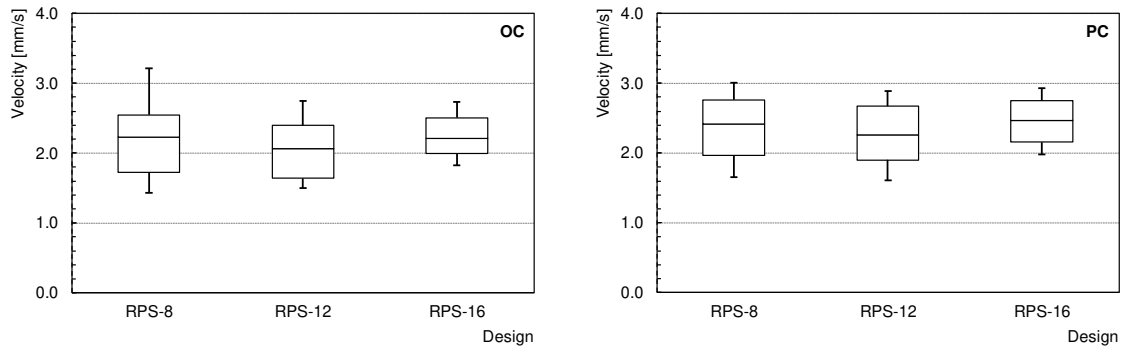


Figure 4.19 Comparison of vibrational uniformity of RPS resonators (no. of measurement points = 100).

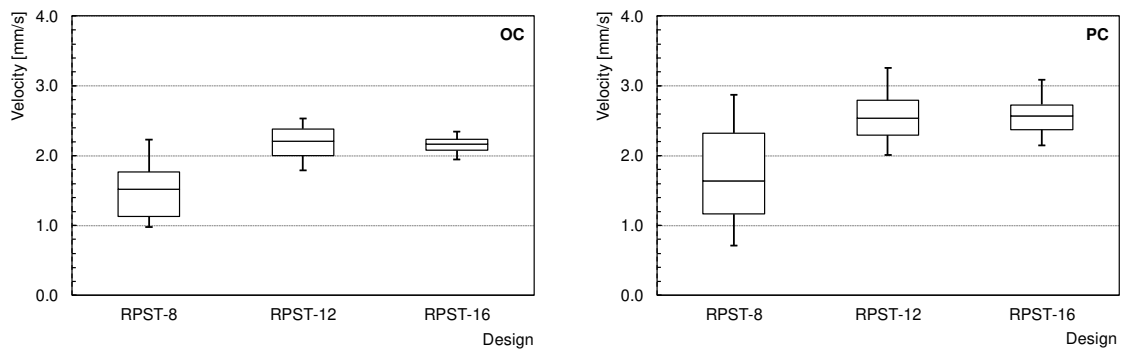


Figure 4.20 Vibrational uniformity of RPST resonators (no. of measurement points = 100).

After analysing the modal parameters, modal separation, vibrational amplitude, and vibrational uniformity of each multiple-orifice designs, the most favourable designs from each type were selected for fabrication and experimental evaluation. These multiple-orifice radial resonator designs were then benchmarked against the basic radial resonator (RP-1), and a commercial high-gain probe-type device. The selected designs are RPS-16 and RPST-16.

4.5 Conclusion

The need for a new resonator design to distribute ultrasonic radiation over a larger surface area led to the design of the multiple-orifice radial resonators. A commercial finite element modelling code, ANSYS, was employed to conceive six multiple-orifice radial resonator configurations through an iterative modal analysis process. The multiple-orifice radial resonator configurations have the same external shape and dimensions and were constructed from the same materials. Each configuration differs from the others in terms of the orifice quantity, size, and position, everything else being equal. Orifices were introduced systematically; the multiple-orifice resonator configurations comprising a primary orifice and a secondary layer of orifices were investigated first, followed by the multiple-orifice resonator configurations that include a tertiary layer of orifices and orifice-links. Mesh independence study was carried out to determine the appropriate mesh density for the simulation runs.

Harmonic response simulations were carried out to investigate modal excitation and to assess the risk of modal coupling. One configuration from each RPS- and RPST-type configurations exhibiting the best characteristics in terms of modal separation, and vibrational amplitude uniformity, were selected for fabrication and experimental evaluation.

In conclusion, this chapter has successfully demonstrated the use of FE modelling technique in the design of complex resonator geometries through virtual prototyping. Further insights can also be drawn from the FE results to aid the selection of the most superior design for physical prototyping and further experimental assessment.

Chapter 5

Experimental Analysis

5.1 Radial resonator assembly

5.1.1 Design selection

The previous chapter outlined the motivation for and the approach to designing multiple-orifice radial resonators. The feasibility of the multiple-orifice radial resonator designs was assessed based primarily on the following criteria:

1. The ability to vibrate in the L1R0 mode close to the design frequency of 20 kHz;
2. Well-isolated tuned mode – i.e. at least 1500 Hz separation from adjacent modes;
3. Vibrational uniformity at the radiating circumferences for a uniform ultrasound field.

FE modelling showed that the RPS-16 and RPST-16 resonators best satisfied the above criteria and were selected for experimental evaluation. The construction, assembly, and characterisation of the radial resonators in terms of their electrical and dynamic behaviour are described in the sections that follow. The characteristics of the multiple-orifice radial resonators are compared against two benchmarks – the first benchmark is the RP-1 radial resonator, which represents the more familiar radial resonator design used in prior works [27,38,205]. The use of RP-1 as a benchmark aims to highlight the effect of structural modifications (through the addition of orifices) on the dynamic and acoustic performance of radial resonators. The second benchmark utilises a commercial high-gain probe-type device as a universal baseline for comparing the performance of the resonators.

5.1.2 Exciter section assembly

The radial resonators were designed such that the emitter sections are replaceable (refer to Figure 4.1). Considering the emitter section's exposure to the cavitation field and its susceptibility to pitting damage, the ability to replace only the worn parts may be more economical than having to replace the whole resonator.

The exciter section is essentially a modified Langevin-type transducer and comprises of four D33 poled piezoceramic rings, four copper electrodes, a stainless steel backmass, an aluminium frontmass, and a socket head cap screw fastener (preload bolt) as shown in Figure 5.1. The

piezoceramic stack was assembled by alternate placement of the piezo-rings and copper electrodes. The piezo-rings were stacked such that adjacent rings have opposite poles, and the piezo-ring closest to the back mass was oriented with its negative pole facing the backmass. The piezo-stack was clamped between the end masses using a standard socket head cap screw fastener. An electrical tape insulates the screw shaft from the live electrodes to prevent electrical arcing due to the small clearance available. The exciter section assembly process is illustrated in Figure 5.2.

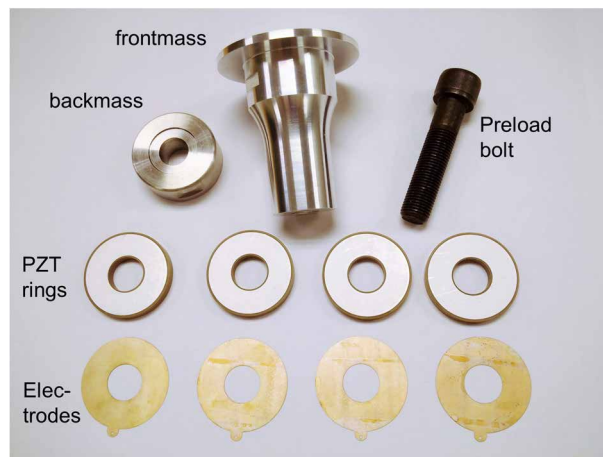


Figure 5.1 Exciter section components.



Figure 5.2 Exciter section assembly steps.

5.1.3 Emitter section and final assembly

Figure 5.3 to Figure 5.5 show the RP-1, RPS-16, and RPST-16 emitter sections and the exciter before mechanical coupling (left), and after mechanical coupling (right). Operation at the design frequency requires that both sections be tightly-coupled because part of the exciter's design length forms part of the emitter's structure as a cylindrical protrusion or 'stub'. This 'stub' provides a

threaded hole for securing the exciter and emitter using an appropriate screw fastener. The incorporation of the 'stub' design is purely an engineering consideration; a stub-less design would make for a longer exciter section, but the overall dimensions of the resonator would remain unchanged. However, a stub-less design would allow for only a very shallow threaded hole due to the presence of the orifices and would complicate the design and manufacture of the emitter sections.

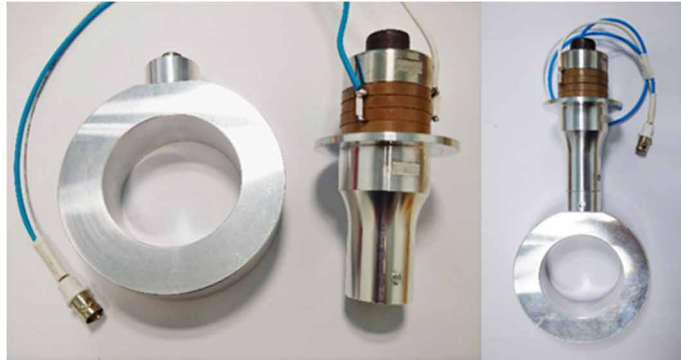


Figure 5.3 Fabricated RP-1 radial resonator.

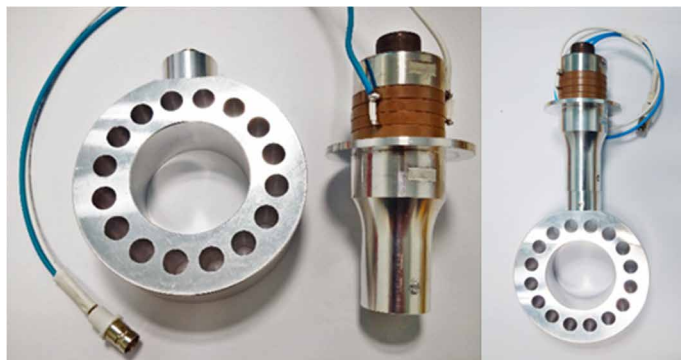


Figure 5.4 Fabricated RPS-16 multiple-orifice radial resonator.

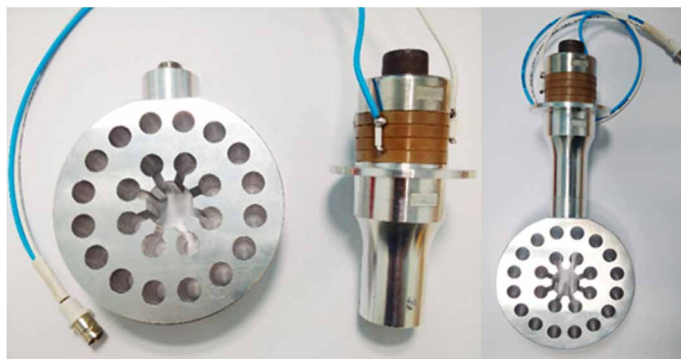


Figure 5.5 Fabricated RPST-16 multiple-orifice radial resonator.

5.2 Preload characteristics

5.2.1 Preloading the radial resonators

Preloading is a necessary step in piezoelectric transducer fabrication, and the extent of preloading can significantly influence the dynamic performance of the device [206]. The preload bolt is sufficiently tensioned to keep the piezoelectric stack in compression at all time, even during dynamic operation. Insufficient preloading can lead to mechanical failure of the PZT due to its low tensile strength σ_{\max} of 20–50 MPa [193], which is at least 1-order of magnitude lower than the metallic transducer parts. As illustrated in Figure 5.6, preloading offsets the resting stress of the ceramic in the negative direction so that a higher strain can be applied without breaking the ceramic. On the other hand, excessive compressive stress can compromise the piezoelectric property of the material. PZT ceramics can withstand stresses up to 250 MPa, but depoling occur at pressures of 20 to 30% of this limit. As a guide, the pre-stress should be in the range of 15-30 MPa [207].

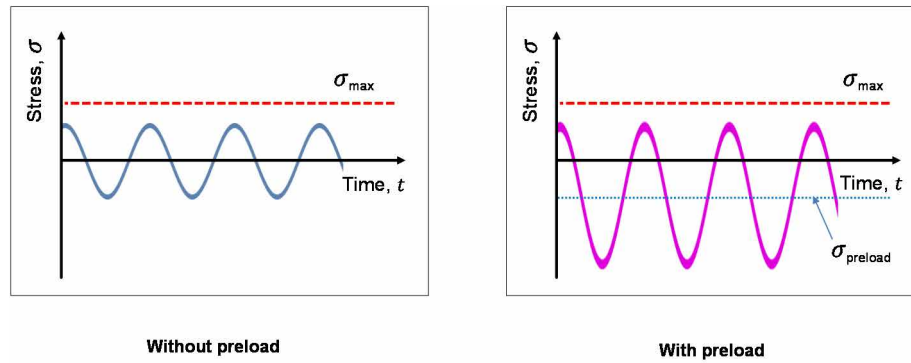


Figure 5.6 Effect of preloading on PZT.

When an external force is applied to a poled piezoceramic, the dimensional change depends on the stiffness of the material and the change of the remnant polarisation [208]. Since piezoceramics produce an electrical charge when subjected to mechanical stress, the applied pre-stress can be estimated by measuring the electric charge produced using the stress-charge equation:

$$q = d_{33}\sigma_{33}A, \quad (5.1)$$

where q (Coulombs) is the charge generated due to the applied stress σ_{33} (N/m^2) in the thickness direction. Application of mechanical stress on the PZT in open circuit condition generates a reaction force that can damage the material. Thus, the PZT terminals were short-circuited during preloading. As shown in Figure 5.7a, the backmass and frontmass were secured with a pair of torque clamps

sandwiched between the jaws of a bench vice such that the PZTs were not subjected to torsion during the preloading.

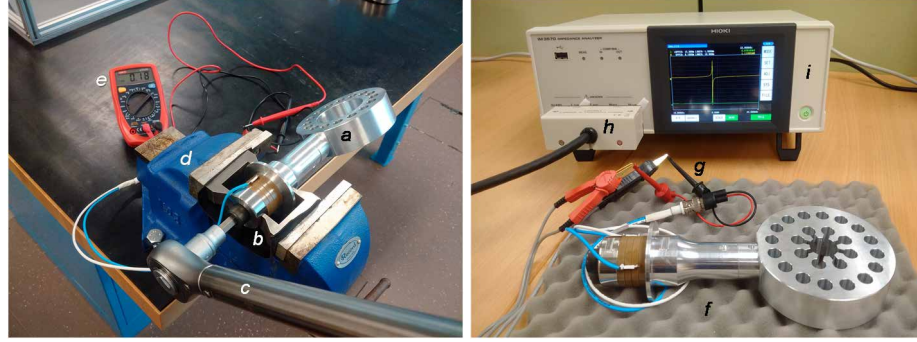


Figure 5.7 Transducer preloading tools and equipment: (a) radial resonator; (b) torqueing clamps; (c) torque wrench; (d) bench vice; (e) multimeter; (f) perforated foam support; (g) test leads; (h) test fixture; and (i) impedance analyser.

Preloading of the transducer assembly was carried out in steps, with each step involving incremental torquing and measurement of the electric charge q generated by the piezoceramic stack. By connecting the electrode terminals to a $1 \mu\text{F}$ capacitor and measuring the voltage V across the capacitor, the charge generated from the preloading step can be calculated using $q = CV$. The applied preload for the step can then be back-calculated using equation (5.1).

A torque wrench (Norbar, TTi250) was used to apply the pre-stress. The appropriate torque T_S (Nm) required for each step is calculated using the following expression [209]:

$$T_S = \frac{F_S}{1000} \left[\frac{D_p}{2} \left(\frac{\mu}{\cos \alpha} + \tan \beta \right) + \mu_n \frac{1}{2} \left(\frac{2}{3} \times \frac{D_H^3 - D_{maj}^3}{D_H^2 - D_{maj}^2} \right) \right]. \quad (5.2)$$

where D_p , D_{maj} , and D_H are the pitch diameter, major diameter, and bolt head diameter respectively; μ and μ_n are the thread friction coefficient and the under-head friction coefficient respectively; α and β are the screw thread half-angle and the lead angle respectively. Bolt coefficients for estimating the required torque for preloading are given in Table 5.1.

Table 5.1 Torque calculation parameters.

D_p (mm)	D_H (mm)	D_{maj} (mm)	α (deg)	β (deg)	μ	μ_n
11.8	19.05	12.7	30	1.96	0.16	0.16

Due to manufacturing tolerances of the piezoelectric device, error of measurement tool, and the approximation of the frictional coefficients, it is important to verify the applied pre-stress at each

step to avoid applying excessive stress to the ceramics. This is done, by first calculating the expected charge q_{calc} that will be generated by the piezoceramic stack and the corresponding expected voltage V_{calc} across a 1 μF capacitor after each preloading step. The applied pre-stress was verified by comparing V_{calc} with the actual voltage V_{meas} measured across the capacitor. As shown in Table 5.2, V_{calc} overestimates V_{meas} by around 10–12 %, which implies that the applied pre-stress is actually lower than the target values. This observation is likely associated with the very conservative assumption of the frictional coefficients μ and μ_n .

Table 5.2 Preloading steps.

Steps	σ_s (N/m ²)	F_s (N)	T_s (Nm)	q_{calc} (C)	V_{calc} (V)	V_{meas} (V)
1	2.15×10^7	2.06×10^4	50	2.10×10^{-5}	21.0	18.8
2	2.58×10^7	2.47×10^4	60	2.52×10^{-5}	25.2	22.2
3	3.01×10^7	2.88×10^4	70	2.94×10^{-5}	29.4	25.9
4	3.23×10^7	3.09×10^4	75	3.15×10^{-5}	31.5	28.4

5.2.2 Impedance analysis (IA) of preload characteristics

For low ultrasonic frequencies in the range of 20–100 kHz, electric impedance between 10–100 ohms are expected. The minimum electrical impedance Z_m (or maximum admittance) is inversely related to the series resonance frequency f_m for the same material [193]. Preloading the PZT causes the polarisation direction of its domains to reorientate and stabilise after a relaxation time which varies from a fraction of a second, to a fraction of an hour [210,211]. After each preloading step, the resonator was allowed to stabilise for at least 24 hours before the impedance spectrum was measured using an impedance analyser with equivalent circuit analysis function (IM3570, Hioki). The effect of pre-stress on Z_m and f_m are shown in Figure 5.8, Figure 5.9, and Figure 5.10.

For the three radial resonators, it was observed that the initial Z_m at low pre-stress was around 150–160 ohms. This value gradually decreased with incremental application of pre-stress. Z_m stabilised at around 31 kN consolidating towards 50–60 ohms, which is close to the output impedance of the excitation signal source.

Meanwhile, the resonance frequency f_m increased with application of pre-stress. This behaviour is explained by the fact that preloading produced a negative strain in PZT rings. Since the thickness mode resonances has an inverse relationship with the thickness (axial length) of the PZT, a negative strain the thickness direction will increase the thickness mode resonance frequency. The increase in

f_m also implies that the reactive components of the resonator are smaller (since $f \propto 1/\sqrt{LC}$). Further, since $L \propto M$ and $C \propto 1/K$, and preloading does not result in a change of mass, the increase in f_m is associated with the overall increase in resonator stiffness [39].

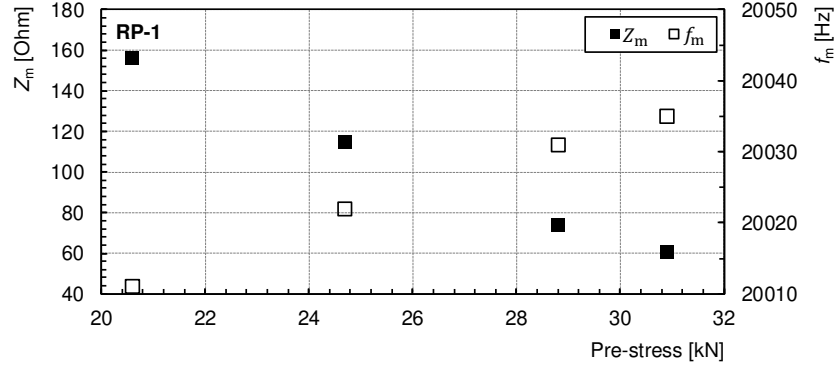


Figure 5.8 Evolution of Z_m and f_m with pre-stress (RP-1).

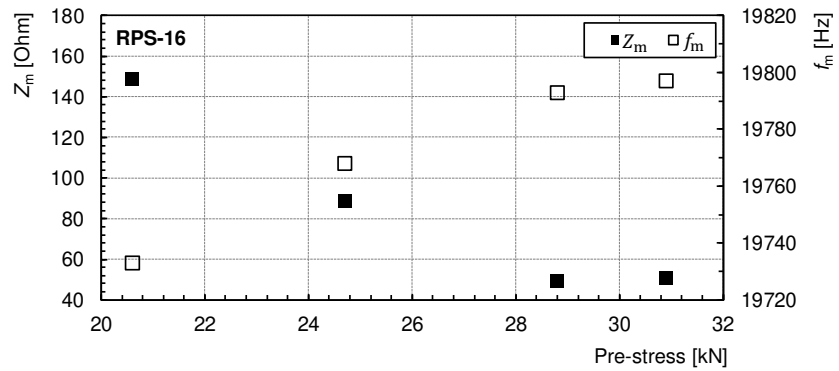


Figure 5.9 Evolution of Z_m and f_m with pre-stress (RPS-16).

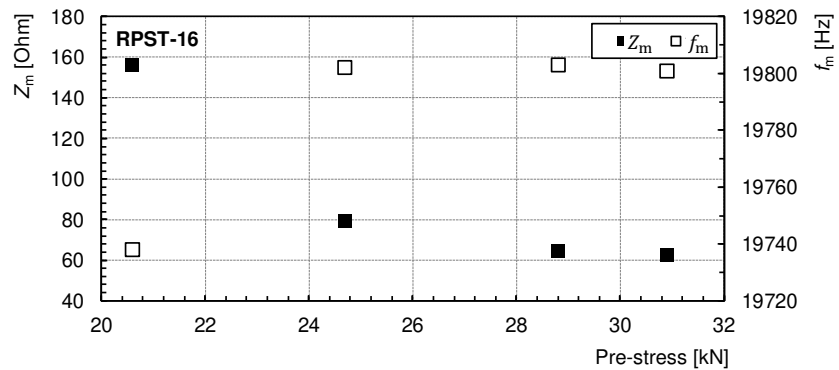


Figure 5.10 Evolution of Z_m and f_m with pre-stress (RPST-16).

5.3 Experimental Modal Analysis (EMA)

5.3.1 Experimental set-up

The experimental modal analyses (EMA) were carried out using a 3D laser Doppler Vibrometer (LDV) to execute simultaneous optical measurements of the tri-axial velocities, $\dot{u}_x, \dot{u}_y, \dot{u}_z$ from each measurement position on a grid of measurement positions. The LDV (CLV-3D, Polytec) comprises a sensor head and a controller. The sensor head generates the laser beams and transmits raw RF signals to the controller which amplifies, conditions, and processes the measurement signals in the orthogonal coordinate system. The resulting vibrational velocities and a reference signal (excitation signal) were fed into a 4-channel data acquisition device (DAQ) which also serve as a front-end to the modal analysis software (ME'scope VES, Vibrant Technology). The DAQ (DT9837C, Data Translation) provides a sampling frequency in the range of 195.3 Hz to 105.469 kHz [212], effectively limiting the modal analysis to a maximum frequency of 52.7 kHz [213]. Figure 5.11 shows the schematic for EMA.

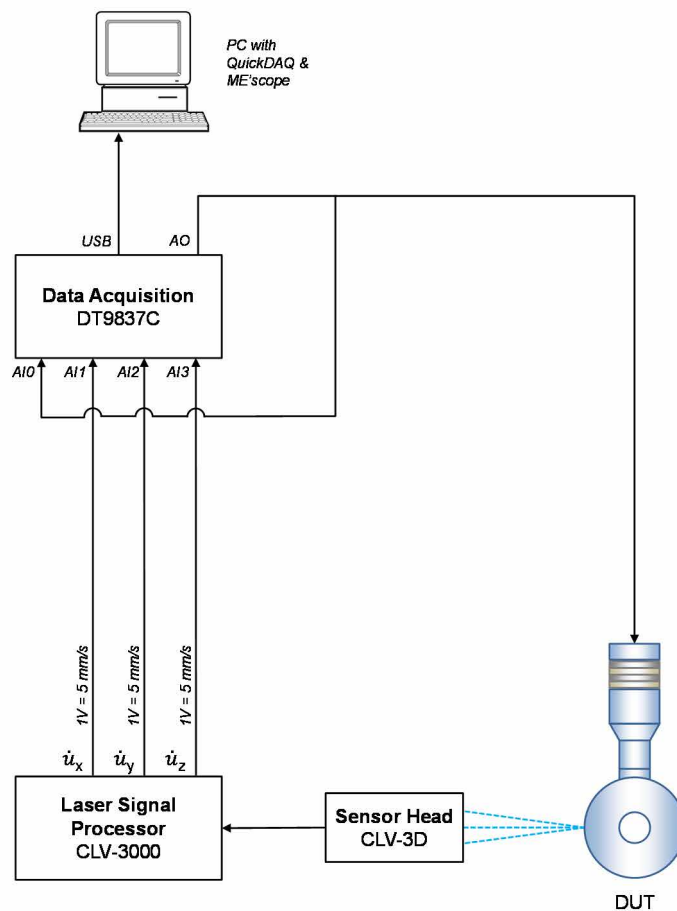


Figure 5.11 EMA schematic.

The built-in analogue output channel of the DAQ front-end device connects directly to the resonator terminals to provide the excitation signal. A random burst signal with a peak-to-peak voltage of 2 V, (± 1 V) was used to excite all frequencies in the defined spectrum range simultaneously, and enable the detection of any interactions between resonances [214,215]. The QuickDAQ FFT (Data Translation) data acquisition and signal processing software acquires the channel data and computes the frequency response function (FRF) associated with each degree of freedom (DOF). This information is then passed to the modal analysis software (ME'scope VES, Vibrant Technology) which in turn computes the modal parameters.

5.3.2 Laser Doppler Vibrometry (LDV)

Laser Doppler Vibrometry is an optical measurement technique that can accurately capture the vibrational response of a structure without introducing potential artefacts arising from sensor loadings. This technique is especially advantageous when measuring the modal response of small structures. The basic LDV comprises a 2-beam interferometer that measures the frequency or phase difference between the reference beam and the test beam. The measurement was made by pointing the laser beams at a point on the vibrating surface. The interaction of the laser and the vibrating surface generates frequency modulation signal due to the Doppler Effect. The velocity information is then recovered in the signal processing unit with the aid of suitable modulators [216].

Unlike the more common 1-D LDV equipment, the CLV-3D directs three laser beams to the measurement target. Figure 5.12 shows the LDV sensor head with the three laser beams intersecting at the measurement point. The top view shows the relationship between the R and L velocity components, and the resolved x and z components. The side view of the same figure shows T velocity component and the resolved y component. As shown, the y component is not only dependent on the T velocity, but also relies on the assumption that y is orthogonal to the plane containing R and L. Therefore, the correct interpretation of the measurement result requires that the three beams intersect at the measurement point (i.e. the focal point).

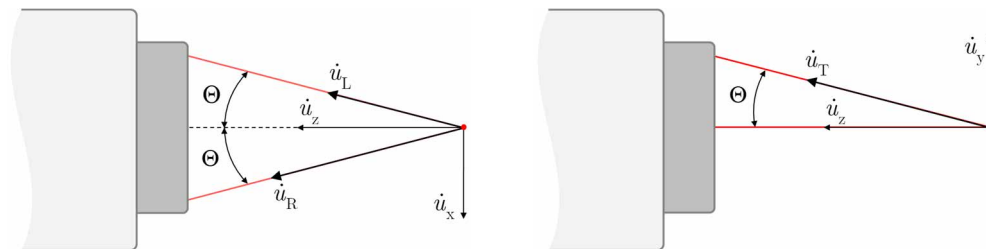


Figure 5.12 Sensor head and laser beams; top view (left); side view (right).

The laser beams R, L, and T, independently measure the velocities of a point on the test object in their respective beam coordinate system. The local coordinate measurements are transformed into the orthogonal coordinate system using [216],

$$\dot{u}_x = \frac{\dot{u}_R - \dot{u}_L}{2 \sin \Theta}, \quad (5.3)$$

$$\dot{u}_y = \frac{\dot{u}_T}{\sin \Theta} - \frac{\dot{u}_R + \dot{u}_L}{2 \sin \Theta}, \text{ and} \quad (5.4)$$

$$\dot{u}_z = \frac{\dot{u}_R + \dot{u}_L}{2 \cos \Theta}, \quad (5.5)$$

where \dot{u} (m/s) is the vibrational velocity. Here, the subscripts R, L, and T represent the laser beam coordinate systems, while subscripts x, y, and z represent the global Cartesian coordinate system.

The mathematical relationship of equations (5.3) to (5.5) becomes more complex when R and L beams are not in the x-z plane. Thus, the sensor head and the device-under-test should be placed on the same platform that is also adequately isolated from ambient vibrations.

When performing EMA on a device with many measurement points, manually positioning the sensor head or the test object at each measurement step can potentially introduce measurement errors due to misalignment. More precise positioning can be achieved by using a combination of fixtures, stages, and jacks. In the current work, the test object was supported by a fixture which has been mounted on a translational stage having maximum travel of 20 mm (LT TS-150, Holmarc). The laser sensor head was serially mounted onto two lab-jacks (LJ 150-100, Holmarc) to provide total travel of 104 mm. The combined operation of the translational stage and the lab-jacks enable precise lateral and vertical adjustments of the laser beam landing position on the test object.

5.3.3 Data acquisition and signal processing

The piezoelectric resonators were excited by random burst signal which ramps up from zero at the beginning and ramps down to zero at the end of each burst. A 5 second “quiet” interval between successive bursts was set to provide sufficient time for the response signal to decay while allowing the transducer to cool down adequately before the next excitation event. Operating the transducer at a stable temperature gives a more predictable dynamic behaviour. Excitation voltage was kept at ± 1 V (2 V peak-to-peak), a level that is not only adequate for EMA but also avoids nonlinear behaviour that is characteristic of PZT-based devices operating at elevated voltages [166]. Further, the high measurement sensitivity (a resolution of < 2 $\mu\text{m/s}$ can be achieved at 20 kHz), and high signal-to-noise (SNR) of the LDV equipment are highly favourable for such test conditions [216].

The sampling frequency is an important consideration in data acquisition. The Nyquist criterion states that the sampling frequency must be at least twice the maximum frequency component of the signal [213]. Violating this criterion result in aliasing, a phenomenon characterised by the false representation of the signal that appears to be at a lower frequency than the actual signal. In the present study, the DAQ device was set to a sampling frequency of 96 kHz to allow analysis up to 48 kHz. This range is sufficient for the present study which deals with ultrasonic frequencies of around 20 kHz. As a further measure, the DAQ device provides anti-aliasing filters which attenuate signals above 57.7 kHz to -100 dB [212].

Following acquisition and digitisation of the analogue signals, the Fast Fourier Transform (FFT) algorithm converts the time domain signals into its frequency domain equivalent. At this point, it is important to note that the FFT process requires that the measured signal be periodic in the sampling window to avoid distortion of the frequency domain data [217]. Failure to meet this condition result in leakage, an error characterised by the incorrect interpretation of amplitudes and frequencies of the measured signal. Thus, it is vital that appropriate steps be taken to ensure leakage-free signals. The random burst reference signal is inherently leakage-free [215], but a weighting function (windowing) was applied to the response signals to ensure that ambient vibrations do not affect the quality of the signal. Acquisition and signal processing were carried out using the QuickDAQ FFT signal processing software. A summary of the acquisition settings is listed in Table 5.3.

Table 5.3 EMA configuration and settings.

Description	Settings	Device / Software
Excitation signal		DT9378C
Signal type	Burst random	
Voltage	2 V peak-to-peak (± 1 V)	
Laser Vibrometer		CLV-3D
Stand-off distance	310 mm	
Decoder module	CLV.M030.B	
Laser signal sensitivity	5 (mm/s)/V	
Acquisition		DT9378C
Input channel scaling	0.2 V/(mm/s)	
Sample rate	96,000 Hz	
Weighting function	Hanning window	
FFT		QuickDAQ FFT
Frequency span	0 – 48,000 Hz	
Frequency resolution	1.4648 Hz	
No. of spectral lines	32,768	
No. of averages	100	
FRF estimator	H1	

5.3.4 Modal parameter extraction

Experimental modal analysis is based on the computation and interpretation of the frequency response function (FRF) defined as the ratio of the output response of a structure to the applied force. Analysing the vibration characteristics of structures at ultrasonic frequencies require that the measurement technique be carefully considered to minimise artefacts in the measurements. Thus, vibration measurements on ultrasonic devices were carried out using a non-contact technique to eliminate the mass-loading effects [218] which can considerably alter the modal response of a structure [219]. The excitation force was not measured since a direct measurement using a load cell would be invasive although the computation of the FRF by definition, requires the input force data. Instead, the excitation voltage was used as an analogue to force since it provides a proportional amplitude and phase relationship [220]. For modal identification, this is acceptable because only relative magnitudes and phase information are needed to represent the mode shapes correctly.

Applying FFT to the sampled data gives linear spectra of the reference and response signals. This frequency domain information is averaged to eliminate noise in the computation of the auto-spectra, and cross-spectrum. The auto-spectra of the input signal $G_{aa}(\omega)$, auto-spectra of the response signal $G_{bb}(\omega)$, and the cross-spectrum $G_{ab}(\omega)$ between the reference and response signals are given by [215],

$$G_{aa}(\omega) = S_a(\omega) \cdot S_a^*(\omega), \quad (5.6)$$

$$G_{bb}(\omega) = S_b(\omega) \cdot S_b^*(\omega), \text{ and} \quad (5.7)$$

$$G_{ba}(\omega) = S_b(\omega) \cdot S_a^*(\omega), \quad (5.8)$$

where $S_a(\omega)$ and $S_b(\omega)$ are the linear Fourier spectrum of the input signal $x(t)$ and the response signal $y(t)$, and $S_a^*(\omega)$ and $S_b^*(\omega)$ are their complex conjugates. The FRF contains information about the natural frequencies, damping, and mode shapes of the system and can be estimated using either one of the following functions [215]:

$$H_1(\omega) = \frac{S_b(\omega) \cdot S_a^*(\omega)}{S_a(\omega) \cdot S_a^*(\omega)} = \frac{G_{ba}}{G_{aa}}, \text{ or} \quad (5.9)$$

$$H_2(\omega) = \frac{S_b(\omega) \cdot S_b^*(\omega)}{S_a(\omega) \cdot S_b^*(\omega)} = \frac{G_{bb}}{G_{ab}}. \quad (5.10)$$

Meanwhile, the coherence function provides an objective indication of how closely related are the reference and response signals – coherence values close to unity signifies good correlation between the response signal and the excitation signal. It should be noted that coherence tends to be low at anti-resonances, or measurement nodes where the responses are low. Coherence is expressed as [215]

$$\gamma^2 = \frac{H_1(\omega)}{H_2(\omega)}. \quad (5.11)$$

The EMA was carried out by measuring the vibration response from various positions on the resonator and taking a reference to a fixed excitation position. The measurement points were selected such that the deformation of the outer circumference, primary orifice, secondary orifices, and tertiary orifices were adequately captured. In the present study, the interest is in identifying low-order radial modes of the emitter sections, which can be sufficiently described from the selected measurement grid. Figure 5.13 shows the wire-frame versions of the resonators as defined in the modal analysis software, with the nodes indicating the measurement points.

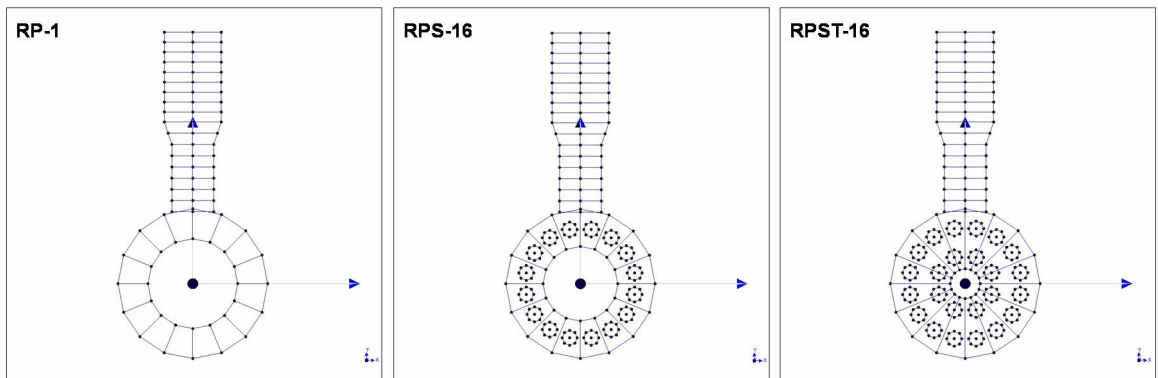


Figure 5.13 EMA measurement points for radial resonators.

The FRFs were assigned to the respective nodes in the computer model of the modal analysis software. This computer program performs curve-fitting of the frequency response measurements to estimate the resonance frequencies, mode shapes, damping of the resonators. The measured mode shapes and associated modal frequencies are then compared with the simulation results to validate the finite element model.

5.4 Resonance and mode shape extraction

5.4.1 Comparison of FE and EMA results

EMA measurements were obtained from the grid points distributed on the circular face of the resonator with the remaining points distributed along the length of the exciter section. This was done with the intention of identifying the radial modes because the generation of strong acoustic pressure relies on the normal component of the vibrational amplitude. However, the grid distribution does not allow for the differentiation of modal orders in the axial direction – a third radial mode with zero-order axial mode (R3,0) cannot be distinguished from its first-order axial mode (R3,1).

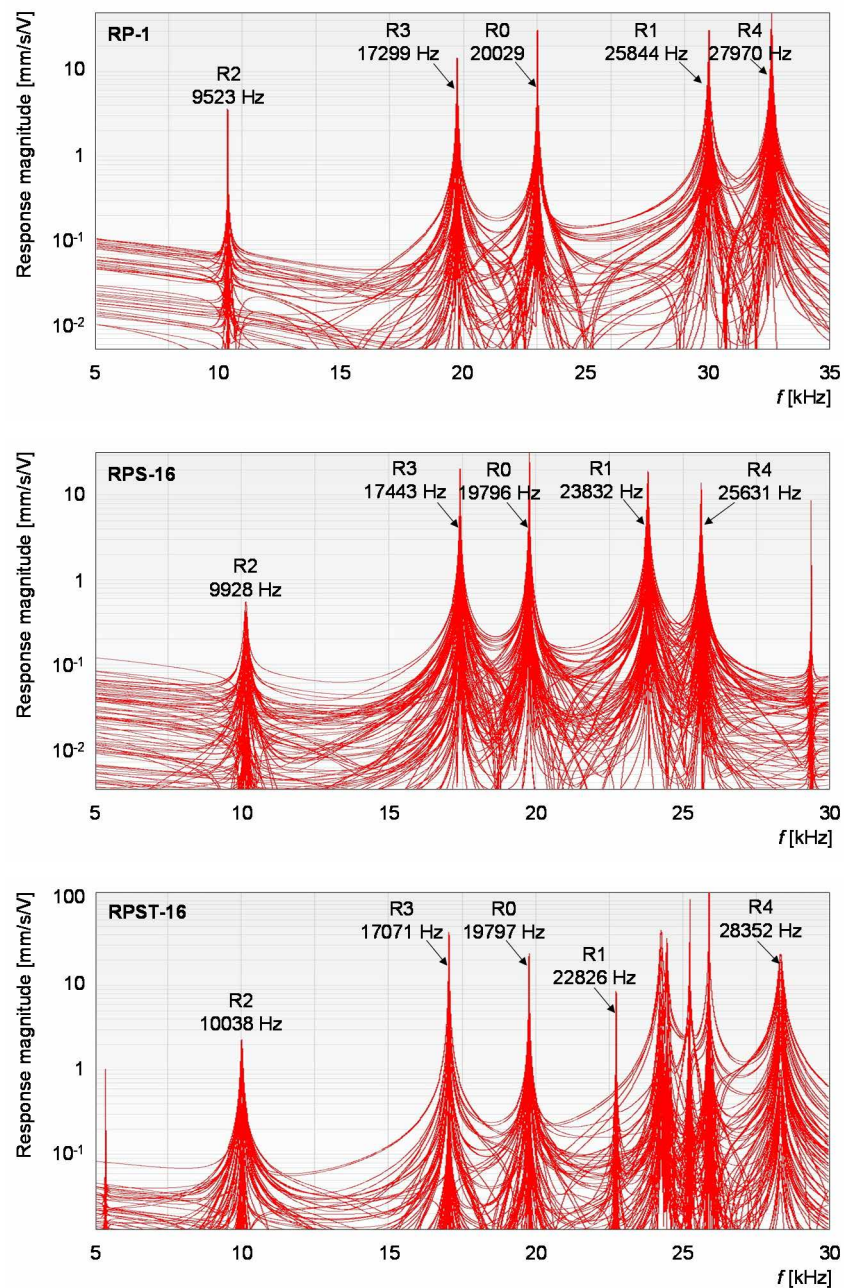


Figure 5.14 FRFs from 48 DOF measurement points per device obtained from EMA.

The curve-fitted FRFs from multiple measurement DOFs were overlaid giving Figure 5.14. In this figure, it is observed that the frequency separation between the fundamental radial mode (R0) and its immediate neighbours is sufficient to prevent any unwanted modal coupling. The R0 mode frequencies for RP-1, RP-16, and RPST-16 are 20029 Hz, 19796 Hz, and 19797 Hz respectively. Immediately adjacent to this tuned mode are the R3 and R1 modes. Across the radial resonator configurations, the R3 mode appeared at 2353–2730 Hz below the R0 mode, while the R1 mode appeared at 3029–5815 Hz above the R0 modes. This represent R0 mode frequency separation of 13.6–29.0% for RP-1, 11.9–20.4% for RPS-16, and 13.8–15.3% for RPST-16 (see Table 5.4).

Table 5.4 Frequency separation between R0 and adjacent modes.

Design	$\Delta f_{R3,R0}$		f_{R0}	$\Delta f_{R1,R0}$	
	(Hz)	(%)		(Hz)	(%)
RP-1	-2730	13.6	20029	+5815	29.0
RPS-16	-2353	11.9	19796	+4036	20.4
RPST-16	-2726	13.8	19797	+3029	15.3

Comparison of the resonance frequencies and mode shapes from the FE predictions and the EMA measurements show very good agreement. As shown in Figure 5.15 to Figure 5.17, the FE model predicted the radial modes found in the sweep range of 8–30 kHz with reasonable accuracy. The absolute percentage difference between the R0 mode frequency found through FE and EMA methods were around 0.30% for the RP-1, RPS-16 and RPST-16 resonators. Meanwhile, the resonance frequencies and mode shapes for higher order radial modes predicted by the FE model have a greater deviation from the EMA results. This may be associated with the sensitivity of the LDV and its susceptibility to ambient vibrations, which give rise to measurement uncertainties. The absolute percentage difference between the modal frequencies found through FE and EMA methods are: 0.20% to 2.50% for the R1 mode; 5.60% to 7.28% for the R2 mode; 0.73% to 1.25% for the R3 mode; and 2.15% to 4.86% for the R4 mode, for the three radial resonators. This percentage errors between FE and EMA are summarised in Table 5.5.

Table 5.5 Modal frequencies percentage error – FE vs. EMA.

Radial modes, R <i>n</i>	% error = $\left[\left(f_{Rn,FE} / f_{Rn,EMA} \right) - 1 \right] \times 100\%$		
	RP-1	RPS-16	RPST-16
R2	-7.28	-5.60	-6.30
R3	+0.73	-1.09	-1.25
R0	+0.30	-0.30	-0.30
R1	-2.50	-0.58	-0.20
R4	+2.95	+2.15	+4.86

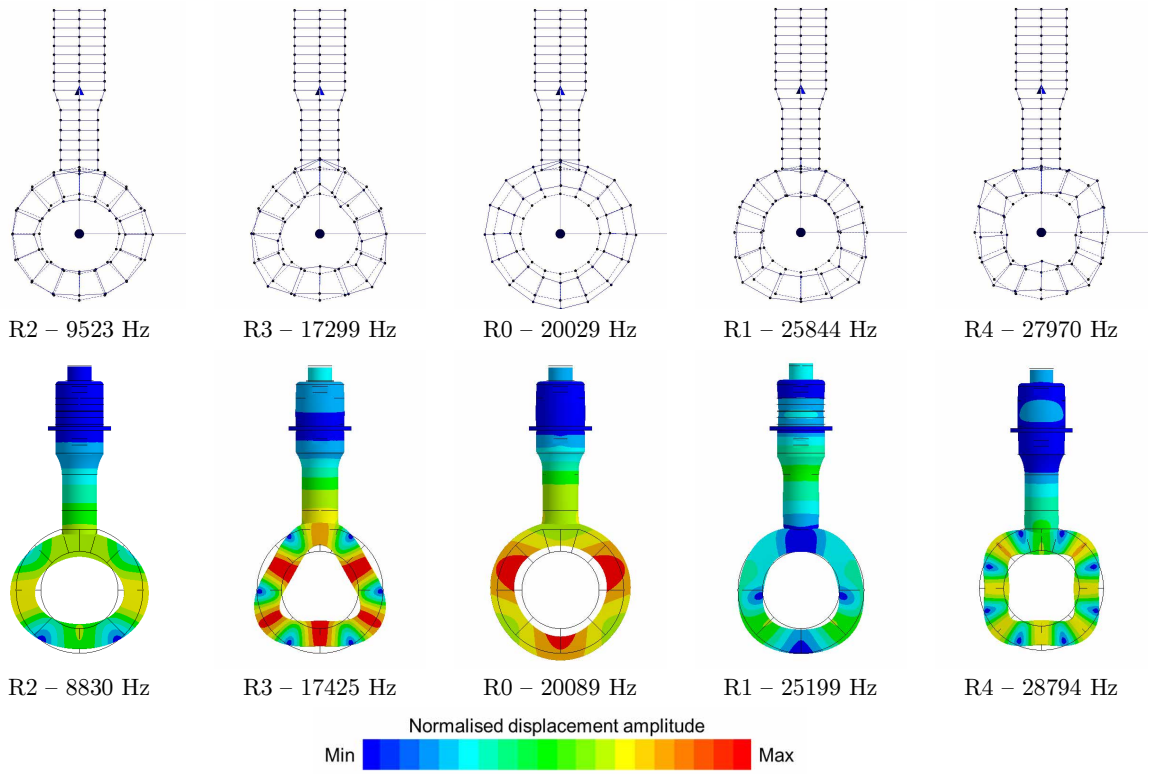


Figure 5.15 Radial modes of RP-1 – EMA (top), FE (bottom).

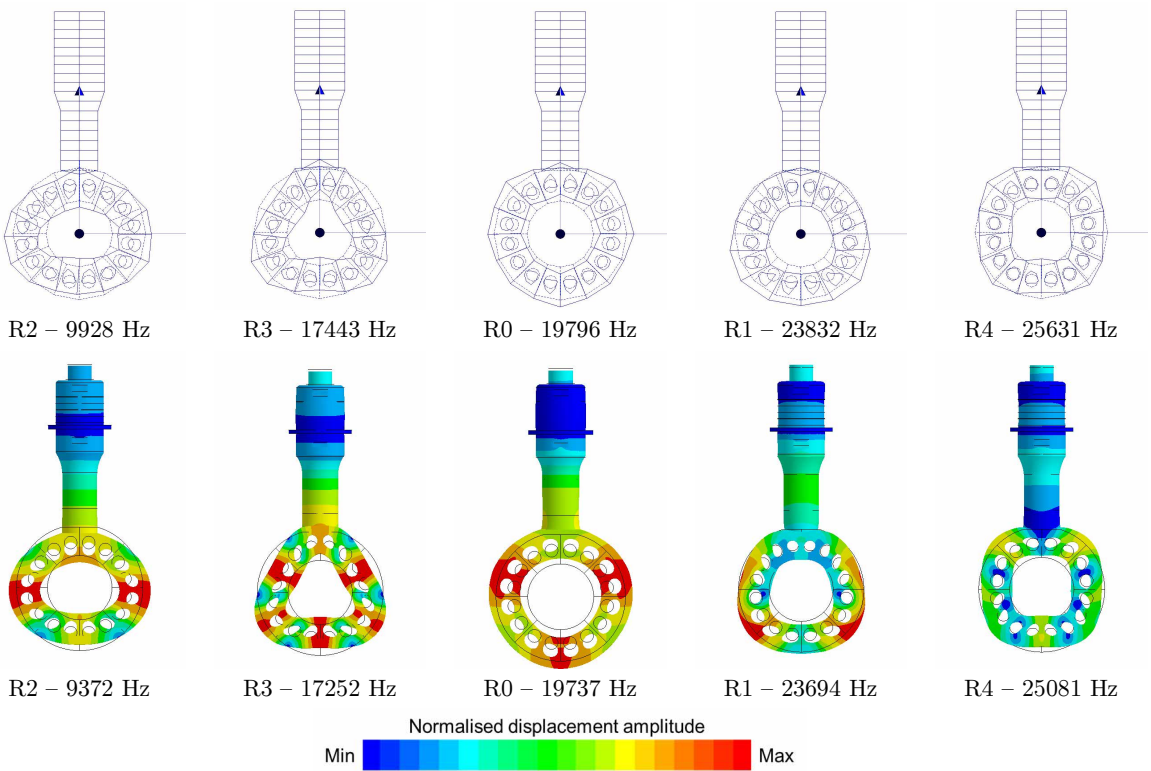


Figure 5.16 Radial modes of RPS-16 – EMA (top), FE (bottom).

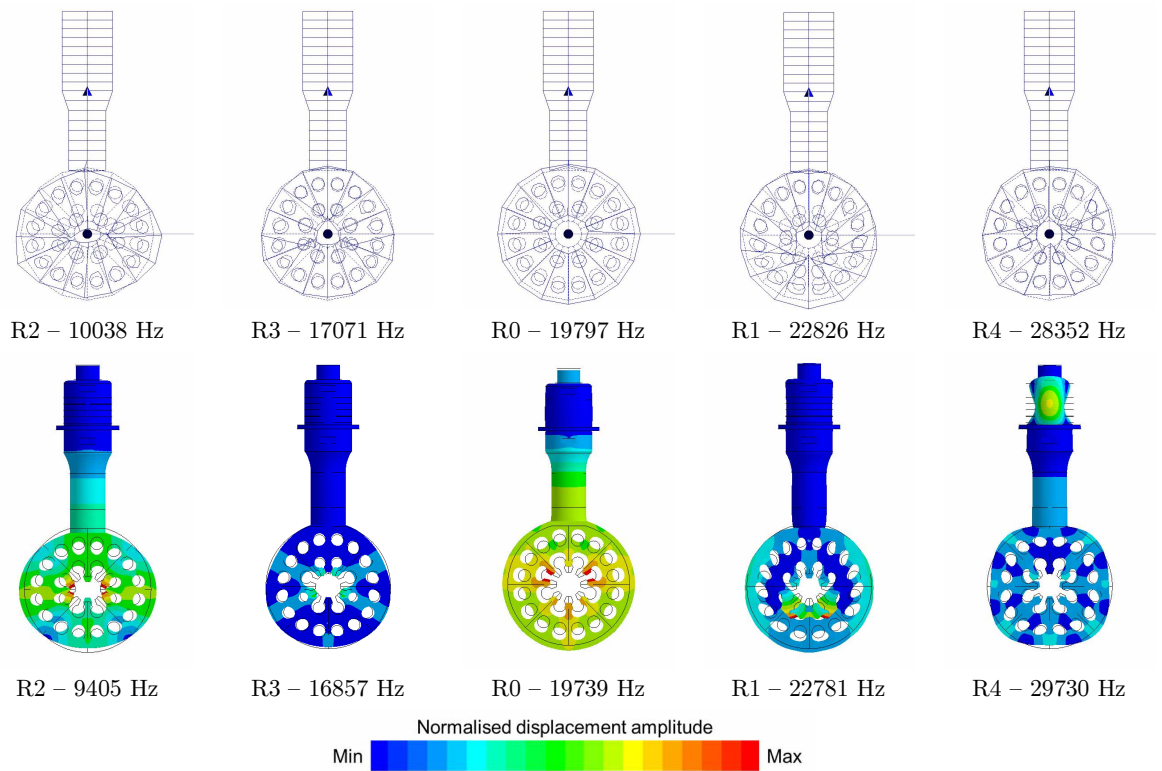


Figure 5.17 Radial modes of RPST-16 – EMA (top), FE (bottom).

It is observed that the FE model under-predicted the R2 frequencies for the three resonators, while R4 frequencies were over-predicted. The largest deviations between FE predictions and EMA measurements were for these two modes (2.15–7.28%) whereas the tuned R0 mode, its adjacent modes R1 and R3 were, by and large, predicted within 1% accuracy. This result suggests that the FE model assumptions of material properties, interactions, and boundaries were reasonably accurate.

5.4.2 Comparison of FE and IA results

Impedance analysis (IA) of the resonator configurations were carried out using an impedance analyser, which provides the low excitation voltage for measuring the electrical admittance and phase angle. For each device, an initial broadband sweep in the range of 10–30 kHz was performed to locate low order radial mode frequencies. A constant voltage of 0.5 V_{pp} was applied across the resonator terminals, and the electrical measurements were obtained at approximately 25 Hz resolution, corresponding to 801 measurement intervals (maximum available for the IA equipment). Before the measurements were carried out, the impedance analyser was calibrated with test probes attached at open circuit and short circuit conditions to ensure reliable data. The sweep duration was set to the slowest configuration possible, with 10 averages per measurement for noise reduction. The broadband admittance and phase angle spectra for the RP-1, RPS-16 and RPST-16 radial resonators are shown in Figure 5.18, Figure 5.19, and Figure 5.20 respectively.

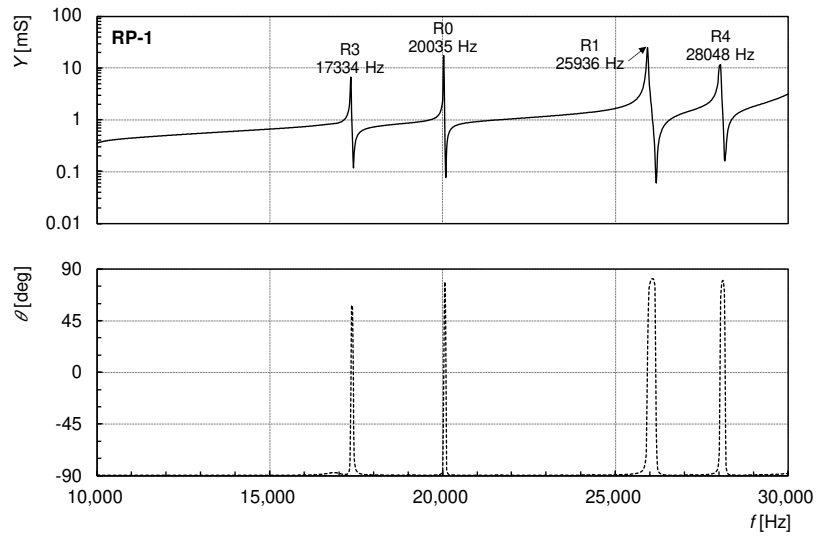


Figure 5.18 Measured broadband admittance (top) and phase angle (bottom) spectra of RP-1.

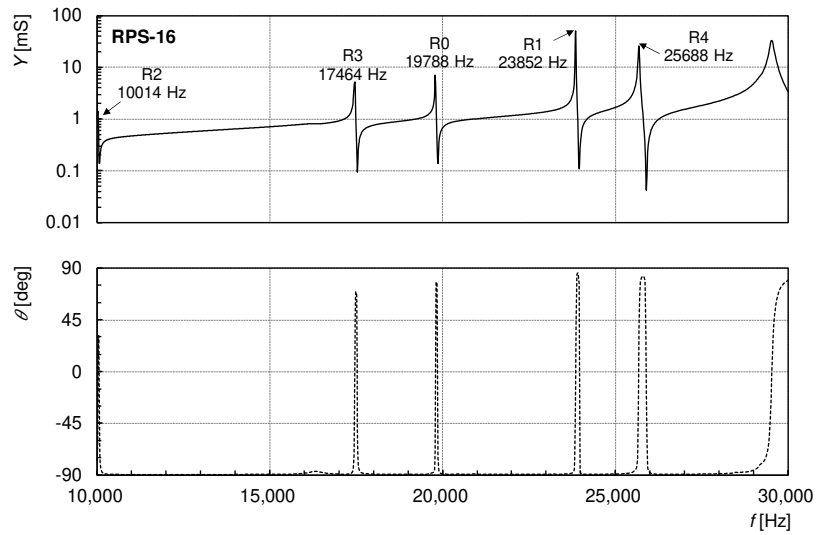


Figure 5.19 Measured broadband admittance (top) and phase angle (bottom) spectra of RPS-16.

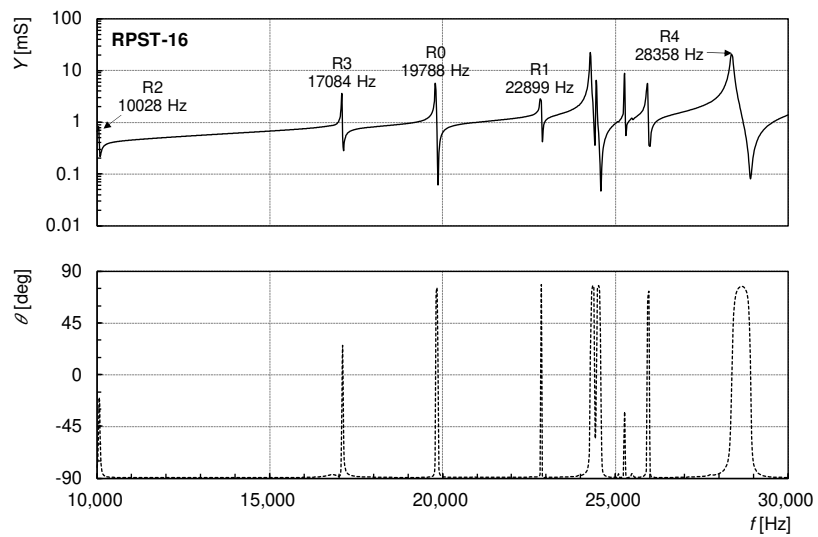


Figure 5.20 Measured broadband admittance (top) and phase angle (bottom) spectra of RPST-16.

Although impedance measurements can only locate the electrical resonances, the mode shapes associated with these resonances cannot be identified through IA alone. FE analysis results can augment the IA by associating the FE-predicted mode shapes to the measured resonance frequencies. This technique is useful for determining the modal parameters of a resonant device in the absence of an LDV, especially since an IA device is widely available and may be procured for less than US\$10k whereas an LDV equipment typically cost more than US\$100k.

In Figure 5.18 to Figure 5.20, the electrical resonances (identified by peaks in the admittance spectrum) were associated to the vibrational mode shapes obtained from the FE model. As shown, the resonance frequencies predicted by the FE model have good correlation with the resonances detected by the IA measurements. Although EMA is always necessary for FE model validation, IA can be an acceptable alternative in cases where the EMA equipment is not available. The absolute percentage difference between the resonance frequencies of the R0 mode found through FE and IA methods are 0.25% to 0.27% for RP-1, RPS-16 and RPST-16. This difference is only marginally smaller than the difference between FE and EMA for the same mode. Meanwhile, the resonance frequencies and mode shapes for higher order radial modes predicted by the FE model were found to have a greater deviation from the IA results. However, the deviations between FE and IA are still smaller than the deviations between FE and EMA for the same modes. This may be associated with measurement uncertainties in EMA, which is more susceptible to ambient vibrations than IA. The latter is relatively well isolated from mechanical vibrations by nature of its measurement principle.

The absolute percentage difference between the resonance frequencies found through FE and IA methods are 0.47% to 2.84% for the R1 mode; 0.47% to 1.33% for the R3 mode; and 2.36% to 4.84% for the R4 mode, for the three resonators. The relatively larger error for R4 mode may be associated with the mesh density and the assumed damping values used since both of these quantities tend to exert greater influence on the FE solution as the mode order increases. The impedance analyser measurement did not detect the R2 mode as it was out of the frequency sweep range of the analyser (set to 10 to 30 kHz). The percentage errors between FE and IA are summarised in Table 5.6.

Table 5.6 Modal frequencies percentage error – FE vs. IA.

Radial modes, R <i>n</i>	% error = $\left[\left(f_{Rn,FE} / f_{Rn,IA} \right) - 1 \right] \times 100\%$		
	RP-1	RPS-16	RPST-16
R2	-	-	-
R3	+0.47	-1.21	-1.33
R0	+0.27	-0.26	-0.25
R1	-2.84	-0.66	-0.47
R4	+2.66	-2.36	+4.84

5.4.3 Correlation between electrical and mechanical resonances

Comparison of the admittance spectra of Figure 5.18 to Figure 5.20 with the corresponding FRFs of Figure 5.15 to Figure 5.17 exemplifies the excellent agreement between the electrical and mechanical resonances. As shown in Figure 5.21, resonances detected optically by the LDV equipment corroborated well with the resonances detected electrically by the impedance analyser. This result shows that at low excitation levels, the frequency at maximum admittance f_m (Hz), is approximately equal to the mechanical resonance frequency f_r [154]. Further, the series electrical resonance f_s (the frequency at which the phase angle passes the zero line from a negative phase angle) is mutually close to f_m and f_r for devices with high mechanical quality factor [154,221].

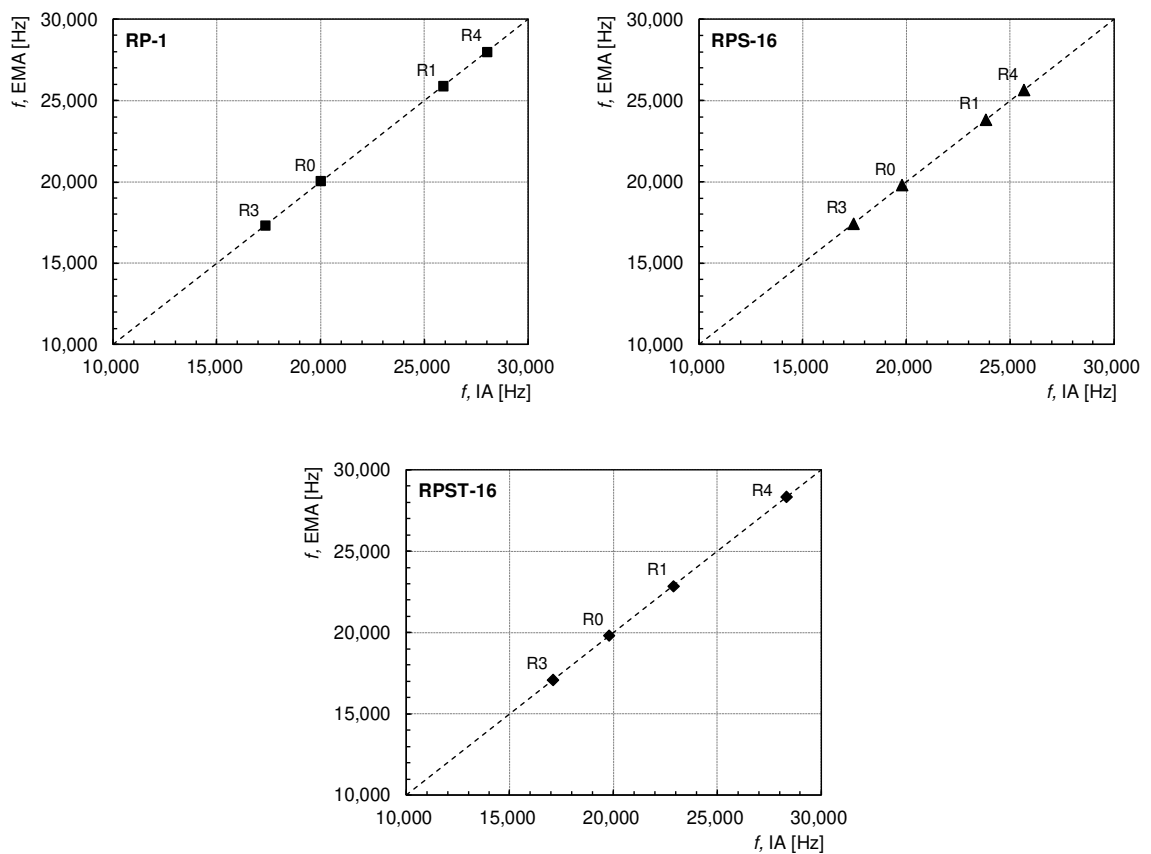


Figure 5.21 Correlation of IA and EMA measured resonances.

5.5 Electromechanical parameters

5.5.1 Resonator equivalent circuit

Piezoelectric transducers are known to exhibit electrical characteristics that are dependent on the elastic, dielectric, and piezoelectric properties of the device, and the types of mechanical loading to which they are subjected. Thus, piezoelectric transducers may be represented as a lumped-parameter equivalent circuit comprising a combination of electrical components that have the overall electrical characteristics that can be used to model the dynamic behaviour of the device.

A simple and robust model that is commonly used is the van Dyke model which comprises four circuit parameters R_1 , L_1 , C_1 , and C_0 to represent the impedance of an unloaded piezoelectric resonator [39]. Figure 5.22 illustrates the relationship between the equivalent circuit (EC) and the mechanical description of a damped 1-DOF spring-mass system of equation (3.1). The clamped capacitance C_0 (F) is a property influenced by the dielectric nature of the piezoelectric material and the cabling, whereas R_1 , L_1 , and C_1 are the motional impedances. The total resistance R_1 is due to mechanical losses in the transducer R_M and the radiation impedance of the working load Z_R , where $Z_R = \rho_L c_L S$ and S is the radiating surface area. In high Q_m transducers, R_M is negligible so that $R_1 \approx Z_R$. The inductance L_1 and capacitance C_1 are related to the transducer mass M , and stiffness K respectively [39].

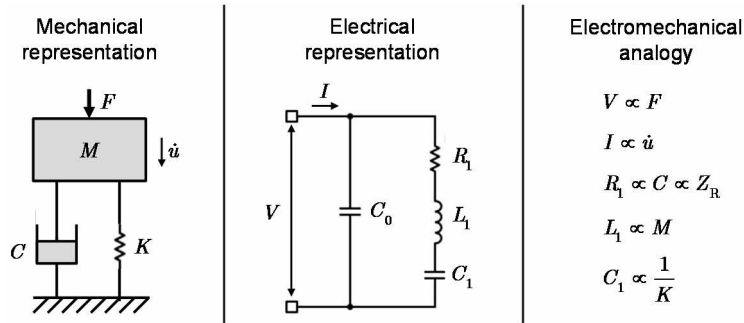


Figure 5.22 Equivalent circuit model of an unloaded piezoelectric resonator [221,222].

The lumped-parameters are valid and frequency independent across a narrow frequency band near resonance [223], provided the excitation is low, and the resonance frequency of the tune mode is sufficiently separated from the frequencies of adjacent modes [197]. The value of the electrical parameters can be calculated from measurements obtained from the impedance analyser using the following expressions [224]:

$$R_1 = 1 / G_{\max}, \quad (5.12)$$

$$L_1 = \frac{1}{4\pi^2 f_s^2 C_1}, \quad (5.13)$$

$$C_1 = C_0 \frac{f_p^2 - f_s^2}{f_s^2}, \text{ and} \quad (5.14)$$

$$C_0 = \frac{1}{2\pi f_p} \sqrt{\frac{G_{\max}}{R_{\max}}}. \quad (5.15)$$

The series resonance frequency f_s , parallel resonance frequency f_p , maximum conductance G_{\max} , and maximum resistance R_{\max} are obtained from the impedance and phase angle measurements. Also, the impedance measurement data are also used to calculate the electromechanical coupling coefficient k_{eff} and the mechanical quality factor Q_m . These two parameters are essential figures of merit (FOM) in piezoelectric transducer characterisation.

The equivalent circuit parameters were verified by regenerating the impedance and phase spectra of each transducer using MATLAB. The error between the measured and calculated response was also quantified. The impedance-phase spectra of the equivalent circuit is given by [225]:

$$Z = \frac{a - jb}{c + jd}, \quad (5.16)$$

where

$$a = \omega^2 C_1 L_1 - 1, \quad (5.17)$$

$$b = \omega C_1 R_1, \quad (5.18)$$

$$c = \omega^2 C_0 C_1 R_1, \text{ and} \quad (5.19)$$

$$d = \omega^3 C_0 C_1 L_1 - \omega(C_0 + C_1). \quad (5.20)$$

For convenience, equation (5.16) can be expressed in the following form,

$$Z = \left(\frac{ac - bd}{c^2 + d^2} \right) - j \left(\frac{ad + bc}{c^2 + d^2} \right), \quad (5.21)$$

so that the impedance magnitude $|Z|$ and phase angle θ can be calculated using,

$$|Z|^2 = \left(\frac{ac - bd}{c^2 + d^2} \right)^2 + \left(\frac{ad + bc}{c^2 + d^2} \right)^2, \text{ and} \quad (5.22)$$

$$\tan \theta = \frac{ad + bc}{bd - ac}. \quad (5.23)$$

5.5.2 Electromechanical coupling coefficient

The electromechanical coupling coefficient k is a measure of the effectiveness with which a piezoceramic material or the device employing such material converts the electrical energy into mechanical energy (and vice versa) [226,227]. This dimensionless quantity was derived from particular combinations of piezoelectric, dielectric, and elastic coefficients, and is used to compare the quality of different piezoelectric materials and devices [197].

The coupling coefficient was calculated from measured frequency values f_s and f_p . There are various expressions for calculating the coupling coefficient, each corresponding to the different modes of excitation and response. For example, k_{31} can be calculated on a plate, k_{33} on a cylinder, k_{15} on a shear plate, and k_p on a disc operating in planar mode. For discs operating in the thickness mode, k_t is used [199]:

$$k_t = \sqrt{\frac{\pi}{2} \cdot \frac{f_s}{f_p} \cot\left(\frac{\pi}{2} \cdot \frac{f_s}{f_p}\right)}. \quad (5.24)$$

Although equation (5.24) may also be used to approximate the coupling coefficient of piezoceramic rings, k_{eff} is used as a more appropriate expression since the frequency constant of a ring is slightly lower than that of a disc. k_{eff} is calculated using the following expression [228]:

$$k_{\text{eff}} = \sqrt{\frac{f_p^2 - f_s^2}{f_p^2}}. \quad (5.25)$$

5.5.3 Mechanical quality factor

The mechanical quality factor Q_m is a dimensionless measure of the mechanical losses of a piezoelectric resonator, which include losses due to material damping, losses from joints, dielectric, backing, and frictional losses. In simple terms, the quality factor of a resonator is the ratio of the energy stored in its reactive components to the energy dissipated in its resistive components (including radiation resistance). The mechanical quality factor is expressed as [222]

$$Q_m = \frac{\sqrt{L_1/C_1}}{R_1}. \quad (5.26)$$

Another expression for Q_m can also be derived by substituting equations (5.12) to (5.15) into equation (5.26) yielding [224,229]

$$Q_m = \frac{f_p^2}{2\pi \cdot f_s \cdot |Z_m| \cdot (C_0 + C_1) \cdot (f_p^2 - f_s^2)}. \quad (5.27)$$

Piezoelectric devices with high Q_m are characterised by a narrowband response (sharper response peak) and thus more suitable for delivering high acoustic power [230]. On the other hand, devices with low Q_m tend to generate substantial heat when driven at resonance, posing problems for the operation.

Q_m can also be determined by measuring the bandwidth of the response centering on the resonance frequency. A more standardised method defined the frequencies f_1 and f_2 positioned to the left and to the right of the resonance frequency f_s , such that the response at f_1 and f_2 are equal to the response at f_s reduced by 3 dB (or a factor of 0.707) [228]. Mathematically,

$$Q_m = \frac{f_s}{f_2 - f_1}. \quad (5.28)$$

This study uses equations (5.26) and (5.27) for calculating Q_m using data from IA.

5.5.4 Comparison of electromechanical parameters

In section 5.4.2, broadband sweep measurements (10–30 kHz) were performed to detect the broadband resonances and also to provide the initial estimate of the R0 mode frequency. The sweeping range was then adjusted such that the R0 mode is framed approximately at the centre of a 400–500 Hz frequency band so that the resonance and anti-resonance frequencies and their

corresponding impedances can be measured [154]. The impedance analyser was set to 801 measurement intervals in the narrowband sweep range, providing a frequency resolution of 0.5–0.625 Hz. The measured (IA) and simulated (EC) impedance and phase of the resonators are shown in Figure 5.23 to Figure 5.26.

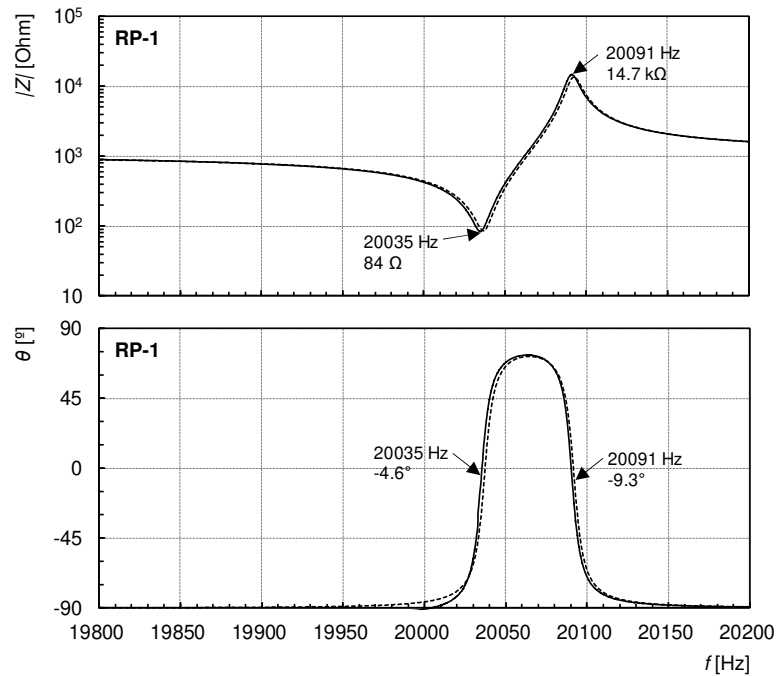


Figure 5.23. Impedance-phase angle spectra of RP-1 from IA (line) and EC model (dash).

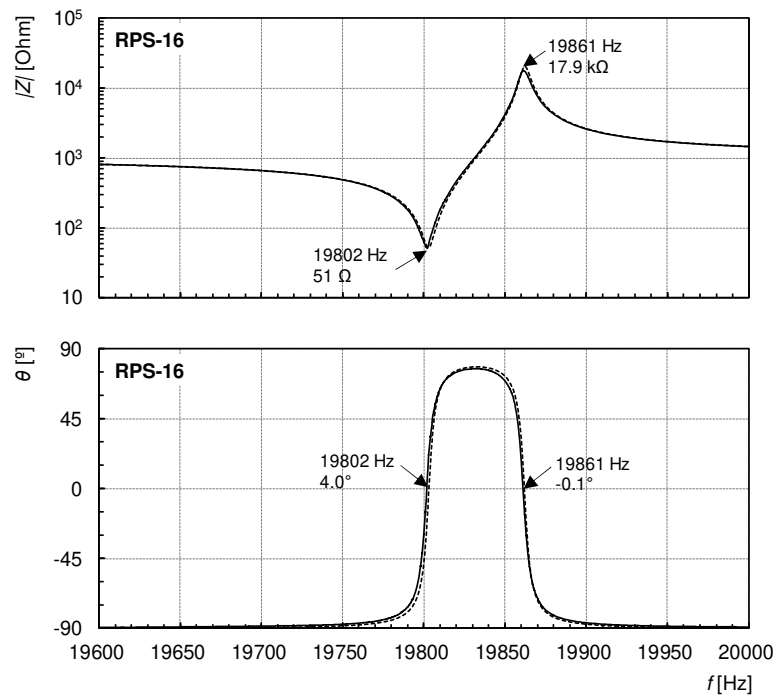


Figure 5.24. Impedance-phase angle spectra of RPS-16 from IA (line) and EC model (dash).

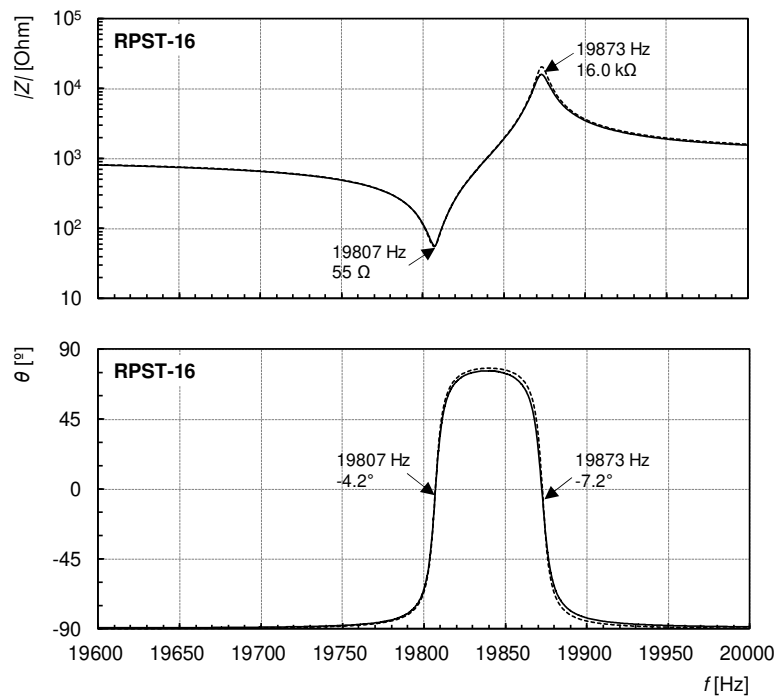


Figure 5.25. Impedance-phase angle spectra of RPST-16 from IA (line) and EC model (dash).

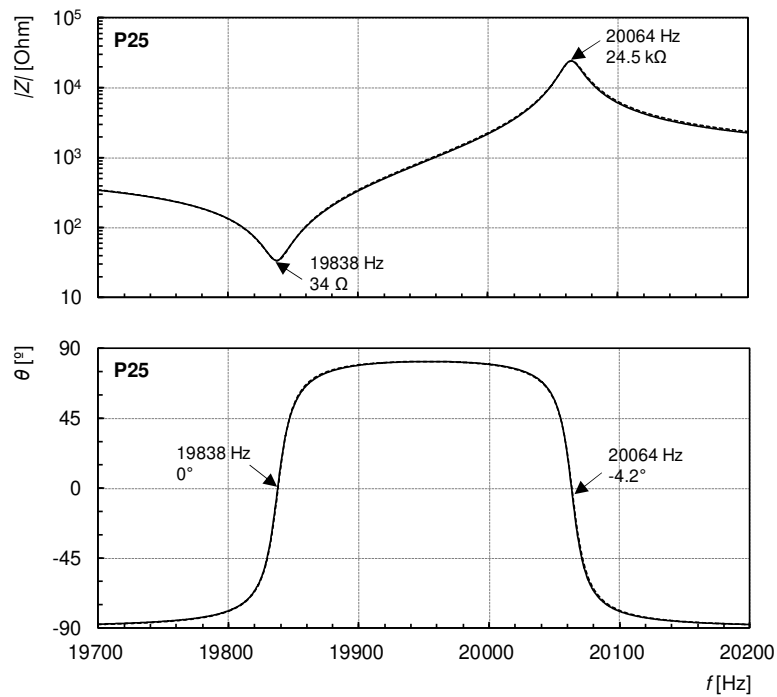


Figure 5.26. Impedance-phase angle spectra of P25 from IA (line) and EC model (dash).

From such measurements, an indication of the resonator's performance can be inferred by noting the values of f_s , f_p , f_m , and f_n . In the case of the three radial resonators and the commercial P25 device, the proximity of f_s and f_m is indicative of high Q_m . Additionally, the frequency difference

between resonance and anti-resonance also indicates the electromechanical coupling behaviour of the transducers – the larger the gap between resonance and anti-resonance frequencies, the better the electromechanical coupling. In Table 5.7 it is shown that $\Delta f_{m,n}$ and $\Delta f_{s,p}$ of the radial resonators are significantly smaller than that of P25. RPST-16 has the highest $\Delta f_{m,n}$ and $\Delta f_{s,p}$ among the three radial resonators, but only around one-third that of the P25 probe.

Table 5.7 Measured (IA) characteristic frequencies and impedances.

	Units	RP-1	RPS-16	RPST-16	P25
f_m	Hz	20035	19802	19807	19838
f_n	Hz	20091	19861	19873	20064
f_s	Hz	20036	19801	19808	19838
f_p	Hz	20091	19861	19872	20064
$ Z_m $	Ω	84	52	55	34
$ Z_n $	Ω	14720	17948	16049	24485
$\Delta f_{m,n}$	Hz	56	59	64	226
$\Delta f_{s,p}$	Hz	55	60	64	226

Figure 5.23 to Figure 5.26 plots the measured impedance and phase angle spectra for the four devices. The measurements were used to estimate the equivalent circuit parameters via equations (5.12) to (5.15) and the impedance-phase spectra were regenerated by substituting the equivalent circuit parameters into equations (5.22) and (5.23) for the van Dyke equivalent circuit model. Table 5.8 provides the equivalent circuit parameters used to generate the impedance-phase spectra plotted in Figure 5.23 to Figure 5.26 (dash). It is observed that the equivalent circuit model has excellent agreement with the impedance analyser measurements.

Table 5.8 Equivalent circuit parameters and figures of merit.

	Units	RP-1	RPS-16	RPST-16	P25
R_1	Ω	85.87	53.08	55.56	33.80
L_1	H	1.57	1.41	1.28	0.32
C_1	pF	40.18	45.79	50.40	200.68
C_0	pF	7308	7673	7550	8758
Q_m	-	2303	3307	2869	1183
k_{eff}	-	0.082	0.085	0.090	0.168

Similarly, the characteristic frequencies can be calculated using the equivalent circuit parameters as follows [225]:

$$f_m = \frac{1}{2\pi} \sqrt{\frac{1}{L_1 C_1}}, \quad (5.29)$$

$$f_n = \frac{1}{2\pi} \sqrt{\frac{C_0 + C_1}{L_1 C_0 C_1}}, \quad (5.30)$$

The corresponding impedances Z_m and Z_n can then be calculated by substituting the calculated values of f_m and f_n into equations (5.22) and (5.23).

Table 5.9 Simulated (EC) characteristic frequencies and impedances.

	Units	RP-1	RPS-16	RPST-16	P25
f_m	Hz	20037	19803	19807	19838
f_n	Hz	20092	19862	19873	20064
$ Z_m $	Ω	86	53	56	34
$ Z_n $	Ω	13725	20573	20277	24285
Error f_m	%	0.010	0.005	0.000	0.000
Error f_n	%	0.005	0.005	0.000	0.000
Error $ Z_m $	%	1.58	2.98	0.14	0.06
Error $ Z_n $	%	6.76	14.63	26.35	0.82

The radial resonators achieved Q_m values that are 53–98% higher than P25. RPS-16 exhibited the highest Q_m among the radial resonators, followed by RPST-16. It is suggested that the addition of orifices influences the peak response of the device by reducing its overall damping. It is also noted that Q_m of the resonators is around 2 to 3 times greater than the Q_m of individual free piezoelectric elements (see Table 4.6). The relatively high Q_m of the transducers compared to its piezoceramic constituent is the direct effect of preloading.

On the other hand, the radial resonators exhibited very poor coupling coefficients. The effective coupling coefficient k_{eff} of the radial resonators is around 50% of the P25 device. The low k_{eff} of the radial resonators corresponded with the narrow gap of 55–64 Hz between series and parallel resonances. In contrast, the gap between series and parallel resonances for P25 is 226 Hz. The results indicate that Q_m and k_{eff} are inversely related relationship. This relationship may be illustrated

through Figure 5.27, which shows that the gap between series and parallel resonance frequencies not only controls the k_{eff} , but also influences Q_m (the sharpness of the response). In trasducer design, it is desirable to maximise both k_{eff} and Q_m to achieve maximum electromechanical conversion efficiency and strong vibration response. Chapter 6 investigates the effect of preload bolt material on k_{eff} , Q_m , and the nonlinear behaviour of the resonators.

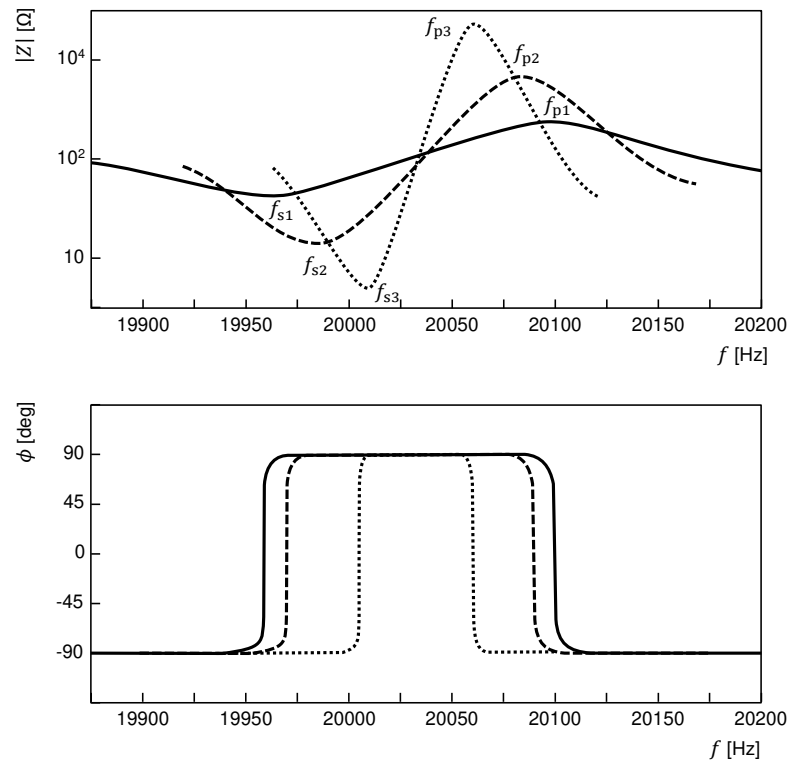


Figure 5.27. ‘Stretching’ of the impedance and phase response spectra.

5.6 Conclusion

Three radial resonators were selected based on their modal and harmonic response characteristics predicted by finite element (FE) analysis. The RP-1 resonator has a more conventional radial horn configuration, whereas the RPS-16 and RPST-16 are the new type of radial resonators having multiple-orifices as the principal feature. The three resonators were fabricated from the same materials and PZTs and have the same principal design and dimensions. Each resonator was subjected to the same assembly process, was characterised using the same equipment, and was analysed based on the same performance criteria.

Experimental modal analysis (EMA) was carried using a 3-dimensional Laser Doppler Vibrometer (LDV), and the results showed excellent agreement with the FE model. In addition, impedance analyser (IA) measurements also corroborated with both EMA and FE results, demonstrating the close analogy between the electrical characteristics of a piezoelectric resonator and its dynamic behaviour.

The representation of the resonator as a four-component equivalent circuit model was also successfully demonstrated, providing additional insight on the influence of geometry, and external load on the behaviour of the resonators. The figures of merit, Q_m and k_{eff} , were also calculated. It was observed that the radial resonators have significantly higher Q_m but lower k_{eff} than the commercial high-gain probe (P25).

In conclusion, this chapter has successfully demonstrated the use of EMA and IA to validate the FE models. In addition, the calculation of the equivalent circuit parameters and the piezoelectric figures of merit from impedance analyser measurement data were also demonstrated.

Chapter 6

Harmonic Response Characterisation

6.1 Harmonic response characterisation (HRC)

6.1.1 Experimental set-up

The resonators were driven by a harmonic signal generated by an arbitrary function generator (AFG) built into a mixed-domain 4-channel oscilloscope (MDO3024, Tektronix) This signal was then amplified by a 60-dB fixed gain amplifier (1000D0, E&I) to drive the resonators. The velocity response of the resonators was measured by a 3-axis Laser Doppler Vibrometer (LDV) comprising of a laser head (CLV-3D, Polytec) and a signal processor (CLV-3000, Polytec). The velocity measurements \dot{u}_x , \dot{u}_y , and \dot{u}_z (mm/s) were fed into a 4-channel data acquisition device (DT9837C, Data Translation) which is connected to a PC installed with a signal processing software to monitor the \dot{u}_x , \dot{u}_y , and \dot{u}_z signals. In addition, the 4-channel oscilloscope was used to capture the function generator output signal, the y-velocity response signal \dot{u}_y , the voltage across the resonator terminals, and the driving current into the resonators. The oscilloscope was connected to a PC with a MATLAB program written and executed to automate the HRC measurements. Harmonic response and nonlinear response measurements were performed at an excitation voltage of less than 30 Vrms to ensure that the vibrational displacement stays within the measurable range of the LDV.

It is critical at this stage to configure the equipment appropriately to avoid systematic errors in the acquired data. In EMA, measurements were carried out at low excitation voltage to ensure resonator operation in the linear regime. Hence, the highest LDV sensitivity of 5 (mm/s)/V was used to capture the sub-micron displacements in the EMA. For HRC, the LDV sensitivity was set to the 125 (mm/s)/V in anticipation of larger displacement amplitudes.

The voltage and current sensor outputs of the power amplifier (PA) were designed for 50 Ω terminations, giving 1 V at each port for every 50 V and 1 A sensed respectively. Setting the input channel of the oscilloscope to 50 Ω input impedance gives a maximum vertical range of only ± 5 V (1 V/division) [231]. This translates to a maximum voltage and current measurements of only ± 250 V and 5 A respectively, which is not sufficient when voltage measurement range of ± 1 kV is desirable. The oscilloscope channel was set to 1 M Ω to enable a maximum vertical range of up to ± 50 V (10

V/division) [231]. Connecting the voltage and current sensor output ports of the PA to 1 M Ω terminals have the effect of halving the scaling factors such that a 1 V at each port now represent 25 V and 0.5 A sensed respectively. The overall effect is that the new channel settings now enable measurement of voltages of up to ± 1.25 kV and currents up to 25 A.

The oscilloscope channel assigned for recording the y-velocity from the LDV was also set to 1 M Ω following the requirements of the LDV [216]. The vibration velocity is obtained from the channel by multiplying the measured voltage by a factor corresponding to the sensitivity setting of the LDV. For HRC, the scaling factor is 125 following the LDV sensitivity setting. Figure 6.1 illustrates the experimental set-up for HRC measurements highlighting the equipment, channel assignments, and input/output settings.

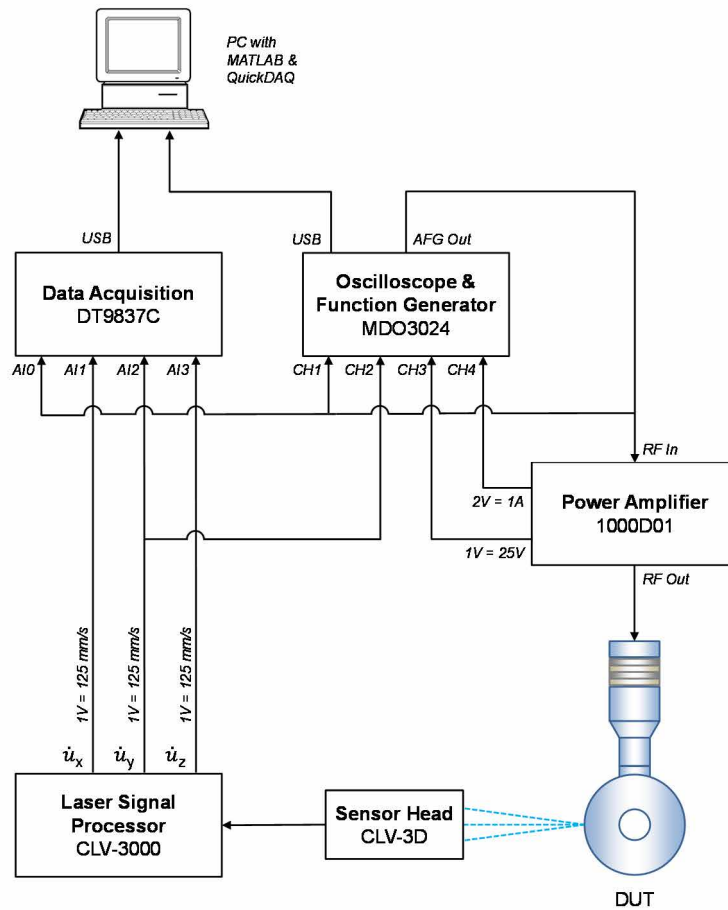


Figure 6.1 HRC schematic.

6.1.2 Measurement procedures and data processing

The vibration response of the resonators was measured from two points representing the mechanical input and output ports respectively. Selection of the input and output measurement points on the P25 resonator is relatively straight-forward since it is half-wave longitudinal-mode device – the input position is nearest to the transducer while the output is measured from the distal end of the resonator as shown in Figure 6.2d.

For the radial resonators, the input measurement point is located at the edge of the connection stub nearest to the exciter section (refer to Figure 4.1 for definitions of resonator parts), while the output measurement point is located at 6 o'clock near the outer circumference of the emitter section as shown in Figure 6.2a-c. At this measurement position, vibration in the y-direction is dominant (x and z displacements are neglected) for pure radial modes, and the y-velocity can be assumed to be equal to the radial-velocity. However, one must ensure that this measurement point is perfectly aligned with the axis of the exciter section. Otherwise, the assumptions will be erroneous.

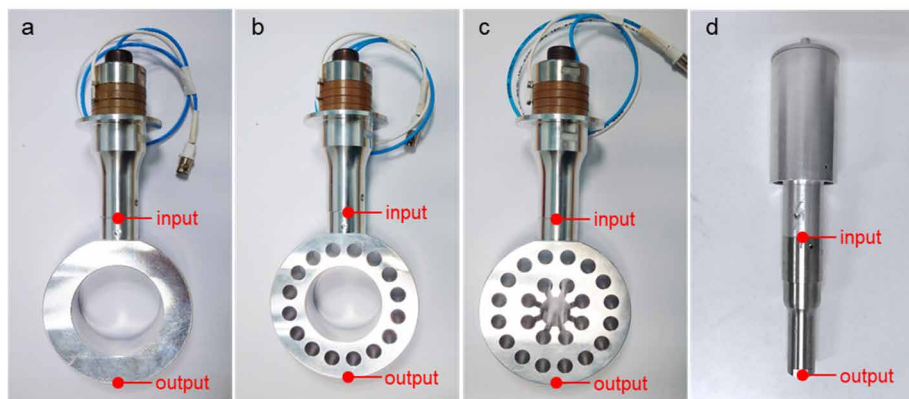


Figure 6.2 HRC measurement points on (a) RP-1; (b) RPS-16; (c) RPST-16; and (d) P25.

The HRC was carried out in a 300–400 Hz bandwidth centered on the resonance frequency of each device. The start and stop frequencies were set before executing the MATLAB program. A fixed frequency interval of 2 Hz was used throughout the measurement process. At each measurement step, a first trigger signal switches on the function generator output. The vibration was allowed 3 seconds to stabilise before the resonator velocity, voltage, and current signals were sampled and their RMS values computed and recorded. A further 2 seconds pause follows to buffer the measurement against any transients induced by the switching of the generator signal. A 10 seconds quiet time immediately follows to attenuate any residual vibrations and to cool down the PZTs. This process was repeated until the last measurement has been recorded at the stop frequency. Measurements were obtained for both forward and reverse frequency sweep directions to investigate the hysteretic

behaviour of the resonators. The input signal is a sine wave with no offset, and the sweeps were performed at 10, 20, 40, 50, and 60 mV (peak-to-peak) signal levels. The amplified voltage into the resonators varies according to the impedance characteristics of the resonators as will be shown in later sections. The actual set-up for HRC is shown in Figure 6.3.



Figure 6.3 HRC equipment: (a) 4-channel DAQ; (b) power amplifier; (c) PC with MATLAB and DAQ software; (d) 4-channel oscilloscope with signal generator; (e) laser signal processor; (f) sensor head; (g) translation stage; (h) resonator fixture; (i) breadboard; (j) lab-jack.

6.1.3 Ultrasonic driver circuit

The ultrasonic generator circuit comprises a signal generator and a Class D power amplifier designed to amplify input signals in the 10–110 kHz range by 60 dB. No advanced control circuitry for frequency-tracking, phase-locking, and impedance-matching were employed [232–235]. This section briefly describes the principle of operation of the ultrasonic driver circuit, with emphasis on the power amplifier operation. This is necessary for correct interpretation of the HRC data.

The power amplifier is capable of producing a maximum power of 1000 Watts across its output connector into a 50 Ω load. The signal from the front panel BNC connector is fed into the input of the pre-amplifier module, and the signal from the output of the pre-amplifier is fed into the pulse width modulator (PWM) via an input drive clamp. The outputs of the PWM are fed into the gate drivers which feed a full-bridge' rectifier, and the output of the bridge is fed into the low-pass filter network to recover the signal waveform which is then amplified and presented at the output port. A simplified block diagram of the ultrasonic driving circuit is shown in Figure 6.4, omitting the complex circuitry of the power amplifier. Here, only voltages and impedances at the input and output

ports of the interconnecting sub-equipment of the driving circuit are relevant for calculating the power flow to the resonators.

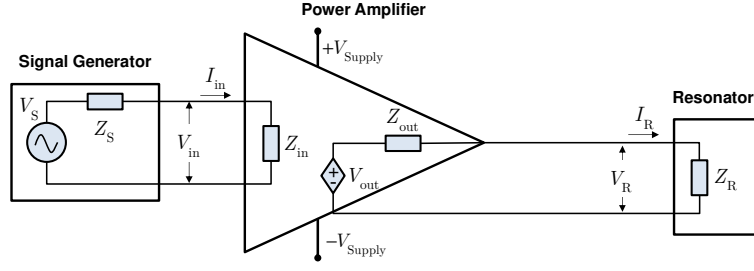


Figure 6.4 Block diagram of ultrasonic generator circuit for driving air-loaded resonators, highlighting the input and output impedances of interconnecting devices ($Z_S = Z_{in} = Z_{out} = 50 \Omega$).

The forward power presented at the output of the power amplifier may not be entirely delivered to the resonator due to losses in transmission arising from unmatched impedances between the PA output Z_{out} and the resonator input Z_R . This loss is proportional to the reflection coefficient Γ expressed as

$$\begin{aligned} \Gamma &= \frac{Z_R - Z_{out}}{Z_R + Z_{out}} \\ &= \frac{(R_R - R_{out}) + j(X_R - X_{out})}{(R_R + R_{out}) + j(X_R + X_{out})}. \end{aligned} \quad (6.1)$$

Taking the magnitude of the complex reflection coefficient and setting the source impedance to be purely resistive (in the present set-up, $Z_{out} = 50 + j0 \Omega$), we obtain an expression for the reflection coefficient magnitude:

$$|\Gamma|^2 = \frac{(R_R - R_{out})^2 + X_R^2}{(R_R + R_{out})^2 + X_R^2}. \quad (6.2)$$

Since the impedances of the resonators are not equal, the voltage appearing across the resonator terminals vary even for the same V_{in} ($V_{in} = V_S$ since $Z_{in} = Z_S = 50 \Omega$). Considering a fixed power amplifier gain of G (60 dB), the relationship between V_R and V_S at different Z_R can be derived by establishing the relationship between the forward power P_F and source power P_S :

$$P_F(\text{dBm}) = G(\text{dB}) + P_S(\text{dBm}). \quad (6.3)$$

Equation (6.3) can be expressed in its linear form as

$$P_F = G \times P_S, \quad (6.4)$$

since

$$P_F(\text{dBm}) = 10 \times \log_{10}(P_F \times 1000), \quad (6.5)$$

$$P_S(\text{dBm}) = 10 \times \log_{10}(P_S \times 1000), \text{ and} \quad (6.6)$$

$$G(\text{dB}) = 10 \times \log_{10}(G). \quad (6.7)$$

If the resonator impedance $|Z_R|$ is equal to the output impedance of the amplifier $|Z_{\text{out}}|$, the power delivered into the resonator is equal to the forward power, i.e. $P_R = P_F$. In reality, resonator impedances do not always match its source. This result in lossy transmission with $P_R < P_F$. Thus P_R can be calculated by factoring in the reflection coefficient Γ :

$$P_R = (1 - \Gamma) \times P_F. \quad (6.8)$$

The load voltage (RMS) and source voltage (RMS) in terms of power and impedance are

$$P_R = V_R^2 / Z_R, \text{ and} \quad (6.9)$$

$$P_S = V_S^2 / Z_S. \quad (6.10)$$

Substituting (6.4),(6.9), and (6.10) into (6.8), we get an expression relating V_S and V_R as

$$V_R^2 = \left(\frac{\Gamma G Z_R}{Z_S} \right) V_S^2. \quad (6.11)$$

Figure 6.5 to Figure 6.7 shows the graphs of V_R , I_R , and P_R against Z_R for small signal voltages ($V_S = 10\text{--}60$ mVpp) used for characterising the harmonic response of unloaded resonators. It should be noted that when comparing responses over a frequency range, the presented resonator voltages and currents are the averaged-RMS values over the said frequency range. On the other hand, when a comparison is made of a response parameter at the resonance frequency, then the presented resonator voltages and currents are the RMS values at that particular frequency.

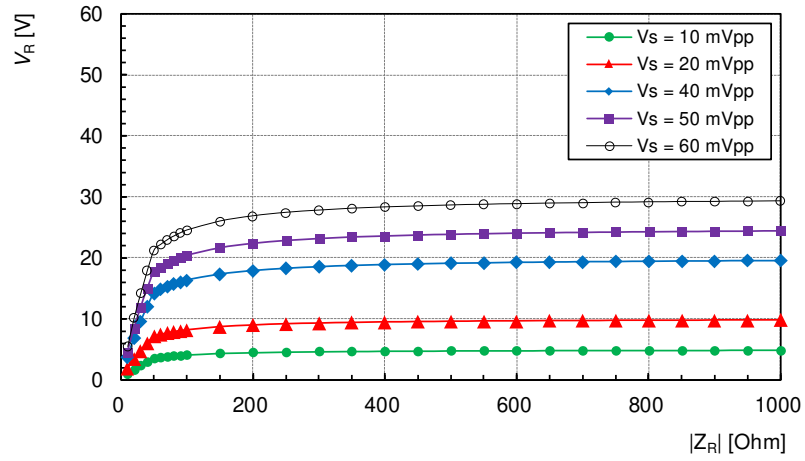


Figure 6.5. V_R (RMS) vs. Z_R at different V_s (peak-to-peak).

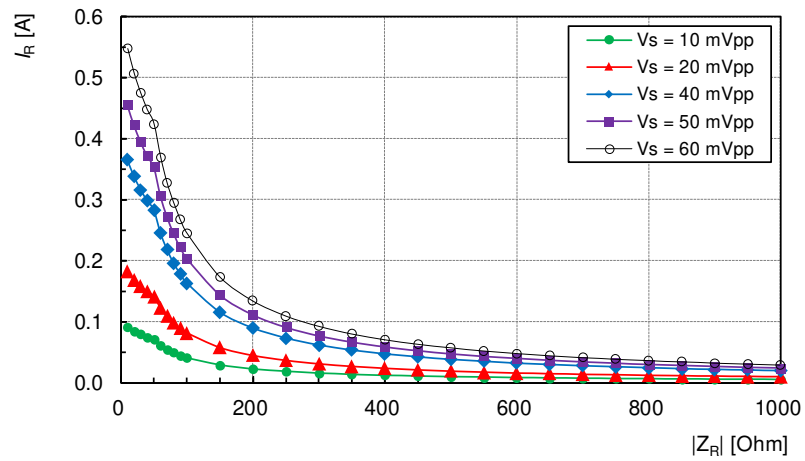


Figure 6.6. I_R (RMS) vs. Z_R at different V_s (peak-to-peak).

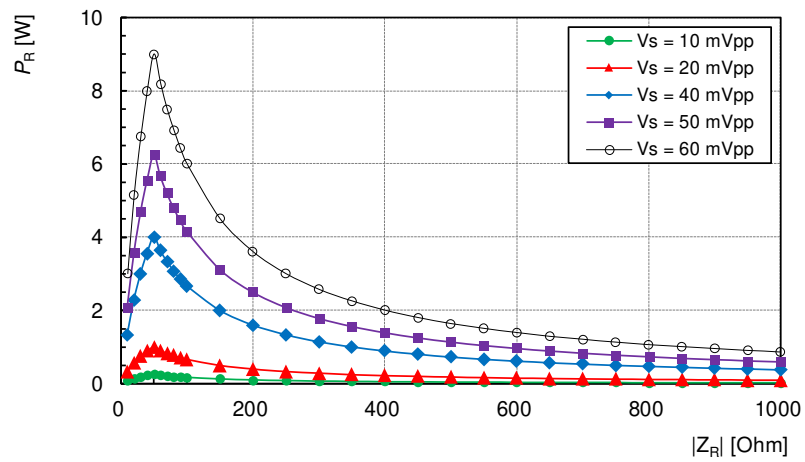


Figure 6.7. P_R (RMS) vs. Z_R at different V_s (peak-to-peak).

6.2 Harmonic response of Alloy Steel-bolted resonators

6.2.1 Voltage responses

Away from the resonance frequencies V_R exhibit asymptotic behaviour, while closer to the resonance frequency a sudden dip occurs. The magnitude of this dip corresponds to Z_m determined earlier (refer to Figure 5.23 to Figure 5.26 and Table 5.7). This behaviour is consistent with the power amplifier output characteristics shown in Figure 6.5, wherein the V_R / Z_R gradient is steep between 0–50 Ω but becomes more gentle between 50–100 Ω . Beyond 100 Ω , V_R approaches the asymptote that is approximately equal to $(V_S / 2) \times 1000$. Thus P25 ($Z_m = 33.80 \Omega$) exhibited a much greater voltage dip compared to the radial resonators ($Z_m = 84.27 \Omega, 51.48 \Omega, 55.41 \Omega$), whereas the difference in voltage dip between RP-1 and RPS-16 is less significant.

A slight ‘peaking’ was also observed before the dip, with P25 exhibiting this characteristic to a greater degree. The ‘peaking’ behaviour suggests an impedance peak, but one can rule out parallel resonance since $f_m > f_n$. Furthermore, the V_R peak should be approximately equal across the four resonators at parallel resonance due to the asymptotic behaviour at high impedances (resonators Z_m range from 14.7 k Ω to 24.5 k Ω). Thus, the origin of the ‘peaking’ behaviour is not known.

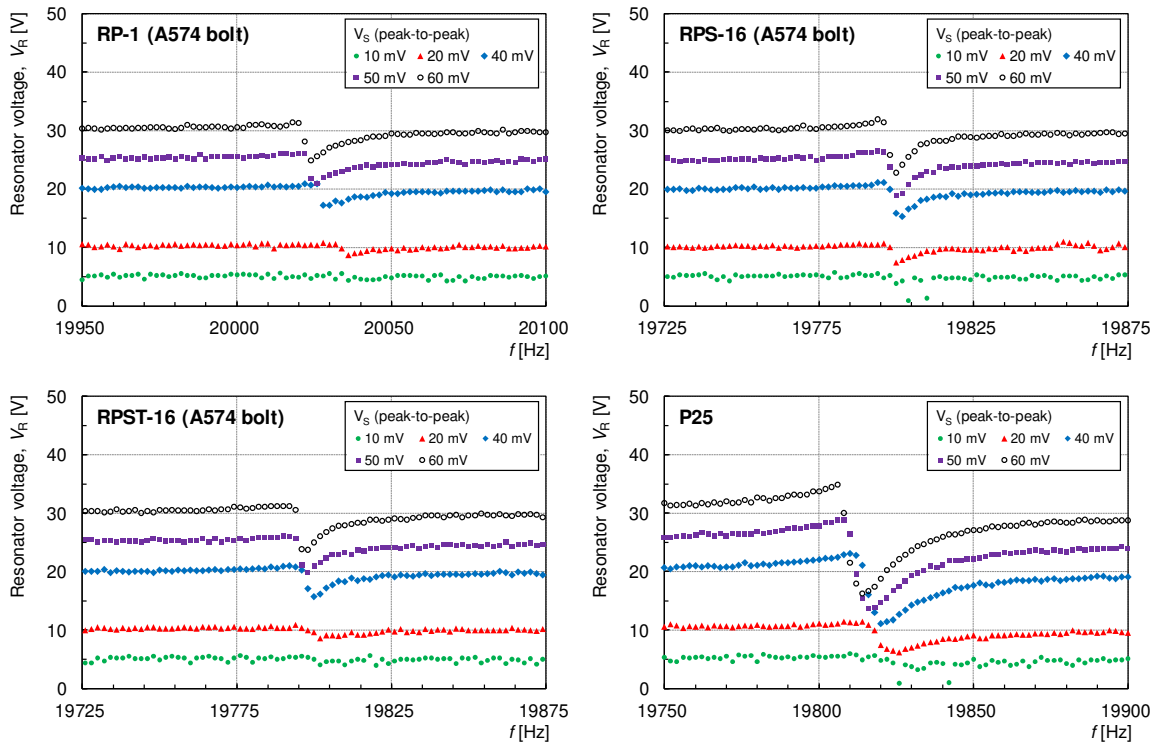


Figure 6.8. Profile of resonator voltages at different PA input signal levels (P25 for comparison).

6.2.2 Harmonic response at different excitation

Resonator responses in terms of peak velocity V_p at five excitation levels (5–30 V) are shown in Figure 6.9, in which the legend indicates the averaged RMS voltage across the frequency range. Within each excitation level, there are very slight variations in V_R due to the differences in Z_R . However, these variations are small, and we consider the voltage to be approximately equal across the resonators. Velocity response from forward and reverse frequency sweeps are plotted in the same graph at each excitation level, and the differences in the measurements were recorded.

The response amplitude for a given excitation can be read off directly from Figure 6.9. In addition, the shape of the response also provides some indication of nonlinear behaviour. Nonlinear behaviour of a piezoelectric device can manifest in the form of resonance frequency shifts, response discontinuities, and hysteresis [166,236]. Hysteretic behaviour, which is the difference in measurements between forward and reverse directional sweeps, can be quantified by identifying the hysteresis region and measuring its hysteretic width [166]. However, the difference between the forward and reverse resonance frequencies are not obvious. Thus, quantification of the hysteretic behaviour requires an alternative approach which will be introduced later. Meanwhile, it suffices to mention that hysteretic behaviour is most obvious in RP-1 and P25, and most subtle in RPS-16, which indicates the varying extent of nonlinearities in the systems.

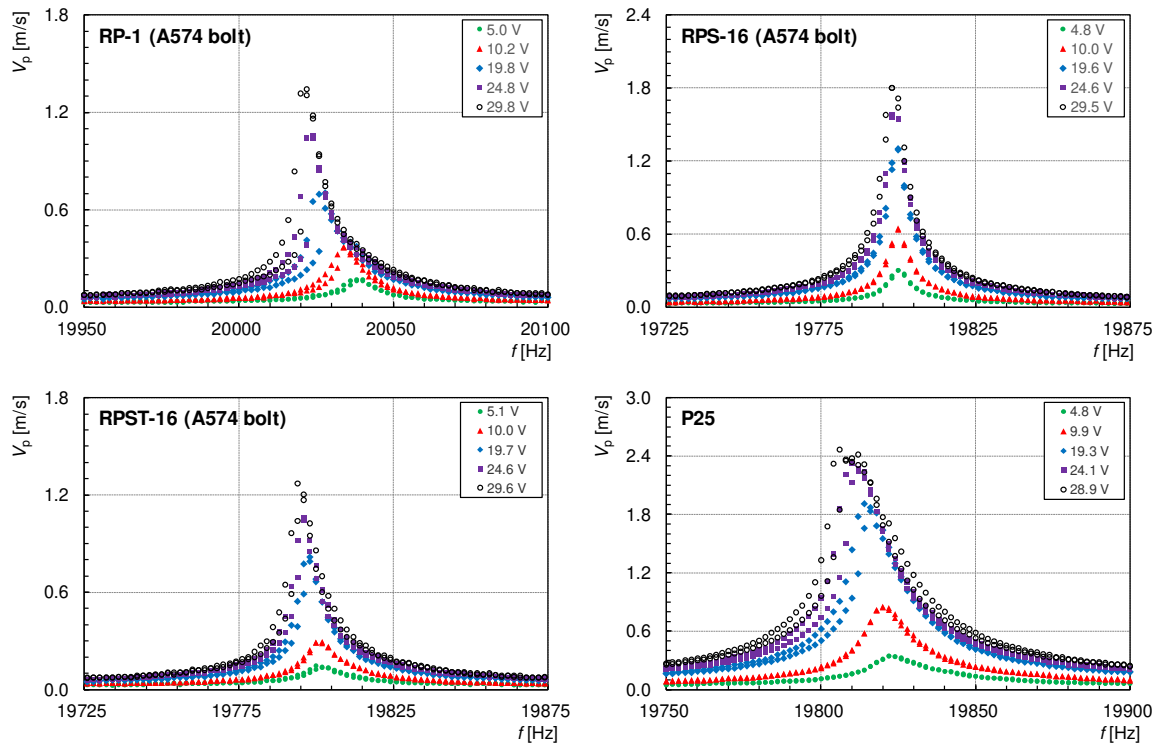


Figure 6.9. Vibration response of A574-bolted radial resonators (P25 for comparison).

The acoustic output may be estimated by substituting the displacement amplitude at resonance into equation (2.2). A uniformity factor β , which is defined as the ratio of the average displacement amplitude along the circumference to the displacement amplitude measured at 6 o'clock position along the same circumference. β is introduced to moderate the single-point measurement of the HRC with the multipoint measurements of the EMA to account for variations in the vibration profile (for P25, $\beta = 1$). Using displacement amplitudes at the same excitation voltage, the acoustic output of the radial resonators relative to the P25 can be estimated based on proportion:

$$P \propto f^4 S^2 (A \times \beta)^2, \quad (6.12)$$

$$\frac{P}{P_{P25}} = \left(\frac{f}{f_{P25}} \right)^4 \left(\frac{S}{S_{P25}} \right)^2 \left(\frac{A \times \beta}{A_{P25}} \right)^2, \quad (6.13)$$

$$P^R = (f^R)^4 (S^R)^2 (A^R \times \beta)^2, \quad (6.14)$$

where P^R , f^R , S^R , and A^R are the relative acoustic output, relative frequency, relative output surface area, and relative displacement amplitude, with respect to P25, respectively. Table 6.1 provides the relative parameters used for the calculation of P^R . The values f and A are obtained from Figure 6.9 at excitation voltage of 30 V. The displacement amplitudes are calculated from the measured vibrational velocities via equation (6.18). A conservative estimate of the relative acoustic output is made by calculating S using only the surface areas of the outer circumference and the primary orifice circumference, neglecting the contributions of the secondary and tertiary orifices. As shown, the radial resonators provide vibrational amplitudes that are 26% to 49% lower than the P25 device. However, the acoustic output of the former is greater than the latter by a factor of 90 to 300, which is significant.

Table 6.1 Calculation of relative acoustic output (A574-bolted resonators and P25) at 30 V excitation.

	RP-1	RPS-16	RPST-16	P25
f (Hz)	20022	19798	19794	19812
S (cm ²)	143	134	100	5
A (μ m)	21	29	20	39
f^R	1	1	1	1
S^R	29	27	20	1
A^R	0.54	0.74	0.51	1
β	0.88	0.87	0.94	1
P^R	190	302	92	1

6.2.3 Displacement, output power, and amplification factor (AF)

Comparison in terms of vibration velocities is less meaningful when the resonance frequencies of the resonators are not equal. The reason being, two resonators can have the same velocity, but the one operating at a higher frequency will, in fact, have a smaller displacement. Fortunately, the resonance frequencies of the four resonators are within 1% from each other so that the comparison made in terms of velocity should corroborate well with that of displacement. Having said that, the comparison in terms of displacement is deemed more appropriate for comparing the dynamic performance of resonators intended for generating strong acoustic fields in water.

Assuming vibrational velocity can be expressed as a sinusoidal wave with velocity amplitude V_p and phase angle θ as

$$\dot{u} = V_p \sin(\omega t - \theta), \quad (6.15)$$

then the expression for displacement can be derived by integrating (6.15) as follows:

$$\begin{aligned} u &= \int \dot{u} dt, \\ &= \int V_p \cos(\omega t - \theta), \\ &= \frac{V_p}{2\pi f} \sin(\omega t - \theta). \end{aligned} \quad (6.16)$$

The coefficient of the sine function in (6.16) is the displacement amplitude:

$$A = \frac{V_p}{2\pi f}. \quad (6.17)$$

Finally, the peak-to-peak displacement is expressed as

$$A_{pp} = \frac{V_p}{\pi f}. \quad (6.18)$$

The input and output peak-to-peak displacements are plotted in the graphs of Figure 6.10. RPS-16 has the highest output displacement amplitude among the radial resonators. At 28.93 μm , the output displacement amplitude of RPS-16 is around 50% higher than RPST-16 and 40% higher than RP-1, for a similar excitation voltage. Compared to P25, RPS-16 output displacement amplitude is around 25% smaller. Although a smaller displacement amplitude is expected for the radial resonators due to the conversion of longitudinal displacement at its input to radial displacement at the circumferential output, the attenuation in amplitude is small compared to the increased area of the output surface. Considering only the outer circumferential surface (OD = 100 mm, thickness = 30

mm), the radial resonators provide a minimum output area S of approximately 90 cm^2 . In contrast, the longitudinal-mode device P25 (output diameter = 25 mm) only provides around 5 cm^2 of output surface. Since the acoustic power $P_{\text{US}} \propto f^4 A^2 S^2$ [109], the smaller displacement amplitude A of the radial resonators is more than compensated for by ability to emit high-power acoustic radiation.

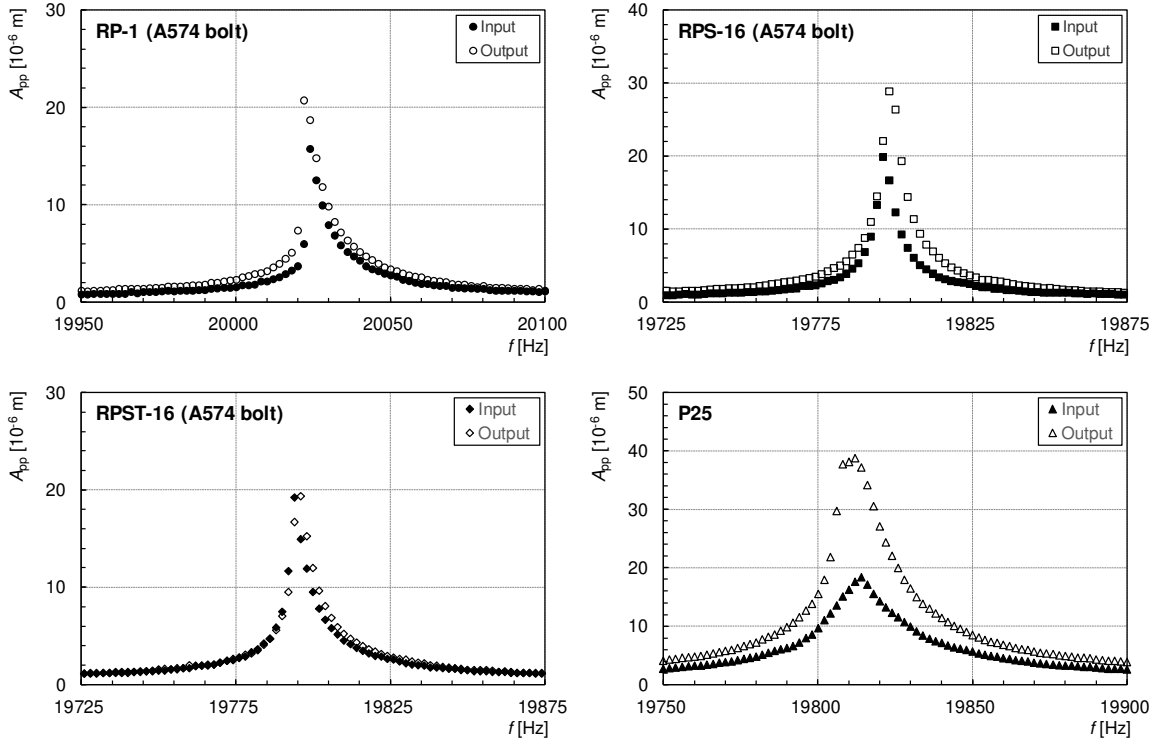


Figure 6.10. Input and output responses of A574-bolted radial resonators (P25 for comparison).

Another parameter of interest when analysing the performance of resonators is the amplification factor (AF), defined by the ratio of output to input displacement amplitudes. P25 has the highest amplification factor overshadowing the radial resonators by more than 30%. This is expected for the high-gain probe with a stepped horn design [237]. Among the radial resonators, RPS-16 has the highest AF followed by RP-1. Displacement amplification is practically negligible for the RPST-16 configuration. The displacement measurements for the four resonators are summarised in Table 6.2.

Table 6.2 Displacement and amplification factor of A574-bolted resonators (P25 for comparison).

	Units	RP-1	RPS-16	RPST-16	P25
Input displacement	10^{-6} m	15.73	19.93	19.21	18.38
Output displacement	10^{-6} m	20.74	28.93	19.37	38.76
Amplification Factor	-	1.32	1.45	1.01	2.11

6.2.4 Frequency shift

The shift in resonance frequency at elevated excitation voltage is a nonlinear effect that arises from a number of contributing factors including changes in piezoelectric, dielectric, and elastic properties of the piezoceramic or Duffing-like ‘softening’ behaviour influenced by the geometric characteristics of the structure [166,236].

Figure 6.11 plots the shift in resonance frequency Δf against the excitation voltage V_R of the resonator. It can be seen that Δf increases with V_R for all resonators but extent of the shift in resonance frequency differs. RP-1 and P25 exhibit the largest Δf , followed by RPST-16. In contrast, Δf for RPS-16 is almost negligible for the range of voltages investigated. At resonator voltage of approximately 25 V (RMS), Δf for RP-1 is around 18 Hz, which is between 1.3 to 8 times that of RPS-16 ($\Delta f \sim 2$ Hz), RPST-16 ($\Delta f \sim 6$ Hz), and P25 ($\Delta f \sim 14$ Hz). Although, Δf is less than 0.1% of the design frequency at excitation voltages below 30 V, a large shift in resonance frequency is anticipated in water-loaded operation where the driving voltage will be in the kV range.

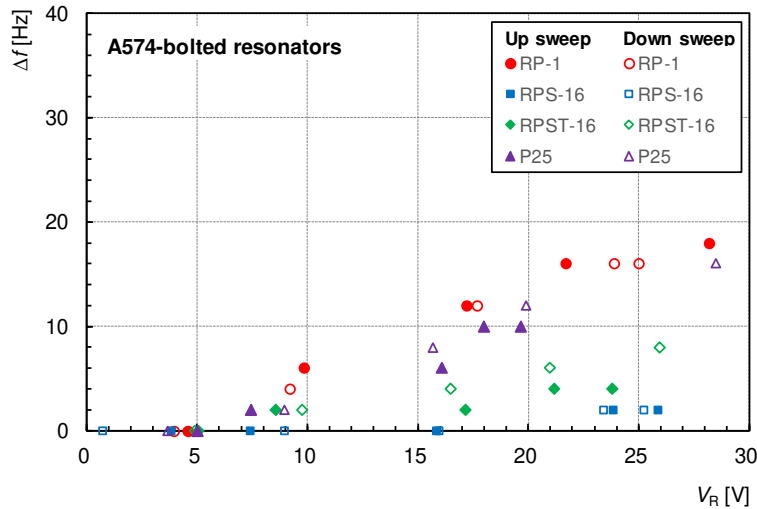


Figure 6.11. Δf vs. V_R (RMS) of A574-bolted resonators (P25 for comparison).

As shown in Figure 6.12, excitation current I_R has the greatest influence on the Δf of RP-1. At around 0.45 A, the Δf of RP-1 is around 18 Hz. In comparison, the Δf of RPS-16, RPST-16, and P25 are below 8 Hz. Based on the slope of the $\Delta f - I_R$ curve, it may be concluded that RPS-16 exhibited the least nonlinear behaviour, followed by P25, followed by RPST-16. Although the conclusions drawn from Figure 6.11 and Figure 6.12 differs slightly, the results can be interpreted as the susceptibility of the resonators to frequency shifts when subjected to increasing excitation forces, versus their susceptibility to the same change when subjected to increasing vibrational

amplitudes. Nevertheless, it can be concluded that the extent of nonlinear behaviour is greatest for RP-1 and smallest for RPS-16 regardless of the reference (voltage or current).

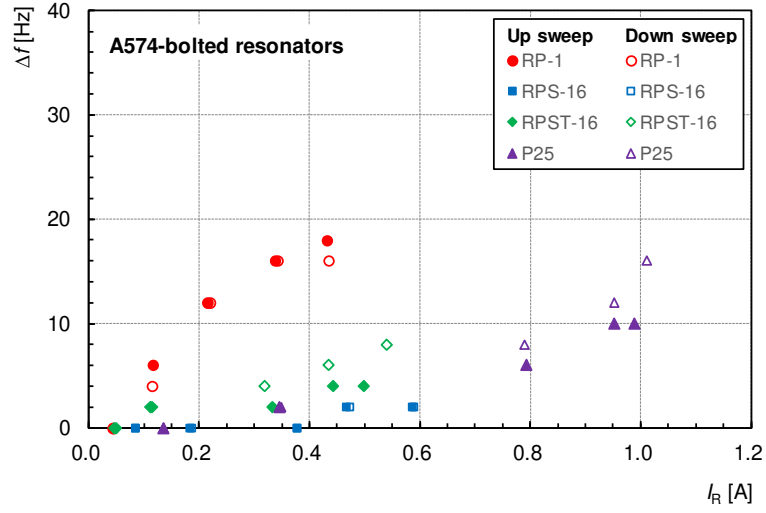


Figure 6.12. Δf vs. I_R (RMS) of A574-bolted resonators (P25 for comparison).

6.2.5 Skewness of vibration response curve

6.2.5.1 Skewness as a measure of nonlinear behaviour

The tendency for piezoceramic elements and piezoelectric transducers to exhibit Duffing-like behaviour when operating at elevated vibrational amplitudes have been documented in previous studies [167,236,238]. A system exhibiting Duffing-like behaviour can be represented by the general equation of motion with an additional cubic term γu^3

$$M\ddot{u} + C\dot{u} + Ku \pm \gamma u^3 = F(t). \quad (6.19)$$

The cubic term is responsible for the backbone curve of the response plot, and its sign determines the direction of the bending [236]. A negative γ indicates stiffness ‘softening’ which result in the curve bending towards the left and therefore a decrease in resonance frequency. Meanwhile, a positive γ indicates increasing stiffness or ‘hardening’ with a corresponding increase resonance frequency.

It is of interest to quantitatively compare the Duffing-like behaviour in the four resonators investigated. One approach is to determine the cubic coefficient γ numerically using an appropriate curve-fitting technique [239]. However, this will be challenging if the bending of the response curve is not significant for the range of voltage investigated. Hence, the curve-fitted data will not provide more insight than is already provided by the experimental data. Further, the response discontinuities

and hysteretic behaviour of the four resonators are subtle and difficult to quantify. Models describing Duffing-like responses of specific systems have also been developed [240], but customising such models to characterise the nonlinear behaviour of the radial resonators is not practical, and the results will be limited in its usefulness for the present work. An alternative, pragmatic approach to quantify the Duffing-like behaviour using a statistical parameter is proposed.

In statistics, skewness is the asymmetry of a distribution in which the distribution curve appear to skew to the left or to the right [241] (see Figure 6.13). Skewness can be quantified to measure the degree with which a distribution deviates from a normal distribution (zero skewness). A negatively skewed distribution is one in which the tail on the left side of the distribution is longer such that the distribution appears to be leaning towards the positive direction. The converse is true for a positively skewed distribution.

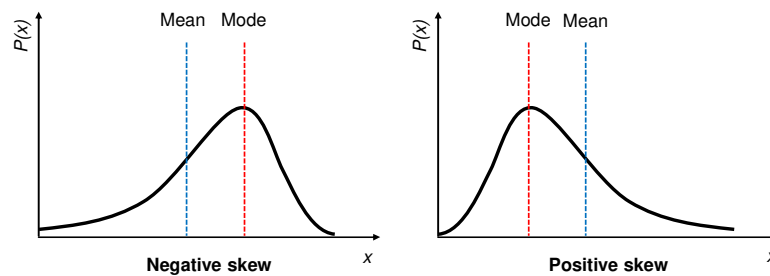


Figure 6.13. Skewness direction.

Assuming the vibration response curve can be processed such that its degree of ‘bending’ can be quantified using the statistical skewness coefficient, then a positive skew indicates stiffness ‘softening’ while a negative skew indicates stiffness ‘hardening’. Thus, the polarity of the skewness coefficient for a particular bending direction is opposite that of the cubic coefficient γ introduced earlier. Although there are several formulations for skewness [242–244], we implement Pearson’s formulation due to its simplicity. The Pearson Skewness coefficients are based on the gap between the mean and the mode of a distribution, and between its mean and median [241].

6.2.5.2 Calculating the skewness of a response curve

The skewness coefficient is a statistical parameter extracted from a probability density function (PDF) or a cumulative distribution function (CDF). On the hand, Figure 6.9 and Figure 6.22 provide the actual vibration amplitude of the resonators as a function of frequency for a particular electrical input rather than a probability. Calculating the skewness coefficients from the vibration response data involve a post-processing procedure having the following steps:

1. Identify the set of vibration response data for which the response curve resemble a normal distribution (not skewed). Typically, the lowest excitation voltage in the range of excitation voltages considered provides such data.
2. Define the analysis window by setting a lower frequency limit f_L and upper-frequency limit f_U such that the peak of the response curve from step 1 is found at a frequency f_M such that $f_M = \frac{1}{2}(f_L + f_U)$. In addition, f_L and f_U must be sufficiently wide to accommodate the bending and shifting of the response curve at the maximum excitation voltage. Subsequent steps consider only data found within f_L and f_U , and applies to the vibration response data for the range of excitation voltages investigated.
3. Convert the response curve to a probability density function $P(f)$ by taking a ratio of the vibration amplitude V_p at a frequency f to the sum of amplitudes in the frequency range f_L to f_U , mathematically expressed as $P(f) = V_{p,f} / \sum_{f_L}^{f_U} V_{p,f}$. At this juncture, it must be noted that $P(f)$ is only a mathematical function with no physical meaning.
4. Calculate the mean μ and standard deviation σ of the distribution using

$$\mu = \sum P(f)f, \text{ and} \quad (6.20)$$

$$\sigma^2 = \sum P(f)f^2 - \mu^2. \quad (6.21)$$

5. Locate the median and mode of the distribution such that

$$\sum_{f_L}^{\text{median}} P(f) = \sum_{\text{median}}^{f_U} P(f) = 0.5, \text{ and} \quad (6.22)$$

$$P(\text{mode}) = \max[P(f)]. \quad (6.23)$$

6. Finally, Pearson's 1st skewness coefficient S_1 and 2nd skewness coefficient S_2 are calculated using the following expressions [241]:

$$S_1 = \frac{\mu - \text{mode}}{\sigma} \text{ and } S_2 = \frac{3(\mu - \text{median})}{\sigma} \quad (6.24)$$

For a perfectly symmetrical distribution, the mean, median, and mode are equal, but in and of itself, these quantities have no physical meaning. Pearson’s formulations are basically founded upon the separation between these quantities as a measure of departure from a symmetrical distribution. The magnitude of the skewness coefficient indicates the degree of skewness, while the sign indicates the skew direction (see Figure 6.13). It must be noted that the proposed method for quantifying Duffing-like vibrational response is meaningful only if the following conditions are met:

1. Any shift in the peak frequency must be accompanied by response curve ‘bending’.
2. There must only be one prominent response peak in the analysis range.

6.2.5.3 Application of described method

Table 6.3 shows the statistical parameters for the RP-1, RPS-16, RPST-16 and P25 resonators extracted from the response curves at an excitation voltage of around 30 V and the corresponding skewness coefficients. It is shown that the 1st and 2nd skewness coefficients are highest for RP-1 for both forward and reverse sweeps. The 1st skewness coefficients of RPST-16 and P25 are 76% and 57% smaller than RP-1. Meanwhile, RPS-16 is almost symmetrical as indicated by the near-zero skewness coefficients at the maximum excitation voltage of 30 V.

Table 6.3 Data for skewness coefficient calculation at $V_{in} = 30$ V (A574-bolted resonators).

	RP-1	RPS-16	RPST-16	P25
Forward sweep				
Mean	20033	19799	19800	19820
Median	20027	19798	19797	19815
Mode	20022	19798	19796	19812
Standard deviation	24.81	36.88	38.92	48.52
1 st Skewness Coefficient	0.42	0.03	0.10	0.18
2 nd Skewness Coefficient	0.68	0.08	0.22	0.34
Reverse sweep				
Mean	20030	19799	19799	19820
Median	20026	19800	19798	19816
Mode	20022	19798	19794	19806
Standard deviation	23.95	36.16	37.61	47.21
1 st Skewness Coefficient	0.36	0.03	0.14	0.29
2 nd Skewness Coefficient	0.57	-0.09	0.095	0.23

Figure 6.14 and Figure 6.15 plot the 1st and 2nd skewness coefficients as a function of the excitation voltage. It is shown that the skewness coefficients increases with voltage, which indicate good agreement with the response measurements. Another important feature is the convergence to zero skewness with decreasing voltage which serves as a test of the correct application of the calculation procedures and validity conditions outlined in section 6.2.5.2. The 2nd skewness coefficient

give negative values for several response curves despite the positive skew direction, an anomaly that does not arise in the calculation of the 1st skewness coefficient. The negative values are artefacts of the calculation procedure which lean on the correct identification of the analysis window and the mode of the response curve (i.e. the resonance frequency). This is in conflict with the definition of the 2st skewness coefficient which is based on median rather than mode. Nonetheless, the skewness coefficients correctly indicate that the multiple orifice devices, particularly RPS-16, exhibit the least nonlinear softening behaviour. In the sections that follow, the influence of preload bolt material on Q_m , k_{eff} , and nonlinear softening behaviour is investigated.

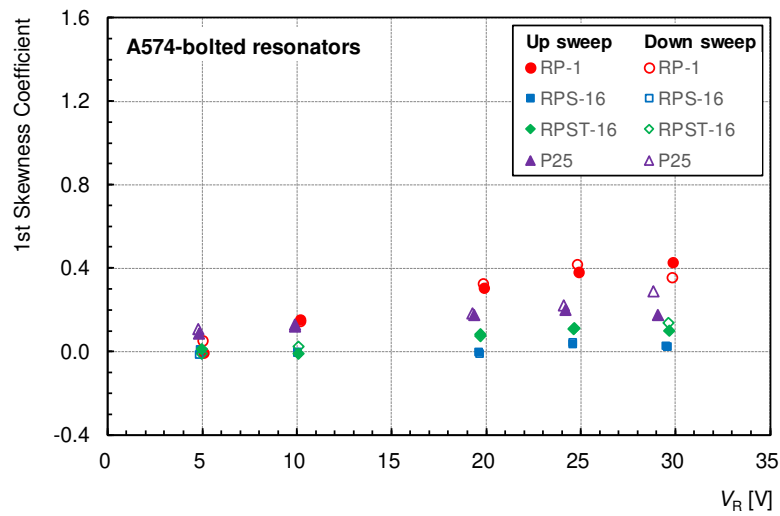


Figure 6.14. 1st skewness coefficients for A574-bolted radial resonators.

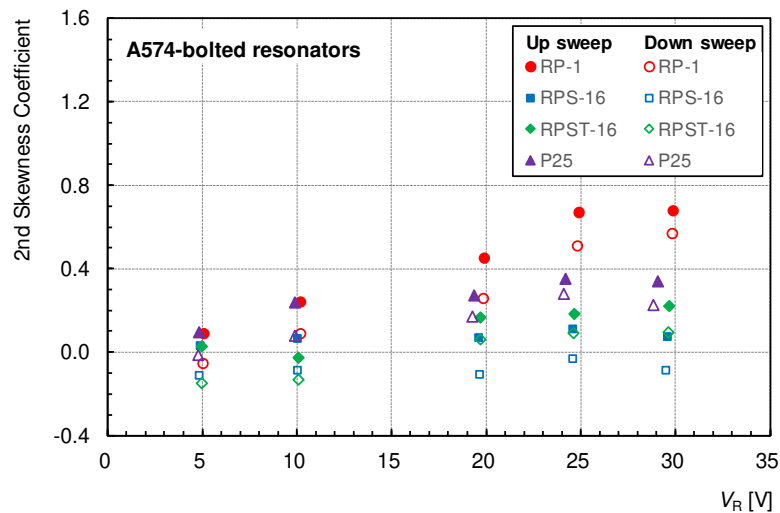


Figure 6.15. 2nd skewness coefficients for A574-bolted radial resonators.

6.3 Beryllium Copper as preload bolt

6.3.1 Selection criteria

The preload bolt is an integral part of a Langevin-type transducer keeping the PZT stack under compression at all times, whether in idle or during operation. Selection of a preload bolt material is often oversimplified by considering only geometric constraints and material strength. This approach has been very successful and has led to many commercialised devices. Nevertheless, it is of interest to study the impact of preload bolt material on the dynamic performance of the resonators.

It is known that a stronger material is preferred to allow for less thread engagement and shorter bolt relative to the length of the transducer. A shorter bolt is ideal because it places the bolt modes at higher frequencies than the design mode, thus avoiding losses due to modal coupling. Further, less thread engagement also translates to less friction loss. Bolt stiffness is another factor to consider when selecting the preload bolt material because it determines how much energy from the PZT stack is absorbed by the bolt [245]. A small preload bolt stiffness relative to the PZT stack stiffness results in a larger coupling coefficient k_{eff} and vice versa. Considering both strength and stiffness simultaneously, a bolt material with high σ^Y / E ratio is, therefore, preferred [176].

Alloy steel built to ASTM A574 is strong and widely used in commercial transducers because of its availability and low cost. Titanium alloy Ti-Al6-4V have also been used because of its strength and corrosion-resistance. It is especially suitable for use in transducers constructed from the same material to maximise acoustic energy transfer [246]. Finally, Beryllium copper has also been suggested, but very few reports on its use as preload bolt material in power ultrasonic devices have been reported [247]. Table 6.4 provides the properties of three preload bolt materials, of which A574 have been used in the present study up to this point. Between Ti-Al6-4V and Beryllium copper C17200, the latter has the higher σ^Y / E . On the other hand, Ti-Al6-4V is lighter and has a higher resonance frequency-to-wavelength ratio (i.e. for a given bolt length, bolt modes are found at a higher frequency when the material is Ti-Al6-4V compared to when the material is C17200). However, since the interest is to improve the coupling coefficient, C17200 was selected.

Table 6.4 Mechanical properties of preload bolt materials [191,248,249].

	Unit	A574	C17200	Ti-Al6-4V
Density	kg/m ³	7850	8250	4430
Res. freq./Wavelength	kHz/m	78.9	77.3	100.8
Young's Modulus, E	GPa	205	125	114
Yield strength, σ^Y	MPa	1205	1030	880
σ^Y / E ratio	-	5.88	8.24	7.71

6.3.2 Impedance analysis of C17200-bolted radial resonators

To investigate the effect of a lower stiffness preload bolt material, the RP-1, RPS-16, and RPST-16 resonators were disassembled, and the alloy steel A574 bolts were replaced with custom-made C17200 bolts. Bolt dimensions and thread specification remain unchanged. The resonator components were inspected for signs of wear following which the resonators were assembled following the procedures outlined in Section 5.1. A preload of around 30 kN was then applied, and the resonators were allowed to rest for at least 24 hours before IA measurements were carried out. Table 6.5 provides the equivalent circuit (EC) parameters and figures of merit of the modified resonators extracted from the measured impedance-phase spectra via a curve-fitting technique [250].

Table 6.5 Equivalent circuit parameters and figures of merit of C17200-bolted resonators.

	Units	RP-1	RPS-16	RPST-16	P25
R_1	Ω	104.47	43.91	67.56	33.80
L_1	H	1.26	1.11	1.00	0.32
C_1	pF	50.26	58.50	64.80	200.68
C_0	pF	7273	7912	7802	8758
Q_m	-	1515	3132	1837	1183
k_{eff}	-	0.093	0.096	0.102	0.168

The impedance-phase spectra of the C17200-bolted radial resonators are shown in Figure 6.16, Figure 6.17, and Figure 6.18. The measured (IA) and the simulated (EC) impedance and phase response were plotted in the same graph where it is shown that the equivalent circuit model has a very good agreement with the measured data. In addition, the impedance-phase response curve of the original resonator (A574-bolted) is also plotted in the same graph for ease of comparison.

The impedance response measurement shows that the use of C17200 bolt reduced both f_m and f_n , but the decrease in f_m is greater than f_n resulting in the widening of the phase window $\Delta f_{m,n}$. This behaviour must be attributed to the C17200 preload bolt because the same trend is observed for the three modified radial resonators. This is indeed the intended effect because the widening of the phase window increases the effective coupling coefficient k_{eff} of the resonators. However, the widening of $\Delta f_{m,n}$ have the effect of reducing the sharpness of the response peak, and the mechanical quality factor Q_m . The competing nature of k_{eff} and Q_m also apply to P25 (and PZT resonators in general) because it is observed that although k_{eff} of P25 is 65–80% higher than the radial resonators, its Q_m is 22–62% lower (see Table 6.5). Results also indicate that k_{eff} and Q_m are not linearly-

related. Thus, there must exist a set of design parameters that provides the optimum combination of k_{eff} and Q_m so that high electromechanical efficiency and strong vibrational response are achieved simultaneously.

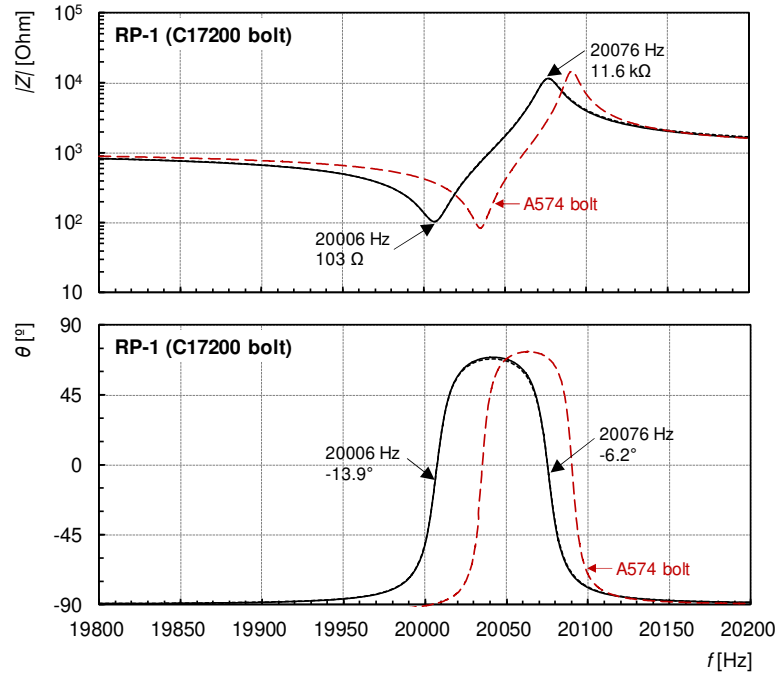


Figure 6.16. Impedance-phase angle spectra of C17200-bolted RP-1 from IA (line) and EC model (short dash); Impedance-phase angle spectra of A574-bolted RP-1 from IA (long dash) plotted for comparison.

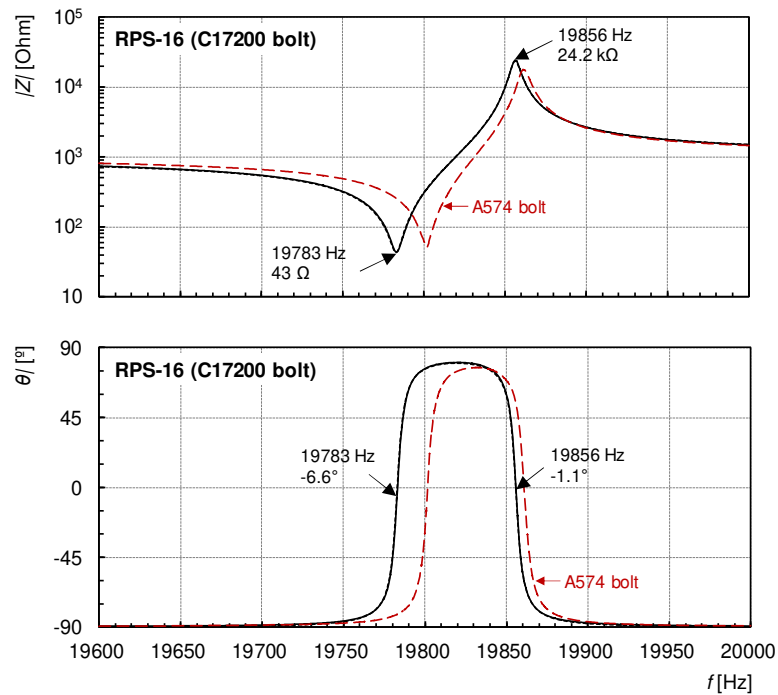


Figure 6.17. Impedance-phase angle spectra of C17200-bolted RPS-16 from IA (line) and EC model (short dash); Impedance-phase angle spectra of A574-bolted RPS-16 from IA (long dash) plotted for comparison.

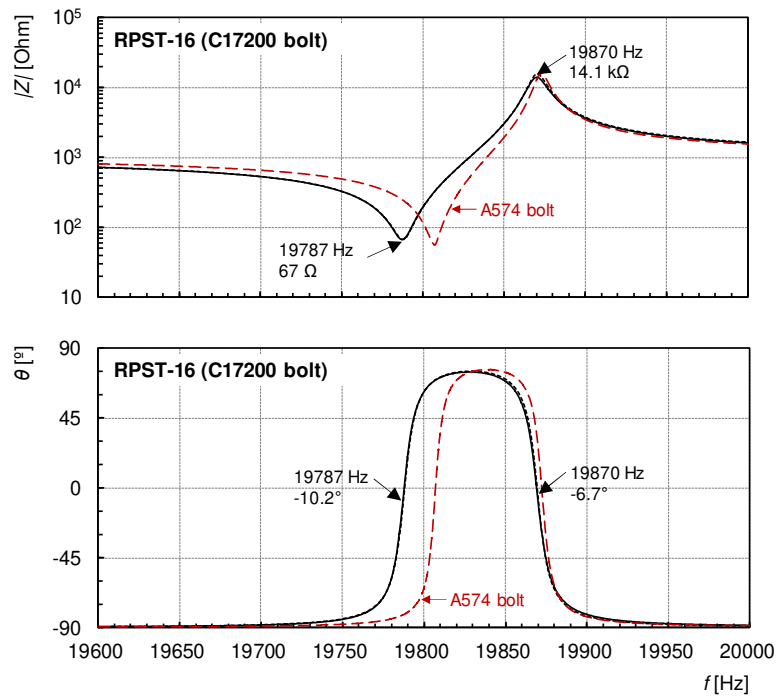


Figure 6.18. Impedance-phase angle spectra of C17200-bolted RPST-16 from IA (line) and EC model (short dash); Impedance-phase angle spectra of A574-bolted RPST-16 from IA (long dash) plotted for comparison.

Table 6.6 summarises the key parameters of the impedance spectra of the C17200-bolted radial resonators. Comparing this with Table 5.7, it is observed that the use of the C17200 bolt reduced the resonance frequency f_m by 19–29 Hz and the anti-resonance frequency f_n by 3–15 Hz resulting in the overall increase of the phase window $\Delta f_{m,n}$ by 14–19 Hz. Meanwhile, $|Z_m|$ increased by around 20Ω for RP-1, and 12Ω for RPST-16, but decreased by around 8Ω for RPS-16. It is not known why the change in impedance for RPS-16 differs in polarity from RP-1 and RPST-16 despite the bolts having the same geometric parameters and being constructed from the same piece of C17200 rod. However, some studies have suggested that impedance may be influenced by the stress distribution within the bolt, friction in the screw threads, and the geometric properties of the resonant structure [176].

Table 6.6 Measured (IA) characteristic frequencies and impedances of C17200-bolted resonators.

	Units	RP-1	RPS-16	RPST-16
f_m	Hz	20006	19783	19787
f_n	Hz	20076	19856	19870
$ Z_m $	Ω	103.71	43.62	66.94
$ Z_n $	Ω	11633.19	24162.62	14142.07
$\Delta f_{m,n}$	Hz	70	73	83

Figure 6.19 and Figure 6.20 compares the k_{eff} and Q_m of the resonators with different preload bolt material. As shown, the change to C17200 bolt from A574 bolt resulted in 13% increase in k_{eff} across the three resonators. The modified RPST-16 has the highest k_{eff} among the three radial resonators, but it is only marginally higher than the k_{eff} of the modified RPS-16. In absolute terms, the differences in the k_{eff} between the RP-1, RPS-16, and RPST-16 are not significant. Compared to P25 and an NCE-81 piezoceramic, which provide k_{eff} of around 0.168 and 0.366 respectively (see Table 5.8 and Table 4.6), the enhanced k_{eff} brought about by the use C17200 bolt is still relatively low. As shown in Figure 6.21, the k_{eff} of the modified radial resonators are between 39–45% lower than the P25 commercial probe. Nonetheless, the investigation has demonstrated that the use of a lower stiffness preload bolt is a feasible method to improve the k_{eff} .

Although the use of C17200 bolt resulted in similar increase in k_{eff} across the three radial resonators, the reduction in Q_m varies. For RPS-16, Q_m decreased by only 5%, whereas RP-1 and RPST-16 suffered 34–36% reduction in Q_m . The disproportionate changes in k_{eff} and Q_m indicate that it is possible to maximise both k_{eff} and Q_m simultaneously. It is then necessary to introduce the overall figure of merit \mathbf{K} defined by the product of k_{eff} and Q_m . As shown in Figure 6.21, RPS-16 has a \mathbf{K} that is 51% higher than P25, while the \mathbf{K} of RPST-16 and RP-1 are 5% and 30% lower than P25 respectively. Thus RPS-16 exhibit the best electromechanical characteristics among the radial resonators.

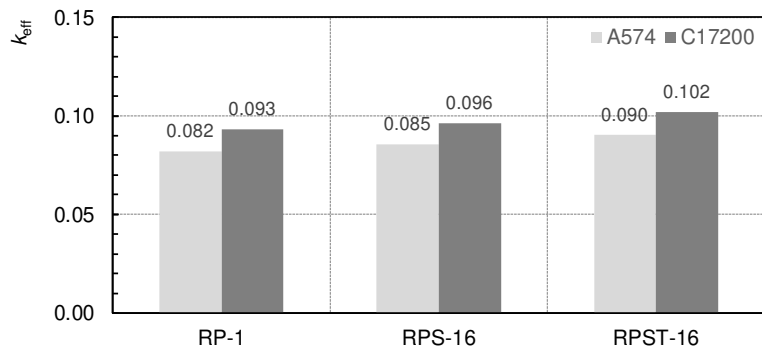


Figure 6.19. Comparison of k_{eff} between A574- and C17200-bolted radial resonators.

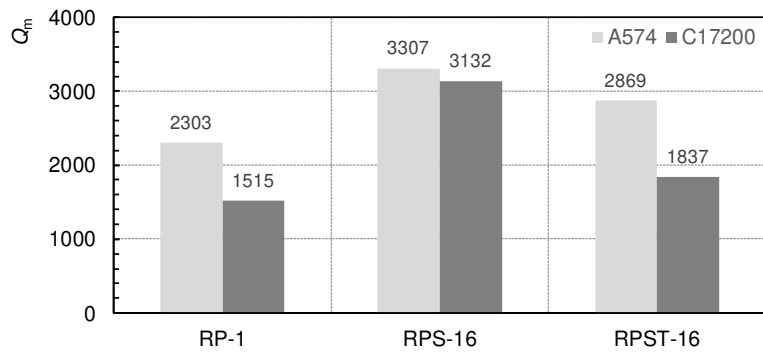


Figure 6.20. Comparison of Q_m between A574- and C17200-bolted radial resonators.

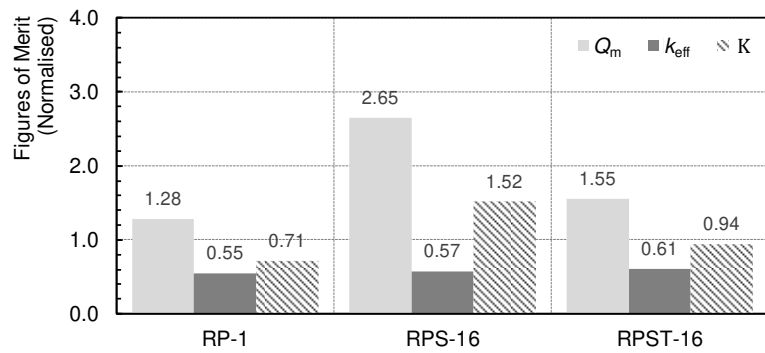


Figure 6.21. Normalised k_{eff} and Q_m of C17200-bolted radial resonators ($k_{\text{eff}} = Q_m = K = 1$ for P25)

6.4 Harmonic response of Beryllium Copper-bolted resonators

6.4.1 Harmonic response at different excitation levels

Velocity response of the resonator from forward and reverse frequency sweeps are shown in Figure 6.22. The response profile of the modified resonators is largely similar to the A574-bolted version presented earlier except RP-1. Here, the Duffing-like behaviour becomes more obvious with increasing excitation voltage. Although the response jumps are still small in the C17200 version of the RP-1, they are now more visible. At an excitation voltage of 29.4 V, response discontinuity is observed between 19970 Hz and 19972 Hz for the forward sweep, and between 19962 Hz and 19964 Hz for the reverse sweep, where the displacement amplitude jumped from 7 μm to 12 μm , and 12 μm to 8.4 μm , respectively.

There is an obvious difference between the hysteretic behaviour of the A574-bolted version and the C17200-bolted versions of RP-1. In the A574 version the hysteresis is observable but the resonance frequencies of the forward and reverse directional sweeps were difficult to distinguish. In contrast, the C17200 version exhibit more pronounced hysteresis. The difference in resonance frequencies between forward and reverse directional sweeps was measured to be around 10 Hz at 29.4 V. Meanwhile, the Duffing-like behaviour of the C17200-bolted RPS-16 and RPST-16 devices remain as subtle as the A574 versions and difficult to quantify using existing methods.

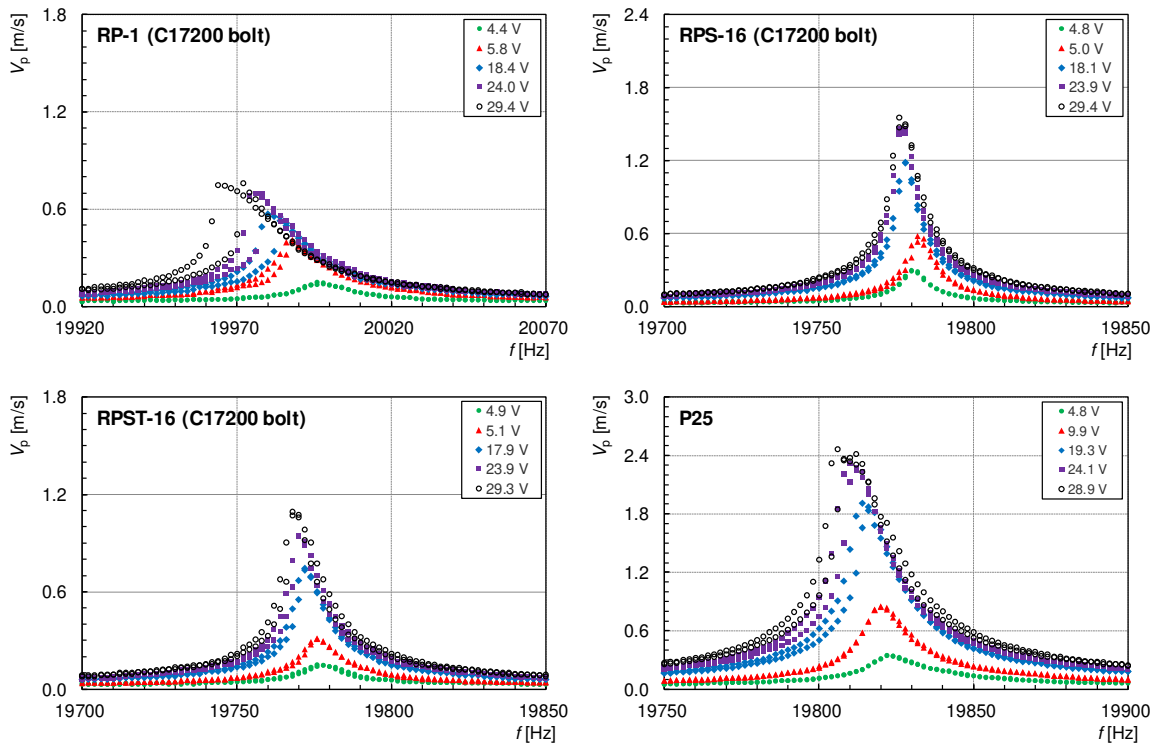


Figure 6.22. Vibration response of C17200-bolted radial resonators (P25 for comparison).

6.4.2 Displacement and amplification factor (AF)

The input and output peak-to-peak displacement response for mean excitation voltage of 30 V (RMS) are plotted in the graphs of Figure 6.23, and the corresponding peak-to-peak displacement amplitudes at the resonance frequencies are tabulated in Table 6.7. It is observed that RPS-16 gives the highest output displacement amplitude among the radial resonators, but its input displacement amplitude is marginally lower than that of RPST-16. The output displacement amplitude of RPS-16 is around 45% greater than that of RPST-16, and more than twice that of RP-1, for a similar excitation voltage. However, the C17200-bolted RPS-16 has an output displacement amplitude that is around 35% smaller than P25.

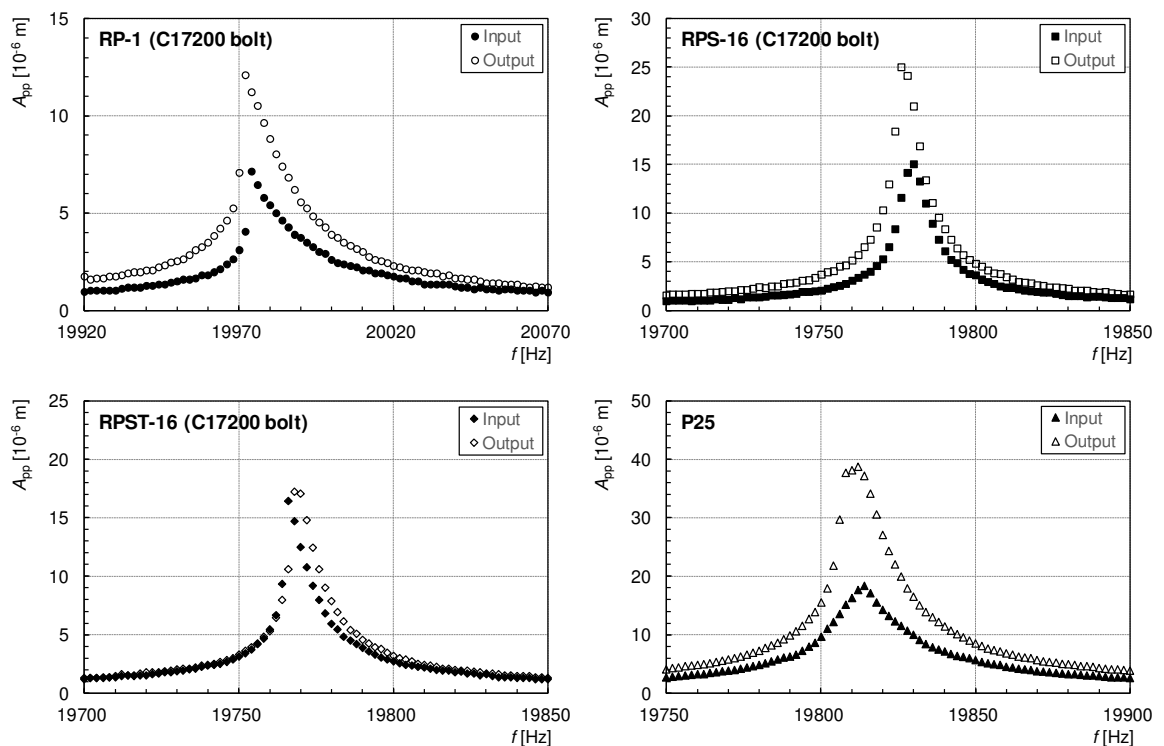


Figure 6.23. Input and output responses of C17200-bolted resonators (P25 for comparison).

Among the C17200-bolted radial resonators, RPS-16 provides the highest AF followed by RP-1, a trend that followed on from the A574-bolted versions. The change of preload bolt material from A574 to C17200 resulted in the overall decrease in output amplitude as shown in Figure 6.24. Specifically, RP-1 output amplitude decreased by around 42% while that of RPS-16 and RPST-16 decreased by approximately 14% and 11% respectively. The C17200 bolt appears to have a significant damping effect on the RP-1 design. Meanwhile, the damping effect of C17200 also appear in the RPS-16 and RPST-16 designs, although to a lesser degree.

Table 6.7 Displacement and amplification factor of C17200-bolted resonators.

	Units	RP-1	RPS-16	RPST-16
Input displacement	10^{-6} m	7.16	15.04	16.42
Output displacement	10^{-6} m	12.11	25.02	17.22
Amplification Factor	-	1.69	1.66	1.05

Interestingly, Figure 6.25 shows that the C17200 preload bolt appears to have induced a positive effect on the amplification factor with RP-1 and RPS-16 exhibiting AF improvements by 28% and 15% respectively, despite the decrease in output amplitude. This is possible only if the input amplitude has decreased to a much greater extent than the decrease in the output amplitude. Comparing the measurements provided in Table 6.2 with Table 6.7, this appears to be the case. The large reduction in input amplitude is associated with the increase in impedance which resulted in lower motional current for the same excitation voltage.

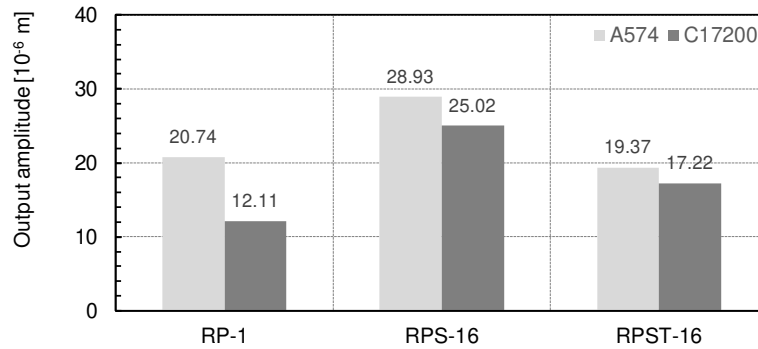


Figure 6.24. Comparison of output displacement amplitude of A574- and C17200-bolted radial resonators.

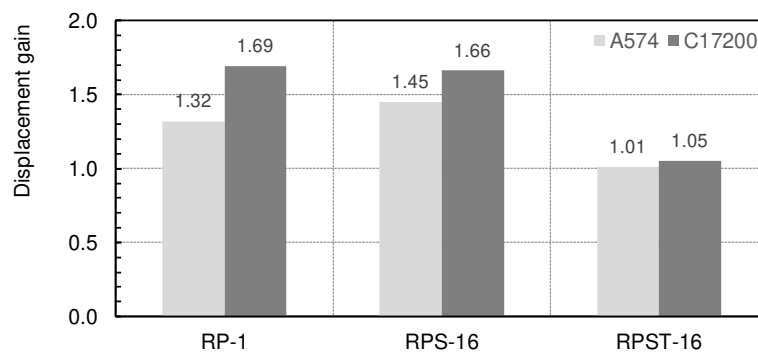


Figure 6.25. Comparison of displacement gains of A574- and C17200-bolted radial resonators.

6.4.3 Frequency shift

In Figure 6.26, the plot of Δf against I_R shows the extent to which the excitation current influences the nonlinear behaviour of the radial resonators. It is observed that all devices exhibited some degree of hysteretic behaviour, which arises from variations in the device stiffness, material interfaces within the device, and the nonlinear piezoelectric and dielectric characteristics of the PZT stack [166,169,238]. From the slope of the graph, it can be deduced that excitation current has the greatest effect on the frequency shift of RP-1. RST-16 appears to be the next most affected by excitation current, whereas RPS-16 and P25 are almost equally susceptible. This order of ranking the nonlinear behaviour of resonators is the same for A574 and C17200 versions of the resonators. However, the susceptibility to frequency shift appears to have been amplified with the used of C17200 bolt. Comparing Figure 6.12 and Figure 6.26, it is observed that the slope $\Delta f / I_R$ is greater for the C17200-bolted resonators. The increase in the steepness of the $\Delta f / I_R$ gradient is most obvious for RP-1 – at 0.3 A the resonance frequency decreased by 14–15 Hz with A574 bolt whereas the resonance frequency decreased by 26–28 Hz with C17200 bolt, which is a significant change in nonlinear behaviour. The Δf of RPST-16 is around 5–6 Hz with an A574 bolt and 8–9 Hz with C17200 bolt at 0.5 A.

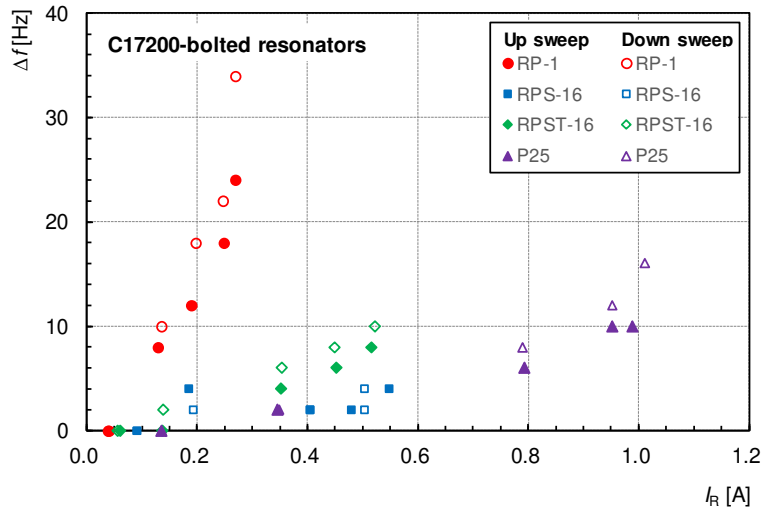


Figure 6.26. Δf vs. I_R (RMS) of C17200-bolted resonators (P25 for comparison).

Comparing the extent of resonance shift among resonators may best be performed by comparing the gradients of the linear fit functions of the group of plots associated with each device. The fit function is obtained through linear regression of the scatter plot with the linear function crossing the vertical axis at zero. Table 6.8 provides the gradient of the linear fit function obtained using a

commercial spreadsheet program. Based on the gradient, it can be deduced that RP-1 exhibited a greatest nonlinear softening behaviour, which seem to be exacerbated by the use of a lower stiffness preload bolt (C17200). In contrast, the low gradient of RPS-16 indicates that the resonator generally operates in the linear regime for the range of excitation currents investigated.

Table 6.8 Gradient of linear fit function for the graph of Δf vs. I_R (RMS).

Preload bolt	RP-1	RPS-16	RPST-16	P25
A574	43.71	2.82	11.14	11.12
C17200	88.42	6.13	15.70	-

6.4.4 Skewness

Pearson's first and second skewness coefficients were calculated from the mean, median, and mode values of the converted response curves of Figure 6.22. The conversion process is described in section 6.2.5. Table 6.9 shows the statistical parameters extracted from the response curves at an excitation voltage of around 30 V and the corresponding skewness coefficients for the four resonators. As shown, the first and second skewness coefficients are highest for RP-1 for both forward and reverse sweeps. On the other hand, RPST-16 has slightly higher skewness than P25 for the forward sweep, but lower skewness than P25 for the reverse sweep. However, taking the average of the forward and reverse sweeps, the skewness of RPST-16 and P25 are approximately equal. RPS-16 has the lowest skewness coefficients among the four resonators.

Table 6.9 Data for skewness coefficient calculation at $V_R = 30$ V (C17200-bolted resonators).

	RP-1	RPS-16	RPST-16	P25
Forward sweep				
Mean	19988	19779	19776	19820
Median	19981	19777	19772	19815
Mode	19972	19776	19768	19812
Standard deviation	42.45	31.22	32.33	48.52
1 st Skewness Coefficient	0.39	0.10	0.24	0.18
2 nd Skewness Coefficient	0.52	0.19	0.36	0.34
Reverse sweep				
Mean	19985	19779	19776	19820
Median	19978	19779	19774	19816
Mode	19964	19778	19768	19806
Standard deviation	41.27	30.90	31.39	47.21
1 st Skewness Coefficient	0.50	0.024	0.25	0.29
2 nd Skewness Coefficient	0.49	-0.03	0.17	0.23

Figure 6.27 and Figure 6.28 compare the skewness coefficients of A574-bolted radial resonators against the C17200-bolted versions. It is observed that the 1st skewness coefficient increased across the board with the use of C17200 preload bolt. The 1st skewness coefficient increased by around 12.8% for RP-1 while that of RPS-16 and RPST-16 increased by 100% and 108% respectively with the use of C17200 preload bolt. Although the percentage increase in 1st skewness coefficient is large for RPS-16 and RPST-16, it is also necessary to consider the absolute values of the skewness coefficients. In particular, the 1st skewness coefficient of RPS-16 increased by a mere 0.03 to a final skewness of 0.06 with a change of bolt material. This change is considered insignificant, and by the near-zero skewness coefficient, RPS-16 operates well within the linear regime in the voltage range considered, be it with an A574 bolt or with C17200 bolt.

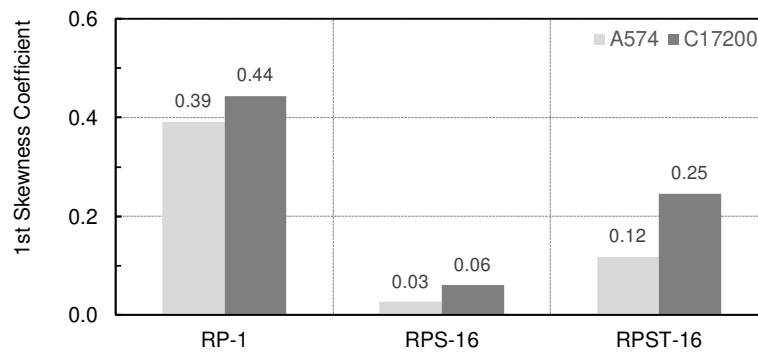


Figure 6.27. Comparison of 1st skewness coefficients at 30 V.

A similar trend can also be observed in Figure 6.28 in which it is shown that RP-1 has the highest skewness, followed by RPST-16. The 2nd skewness coefficient of RPS-16, which is calculated using mean and median, is close to zero, similar to the skewness coefficient calculated from mean and mode. Replacement of A574 bolt with C17200 bolt was shown to reduce the 2nd skewness coefficient by around 20% for RP-1.

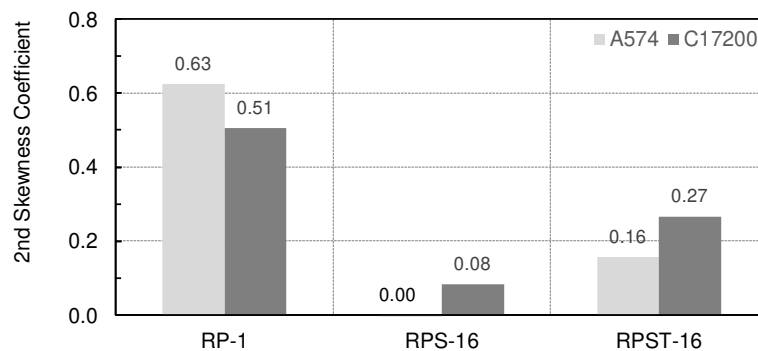


Figure 6.28. Comparison of 2nd skewness coefficients at 30 V.

The increase in the 2nd skewness coefficient for RPS-16 and RPST-16 is consistent with observations and corroborated with the calculated 1st skewness coefficient. On the other hand, the 2nd skewness coefficient for the modified RP-1 resonator is lower than the original A574-bolted version. This result contradicts the observation of the response curves of Figure 6.9 and Figure 6.22 where it was shown that the C17200-bolted version clearly exhibited a greater extent of bending. This anomaly arises from the fact that the 2nd skewness coefficient is calculated from the median which has no physical meaning in the actual response curve. Instead, calculation of skewness based on mode is more appropriate since the mode refers to the frequency at peak response.

The behaviour RPS-16 present another extreme in that the low stiffness of C17200 relative to A574 has a negligible impact on the overall nonlinear behaviour of the resonator. The increase in skewness coefficient with the change to a preload bolt with lower stiffness is expected to ‘soften’ the stiffness of the resonator as was demonstrated in the RP-1 and RPS-16 devices. For RPS-16, the stiffness coefficient showed an increase of 0.08 points. This demonstrates two things: (1) the use of the statistical skewness coefficient to quantify nonlinear behaviour can detect very subtle changes in the Duffing-like behaviour; and (2) the RPS-16 multiple-orifice configuration increases the stiffness of the structure and is resilient to ‘softening’ effect induced by material changes.

6.5 Current vs. vibrational amplitude

Figure 6.29 plots the current drawn by the resonators against the vibrational amplitudes for excitation voltages up to 30 V (RMS) in the frequency range as shown in Figure 6.9 and Figure 6.22. The scatter plots include all current and vibration amplitude data collected from the frequency sweep, including data at the resonance frequency and data away from the resonance frequencies. As shown in Figure 6.29, the vibration amplitude is proportional to the current drawn and this relationship is not limited to resonance frequencies only. Nonetheless, the current drawn is maximum at the resonance frequency, which is the expected behaviour for PZT-based devices.

A linear fit function is computed so that the dynamic performance of the resonator with respect to current drawn can be compared quantitatively. The gradient of the linear fit function indicates the ability of the resonator to translate current into motion. Therefore the higher the gradient, the better the resonator since more work is done for the same amount of current drawn. It is observed that A574-bolted resonators provide higher vibrational amplitudes than the C17200-bolted versions for the same current drawn. This is true for the three radial resonators (RP-1, RPS-16, and RPST-16). While it has been established that the vibrational amplitudes of the radial resonators are lower than P25, the gradients show that RP-1 and RPS-16 generate higher displacements than P25 for the

same current drawn. However, it must be noted that to achieve the particular current (and therefore displacement), higher voltages are needed for the radial resonators compared to P25.

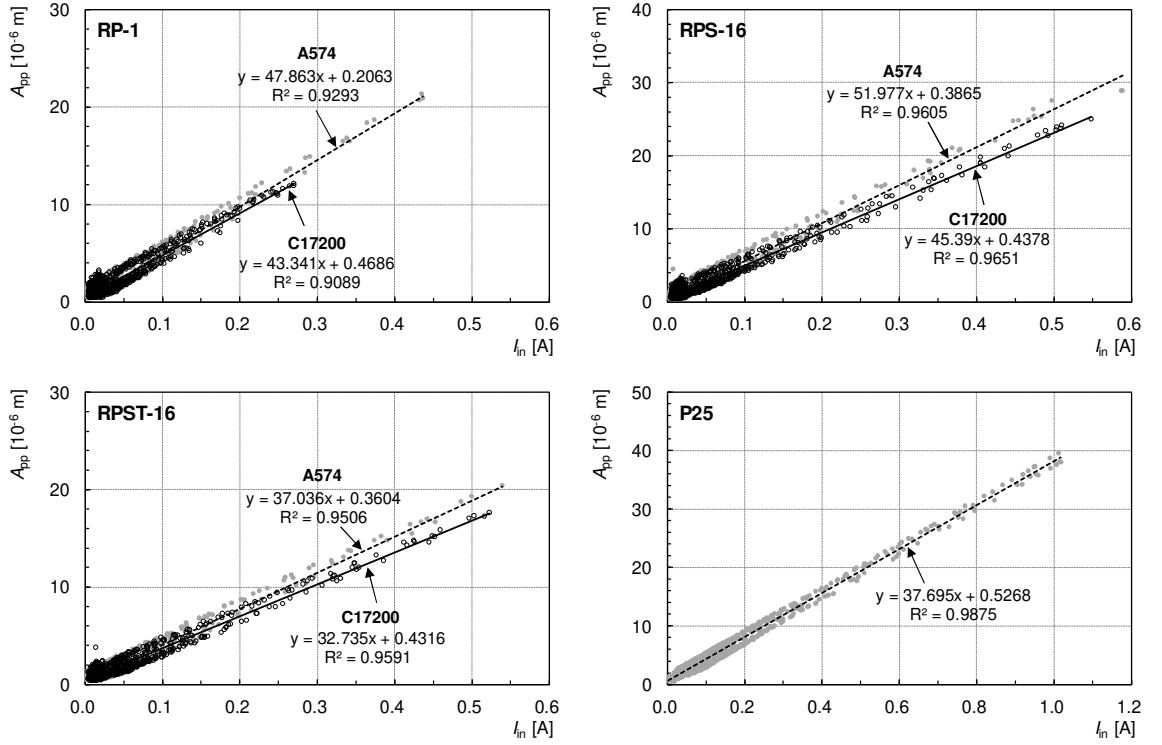


Figure 6.29. Current vs. displacement amplitude.

6.6 Conclusion

Harmonic response characterisation of the three radial resonators and a commercial high-gain probe P25 have been carried out successfully. It was noted that the radial resonators generally have lower vibrational amplitude and amplification factor compared to P25. This is an expected behaviour attributed to the distribution of the stress-wave energy over a larger surface area of the radial resonators. However, the increase in the radiating surface areas provided by the radial resonators (at least 20 times the surface area of P25) more than compensate for their low vibrational amplitude. Thus, significantly more acoustic energy can be emitted from the radial resonator than the commercial probe-type device

Nonlinear behaviour of the resonators was also investigated by applying voltages up to 30 V (RMS) across the resonator terminals over a sweeping frequency. It was observed that RP-1 design was most susceptible to frequency shift with the elevation of excitation voltage, followed by RPST. A new quantitative measure of Duffing-like behaviour was also introduced through statistical manipulation to derive the ‘skewness’ of the response curves. The skewness coefficient is analogous

to the cubic term of the Duffing equation but with opposite polarity, and have been successfully utilised to quantify the relative nonlinear behaviour of the resonators. This new technique showed that RP-1 exhibited the greatest extent of nonlinear behaviour, an outcome that is in agreement with observations. Meanwhile, RPS-16 exhibited the least nonlinear behaviour among the four devices including the conventional P25.

The effect of preload bolt material on the electromechanical behaviour of the resonators was also investigated. This investigation was motivated by the need to improve the k_{eff} which is related to the quality of interactions between the parts of the resonators [227,251]. Beryllium copper C17200, which provided a high strength-to-stiffness ratio, was selected as the alternative preload bolt material to alloy steel A574. Results showed that the modified resonators exhibited 13% higher k_{eff} than the original versions comprising of A574 bolts, but the Q_m decreased by 34-36% for RP-1 and RPST-16. Meanwhile, Q_m of RPS-16 decreased by only 5%. Further, RPS-16 continue to exhibit the least nonlinear behaviour in the voltage range considered whether be it with an A574 bolt or a C17200 bolt. While results have shown that the use of a low-stiffness bolt like C17200 has a ‘softening’ effect on the overall structure, this effect appears to be small compared to the stiffness induced by the multiple-orifice configuration of the RPS-16 design. Considering both k_{eff} and Q_m simultaneously leads to an overall figure of merit K , which showed that RPS-16 exhibited the best electromechanical characteristics of the four resonators investigated.

Chapter 7

Inactivation of Zooplankton

7.1 Experimental set-up and procedures

This chapter investigates the resonator performance in its intended operating environment. Although the dynamic behaviour of the resonators under no-load condition has been analysed, their dynamic behaviour in water can be markedly different. Compared to conventional probe-type devices, the acoustic loading effect was shown to exert a greater influence on the electromechanical characteristics and dynamic behaviour of the radial resonators due to their large output surface areas [35]. The present work investigates how acoustic loading will influence the electromechanical characteristics, dynamic behaviour, and zooplankton inactivation efficacy of the radial resonators.

7.1.1 Equipment and apparatus

A custom-made glass tank with dimensions of 150 x 80 x 150 mm (length x breadth x height) was used as the sonication vessel and can hold approximately 1100 cm³ of water with the emitter section of the resonators fully submerged. The same fixture used in EMA, HRC, and IA measurements was also used to support the resonators in the inactivation study. Figure 7.1 shows the relative placement of the fixture, resonators, and sonication tank during the zooplankton inactivation experiments.

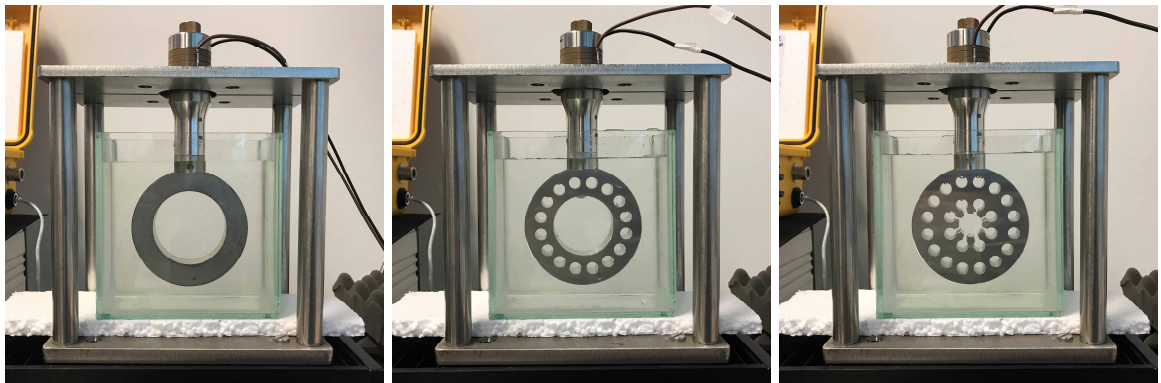


Figure 7.1. Mechanical set-up for inactivation experiments; RP-1, RPS-16, RPST-16 (left to right).

The resonators were driven by a fixed gain power amplifier (1000D01, E&I) which takes in the source signal from an arbitrary function generator (MDO3024, Tektronix) programmed to output 20 kHz sine wave with a voltage offset equal to half of the peak-to-peak signal. Signal offsetting ensures that the voltage presented across the resonator is always positive to avoid depoling the PZT due to excessive negative voltage. The power amplifier drives the resonators through three compensation inductors connected in series with the resonator. This is done to transmit sufficient electrical power to the resonator (refer to section 7.2.2 for more details).

7.1.2 Breeding and harvesting of test organisms

Two types of zooplankton were used in the inactivation experiments to investigate the effect of organism type on the ultrasonic inactivation. The two organisms are *Artemia* sp. and *Daphnia* sp. *Artemia* sp., a marine crustacean, is widely used as a standard indicator organism in the evaluation of ballast water treatment systems [29,90]. They are easy to breed, and their larvae are commonly hatched in the laboratory to provide a continuous supply of test organisms. The present research uses *Artemia* nauplii obtained through breeding. The culture tank was prepared by filling it with 1000 cm³ of distilled water and dissolving around 30 g of sea salt to achieve a salinity of 30–35 ppt. Commercially supplied cysts of *Artemia* sp. were placed in the culture tank provisioned with a continuous supply of oxygen through an air pump and a diffuser. A light source was irradiated into the tank to warm up the tank slightly above the ambient temperature of 23 °C. The nauplii of *Artemia* sp. hatched after 24 h and were used within two days after hatching.

Daphnia sp., which is a freshwater cladoceran, were purchased from a local aquarium on the same day they were used for the experiments.

7.1.3 Experimental procedures

Before every experimental run, the sonication tank was partially filled with a new batch of saline water (30–35 ppt). The *Artemia* nauplii were extracted from the culture tank using a pipette with 1 ml disposable tip and transferred to a Petri dish for pre-test enumeration. With the aid of a magnifying glass and a tally counter, the nauplii were enumerated as they were released into the container. This process was repeated until approximately 300 counts of *Artemia* nauplii spread over several Petri dishes have been transferred. The nauplii and saline water in the Petri dishes were then poured into the sonication tank containing clean saline water. The Petri dishes were rinsed using saline water with the aid of a spray bottle, and its effluent was released into the sonication tank to ensure complete transfer of specimen. Saline water was added to the sonication tank until the water level reached the mark indicating water volume of 1100 cm³. The process described above was

repeated for each inactivation experimental run. Figure 7.2 shows the *Artemia* sp. culture tank with cysts at the tank bottom, and hatched nauplii suspended in the saline water; the pre-sonication *Artemia* nauplii enumeration inside a Petri dish; and the post-sonication transfer and enumeration of surviving *Artemia* nauplii.



Figure 7.2. *Artemia* sp. culture tank; Petri dish with cultured *Artemia* sp. nauplii; pre-sonication and post-sonication enumeration of *Artemia* nauplii (left to right).

Cumulative exposure and discrete exposure experiments were carried out to investigate the effect of ultrasound-induced mixing on the inactivation efficacy. In actual application, flow rates will be high ($> 100 \text{ m}^3/\text{h}$), and exposure duration will be very short (less than 1 s). Thus, ultrasound-induced mixing will have limited benefit in flow-through scenarios. However, such short exposures will be very challenging to replicate in the laboratory, and the results will not be repeatable. To compare the relative biological inactivation efficacy of the resonators, the present study uses ultrasound exposure durations of 1, 2, 3, 12, 24, 36, 48, and 60 s.

Two types of ultrasound exposure methods were carried out to investigate the influence of cumulative and discrete ultrasound exposures on zooplankton inactivation. In the cumulative exposure experiments, the zooplankton specimen was given five ultrasound exposures, each lasting 12 s. At the end of each exposure, the resonator was removed from the sonication tank, and the water was left to settle for at least 5 min. The number of surviving nauplii were then enumerated directly by inspecting the sonication tank with the aid of a magnifying glass. The number of surviving nauplii would have reduced to a manageable quantity to allow direct enumeration without the need to employ serial dilution technique [91]. In the discrete exposure experiments, nauplii of *Artemia* sp. were subjected to one exposure of ultrasound lasting 1, 2, and 3 s. After each exposure, the resonator was removed from the sonication tank, and the water was left to settle for at least 5 min. The surviving nauplii were then extracted from the sonication tank using a 1 ml pipette and transferred into a counting dish, enumerating the number of surviving nauplii as they were released from the pipette. Once all the surviving nauplii have been accounted for, a new batch of *Artemia* nauplii and saline water was then prepared for the next experimental run. Each exposure duration was carried

out three times to ensure repeatability. The inactivation rate was calculated as the ratio of surviving nauplii to the initial numbers. The process described above is illustrated in Figure 7.3.

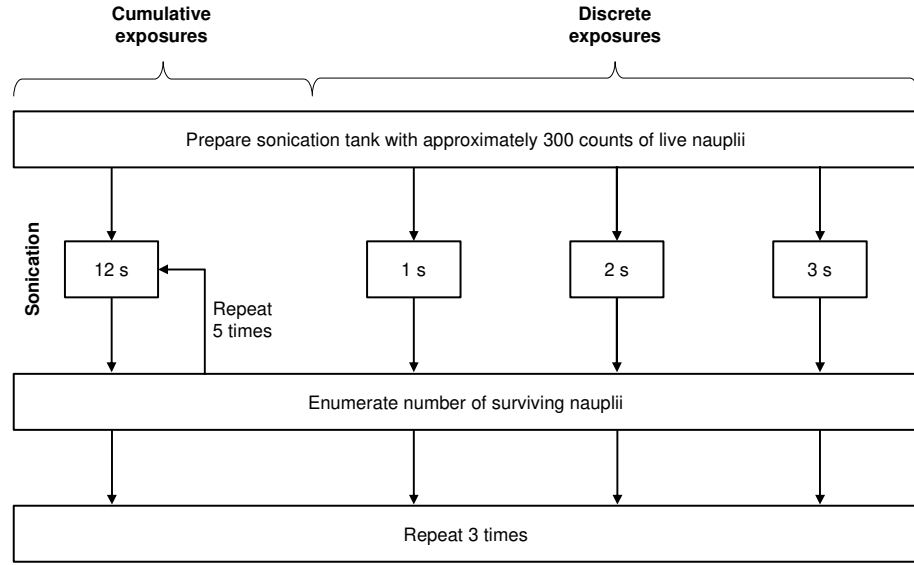


Figure 7.3. Process for cumulative exposure and discrete exposure inactivation experiments,

7.2 Driving of water-loaded resonators

7.2.1 Transmission cable impedance consideration

Maximum power transfer occurs when the source and load impedance are complex conjugates of each other. Although power transfer between the source and the load will involve transmission through cables of finite impedances, for short length its influence on power transmission can be neglected. This is shown by considering the general transmission line equation looking into the cable having load Z_L terminated at the distal end. For very short cables, signal attenuation is neglected, and the simplified transmission line equation is [252],

$$Z_{in} = Z_o \frac{Z_L + Z_o \tan(j\beta L)}{Z_o + Z_L \tan(j\beta L)}. \quad (7.1)$$

where Z_o (Ω), β (radians/m) and L (m) are the characteristic impedance of the line, phase constant, and cable length respectively.

Assuming the values of $L = 2$ m, $c = 3 \times 10^8$ m/s, and $f = 20$ kHz, the cable length in terms of the transmission wavelength is $L = \lambda / 7500$. Further, since $\beta L = 2\pi / 7500$ ($\beta = 2\pi f / c = 2\pi / \lambda$) is small, (7.1) is reduced to

$$Z_{\text{in}} = Z_L. \quad (7.2)$$

Considering the relatively short length ($L \ll \lambda / 4$) of transmission cable used in the experiments, the ability of the power amplifier to supply sufficient voltage and current to the resonators depends primarily on the impedance of the resonators.

7.2.2 Compensation of capacitive reactance

Impedance analyser measurements showed that the RP-1, RPS-16, and RPST-16 resonators exhibit significantly higher capacitive reactance when subjected to water-load than when it is unloaded. As a result of the large reactance, the resonator impedance magnitude is in the range of 1000Ω , which can be very challenging to drive. For example, achieving a motional current of 1 A into a 1000Ω resonator would require a driving voltage of at least 1 kV. This is assuming the voltage and power presented at the output of the driver arrives at the resonator. In reality, the resonator receives only a small fraction of this outgoing power due to the large mismatch between the electrical impedances of the source and the resonator (refer to section 6.1.3).

Most commercial ultrasonic systems include impedance matching [253,254] capability into their generators to provide efficient operation of the ultrasonic device. Further, phase-locked loop control [232,255,256] is also a standard feature in many commercial ultrasonic systems to ensure that the driving voltage and current are always in-phase for maximum power delivery and efficient operation. However, these complex control circuitry were optimised for specific devices and tend to have a narrow operating bandwidth. Thus commercially-available ultrasonic generators may not be suitable for driving the radial resonators which exhibit very different electromechanical characteristics (operating frequency, quality factor, bandwidth, etc.) from commercial transducers.

The impedance of a piezoelectric resonator at series resonance exhibit slight capacitive behaviour. However, when the output face of the resonator is subjected to water load, the capacitive reactance increases tremendously. In order to drive the water-loaded resonators effectively, the capacitive reactance needs to be eliminated or reduced. The most pragmatic solution which avoids the use of complex control circuitry would be to connect one or more inductors in series with the resonator so that the positive reactance of the inductors offsets the negative reactance of the loaded resonator. Figure 7.4 shows the schematic of the driving circuit used in the present zooplankton inactivation experiments.

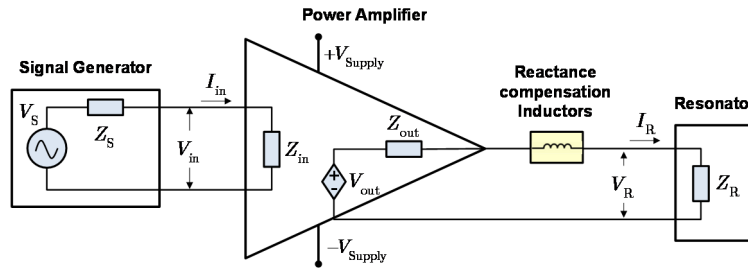


Figure 7.4 Block diagram of modified ultrasonic generator circuit for driving water-loaded resonators, highlighting the input and output impedances of interconnecting devices ($Z_S = Z_{in} = Z_{out} = 50 \Omega$).

To determine the inductance required, consider first the complex impedance Z_R of a water-loaded resonator connected in series with compensating inductors,

$$Z_R = \overbrace{(R + X_C)}^{\text{resonator components}} + \overbrace{X_L}^{\text{reactance compensation}} \quad . \quad (7.3)$$

where R is the electrical resistance of the resonator, X_C is the capacitive reactance of the water-loaded resonator, and X_L is the total reactance of the compensation inductors. Ideally, X_C and X_L should cancel each other so that the required inductance L can be calculated using,

$$X_L = -X_C = 2\pi fL. \quad (7.4)$$

Table 7.1 provides the impedance and phase measurements of RP-1, RPS-16, and RPST-16 radial resonators when their emitter sections were fully submerged in water. The real and imaginary components of the impedance (R and X_C) were calculated, and the inductance required to offset the capacitive reactance were given in the last column of the same table. Although the goal is to select an inductor that satisfies (7.4), this requirement is difficult to achieve because resonators exhibiting varying degree of capacitive behaviour were driven by the same driving circuit. Further, high-frequency inductors with high inductance (~ 8 mH), and high power rating (~ 1 kW) are not readily available. Nonetheless, a solution was found through the use of three slightly oversized inductors which provided a total inductance of 9.3 mH.

Table 7.1 Calculation of reactance compensation inductance.

Device	$ Z $ (Ω)	θ ($^\circ$)	R (Ω)	X_C (Ω)	L (mH)
RP-1	1038	-86.5	216	-1036	8.2
RPS-16	959	-89.4	10	-959	7.6
RPST-16	933	-80.5	154	-921	7.3

Figure 7.5 to Figure 7.7 plot the impedance-phase spectra of the radial resonators under water-load, with and without the inductive compensation. As shown, the inductors have a significant positive effect on the electrical characteristics of the resonators in terms of reducing the impedance magnitude. The absolute values of the phase angles were reduced by 20–30% indicating a reduction in the overall reactance, but the phase angles are now positive indicating overcompensation.

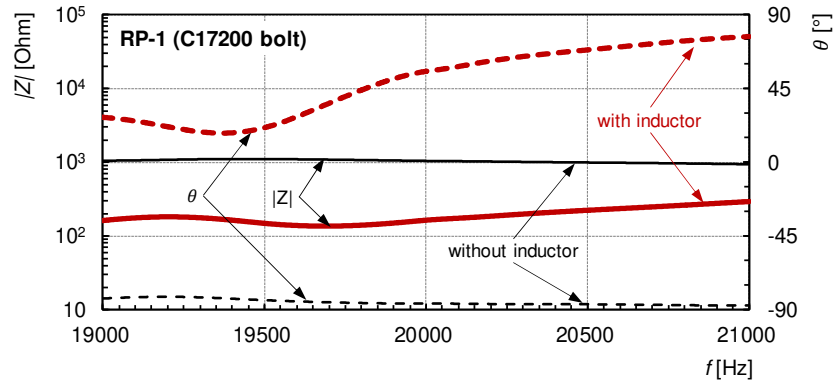


Figure 7.5. Effect of reactance compensation on the impedance-phase spectra of RP-1.

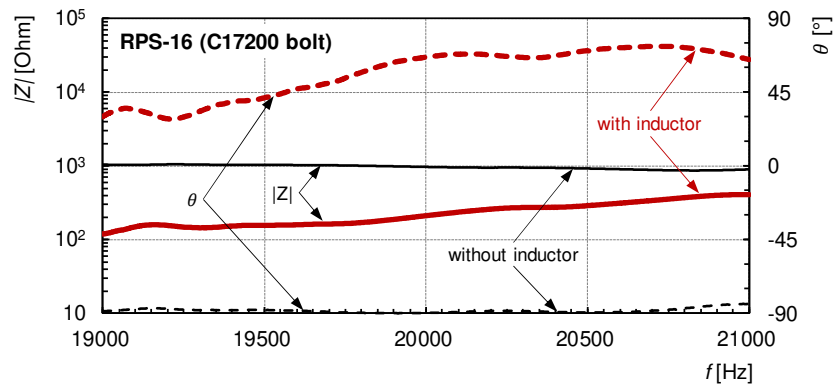


Figure 7.6. Effect of reactance compensation on the impedance-phase spectra of RPS-16.

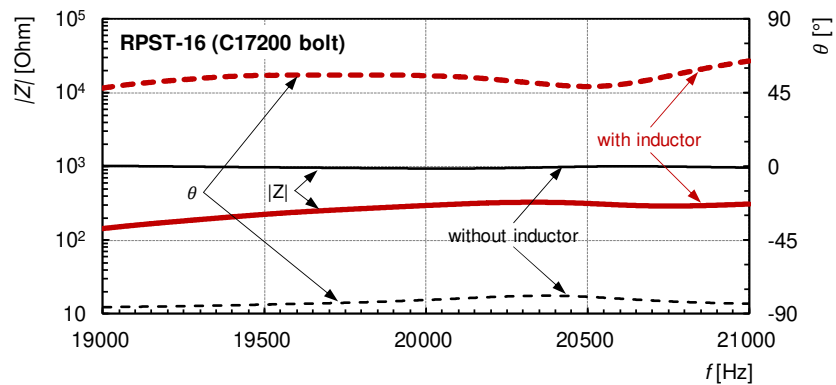


Figure 7.7. Effect of reactance compensation on the impedance-phase spectra of RPST-16.

Table 7.2 provides the impedance and phase measurements of the water-loaded radial resonators with reactance compensation. As shown, the use of the inductors increased the overall resistance for RPS-16 and RPST-16, which can be interpreted as the resistance introduced by the inductor coil. A similar behaviour is expected of RP-1 but measurement showed a reduction in resistance instead. Although the source of this anomaly was not established, the total reactance X_{LC} now ranges from 150 to 252 Ω , which is around 72% to 85% lower than the reactance without inductive compensation. Zero reactance may be achieved by re-sourcing smaller inductors, or adding one or more compensation capacitors (providing a total capacitance C as shown in Table 7.2) in series with the inductors to shift the reactance in the negative direction. However, since electronics is not the focus of the present research, no further changes were made to the driving circuit.

Table 7.2 Impedance and phase angle with reactance compensation inductors.

Device	$ Z $ (Ω)	θ ($^\circ$)	R (Ω)	X_{LC} (Ω)	C (nF)
RP-1	176	58.6	92	150	53
RPS-16	234	68.3	87	217	36
RPST-16	308	54.8	177	252	31

Figure 7.8 shows the effect of the reactance compensation inductors on the resonator voltage V_R and power $V_R I_R$ for power amplifier input signal V_S of 100–800 mV. It is evident that the use of the inductors resulted in significant improvement in voltage and power reception of the water-loaded resonators. Although the driving circuit is far from efficient (due to the large voltage-current phase angle), the present driving circuit configuration is considered adequate to drive the water-loaded resonators to achieve measurable and meaningful zooplankton inactivation rates.

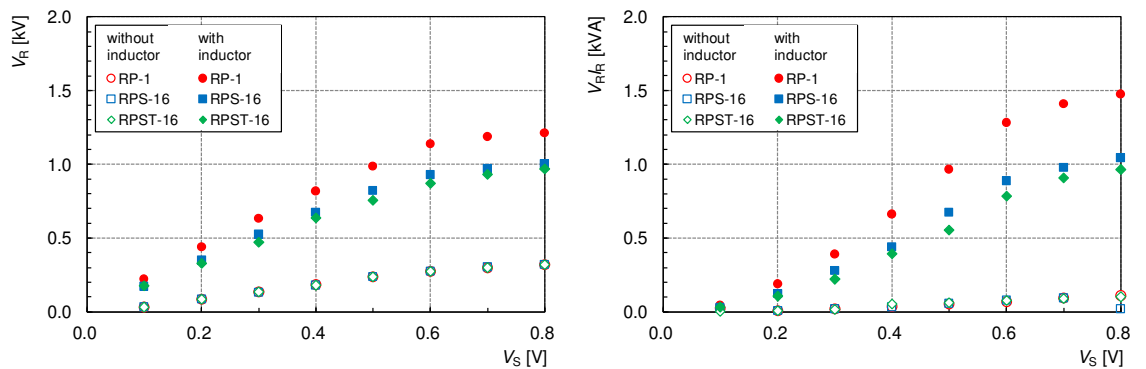


Figure 7.8 Effect of reactance compensation inductors on resonator voltage and power.

7.3 Calorimetric measurement of ultrasonic energy density

Input electrical power into the resonators can be calculated from the voltage, current, and phase angle measurements. However, electrical power does not provide a good indication of the ultrasonic power delivered for zooplankton inactivation since the electroacoustic conversion efficiency varies from device to device. It is more appropriate to compare resonator performance in terms of ultrasonic power density P_{US} (W/cm^3) or ultrasonic intensity I_{US} (W/cm^2) because these parameters relate to the ultrasonic power emitted by the resonators [257–259]. Electrical power input becomes important when evaluating the electro-mechano-acoustical conversion efficiency of the resonator, which is not the focus of the present research.

Ultrasonic energy density delivered to the treatment volume was determined using calorimetric analysis. In this method, the temperature rise of water due to the absorption of the ultrasound waves is used to calculate the ultrasonic power density and ultrasonic intensity:

$$P_{\text{US}} = \frac{mc_p (\Delta T / \Delta t)}{\text{volume}}, \text{ and} \quad (7.5)$$

$$I_{\text{US}} = \frac{mc_p (\Delta T / \Delta t)}{\text{output area}}, \quad (7.6)$$

Where m (kg) is the mass of water, c_p (J/kg.K) is the specific heat of water, ΔT (K or °C) is the temperature rise due to ultrasound exposure, and Δt (s) is the sonication time at 100% duty cycle. Thus, ultrasonic power density is the ultrasonic power dissipated per unit volume of the treatment vessel while the ultrasonic intensity is the ultrasonic power emitted per unit output surface area of the resonator. The specific heat of water in the experimental temperature range of 20–25 °C is taken as 4184 J/kg.K [260].

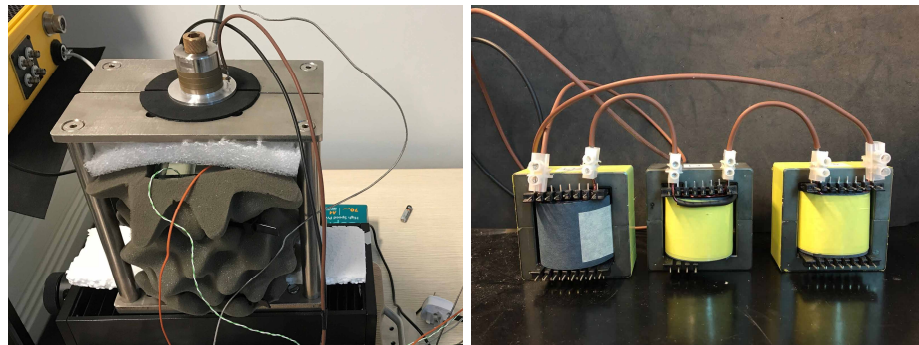


Figure 7.9. Calorimetric test tank with insulation (left); reactance compensation inductors (right).

The calorimetric measurement system comprises a 150 x 80 x 150 mm (length x breadth x height) glass tank covered by a layer of 50 mm thick insulation foam to prevent heat loss. Three thermocouple probes were used for temperature measurement – two probes were placed at different positions inside the tank, and one probe was secured on the external glass surface. A power amplifier drove the resonators through three inductors connected in series to offset the large capacitive reactance of the water-loaded resonators. Figure 7.9 shows the calorimetric measurement of the radial resonator and the three reactance compensation inductors.

A high voltage differential probe (THDP0100, Tektronix), and a current probe (TCP0150A) measures the voltage and current drawn by the resonators, while the voltage and current sensors of the power amplifier monitor the voltage and current into the inductors. The calorimetric experiments were performed in a climatic-controlled laboratory with an ambient temperature of around 22 °C. The overall schematic for the calorimetric experimental set-up is shown Figure 7.10.

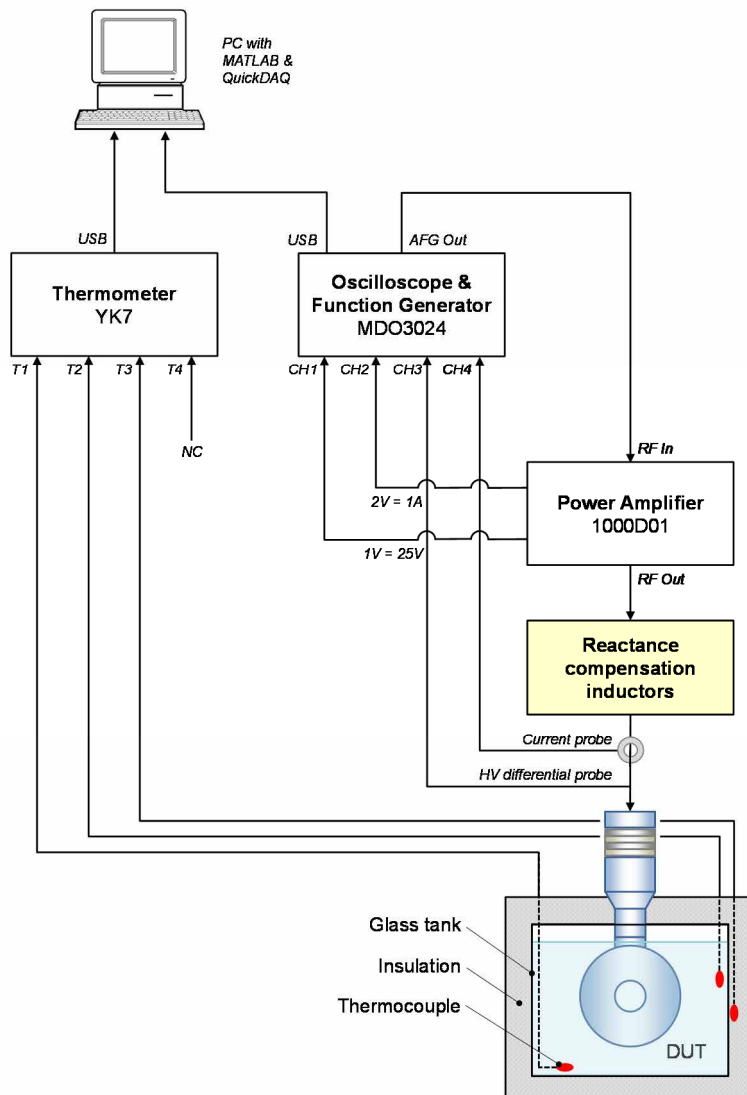


Figure 7.10. Schematic of experimental set-up for calorimetric analysis.

A trial experiment was performed to determine the sonication duration required to increase the temperature of water to a measurable level. During the trial experiment, the in-tank temperature measurements fluctuated considerably during sonication but stabilised when the resonators are switched off. This phenomenon, which affects only the temperature sensors that were exposed to the ultrasound field, is attributed to viscous heating of the sensor and not due to the increase in water temperature [261]. The viscous heating effect is eliminated by measuring and recording the water temperature before sonication and continuing to record the water temperature after sonication. The rise in water temperature due to sonication can then be calculated using the pre-sonication and post-sonication measurements, while the time interval Δt was measured from the time the resonator was first energised to the time it was last switched off in the measurement set.

In this study, one measurement set comprises of temperature measurements recorded at 1 s intervals over a total duration of 840 s. The sonication duration was set to 600 s at 50% duty cycle, while the pre-sonication and post-sonication durations were set to 120 seconds each. Figure 7.11 shows the temperature evolution during a calorimetric experiment performed to determine the ultrasonic power emitted by the resonators. The calorimetric measurements were carried out with pulsing power (1 s on, and 1 s off) to avoid overheating the PZTs which can contribute to experimental uncertainty. Three sets of measurements were recorded for each power setting to ensure repeatability. The ultrasonic power density used in the biological inactivation experiments, which was performed at 100% duty cycle (non-pulsing output), was calculated by multiplying the result of (7.5) by a factor 2.

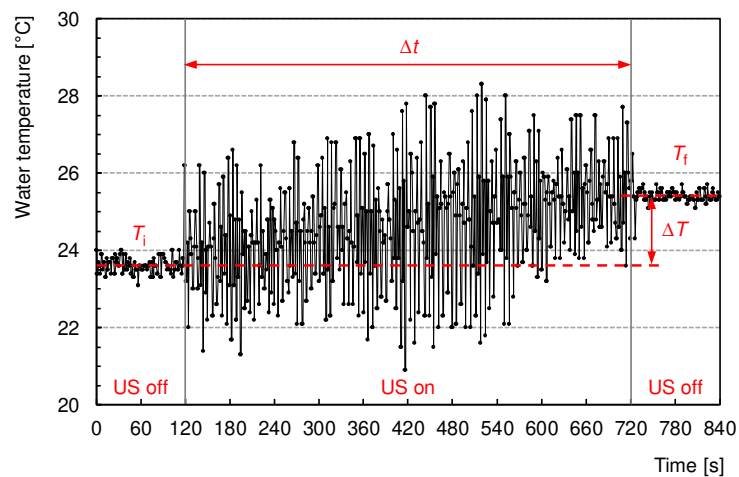


Figure 7.11. Example of calorimetric analysis using actual data from RPS-16.

7.4 Evaluation of US treatment efficacy

The excitation voltages were chosen to achieve a similar ultrasonic power density across the four resonators. In addition, the ultrasonic intensity was calculated by taking a ratio of the ultrasonic power output to the output surface area of the resonator. The output area of the RP-1 was estimated from its external and internal circumference (OD 100 mm, ID 61 mm), and the output area of P25 was calculated using its output diameter of 25 mm. For the multiple-orifice resonators RPS-16 and RPST-16, two estimates of the output surface areas were calculated because it was not yet known if the small orifices were capable of emitting ultrasonic radiation. The low-value output area is the total radiating area provided by the external circumference and the primary orifice circumference, while the high-value includes the total internal surface areas of the orifices. The cavity volume formed by the orifices was also calculated. Table 7.3 provides the output areas and orifice volumes of the resonators. It should be noted that for RP-1 and RPS-16, the central orifice volume refers to the volume enclosed by the primary orifice only. Whereas for RPST-16, the central orifice volume is the sum of volumes bounded by the primary orifice, secondary orifices, and the orifice-links.

Table 7.3 Resonator output area and volume of orifices.

	RP-1	RPS-16	RPST-16	P25
Output area (cm ²)				
Low value	143	134	100	5
High value	143	253	312	5
Orifice volume (cm ³)				
All orifices	88	97	67	-
Excl. outer orifice layer	88	61	48	-

Table 7.4 provides the data obtained from calorimetric experiments. The ultrasonic power density was calculated using (7.5) and sonication tank volume of 1100 cm³. The calculations showed that the ultrasonic power density of the four resonators are similar, and a reasonably fair comparison of the resonator inactivation performance can be made. For completion, the ultrasonic intensity was calculated using (7.6) and the low-value estimates of the output area.

Table 7.4 Calculation of ultrasonic power density from calorimetric measurement data.

Device	T_i (°C)	T_f (°C)	ΔT (°C)	Δt (s)	P_{US} (mW/cm ³)	I_{US} (mW/cm ²)
RP-1	21.73±0.23	23.32±0.38	1.59±0.16	300	22.13	170
RPS-16	22.10±0.01	23.68±0.02	1.58±0.03	300	22.03	181
RPST-16	21.94±0.03	23.67±0.08	1.73±0.11	300	24.19	157
P25	21.03±0.02	22.88±0.08	1.85±0.06	300	25.76	5667

Figure 7.12 shows the percentage of surviving *Artemia* nauplii as a function of cumulative exposures to 20 kHz ultrasound field. Results showed that RP-1 was most effective for nauplii inactivation, achieving more than 90% reduction with two exposures (24 s) at power density of 22 mW/cm³. Meanwhile, RPST-16 produced the lowest inactivation rate, achieving only around 80% reduction with five exposures (60 s) albeit at a slightly higher power density of 24 mW/cm³. RPS-16 and P25 provided similar inactivation rates in the first 12 s of exposure. Beyond the first exposure, RPS-16 became less effective than P25 as indicated by the slope of the inactivation curve. P25 achieved more than 90% reduction in *Artemia* nauplii population after three exposures (36 s) at ultrasonic power density of 26 mW/cm³, while RPS-16 achieved around 84% nauplii reduction in the same period but at a lower power density of 22 mW/cm³.

The percentage of surviving *Artemia* nauplii as a function of cumulative ultrasonic energy density delivered (defined as the product of ultrasonic power density and exposure time) as shown in Figure 7.13 was calculated by taking a product of ultrasonic power density and the exposure time. Although ultrasonic energy density delivered has a direct relationship with sonication time, plotting the nauplii inactivation in terms of ultrasonic energy density demonstrates that inactivation efficacy is not entirely determined by dosage, but also dependent on the design of the resonator. Results showed that RP-1 required only 530 mJ/cm³ to achieve 95% nauplii inactivation, but complete elimination of the nauplii population required 50% more ultrasonic energy density (800 mJ/cm³), which is substantial. Similarly, RPS-16 required an ultrasonic energy density of 1060 mJ/cm³ to achieve 90% nauplii reduction, and more than 1320 mJ/cm³ to achieve 100% inactivation. Meanwhile, RPST-16 achieved only 80% nauplii inactivation with an ultrasonic energy density of 1450 mJ/cm³. Thus, RP-1 provides the highest inactivation rate while RPST-16 was found to be the least effective for power density and exposure times considered.

It was also observed that short ultrasound exposures tend to favour the radial resonators over the probe-type device (P25). As shown in Figure 7.14, the three radial resonators produced higher inactivation rates than P25, indicating the significance of acoustic streaming in the overall treatment efficacy. Longitudinal-mode devices like P25 provides an effective treatment zone that is limited to around 10 to 20 mm from the output face [262]. For such devices, effective treatment requires both high-intensity field generation and efficient mixing to expose entire treatment volume to high-intensity ultrasound field. P25 generates a highly directional acoustic field which can induce a mixing effect that is more effective than the mixing effect produced by the radial resonators [263,264]. Thus, P25 performs better with increasing exposure time compared to the three radial resonators. On the other hand, the radial resonators effected in significantly higher nauplii reductions compared to P25, despite generating significantly lower ultrasonic intensities, indicating the significance of a well-distributed ultrasound field.

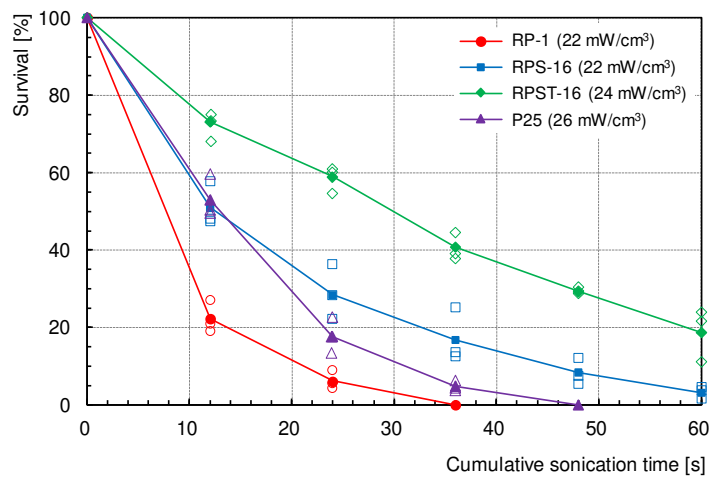


Figure 7.12. Effect of cumulative ultrasound exposure on *Artemia* sp. survival for different resonators; actual survival (open markers); mean survival calculated from 3 samples (closed markers).

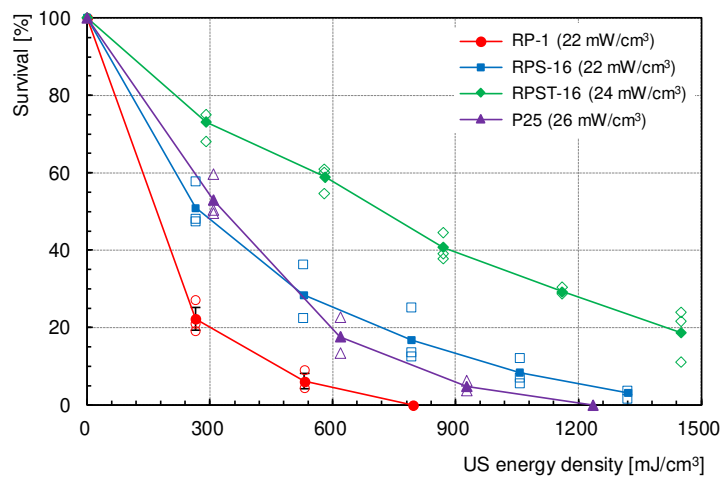


Figure 7.13. Effect of cumulative ultrasound energy density on *Artemia* sp. survival for different resonators; actual survival (open markers); mean survival calculated from 3 samples (closed markers).

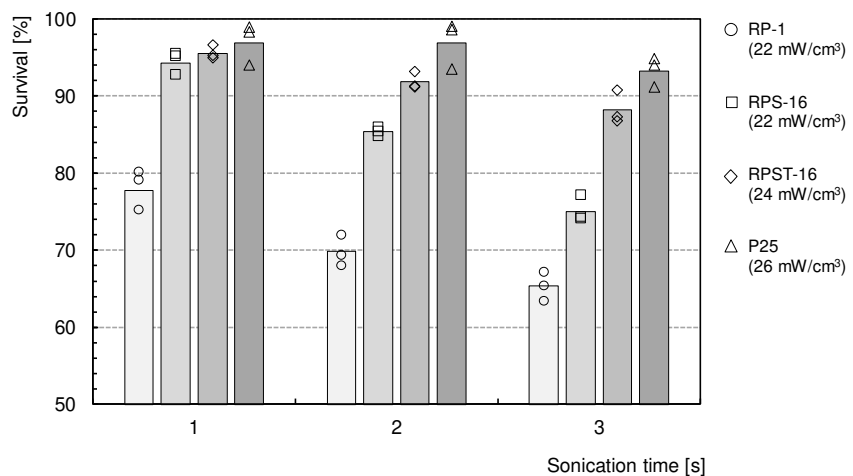


Figure 7.14. Effect of discrete ultrasound exposures on *Artemia* sp. survival for different resonators; actual survival (open markers); mean survival calculated from 3 samples (bars).

It is evident from Figure 7.12 to Figure 7.14 that RP-1 exhibited the most superior inactivation performance compared to the multiple-orifice resonators, for both short and long exposures. This is an unexpected result considering that RP-1 exhibited the highly nonlinear behaviour, low vibrational amplitude, and low mechanical quality factor compared to RPS-16 and RPST-16 when characterised under no-load conditions. This relatively superior acoustic performance may be associated with the overall low impedance and low reactance after inductive compensation (see Table 7.2), leading to the relatively more efficient conversion of electrical energy (see Figure 7.8). Another possibility is that the inactivation efficacy may be associated with the volume of the orifices where high-intensity ultrasound field is expected to concentrate. Based on this reasoning, RPS-16 is expected to produce a higher inactivation rate than RP-1 by virtue of the total orifice volume (see Table 7.3). However, this is not the case. On the other hand, if the outermost orifice layer (for RPS-16, this refers to the secondary orifices; for RPST-16 this refers to the tertiary orifices) was excluded from the calculation, the resulting orifice volumes will then corroborate well with the inactivation results. This suggests that the cavity enclosing the geometric centre of the radial resonator has a significant contribution to the overall treatment effect.

Previous studies on ultrasonic inactivation of *Artemia nauplii* have established that the destructive effect of low-frequency ultrasound is primarily dependent on the applied ultrasonic energy density, rather than the individual effects of intensity and exposure time [29,48,90]. In other words, a particular percentage inactivation would require a specific ultrasonic energy density that can be realised with any combination of power density and exposure time. On the other hand, the present research has shown that inactivation rates are also dependent on the ultrasonic device since their ability to translate the applied ultrasonic energy to the desired destructive effects can vary considerably.

Table 7.5 compares the present work with previous investigations by Holm et al. [48] and Bazyar et al. [90]. For ease of comparison, results from Holm et al. and Bazyar et al. have been converted to the same base units as the present study. The DRED and DRT, which are defined as the energy density and the retention time required to effect in 90% reduction in organism population were adopted from Holm et al. Most of the data in Table 7.5 were extracted from the respective original articles, while the ones marked with an asterisk (*) are estimates based on a combination of data provided by the article and data from the original equipment manufacturer [265].

Holm et al. used a laboratory-scale flow-through reactor consisting of a 12.4 cm³ glass vessel and titanium probe with output diameter of around 1.26 cm. It was found that a 90% inactivation of *Artemia nauplii* requires an energy density of 8000 mJ/cm³, which translates to around 2200 W/(m³/h). This is an enormous amount of energy considering a full-scale ballast water treatment system employing ultrasound as its primary treatment method would require more power than a

typical auxiliary generator (1 MW) can deliver to process ballast water at 500 m³/h. More recently, Bazyar et al. performed a similar inactivation study but this time using an industrial-grade sonoreactor consisting of at least 28 individual longitudinal transducers mounted on a circular pipe. The sonoreactor was configured such that the flow is constrained to a 15 mm channel formed between two concentric pipes, ensuring an even ultrasound exposure. Evidently, this strategy was very successful, enabling 90% nauplii inactivation rate with only one-tenth the energy consumption of Holm et al. The present work using the RP-1 resonator achieved even better results. At a DRED of less than 530 mJ/cm³, the RP-1 device provided at least 30% reduction in energy consumption compared to Bazyar et al. On the other hand, the RPS-16 multiple orifice device required around 35% more energy to achieve the same inactivation rate. Although the inactivation performance of the multiple orifice resonators (RPS-16 and RPST-16) were below expectation under static water conditions, the presence of orifices may be an advantage under flow conditions due to the combined effects of ultrasonic and hydrodynamic cavitation [64,266–268].

Table 7.5 Comparison of ultrasonic inactivation performance with previous studies [48,90].

	Holm et. al., 2008	Bazyar et al., 2013	Present study
Target organism	<i>Artemia</i> nauplii	<i>Artemia</i> nauplii	<i>Artemia</i> nauplii
Configuration	Flow-through	Flow through	Static tank
Resonator mode	Longitudinal	Longitudinal	Radial
No. of resonators	1	28–32*	1
Frequency (kHz)	19	25	20
Vessel volume (cm ³)	12.4	2900	1100
Flow rates (cm ³ /s)	3, 14, 23	181–1450*	-
Intensity (mW/cm ²)	19700	222–2030*	170, 194
Power density (mW/cm ³)	2000	48–384	22
DRED (mJ/cm ³)	8000	786	<530 (RP-1), 1060 (RPS-16)
DRT (s)	4	2–16	<24 (RP-1), <48 (RPS-16)
Specific consumption (W/(m ³ /h))	2200	220	150 (RP-1), 290 (RPS-16)

Compared to previous works, the present study was performed at power densities that are 10 to 100 times lower. It can be appreciated that the operating capacity of the radial resonators were not fully utilised in the experiments, and there is ample room to increase the ultrasonic power density further. Figure 7.15 demonstrates the effect an increase in the power density has on the survival *Artemia* nauplii. It was shown that an 18% increase in ultrasonic power density reduced nauplii survival by 5–7.5% for exposure durations of 1–3 s. Here, the RPS-16 resonator was used as an example, and a similar effect can be anticipated with either RP-1 or RPST-16 resonators. Thus, there is a potential to reduce the treatment time or DRT to a length that befits a flow-through

treatment configuration. In addition, the radial resonators of the current work offer a real potential for capital cost reduction through the use of fewer resonators and associated equipment to achieve the desired inactivation rate and DRED.

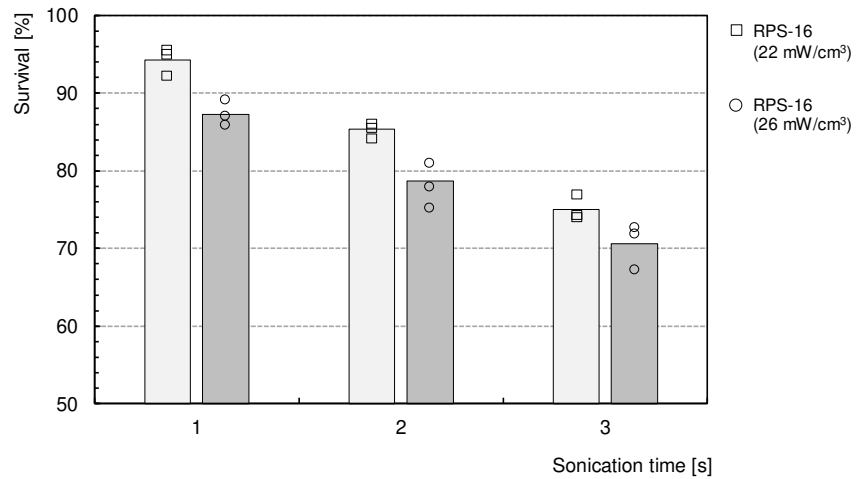


Figure 7.15. Effect of ultrasonic power density on *Artemia* sp. survival; actual survival (open markers); mean survival calculate from 3 samples (bars).

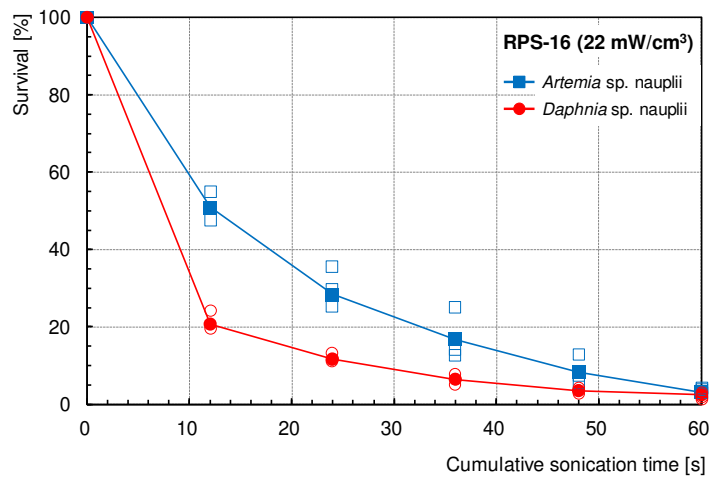


Figure 7.16. Comparison of *Artemia* sp. and *Daphnia* sp. survival with ultrasound exposure; actual survival (open markers); mean survival calculated from 3 samples (closed markers).

Inactivation experiments were also performed on *Daphnia* sp. to investigate the effect of organism sensitivity on inactivation efficacy. As shown in Figure 7.16, *Daphnia* sp. was more vulnerable to ultrasound exposure than *Artemia* nauplii. Using RPS-16 as the source of ultrasound field, the DRED for *Daphnia* sp. was estimated to be around 500–530 mJ/cm³ while the DRT was around 22–24 s. Thus the energy required to reduce the *Daphnia* sp. population by 90% is half of that required to reduce the *Artemia* nauplii population by the same amount. The results showed that low-frequency ultrasound is effective against the two eukaryotic model organisms, but the

treatment efficacy can differ considerably between species [90]. The treatment effect is also influenced by the sonication frequency and the size of the organism. Lurling and Tolman [269] observed that 44 kHz ultrasound exerted a stronger effect on *Daphnia* sp. than 20 kHz, but both frequencies are considered lethal with prolonged exposures. The correlation between treatment efficacy and exposure time may be associated with a more uniform ultrasound exposure due to mixing. Further, it has been established that prolonged ultrasonic exposure favours free radical generation which can contribute to the degradation of biological cells, regardless of ultrasound intensity [257].

The images of the test organisms before and after sonication were captured using a microscope (BX51, Olympus) at 5x and 10x magnification, without any fixation or staining medium. Figure 7.17 shows the dorsal view of a live nauplii of *Artemia* sp. before ultrasound exposure and the lateral view after ultrasound exposure. Similarly, Figure 7.18 shows the dorsal view of a live *Daphnia* sp. before ultrasound exposure and the lateral view after ultrasound exposure. The live specimens were motile and relatively more difficult to photograph, but most of the body parts of the respective specimens were discernible. The body length of 700–800 μm and the identified parts of the micrographed *Artemia* sp. indicate Metanauplius II stage. The head, antenna, antennula, exopodite, and thoracic segments [270] were clearly seen in the motile specimen. The same body parts were less visible in the post-sonication micrograph, but the general shape and principal features of the species were largely conserved. However, compared to the live specimen, the dead specimen appear more transparent and its interior seemed completely obliterated, leaving only the shell relatively intact. Meanwhile, comparing the micrograph of the live *Daphnia* sp. with the morphological landmarks described in Mittmann et al. [271] suggests an adult male cladoceran due to its relatively small size and the absence of cysts in its thoracic segment. Compared to *Artemia* sp. the anatomy of *Daphnia* was more visible due to its clear carapace, showing most of the internal organs at work, including the heart. The post-sonication image of the *Daphnia* sp. specimen showed the absence of antenna and other appendages that were visible in the live specimen, and an almost empty carapace. The post-sonication micrographs of *Artemia* sp. and *Daphnia* sp. suggest that ultrasound was not only capable of maiming the organism externally, but was also able to penetrate the shell of the specimens and inactivate them from within by destroying their internal organs.



Figure 7.17. Micrograph of *Artemia* sp. nauplii before (left) and after (right) sonication.

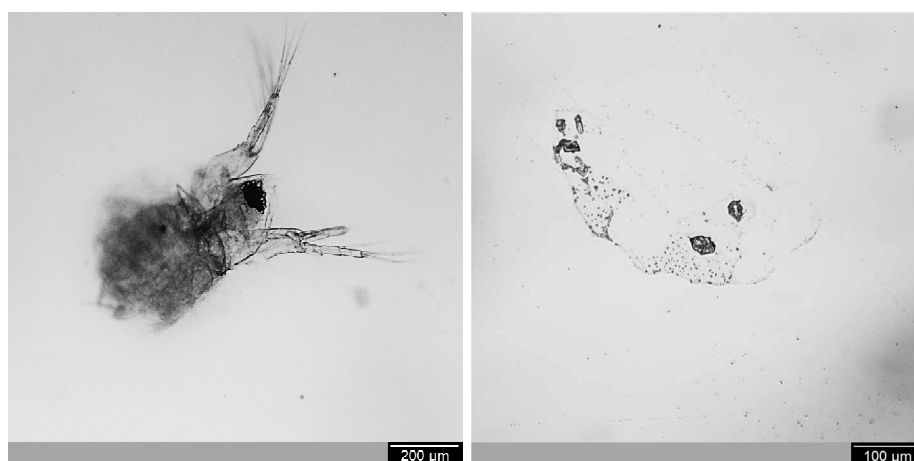


Figure 7.18. Micrograph of *Daphnia* sp. before (left) and after (right) sonication.

7.5 Flow-through reactor scale-up design

From the outset, the radial resonators were designed for application in a cylindrical reactor. The annular-shape of the radiator section enable the devices to be aligned concentrically with the reactor, so that ultrasound field exposure is relatively uniform in the angular direction. Figure 7.19 shows the simulated acoustic field generated by the radial resonators in a rectangular tank similar to the one used in the inactivation experiments. As shown, that the simulated ultrasound pressure distributions are highly axisymmetric around the primary orifice origins and decay with increasing distance from radiating surfaces. Such symmetry was also observed in the Sonochemiluminescence (SCL) experiments performed by Hunter [40], making a case for the use of a cylindrical reactor having the emitter section concentrically positioned within, as opposed to a rectangular reactor in which the weak acoustic reception zones in the corners are unavoidable.

For flow-through applications such as in-line ballast water treatment, a cylindrical reactor can be designed with flanges and resonator insertion points with relative ease. Standard pipes are readily available and with careful selection of fittings, an ultrasonic reactor can be assembled at relatively low cost. From the academic perspective, it is of interest to determine the optimum gap between the external circumference of the emitter and the internal surface of the reactor. In reality, practical considerations such as material availability, cost of fabrication, and operation and maintenance access can have far greater weightage than a highly-customised optimal design.

Figure 7.20 exemplifies an ultrasonic reactor design that incorporates the practical considerations mentioned earlier. In this prototype, a 150 nb (nominal bore), schedule 40 stainless steel pipe constructed to ANSI/ASTM B36.10M [272] was selected for the reactor body. This pipe provides a clearance of around 27 mm around the emitter, enabling manual installation and removal of the radiator from pipe body to be carried out with relative ease. More clearance can be achieved by using a pipe one size larger (200 nb, schedule 40) but the treatment impact of the weaker acoustic field further away from the emitter will have to be evaluated carefully.

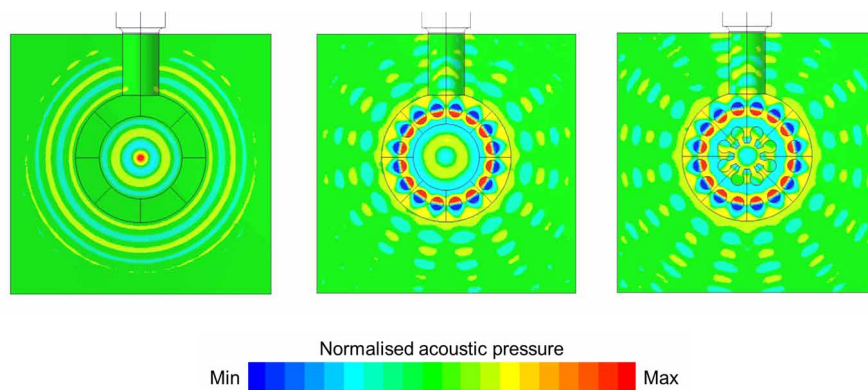


Figure 7.19. Simulated acoustic pressure contours; RP-1 (left); RPS-16 (middle); RPST-16 (right).

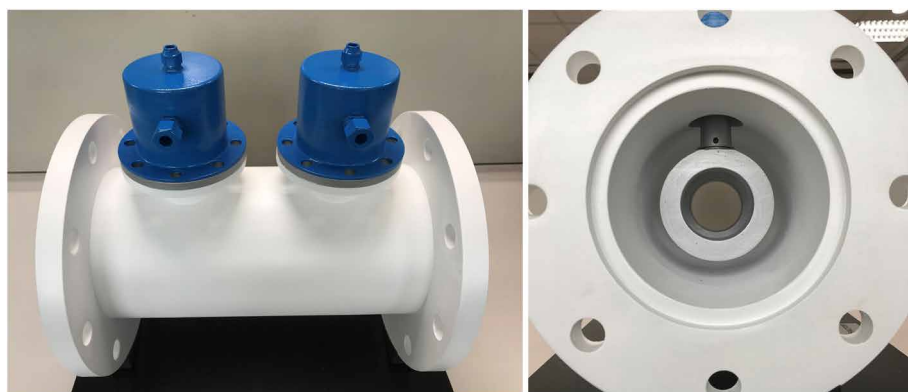


Figure 7.20. Flow-through reactor with two radial resonators; side view (left); flange view (right).

It should also be recognised that the multiple orifice resonator can behave as a flow constrictor which has the ability to generate microbubbles through hydrodynamic cavitation. Although the extent with which cavitation bubble are generated hydrodynamically is dependent on the liquid pressure, flow rate, and the configuration of the resonator, the combination of ultrasonic cavitation (UC) and hydrodynamic cavitation (HC) complex inactivation mechanisms that has been shown to be more potent than the individual effects of UC and HC [267,273]. Thus, it is necessary to perform biosimetric studies to determine the treatment efficacy of the reactor under different operating conditions to determine the operating range of the reactor. Once the characteristics of the ultrasonic reactor system has been comprehensively understood, scale-up design to meet the required flows and inactivation rates can then be carried out by arranging the multiple units of the reactor in series or parallel as shown in Figure 7.21.

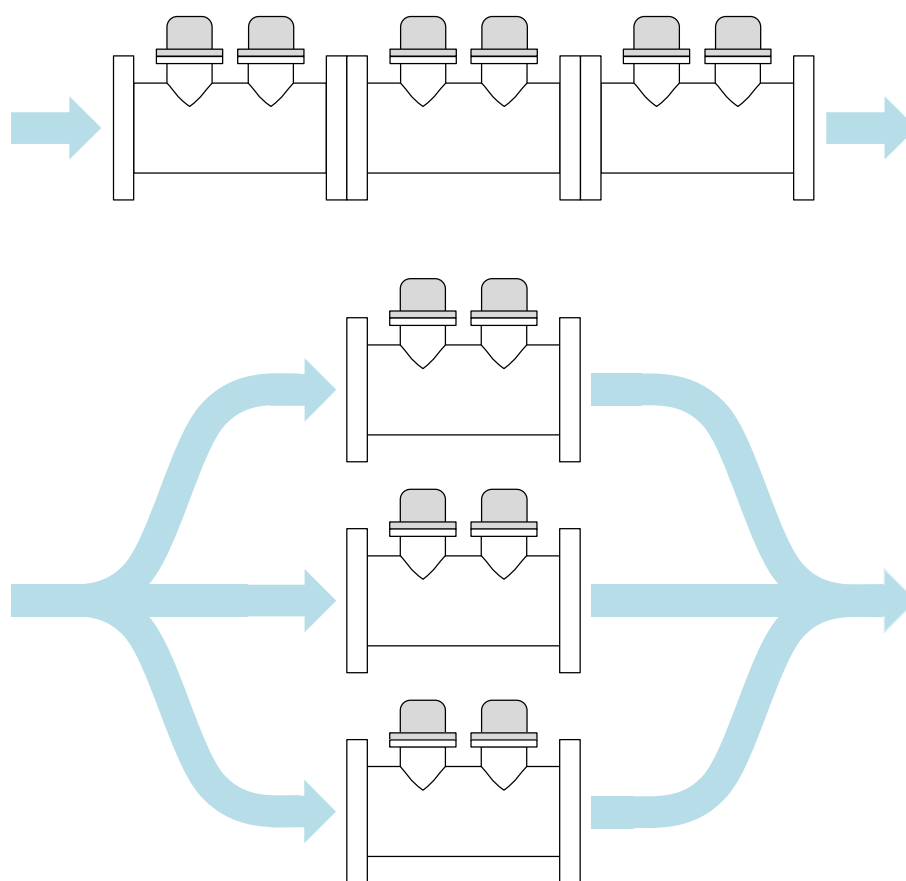


Figure 7.21. Serial (top) and parallel (bottom) arrangement of the flow-through US reactor.

7.6 Conclusion

Analysis of the water-loaded impedance and phase response of the resonators revealed a significant increase in impedance magnitude from their unloaded values. The high impedance inhibited the power transfer between the driving circuit and the resonators, and increases the risk of power amplifier damage due to the large voltage standing wave ratio (VSWR). Moreover, the phase angle of the resonators were negative and close to 90° , indicating sizeable capacitive reactance. A simple solution using three serial inductors was implemented to compensate the capacitive reactance, resulting in considerable improvement in power reception of the resonators.

The zooplankton inactivation performance of the radial resonators was compared with a commercial longitudinal mode device in terms of the DRED and DRT. Ultrasonic power density and intensity were determined from calorimetric experiments, and the corresponding DRED values were calculated. Results showed that the biological inactivation efficacy provided by the radial resonators were similar to or better than the commercial longitudinal device. In addition, the DRED achieved with a single radial resonator was comparable or better than a commercial ultrasonic treatment system comprising of 28–32 transducers [261].

In conclusion, the radial resonators exhibited very promising electrical, mechanical, and acoustical characteristics that offer real prospect for further development into an effective, cost-efficient, and scalable system. If successfully developed, such system can be a viable alternative solution for ballast water treatment.

Chapter 8

Conclusions

8.1 Summary and main contributions

Invasive marine organisms are detrimental to the marine ecosystem, causing disruption to fisheries, destroying assets, and poses a risk to human health. This threat has led to a worldwide initiative to limit the exportation of invasive marine organisms through mandatory treatment of ballast water to ensure that the concentrations of indicator organisms meet the discharge requirements. Numerous studies have demonstrated the ability of ultrasound to eliminate bacteria, phytoplankton, and zooplankton in marine water, but the industrial-scale implementation of the technology is severely lacking. This lack of implementation may be attributed to the high power consumption of ultrasonic treatment systems, and the fact that application of ultrasound in large-scale water treatment processes is relatively new. Further, earlier investigations suggested that the capital and running cost of ultrasonic ballast water treatment system would be too prohibitive [29,48], and not competitive with more conventional treatment methods such as UV irradiation and electrochemical treatment. Unfortunately, many of these earlier investigations were carried out at unrealistic flow-rates and utilised conventional ultrasound equipment that were not purposefully designed for water treatment despite their known inherent limitations.

The present research recognises the limitations of the current technology and attempts to overcome the technological barrier by addressing specific design aspects of the ultrasonic resonators. The objective is to derive one or more resonator configurations that can generate intense and well-distributed ultrasound field with relatively low energy consumption. Toward this end, a new type of resonator based on the fundamental radial horn design was developed using finite element (FE) modelling. Particular attention was given to the identification of vibrational modes, and how the resonance frequency, response amplitude, response bandwidth, and modal separation varies with geometric modification. Unlike previous radial horns, the new radial resonators integrated active piezoelectric elements into the assembly which amalgamated a longitudinal-mode and a radial-mode sections. The present work also set a precedent for the incorporation of orifices in the radial resonator design. Such design feature was shown to overcome the output area limitation of conventional devices, and present a real opportunity to achieve high biological inactivation rates with considerably

fewer devices and lower energy consumption. The RP-1, RPS-16, and RPST-16 configurations exhibited the most desirable characteristics in terms of modal separation, vibrational uniformity, and stresses, and were selected for fabrication and experimental evaluation.

Experimental modal analysis (EMA) was performed using a Laser Doppler Vibrometer (LDV) to validate the FE model predictions and to estimate the modal parameters of the fabricated resonators. Results showed excellent correlation between the FE model and the measured resonance frequencies of the tuned mode and the modes immediately adjacent to the tuned mode. Further away from the design frequency, the FE predictions increasingly deviated from the measurement. Impedance analyser (IA) measurements were carried out to determine the resonance and anti-resonance frequencies, and the corresponding impedance magnitudes at these two operating regimes. The electrical resonance frequencies measured by the impedance analyser corroborated with both EMA and FE results, demonstrating the close analogy between the electrical characteristics of a piezoelectric resonator and its dynamic behaviour. Further, the four-component equivalent circuit representation of the resonators was also in excellent agreement with the IA measurements, providing additional insight into the electromechanical characteristics of the resonators. Based on the equivalent circuit parameters, the quality factor and coupling coefficient of the resonators were calculated. Results showed that the radial resonators exhibited significantly high mechanical quality factors compared to a commercial probe-type device, but lower coupling coefficients. A substitution of the alloy steel preload bolt with a beryllium copper version improved the coupling coefficient by approximately 13%, indicating the opportunity to improve the electromechanical characteristics of the resonators using alternative materials.

Harmonic response characterisation of three radial resonators and a commercial high-gain probe was carried out using non-contact measurement technique (LDV) and a driving circuit comprising a signal generator and a power amplifier. Measurements showed that the radial resonators generated lower vibrational amplitudes and amplification factors compared to the commercial device, indicating the distribution of the stress-wave energy over larger radiating surface areas. However, the radial resonators provide radiating surface areas that are at least 20 times that of the commercial device. Despite the lower vibrational amplitudes, the ability to distribute and radiate more acoustic energy over a larger surface area is an advantage. A sine sweep excitation voltage was used to characterise the nonlinear behaviour of the resonators at different levels of excitation. Results showed that the vibrational response of the resonators were mostly in the linear regime at low excitation voltages, and slight shifts in frequencies were observed as the voltage increased. The Duffing-like nonlinear softening behaviour was most pronounced for RP-1, and the use of a low-stiffness preload bolt was shown to exacerbate this behaviour. Meanwhile, the RPS-16 and RPST-16 resonators were relatively more “stiff” compared to RP-1 and P25 for the range of voltages investigated. Replacement of the

alloy steel bolt (A574) with a lower-stiffness beryllium copper bolt (C17200), increased the coupling coefficient but reduced the mechanical quality factor of the radial resonators. Nonetheless, the use of the C17200 bolt resulted in the overall enhancement of the electromechanical figure of merit to a level that is comparable to the commercial high-gain probe. A new quantitative measure of Duffing-like nonlinear softening behaviour was also introduced. This method, which is an adaptation of the statistical ‘skewness’ coefficient, was successfully utilised to quantify the relative nonlinear behaviour of the resonators.

Finally, the water-loaded characteristics of the radial resonators and their ability to generate biologically destructive ultrasound field in water were investigated. Impedance analyser (IA) measurements of the water-loaded resonators showed large capacitive reactance and high impedance magnitude. The high impedance inhibited the power transfer between the driving circuit and the resonators, but this was mitigated by connecting three inductors in series with the resonator to improve the power reception of the resonators significantly. The inactivation experiments were carried out using the modified driving circuit, and model zooplankton species were used to benchmark the inactivation performance of the radial resonators. Calorimetric analysis was performed to determine the acoustic energy radiated into the fluid and the DRED was calculated for each ultrasound exposure. Results showed that zooplankton inactivation efficacy achieved with the radial resonators was similar to or better than the commercial longitudinal device. Further, the DRED achieved with a single radial resonator was comparable to or better than the commercial ultrasonic treatment system that uses dozens of transducers [261]. Microscopic images of the model zooplankton specimens before and after ultrasound exposure showed physical and physiological damage to the organisms. Based on the current study, the promising electrical, mechanical, and acoustical characteristics of the radial resonators present an excellent opportunity for further development towards an efficient and cost-effective industrial-scale ballast water treatment system.

8.2 Recommendations for future work

In the present work, a new type of radial resonator have been developed and its ability to inactivate model zooplankton species was shown to be a significant improvement from previous work. Further improvement may be realised by exploring various methods to enhance the electromechanical coupling coefficient and the mechanical quality factor of the resonators. Possibilities include utilising alternative PZT materials, utilising larger diameter PZT rings, exploring alternative bolt materials that have a high strength-to-stiffness ratio, and performing geometric modifications to the radial resonator design to reduce its overall stiffness.

It is typical to characterise piezoelectric transducers based on its electromechanical behaviour in unloaded conditions (i.e. in air), even for devices that are intended for application in water or other dense and viscous mediums. When driving such transducers, it is imperative that losses are kept to the minimum by driving the transducers at resonance while ensuring a well-matched driving circuit. Such circuit will deliver the maximum power to the transducer and enable the system to operate at maximum efficiency. Viscous damping and radiation resistance can have a negative impact on the electromechanical characteristics of the resonators, and can lead to poor loaded performance. Further, ceramic-based transducers are known to exhibit highly nonlinear behaviour at high driving amplitudes. This presents a serious limitation in high-power applications [274]. Thus, emphasis must be given to the design of the ultrasonic driving circuit to ensure optimum performance in a dynamic loading environment.

Bacteria and phytoplankton are known to be more resilient to low-frequency ultrasound than zooplankton, requiring at least 1 and two orders of magnitude more ultrasonic energy respectively, to reduce to acceptable levels using conventional ultrasonic device [48]. While the present research has shown a significant reduction in power requirements for inactivation of *Artemia* sp. nauplii and *Daphnia* sp., it would be worthwhile to investigate the efficacy of the radial resonators in the inactivation or growth inhibition of indicator bacteria and phytoplankton species such as *E. coli*, *V. cholera*, *Tetraselmis*, and, *Odontella*. One can also consider operating the radial resonators at different higher-order harmonics to specifically target the bacteria [67,104,105] and phytoplankton [52,99]. Once the appropriate frequencies have been established, a reactor comprising of multiple radial resonators operating at different frequencies can be developed, and the multi-frequency system can be tested with simulated ballast water containing a mix of bacteria, phytoplankton, and zooplankton species to establish its efficacy.

Ultrasonic cavitation is a complex physical phenomenon influenced by many factors, including the static pressure and temperature of the medium [275], sonication frequency and intensity [72,276], constituent of dissolved gases [44], surface tension and viscosity of the medium [277], and so on. Formation of cavitation bubble clouds by ultrasound irradiation can be an energy intensive process due to the high negative pressures required for bubble inception, growth, and implosion. At atmospheric pressure, the threshold for cavitation varies from -0.1 MPa in distilled water saturated with air, to -1.5 to -2 MPa for distilled water degassed at 0.02% saturation [278]. Microbubble injection can reduce the cavitation threshold considerably, and intensifies ultrasonic cavitation via a lower energy pathway [279]. It is suggested to incorporate microbubble injection in the ultrasonic treatment system of the present work and investigate the effect of injector parameters (gas constituents, bubble size distribution, flow rate, etc.) on treatment efficacy of the system.

Hydrodynamic cavitation (HC) has been shown to generate a higher density of cavitation bubbles compared to ultrasonic cavitation (UC), for the same power input [132,280,281]. However, HC produces cavitation bubble that has weaker implosion effects compared to UC. The simultaneous effects of HC and UC in a hybrid cavitation system have been shown to improve inactivation efficacy, reduce energy consumption, and reduce cost significantly [267,273]. The multiple-orifice radial resonators (RPS- and RPST-types) of the present research were designed for application in a flow-through cylindrical reactor. In a passive flow-through operation, the presence of the radial resonators provides the constriction necessary for hydrodynamic cavitation [282]. The hybrid operation is put into effect by energising the resonators to generate cavitation bubbles both acoustically and hydrodynamically. Past research have positively demonstrated the application of hybrid cavitation in water treatment, and it will be worthwhile to investigate how the use of the multiple orifice radial resonators can further enhance the treatment effect.

Research have also shown that the deagglomeration of suspended particles by low-frequency ultrasound can significantly improve UV treatment efficiency in turbid waters [90]. Further pre-treatment through ultrasound exposure can have a positive impact on the overall treatment performance by declumping and exposing the pathogens to UV radiation and cavitation field [89,90,95,96]. Further, researchers have established that a synergy between US and UV irradiation can produce a robust treatment system that overcomes the limitations of the individual technologies [24,29,48,283]. Thus, it may also be worthwhile to investigate if the use of the radial resonator can further enhance the treatment efficacy of a US-assisted UV treatment system.

References

- [1] A. Taylor, G. Rigby, S. Gollasch, M. Voigt, G. Hallegraeff, T. McCollin, A. Jelmert, Preventive treatment and control techniques for ballast water, in: *Invasive Aquatic Species of Europe Distribution, Impacts and Management*, Springer Netherlands, Dordrecht, 2002: pp. 484–507.
- [2] J.T. Cariton, J.B. Geller, Ecological roulette: the global transport of nonindigenous marine organisms, *Science*. 261 (1993) 78–82.
- [3] J.D. Rothlisberger, D.C. Finnoff, R.M. Cooke, D.M. Lodge, Ship-borne nonindigenous species diminish Great Lakes ecosystem services, *Ecosystems*. 15 (2012) 1–15.
- [4] S. Gollasch, *Is ballast water a major dispersal mechanism for marine organisms?*, Springer Berlin Heidelberg, Berlin, Heidelberg, 2007.
- [5] International Maritime Organisation, *International Convention for the Control and Management of Ship's Ballast Water and Sediments (BWM)*, (2004).
- [6] Riviera Maritime Media Ltd, *Ballast water treatment systems directory*, *Ballast Water Treatment Technology*. (2016) 67–72.
- [7] Americal Bureau of Shipping, *Guide for ballast water treatment*, 2016.
- [8] R. Balaji, O.B. Yaakob, Emerging ballast water treatment technologies: a review, *Journal of Sustainability Science and Management*. 6 (2011) 126–138.
- [9] I. Min, H. Hwang, D. Moon, J. Lee, Implementation of ballast water treatment system using electrolysis, in: *2013 13th International Conference on Control, Automation and Systems (ICCAS 2013)*, IEEE, 2013: pp. 1421–1424.
- [10] B. Werschkun, S. Banerji, O.C. Basurko, M. David, F. Fuhr, S. Gollasch, T. Grummt, M. Haarich, A.N. Jha, S. Kacan, A. Kehrer, J. Linders, E. Mesbahi, D. Pughiuc, S.D. Richardson, B. Schwarz-Schulz, A. Shah, N. Theobald, U. von Gunten, S. Wieck, T. Höfer, Emerging risks from ballast water treatment: the run-up to the international ballast water management convention, *Chemosphere*. 112 (2014) 256–266.
- [11] ClassNK, *Latest information of approval of ballast water management system*, 2016.
- [12] R.C. Smith, J.J. Cullen, Effects of UV radiation on phytoplankton, *Reviews of Geophysics*. 33 (1995) 1211–1223.
- [13] O. Casas-Monroy, R.D. Linley, P.-S. Chan, J. Kydd, J. Vanden Byllaardt, S. Bailey, Evaluating efficacy of filtration+UV-C radiation for ballast water treatment at different temperatures, *Journal of Sea Research*. (2017).
- [14] L. Liu, X. Chu, P. Chen, Y. Xiao, J. Hu, Effects of water quality on inactivation and repair of *Microcystis viridis* and *Tetraselmis suecica* following medium-pressure UV irradiation, *Chemosphere*. 163 (2016) 209–216.
- [15] DNV GL, *USCG makes decision on use of MPN method for ballast water management systems*, (2015). <https://www.dnvgl.com/news/uscg-makes-decision-on-use-of-mpn-method-for-ballast-water-management-systems-52160>.
- [16] N. Narkis, R. Armon, R. Offer, F. Orshansky, E. Friedland, Effect of suspended solids on wastewater disinfection efficiency by chlorine dioxide, *Water Research*. 29 (1995) 227–236.
- [17] J.L. Darby, K.E. Snider, G. Tchobanoglous, Ultraviolet disinfection for wastewater reclamation and reuse subject to restrictive standards, *Water Environment Research*. 65 (1993) 169–180.
- [18] National Research Council, *Stemming the Tide*, National Academies Press, Washington,

- D.C., 1996.
- [19] T.L. Maddox, On-board water treatment and management process and apparatus, 7595003, 2009.
- [20] L. Wang, Z.H. Oh, Ballast water treatment system, 9181109, 2015.
- [21] GEA Westfalia Separator Group GmbH, GEA BallastMaster, (2015).
- [22] M.-Y. Wu, J.-R. Wu, Apparatus and method for ultrasound treatment for ballast water management, 20120061329, 2012.
- [23] P.K. Stumpf, D.E. Green, J.F.W. Smith, Ultrasonic disintegration as method of extracting bacterial enzymes, *Journal of Bacteriology*. 51 (1946) 487–493.
- [24] R. a Brizzolara, E.R. Holm, D.M. Stamper, Disinfection of water by ultrasound: application to ballast water treatment, Technical Report. NSWCCD-61- (2006) 1–42.
- [25] D.L. Bradley, W.D. Wilson, Acoustic Impedance of Sea Water as a Function of Temperature, Pressure and Salinity (No. NOLTR-66-146), NAVAL ORDNANCE LAB WHITE OAK MD. (1966).
- [26] M.R. Gavand, J.B. McClintock, C.D. Amsler, R.W. Peters, R.A. Angus, Effects of sonication and advanced chemical oxidants on the unicellular green alga *Dunaliella tertiolecta* and cysts, larvae and adults of the brine shrimp *Artemia salina*: A prospective treatment to eradicate invasive organisms from ballast water, *Marine Pollution Bulletin*. 54 (2007) 1777–1788.
- [27] G. Hunter, M. Lucas, I. Watson, R. Parton, A radial mode ultrasonic horn for the inactivation of *Escherichia coli* K12, *Ultrasonics Sonochemistry*. 15 (2008) 101–109.
- [28] A.F. Collings, P.B. Gwan, M.T. Binet, J.L. Stauber, Treatment of ballast water by high power ultrasonics, *Proceedings of the 19th International Congress on Acoustics, Revista de Acustica*. 38 (2007).
- [29] D.M. Stamper, E.R. Holm, R.A. Brizzolara, Exposure times and energy densities for ultrasonic disinfection of *Escherichia coli*, *Pseudomonas aeruginosa*, *Enterococcus avium*, and sewage, *Journal of Environmental Engineering and Science*. 7 (2008) 139–146.
- [30] S. Müller, M. Fischper, S. Mottyll, R. Skoda, J. Hussong, Analysis of the cavitating flow induced by an ultrasonic horn – Experimental investigation on the influence of actuation phase, amplitude and geometrical boundary conditions, *EPJ Web of Conferences*. 67 (2014) 02079.
- [31] I. Tzanakis, G.S.B. Lebon, D.G. Eskin, K.A. Pericleous, Characterizing the cavitation development and acoustic spectrum in various liquids, *Ultrasonics Sonochemistry*. 34 (2017) 651–662.
- [32] T.. Leighton, Bubble population phenomena in acoustic cavitation, *Ultrasonics Sonochemistry*. 2 (1995) S123–S136.
- [33] P. Rajasekhar, L. Fan, T. Nguyen, F. a. Roddick, A review of the use of sonication to control cyanobacterial blooms, *Water Research*. 46 (2012) 4319–4329.
- [34] P.R. Gogate, V.S. Sutkar, A.B. Pandit, Sonochemical reactors: Important design and scale up considerations with a special emphasis on heterogeneous systems, *Chemical Engineering Journal*. 166 (2011) 1066–1082.
- [35] H. Osman, F. Lim, M. Lucas, Parametric study of multiple orifice ultrasonic resonators, in: 46th Annual Symposium of the Ultrasonic Industry Association (UIA46), Dresden, Germany, 2017.
- [36] Z. Wei, J. a. Kosterman, R. Xiao, G.-Y. Pee, M. Cai, L.K. Weavers, Designing and characterizing a multi-stepped ultrasonic horn for enhanced sonochemical performance, *Ultrasonics Sonochemistry*. 27 (2015) 325–333.
- [37] S. Lin, T. Hua, J. Hu, W. Hu, Z. Fu, L. Xu, High power ultrasonic radiator in liquid, *Acta Acustica United with Acustica*. 97 (2011) 544–552.
- [38] L. Xu, S. Lin, W. Hu, Optimization design of high power ultrasonic circular ring radiator in coupled vibration, *Ultrasonics*. 51 (2011) 815–823.
- [39] D. Ensminger, L.J. Bond, Fundamental equations employed in ultrasonic design and applications, in: *Ultrasonics Fundamentals, Technologies, and Applications*, 3rd editio, CRC

- Press, Boca Raton, Florida, 2012: pp. 101–140.
- [40] G. Hunter, Bacterial inactivation using radial mode ultrasonic devices, University of Glasgow, 2008.
- [41] B. Niemczewski, A comparison of ultrasonic cavitation intensity in liquids, *Ultrasonics*. 18 (1980) 107–110.
- [42] S. Ceccio, S. Gowing, Y.T. Shen, The effects of salt water on bubble cavitation, *Journal of Fluids Engineering*. 119 (1997) 155.
- [43] B.M. Borkent, M. Arora, C.-D. Ohl, Reproducible cavitation activity in water-particle suspensions., *The Journal of the Acoustical Society of America*. 121 (2007) 1406–1412.
- [44] B.K. Kang, M.S. Kim, J.G. Park, Effect of dissolved gases in water on acoustic cavitation and bubble growth rate in 0.83 MHz megasonic of interest to wafer cleaning, *Ultrasonics Sonochemistry*. 21 (2014) 1496–1503.
- [45] P. Dupont, Cavitating flow calculations in industry, *International Journal of Rotating Machinery*. 9 (2003) 163–170.
- [46] M. Gholami, R. Mirzaie, R. Mohammadi, Z. Zarghampour, A. Afshari, Destruction of *Escherichia coli* and *Enterococcus faecalis* using Low Frequency Ultrasound Technology: A Response Surface Methodology, *Health Scope*. 3 (2014) 1–9.
- [47] E.M. Joyce, X. Wu, T.J. Mason, Effect of ultrasonic frequency and power on algae suspensions, *Journal of Environmental Science and Health, Part A*. 45 (2010) 863–866.
- [48] E.R. Holm, D.M. Stamper, R. a. Brizzolara, L. Barnes, N. Deamer, J.M. Burkholder, Sonication of bacteria, phytoplankton and zooplankton: Application to treatment of ballast water, *Marine Pollution Bulletin*. 56 (2008) 1201–1208.
- [49] V. Naddeo, A. Cesaro, D. Mantzavinou, D. Fatta-Kassinos, V. Belgiorno, Water and wastewater disinfection by ultrasound irradiation - a critical review, *Global NEST Journal*. 16 (2014) 561–577.
- [50] T.J. Mason, *Sonochemistry*, Oxford University Press, 1999.
- [51] G. Zhang, P. Zhang, B. Wang, H. LIU, Ultrasonic frequency effects on the removal of *Microcystis aeruginosa*, *Ultrasonics Sonochemistry*. 13 (2006) 446–450.
- [52] J.W. Tang, Q.Y. Wu, H.W. Hao, Y. Chen, M. Wu, Effect of 1.7 MHz ultrasound on a gas-vacuolate cyanobacterium and a gas-vacuole negative cyanobacterium, *Colloids and Surfaces B: Biointerfaces*. 36 (2004) 115–121.
- [53] X. Wu, E.M. Joyce, T.J. Mason, The effects of ultrasound on cyanobacteria, *Harmful Algae*. 10 (2011) 738–743.
- [54] M. Kurokawa, P.M. King, X. Wu, E.M. Joyce, T.J. Mason, K. Yamamoto, Effect of sonication frequency on the disruption of algae, *Ultrasonics Sonochemistry*. 31 (2016) 157–162.
- [55] C.-Y. Ahn, M.-H. Park, S.-H. Joung, H.-S. Kim, K.-Y. Jang, H.-M. Oh, Growth Inhibition of Cyanobacteria by Ultrasonic Radiation: Laboratory and Enclosure Studies, *Environmental Science & Technology*. 37 (2003) 3031–3037.
- [56] G. Cum, G. Galli, R. Gallo, A. Spadaro, Role of frequency in the ultrasonic activation of chemical reactions, *Ultrasonics*. 30 (1992) 267–270.
- [57] P. V. Zinin, J.S. Allen, V.M. Levin, Mechanical resonances of bacteria cells, *Physical Review E*. 72 (2005) 061907.
- [58] K.S. Suslick, Y. Didenko, M.M. Fang, T. Hyeon, K.J. Kolbeck, W.B. McNamara, M.M. Mdleleni, M. Wong, Acoustic cavitation and its chemical consequences, *Philosophical Transactions of the Royal Society A: Mathematical, Physical and Engineering Sciences*. 357 (1999) 335–353.
- [59] T.G. Leighton, The principles of cavitation, in: M.J.W. Povey, T.J. Mason (Eds.), *Ultrasound in Food Processing*, 1st ed., Springer, 1997: pp. 151–182.
- [60] T. Leong, M. Ashokkumar, K. Sandra, The fundamentals of power ultrasound - A review, *Acoustics Australia*. 39 (2011) 54–63.
- [61] J.-P. Franc, J.-M. Michel, *Fundamentals of Cavitation*, Kluwer Academic Publishers,

Dordrecht, 2005.

- [62] K.S. Suslick, The Chemical Effects of Ultrasound, *Scientific American*. 260 (1989) 80–86.
- [63] G.J. Ball, B.P. Howell, T.G. Leighton, M.J. Schofield, Shock-induced collapse of a cylindrical air cavity in water: a Free-Lagrange simulation, *Shock Waves*. 10 (2000) 265–276.
- [64] S.S. Sawant, A.C. Anil, V. Krishnamurthy, C. Gaonkar, J. Kolwalkar, L. Khandeparker, D. Desai, A.V. Mahulkar, V.V. Ranade, A.B. Pandit, Effect of hydrodynamic cavitation on zooplankton: A tool for disinfection, *Biochemical Engineering Journal*. 42 (2008) 320–328.
- [65] S. Guo, H.P. Lee, B.C. Khoo, Inhibitory effect of ultrasound on barnacle (*Amphibalanus amphitrite*) cyprid settlement, *Journal of Experimental Marine Biology and Ecology*. 409 (2011) 253–258.
- [66] P. Li, Y. Song, S. Yu, Removal of *Microcystis aeruginosa* using hydrodynamic cavitation: Performance and mechanisms, *Water Research*. 62 (2014) 241–248.
- [67] I. Hua, J.E. Thompson, Inactivation of *Escherichia coli* by sonication at discrete ultrasonic frequencies, *Water Research*. 34 (2000) 3888–3893.
- [68] R. Chand, D.H. Bremner, K.C. Namkung, P.J. Collier, P.R. Gogate, Water disinfection using the novel approach of ozone and a liquid whistle reactor, *Biochemical Engineering Journal*. 35 (2007) 357–364.
- [69] L. Mezule, S. Tsyfansky, V. Yakushevich, T. Juhna, A simple technique for water disinfection with hydrodynamic cavitation: Effect on survival of *Escherichia coli*, *Desalination*. 248 (2009) 152–159.
- [70] J.-L. Laborde, C. Bouyer, J.-P. Caltagirone, A. Gérard, Acoustic bubble cavitation at low frequencies, *Ultrasonics*. 36 (1998) 589–594.
- [71] S. Gao, Y. Hemar, M. Ashokkumar, S. Paturel, G.D. Lewis, Inactivation of bacteria and yeast using high-frequency ultrasound treatment, *Water Research*. 60 (2014) 93–104.
- [72] A. Brotchie, F. Grieser, M. Ashokkumar, Effect of power and frequency on bubble-size distributions in acoustic cavitation, *Physical Review Letters*. 102 (2009) 1–4.
- [73] T.Y. Wu, N. Guo, C.Y. Teh, J.X.W. Hay, *Advances in Ultrasound Technology for Environmental Remediation*, Springer Netherlands, Dordrecht, 2013.
- [74] J. Collis, R. Manasseh, P. Liovic, P. Tho, A. Ooi, K. Petkovic-Duran, Y. Zhu, Cavitation microstreaming and stress fields created by microbubbles, *Ultrasonics*. 50 (2010) 273–279.
- [75] S.J. Lighthill, Acoustic streaming, *Journal of Sound and Vibration*. 61 (1978) 391–418.
- [76] NCRP (National Council on Radiation Protection and Measurements), Report No. 140. Exposure criteria for medical diagnostic ultrasound: II. Criteria based on all known mechanisms, n.d.
- [77] S.S. Save, a. B. Pandit, J.B. Joshi, Microbial cell disruption: role of cavitation, *Chemical Engineering Journal and the Biochemical Engineering Journal*. 55 (1994) 67–72.
- [78] M. Furuta, Inactivation of *Escherichia coli* by ultrasonic irradiation, *Ultrasonics Sonochemistry*. 11 (2004) 57–60.
- [79] A. Abe, H. Mimura, H. Ishida, K. Yoshida, The effect of shock pressures on the inactivation of a marine *Vibrio* sp., *Shock Waves*. 17 (2007) 143–151.
- [80] G. Loraine, G. Chahine, C.T. Hsiao, J.K. Choi, P. Aley, Disinfection of gram-negative and gram-positive bacteria using DynaJets?? hydrodynamic cavitating jets, *Ultrasonics Sonochemistry*. 19 (2012) 710–717.
- [81] S. Broekman, O. Pohlmann, E.S. Beardwood, E.C. de Meulenaer, Ultrasonic treatment for microbiological control of water systems, *Ultrasonics Sonochemistry*. 17 (2010) 1041–1048.
- [82] T.G. Leighton, *The Acoustic Bubble*, Academic Press, 1997.
- [83] Y. He, K. Vinodgopal, M. Ashokkumar, F. Grieser, Sonochemical synthesis of ruthenium nanoparticles, *Research on Chemical Intermediates*. 32 (2006) 709–715.
- [84] L.A. Crum, Comments on the evolving field of sonochemistry by a cavitation physicist, *Ultrasonics Sonochemistry*. 2 (1995) S147–S152.
- [85] R.M.G. Boucher, Sonochemistry at low and high ultrasonic frequencies, *British Chemical Engineering*. 15 (1970) 363.

- [86] D.M. Kirpalani, K.J. McQuinn, Experimental quantification of cavitation yield revisited: focus on high frequency ultrasound reactors, *Ultrasonics Sonochemistry*. 13 (2006) 1–5.
- [87] M. Sivakumar, A.B. Pandit, Wastewater treatment: A novel energy efficient hydrodynamic cavitation technique, *Ultrasonics Sonochemistry*. 9 (2002) 123–131.
- [88] M.F. Dadjour, C. Ogino, S. Matsumura, N. Shimizu, Kinetics of disinfection of *Escherichia coli* by catalytic ultrasonic irradiation with TiO₂, *Biochemical Engineering Journal*. 25 (2005) 243–248.
- [89] J. Sassi, J. Rytönen, S. Viitasalo, E. Leppäkoski, Experiments with ultraviolet light, ultrasound and ozone technologies for onboard ballast water treatment, VTT Tiedotteita - Valtion Teknillinen Tutkimuskeskus. (2005).
- [90] L.A.A. Bazyar, W. Kloas, R. Jung, R. Ariav, K. Knopf, Low frequency ultrasound and UV-C for elimination of pathogens in recirculating aquaculture systems, *Ultrasonics Sonochemistry*. 20 (2013) 1211–1216.
- [91] J.J. Cullen, H.L. MacIntyre, On the use of the serial dilution culture method to enumerate viable phytoplankton in natural communities of plankton subjected to ballast water treatment, *Journal of Applied Phycology*. 28 (2016) 279–298.
- [92] J.F. Gillooly, Effect of body size and temperature on generation time in zooplankton, *Journal of Plankton Research*. 22 (2000) 241–251.
- [93] K.S. Suslick, T.J. Matula, Ultrasonic physical mechanisms and chemical effects, in: J. Webster (Ed.), *Wiley Encyclopedia of Electrical and Electronics Engineering*, John Wiley & Sons, Inc., Hoboken, NJ, USA, 1999: pp. 646–657.
- [94] S.J. Doctycz, K.S. Suslick, Interparticle collisions driven by ultrasound, *Science*. 247 (1990) 1067–1069.
- [95] E. Mesbahi, Latest results from testing seven different technologies under the EU MARTOB project- Where do we stand now?, in: *2nd International Ballast Water Treatment: R&D Symposium*, 2003: pp. 1–23.
- [96] S. Viitasalo, J. Sassi, J. Rytönen, E. Leppäkoski, Ozone, ultraviolet light, ultrasound, and hydrogen peroxide as ballast water treatments - experiments with mesozooplankton in low-saline brackish water, *Journal of Marine Environmental Engineering*. 8 (2005) 35–55.
- [97] T.-J. Lee, K. Nakano, M. Matsumura, A novel strategy for cyanobacterial bloom control by ultrasonic irradiation, *Water Science and Technology*. 46 (2002) 207 LP-215.
- [98] D.J.J. Leclercq, C.Q. Howard, P. Hobson, S. Dickson, A.C. Zander, M. Burch, Controlling cyanobacteria with ultrasound, *Internoise 2014*. (2014) 1–10.
- [99] H. Hao, M. Wu, Y. Chen, J. Tang, Q. Wu, Cyanobacterial bloom control by ultrasonic irradiation at 20 kHz and 1.7 MHz, *Journal of Environmental Science and Health, Part A*. 39 (2004) 1435–1446.
- [100] K. Yamamoto, P.M. King, X. Wu, T.J. Mason, E.M. Joyce, Effect of ultrasonic frequency and power on the disruption of algal cells, *Ultrasonics Sonochemistry*. 24 (2015) 165–171.
- [101] B. Ma, Y. Chen, H. Hao, M. Wu, B. Wang, H. Lv, G. Zhang, Influence of ultrasonic field on microcystins produced by bloom-forming algae, *Colloids and Surfaces B: Biointerfaces*. 41 (2005) 197–201.
- [102] D. Purcell, S.A. Parsons, B. Jefferson, The influence of ultrasound frequency and power, on the algal species *Microcystis aeruginosa*, *Aphanizomenon flos-aquae*, *Scenedesmus subspicatus* and *Melosira* sp., *Environmental Technology*. 34 (2013) 2477–2490.
- [103] United States Coast Guard, Ballast water management for control of nonindigenous species in waters of the United States, 33 CFR Part 151, Subpart D. (n.d.).
- [104] R. Kumar, N. Yadav, L. Rawat, M.K. Goyal, Effect of two waves of ultrasonic on waste water treatment, *Journal of Chemical Engineering & Process Technology*. 05 (2014) 3–8.
- [105] S. Koda, M. Miyamoto, M. Toma, T. Matsuoka, M. Maebayashi, Inactivation of *Escherichia coli* and *Streptococcus mutans* by ultrasound at 500 kHz, *Ultrasonics Sonochemistry*. 16 (2009) 655–659.
- [106] T. Blume, U. Neis, Improved wastewater disinfection by ultrasonic pre-treatment, *Ultrasonics*

- Sonochemistry. 11 (2004) 333–336.
- [107] H. Duckhouse, T.J. Mason, S.S. Phull, J.P. Lorimer, The effect of sonication on microbial disinfection using hypochlorite, *Ultrasonics Sonochemistry*. 11 (2004) 173–176.
- [108] A. Al Bsoul, J.-P. Magnin, N. Commenges-Bernole, N. Gondrexon, J. Willison, C. Petrier, Effectiveness of ultrasound for the destruction of *Mycobacterium* sp. strain (6PY1), *Ultrasonics Sonochemistry*. 17 (2010) 106–110.
- [109] J.A. Gallego-Juárez, K.F. Graff, *Power ultrasonics: applications of high-intensity ultrasound*, Woodhead Publishing, 2014.
- [110] A. Moussatov, R. Mettin, C. Granger, T. Tervo, B. Dubus, W. Lauterborn, Evolution of acoustic cavitation structures near larger emitting surface, in: *Proceedings of the World Congress on Ultrasonics*, Paris, France, 2003: pp. 955–958.
- [111] S.L. Peshkovsky, M.L. Friedman, W.A. Hawkins, *Ultrasonic rod waveguide radiator*, 7156201, 2007.
- [112] S.L. Peshkovsky, A.S. Peshkovsky, Matching a transducer to water at cavitation: Acoustic horn design principles, *Ultrasonics Sonochemistry*. 14 (2007) 314–322.
- [113] S.L. Peshkovsky, A.S. Peshkovsky, High capacity ultrasonic reactor system, 8651230, 2014.
- [114] M.J.R. Young, C.E. Winsper, D.H. Sansome, The effect of tool attachment on the resonant characteristics of ultrasonic waveguides, *Applied Acoustics*. 3 (1970) 217–224.
- [115] M. Lucas, Vibration sensitivity in the design of ultrasonic forming dies, *Ultrasonics*. 34 (1996) 35–41.
- [116] F.F.H. Rawson, *Fluid processing*, 1994.
- [117] M.M. van Iersel, N.E. Benes, J.T.F. Keurentjes, Importance of acoustic shielding in sonochemistry, *Ultrasonics Sonochemistry*. 15 (2008) 294–300.
- [118] M.H. Entezari, P. Kruus, Effect of frequency on sonochemical reactions II. Temperature and intensity effects, *Ultrasonics Sonochemistry*. 3 (1996) 19–24.
- [119] P.B. Clark, *Apparatus for treating fluids with ultrasounds*, 7198724, 2007.
- [120] Z. Liang, G. Zhou, Y. Zhang, Z. Li, S. Lin, Vibration analysis and sound field characteristics of a tubular ultrasonic radiator, *Ultrasonics*. 45 (2006) 146–151.
- [121] H.R. Hamidzadeh, R.N. Jazar, *Vibrations of Thick Cylindrical Structures*, Springer US, Boston, MA, 2010.
- [122] L. Shuyu, F. Zhiqiang, Z. Xiaoli, W. Yong, H. Jing, Radial vibration and ultrasonic field of a long tubular ultrasonic radiator, *Ultrasonics Sonochemistry*. 20 (2013) 1161–1167.
- [123] L. Xu, Investigation of a cup-shaped ultrasonic transducer operated in the full-wave vibrational mode, *Ultrasonics*. 59 (2015) 109–118.
- [124] L. Xu, S. Liu, P. Xu, M. Chen, The vibrational properties of the high power ultrasonic focused radiator with rodlike and tubular structures in a composite vibration, *Applied Acoustics*. 87 (2015) 72–82.
- [125] Z. Wei, J.A. Kosterman, A multi-stepped ultrasonic horn for industrial scale processes, in: *44th Annual Symposium of the Ultrasonic Industry Association*, Washington, D.C., USA, 2015.
- [126] H.N. McMurray, B.P. Wilson, Mechanistic and spatial study of ultrasonically induced luminol chemiluminescence, *The Journal of Physical Chemistry A*. 103 (1999) 3955–3962.
- [127] M.-Y. Wu, J.-R. Wu, *BallastSolution: An innovative solution for ship ballast water management*, in: *6th International Conference and Exhibition on Ballast Water Management*, Singapore, 2012.
- [128] Wuxi Brightsky Electronic Co. Ltd, BSKY Ballast Water Management System, (n.d.). <http://www.bsky.cn/english/product.asp?plt=81&Pone=3&Ptwo=21&Pthree=0> (accessed 4 July 2016).
- [129] Qingdao Headway Technology Co. Ltd, OceanGuard BWMS, (n.d.). <http://www.headwaytech.com/en/pxx.asp?id=7-10&str=AEOP> Technology (accessed 4 July 2016).
- [130] Hielscher Ultrasonics GmbH, Ultrasonic ballast water disinfection, (n.d.).

- <https://www.hielscher.com/ultrasonic-ballast-water-disinfection.htm> (accessed 4 July 2016).
- [131] C. Shea, An ultrasound ballast blaster, *The Wall Street Journal*. (2012).
- [132] M. V. Bagal, P.R. Gogate, Wastewater treatment using hybrid treatment schemes based on cavitation and Fenton chemistry: A review, *Ultrasonics Sonochemistry*. 21 (2014) 1–14.
- [133] Tierratech, TT-8000, (n.d.). <http://www.tierratech.com/US/cp23/cf6/pr103/tt-8000>.
- [134] B. Carlin, *Supersonic agitation*, 2578505, 1951.
- [135] H.T. Sawyer, *Apparatus for enhancing chemical reactions*, 4168295, 1979.
- [136] A. Shoh, *Sonic or ultrasonic processing apparatus*, 4016436, 1977.
- [137] P. Vaxelaire, *Modular unit for a tubular ultrasonic reactor*, 5384508, 1995.
- [138] B.D. Fitzgerald, *Apparatus for ultrasonic treatment of liquids*, 2585103, 1952.
- [139] J.A. Vaningen, R.H. Maddocks, A.L. Carter, *Method of and apparatus for debubbling liquids*, 3904392, 1975.
- [140] E. Babaev, *Ultrasonic method of treating a continuous flow of fluid*, 56611993, 1997.
- [141] R.D. Haggett, K.J. KarisAllen, G.A. Hranov, *Flowthrough device for the ultrasonic destruction of microorganism in fluids*, 20020164274, 2002.
- [142] R. Bruce, *Some fundamentals of mineralogy and geochemistry.*, Department of Geology, University of Georgia, Athens, Georgia. (2006) 30602–2501.
- [143] F. Culkin, N. Smith, Determination of the concentration of potassium chloride solution having the same electrical conductivity, at 15°C and infinite frequency, as standard seawater of salinity 35.0000 ‰ (Chlorinity 19.37394 ‰), *IEEE Journal of Oceanic Engineering*. 5 (1980) 22–23.
- [144] S. Levitus, T.P. Boyer, *World ocean atlas 1994. Volume 4. Temperature*, United States, 1994.
- [145] S. Takahashi, E. Yamamoto, N. Uetake, R. Motegi, Change of the ultrasonic characteristics with stress in some steels and aluminium alloys, *Journal of Materials Science*. 13 (1978) 843–850.
- [146] F.J. Arnold, M.S. Goncalves, L.L. Bravo-Roger, S.S. Muhlen, Electric impedance of piezoelectric ceramics under acoustic loads, *ECTI Transactions on Electrical Engineering, Electronics, and Communications*. 12 (2014) 48–54.
- [147] A.W. Leissa, *Vibration of Plates*, 2nd ed., The Acoustical Society of America, New York, 1993.
- [148] J.B. Fahline, Computing fluid-coupled resonance frequencies, mode shapes, and damping loss factors using the singular value decomposition, *The Journal of the Acoustical Society of America*. 115 (2004) 1474.
- [149] U.S. Lindholm, D.D. Kana, W.-H. Chu, H.N. Abramson, Elastic vibration characteristics of cantilever plates in water, *Journal of Ship Research*. 9 (1965) 11–22.
- [150] H. Lamb, On the vibrations of an elastic plate in contact with water, *Proceedings of the Royal Society A: Mathematical, Physical and Engineering Sciences*. 98 (1920) 205–216.
- [151] G. Sauerbrey, Verwendung von Schwingquarzen zur Wagung dunner Schichten und zur Mikrowagung, *Zeitschrift Fur Physik*. 155 (1959) 206–222.
- [152] K.K. Kanazawa, J.G. Gordon, Frequency of a quartz microbalance in contact with liquid, *Analytical Chemistry*. 57 (1985) 1770–1771.
- [153] W.D. Hunt, D.D. Stubbs, Sang-Hun Lee, Time-dependent signatures of acoustic wave biosensors, *Proceedings of the IEEE*. 91 (2003) 890–901.
- [154] M. Prokic, *Piezoelectric transducers modeling and characterisation*, MP Interconsulting, Le Locle, Switzerland, 2004.
- [155] S. Cochran, Piezoelectricity and basic configurations for piezoelectric ultrasonic transducers, in: *Ultrasonic Transducers*, Elsevier, 2012: pp. 3–35.
- [156] A. Trogé, R.L. O’Leary, G. Hayward, R.A. Pethrick, A.J. Mullholland, Properties of photocured epoxy resin materials for application in piezoelectric ultrasonic transducer matching layers, *The Journal of the Acoustical Society of America*. 128 (2010) 2704–2714.
- [157] D. Callens, C. Bruneel, J. Assaad, Matching ultrasonic transducer using two matching layers where one of them is glue, *NDT & E International*. 37 (2004) 591–596.

- [158] Qifa Zhou, Jung Cha, Yuhong Huang, Rui Zhang, Wenwu Cao, K.K. Shung, Alumina/epoxy nanocomposite matching layers for high-frequency ultrasound transducer application, *IEEE Transactions on Ultrasonics, Ferroelectrics and Frequency Control*. 56 (2009) 213–219.
- [159] H.J. Fang, Y. Chen, C.M. Wong, W.B. Qiu, H.L.W. Chan, J.Y. Dai, Q. Li, Q.F. Yan, Anodic aluminum oxide–epoxy composite acoustic matching layers for ultrasonic transducer application, *Ultrasonics*. 70 (2016) 29–33.
- [160] K.A. Mørch, Cavitation inception from bubble nuclei, *Interface Focus*. 5 (2015) 20150006.
- [161] P.R. Gogate, A.M. Wilhelm, A.B. Pandit, Some aspects of the design of sonochemical reactors, *Ultrasonics Sonochemistry*. 10 (2003) 325–330.
- [162] J.W. Kang, Y. Sen Hu, J.Y. Ma, T.Y. Huang, Effect of different air content on cavitation with ultrasonic treatment, *Advanced Materials Research*. 655–657 (2013) 43–47.
- [163] L. Liu, Y. Yang, P. Liu, W. Tan, The influence of air content in water on ultrasonic cavitation field, *Ultrasonics Sonochemistry*. 21 (2014) 566–571.
- [164] H. Arakawa, Lethal effects caused by suspended particles and sediment load on zoospores and gametophytes of the brown alga *Eisenia bicyclis*, *Fisheries Science*. 71 (2005) 133–140.
- [165] N. Mezhoud, M. Temimi, J. Zhao, M.R. Al Shehhi, H. Ghedira, Analysis of the spatio-temporal variability of seawater quality in the southeastern Arabian Gulf, *Marine Pollution Bulletin*. 106 (2016) 127–138.
- [166] A. Mathieson, A. Cardoni, N. Cerisola, M. Lucas, Understanding nonlinear vibration behaviours in high-power ultrasonic surgical devices, *Proceedings of the Royal Society A: Mathematical, Physical and Engineering Sciences*. 471 (2015) 20140906–20140906.
- [167] M. Umeda, K. Nakamura, S. Ueha, Effects of vibration stress and temperature on the characteristics of piezoelectric ceramics under high vibration amplitude Levels measured by electrical transient responses, *Japanese Journal of Applied Physics*. 38 (1999) 5581–5585.
- [168] A.C. Mathieson, Nonlinear characterisation of power ultrasonic devices used in bone surgery, (2012).
- [169] E. Riera, A. Cardoni, A. Blanco, V. Acosta, J. Gallego-Juárez, Characterising the nonlinear dynamics of power ultrasonic systems, in: *Internoise 2010*, Lisbon, Portugal, 2010.
- [170] K. Agbossou, J.-L. Dion, S. Carignan, M. Abdelkrim, A. Cheriti, Class D amplifier for a power piezoelectric load, *IEEE Transactions on Ultrasonics, Ferroelectrics and Frequency Control*. 47 (2000) 1036–1041.
- [171] A. Erturk, D.J. Inman, *Piezoelectric Energy Harvesting*, John Wiley & Sons, Ltd, Chichester, UK, 2011.
- [172] E. Wang, T. Nelson, R. Rauch, C. Gmbh, Back to elements - tetrahedra vs . hexahedra, in: *Proceedings of the International Ansys Conference*, 2004.
- [173] ANSYS Inc., *ANSYS Mechanical User’s Guide*, ANSYS Manual. 15317 (2014) 724–746.
- [174] H.D. Al-Budairi, Design and analysis of ultrasonic horns operating in longitudinal and torsional vibration, (2012).
- [175] P. Harkness, A. Cardoni, J. Russell, M. Lucas, Designing a hollow Langevin transducer for ultrasonic coring, *Applied Mechanics and Materials*. 24–25 (2010) 65–70.
- [176] D.A. DeAngelis, G.W. Schulze, K.S. Wong, Optimizing piezoelectric stack preload bolts in ultrasonic transducers, *Physics Procedia*. 63 (2015) 11–20.
- [177] ANSYS Inc., *ANSYS Mechanical APDL Theory Reference*, (2013).
- [178] Noliac A/S, *Materials*, (2016).
- [179] A.C. Acton, Clustering results around peaks for full-harmonic analyses in ANSYS, (2008).
- [180] A. Iula, N. Lamberti, R. Carotenuto, M. Pappalardo, A 3-D model of the classical Langevin transducer, in: *1997 IEEE Ultrasonics Symposium Proceedings An International Symposium (Cat No97CH36118)*, IEEE, n.d.: pp. 987–990.
- [181] J.A. McFadden, Radial vibrations of thick-walled hollow cylinders, *The Journal of the Acoustical Society of America*. 26 (1954) 714.
- [182] G. Li, G.A. Lamberton, J.R. Gladden, Acoustic modes of finite length homogeneous and layered cylindrical shells: Single and multiwall carbon nanotubes, *Journal of Applied Physics*.

- 104 (2008) 1–7.
- [183] M. Lucas, A. Cardoni, M.P. Cartmell, F.C.N. Lim, M. Lucas, M.P. Cartmell, F.C.N. Lim, Controlling the effects of modal interactions in ultrasonic cutting devices, in: 5th World Congress on Ultrasonics, Paris, France, 2003: pp. 49–56.
- [184] A. Mathieson, M. Lucas, Minimizing the excitation of parasitic modes of vibration in slender power ultrasonic devices, *Physics Procedia*. 63 (2015) 42–46.
- [185] E.A. Neppiras, The pre-stressed piezoelectric sandwich transducer, in: *Ultrasonics International 1973 Conference Proceedings*, 1973: pp. 295–302.
- [186] I. Stanasel, F. Ardelean, The parametric design of the ultrasonic exponential horns, *Nonconventional Technologies Review*. (2010).
- [187] A. Abdullah, M. Shahini, A. Pak, An approach to design a high power piezoelectric ultrasonic transducer, *Journal of Electroceramics*. 22 (2009) 369–382.
- [188] A. Pramanik, Problems and solutions in machining of titanium alloys, *The International Journal of Advanced Manufacturing Technology*. 70 (2014) 919–928.
- [189] ASM Aerospace Specification Metals Inc., Aluminium 7075-T6; 7075-T651, (n.d.). <http://asm.matweb.com/search/SpecificMaterial.asp?bassnum=MA7075T6> (accessed 25 October 2015).
- [190] MatWeb, AK Steel 316L Austenitic Stainless steel, (n.d.). <http://www.matweb.com/search/datasheet.aspx?matguid=9e9ab696974044cab4a7fd83687934eb&cckck=1> (accessed 27 April 2016).
- [191] ASM Aerospace Specification Metals Inc., Titanium Ti-6Al-4V (Grade 5) Annealed, (n.d.). <http://asm.matweb.com/search/SpecificMaterial.asp?bassnum=MTP641> (accessed 27 April 2016).
- [192] Unbrako, Engineering Guide - Socket Products, (n.d.).
- [193] J.A. Gallego-Juarez, Piezoelectric ceramics and ultrasonic transducers, *Journal of Physics E: Scientific Instruments*. 22 (1989) 804–816.
- [194] Department of Defense, Military standard - Piezoelectric ceramic material and measurements guidelines for sonar transducers, MIL-STD-1376B(SH), (1995).
- [195] T. Malysh, J. Erhart, Electric field applicability limits for PZT ceramics, *Ferroelectrics*. 319 (2005) 45–56.
- [196] Boston Piezo Optics Inc., Equivalent ceramic materials, (n.d.). <http://bostonpiezooptics.com/equivalent-ceramic-materials> (accessed 11 May 2016).
- [197] IEEE standard on piezoelectricity, ANSI/IEEE Std 176-1987. (1988).
- [198] IEEE standard definitions and methods of measurement for piezoelectric vibrators, IEEE Std No 177. (1966).
- [199] T.L. Jordan, Piezoelectric ceramic characterization, NASA/CR-2001-211225 ICASE Report No 2001-28. (2001).
- [200] C. Kameswara Rao, Torsional frequencies and mode shapes of generally constrained shafts and piping, *Journal of Sound and Vibration*. 125 (1988) 115–121.
- [201] J.H.B. Zarek, B.M. Gibbs, The derivation of eigenvalues and mode shapes for the bending motion of a damped beam with general end conditions, *Journal of Sound and Vibration*. 78 (1981) 185–196.
- [202] Q.S. Li, Exact solutions for free longitudinal vibration of stepped non-uniform rods, *Applied Acoustics*. 60 (2000) 13–28.
- [203] T. Koga, Free vibrations of circular cylindrical shells, *JSME International Journal Ser 1, Solid Mechanics, Strength of Materials*. 32 (1989) 311–319.
- [204] K. O’Shea, Enhanced vibration control of ultrasonic tooling using finite element analysis, in: *Proc ASME, Vibration Analysis - Analytical and Computational*, 1991: pp. 259–265.
- [205] K. Asai, A. Takeuchi, A new hollow cylindrical ultrasonic wave radiator, *Japanese Journal of Applied Physics*. 20 (1981) 169–172.
- [206] PI Ceramic GmbH, Piezoelectric actuators: components, technologies, operation, (n.d.).
- [207] American Piezo, Piezo-Mechanics: An Introduction, Mackeyville, PA, 2016.

- [208] D. Zhou, M. Kamlah, D. Munz, Effects of uniaxial prestress on the ferroelectric hysteretic response of soft PZT, *Journal of the European Ceramic Society*. 25 (2005) 425–432.
- [209] Tonichi, Bolt Tightening, in: *Tonichi Torque Handbook Vol 7*, 2008.
- [210] A. Muliana, Time dependent behavior of ferroelectric materials undergoing changes in their material properties with electric field and temperature, *International Journal of Solids and Structures*. 48 (2011) 2718–2731.
- [211] C. Jullian, J.F. Li, D. Viehland, Comparisons of polarization switching in “hard,” “soft,” and relaxor ferroelectrics, *Journal of Applied Physics*. 95 (2004) 4316–4318.
- [212] Data Translation, DT9837 series user manual, (2016).
- [213] H. Nyquist, Certain topics in telegraph transmission theory, *Transactions of the American Institute of Electrical Engineers*. 47 (1928) 617–644.
- [214] J. van Baren, What is random vibration testing?, *Sound and Vibration*. (2012) 9–12.
- [215] P. Avitabile, Experimental modal analysis a simple non-mathematical presentation, *Sound and Vibration*. (2001) 1–11.
- [216] Polytec GmbH, User manual 3D laser vibrometer 3D-LV, (n.d.).
- [217] M. Cerna, A.F. Harvey, *The fundamentals of FFT-based signal analysis and measurement*, National Instruments. Applicatio (2000) 1–20.
- [218] M.R. Ashory, Assessment of the mass-loading effects of accelerometers in modal testing, in: *Proceedings of the 20th International Modal Analysis Conference, 2002*: pp. 1027–1031.
- [219] S. Bi, J. Ren, W. Wang, G. Zong, Elimination of transducer mass loading effects in shaker modal testing, *Mechanical Systems and Signal Processing*. 38 (2013) 265–275.
- [220] G.M. Chapman, M. Lucas, Frequency analysis of an ultrasonically excited thick cylinder, *International Journal of Mechanical Sciences*. 32 (1990) 205–214.
- [221] D.A. Berlincourt, D.R. Curran, H. Jaffe, Piezoelectric and piezomagnetic materials and their function in transducers, in: *Physical Acoustics*, Elsevier, 1964: pp. 169–270.
- [222] D. Ensminger, L.J. Bond, Basic design of ultrasonic transducers, in: *Ultrasonics Fundamentals, Technologies, and Applications*, 3rd editio, CRC Press, Boca Raton, Florida, 2012: pp. 171–218.
- [223] S. Sherrit, H.D. Wiederick, B.K. Mukherjee, Accurate equivalent circuits for unloaded piezoelectric resonators, in: *1997 IEEE Ultrasonics Symposium Proceedings An International Symposium (Cat No97CH36118)*, IEEE, n.d.: pp. 931–935.
- [224] L. Amarande, C. Miclea, C. Tanasoiu, Evaluation of the accuracy in determining the mechanical quality factor for piezoceramic resonators, *Ferroelectrics*. 350 (2007) 38–47.
- [225] T. Suzuki, Y. Mizutani, H. Ikeda, H. Yoshida, Impedance characteristic of ultrasonic transducer operated as load of MOSFET DC-to-RF power inverter, in: *Proceedings of the 1996 IEEE IECON 22nd International Conference on Industrial Electronics, Control, and Instrumentation*, IEEE, n.d.: pp. 987–990.
- [226] G.A. Lesieutre, C.L. Davis, Can a coupling coefficient of a piezoelectric device be higher than those of its active material?, *Journal of Intelligent Material Systems and Structures*. 8 (1997) 859–867.
- [227] A. Mohammed, General definition of transducer coupling coefficient and some applications, *The Journal of the Acoustical Society of America*. 36 (1964) 1012–1012.
- [228] British Standards Institution, EN50324-2: Piezoelectric properties of ceramic materials and components - part 2: methods of measurement - low power, (2002).
- [229] IRE standards on piezoelectric crystals - the piezoelectric vibrator: definitions and methods of measurement, *Proceedings of the IRE*. 45 (1957) 353–358.
- [230] K. Uchino, Y. Zhuang, S.O. Ural, Loss determination methodology for a piezoelectric ceramic: new phenomenological theory and experimental proposals, *Journal of Advanced Dielectrics*. 01 (2011) 17–31.
- [231] Tektronix, MDO3000 series, mixed domain oscilloscopes, specifications and performance verification, technical reference, (n.d.) 3.
- [232] V.N. Khmelev, R. V. Barsukov, V. Barsukov, A.N. Slivin, S.N. Tchyganok, System of phase-

- locked-loop frequency control of ultrasonic generators, in: 2001 Siberian Russian Student Workshop on Electron Devices and Materials Proceedings 2nd Annual (IEEE Cat No01EX469), Novosibirsk State Tech. Univ, n.d.: pp. 56–57.
- [233] L. Xiao, S. Zhou, Y. Ye, Y. Xu, Circuit design of intelligent frequency tracking for ultrasonic cell disruption system, in: 2016 9th International Congress on Image and Signal Processing, BioMedical Engineering and Informatics (CISP-BMEI), IEEE, 2016: pp. 1611–1615.
- [234] T.C. Chen, C.H. Yu, M.C. Tsai, A new driver based on dual-mode frequency and phase control for traveling-wave type ultrasonic motor, *Energy Conversion and Management*. 49 (2008) 2767–2775.
- [235] Q. Peng, H. Wang, X. Su, X. Lu, A new design of the high-power ultrasonic generator, in: Chinese Control and Decision Conference, 2008: pp. 3800–3803.
- [236] N. Aurelle, D. Guyomar, C. Richard, P. Gonnard, L. Eyraud, Nonlinear behavior of an ultrasonic transducer, *Ultrasonics*. 34 (1996) 187–191.
- [237] M. Tadvi, A. Pandey, J. Prajapati, J. Shah, Design and development of sonotrode for ultrasonic drilling, in: Volume 2B: Advanced Manufacturing, ASME, 2015: p. V02BT02A061.
- [238] D. Guyomar, B. Ducharne, G. Sebald, High nonlinearities in Langevin transducer: a comprehensive model, *Ultrasonics*. 51 (2011) 1006–1013.
- [239] Y. Liu, T. Morita, Simplified evaluation method for piezoelectric nonlinear vibration under high power operation, in: Proceedings of Symposium on Ultrasonic Electronics, Tsukuba, Japan, 2015.
- [240] G. Sebald, H. Kuwano, D. Guyomar, B. Ducharne, Experimental Duffing oscillator for broadband piezoelectric energy harvesting, *Smart Materials and Structures*. 20 (2011) 102001.
- [241] E.W. Weisstein, Skewness, *MathWorld - A Wolfram Web Resource*. (n.d.). <http://mathworld.wolfram.com/Skewness.html> (accessed 12 January 2018).
- [242] J.R.M. Hosking, Moments or L moments? An example comparing two measures of distributional shape, *The American Statistician*. 46 (1992) 186.
- [243] G. Brys, M. Hubert, A. Struyf, A robust measure of skewness, *Journal of Computational and Graphical Statistics*. 13 (2004) 996–1017.
- [244] R.A. Groeneveld, G. Meeden, Measuring skewness and kurtosis, *The Statistician*. 33 (1984) 391.
- [245] C.H. Sherman, J.L. Butler, *Transducers and arrays for underwater sound*, Springer New York, New York, NY, 2007.
- [246] H. Al-Budairi, M. Lucas, P. Harkness, A design approach for longitudinal–torsional ultrasonic transducers, *Sensors and Actuators A: Physical*. 198 (2013) 99–106.
- [247] M.R. Bose, V. Mohanan, K.G. Jacob, N. Ravi, R.M.R. Vishnubhatla, Development of a broadband transducer, in: V. Chander, P.R.S. Pillai (Eds.), *Proceedings of the National Symposium on Ocean Electronics*, Allied Publishers Pvt. Ltd., Cochin, India, 2003: pp. 202–206.
- [248] MatWeb, Beryllium Copper, (n.d.). <http://www.matweb.com/search/datasheet.aspx?matguid=bbe220809bb144eb9c2f3672da24ccda&cckck=1> (accessed 28 December 2017).
- [249] MatWeb, AISI 4140 Steel, (n.d.). <http://www.matweb.com/search/DataSheet.aspx?MatGUID=b7826d8859cc421a9c0df6087d4f3ed4> (accessed 28 December 2017).
- [250] M.J. Guan, W.H. Liao, On the equivalent circuit models of piezoelectric ceramics, *Ferroelectrics*. 386 (2009) 77–87.
- [251] G.G. Yaralioglu, A.S. Ergun, B. Bayram, E. Haeggstrom, B.T. Khuri-Yakub, Calculation and measurement of electromechanical coupling coefficient of capacitive micromachined ultrasonic transducers, *IEEE Transactions on Ultrasonics, Ferroelectrics and Frequency Control*. 50 (2003) 449–456.
- [252] P.C. Magnusson, G.C. Alexander, V.K. Tripathi, A. Weisshaar, *Transmission Lines and Wave Propagation*, Fourth Edi, CRC Press, 2000.

- [253] M. Garcia-Rodriguez, J. Garcia-Alvarez, Y. Yañez, M.J. Garcia-Hernandez, J. Salazar, A. Turo, J.A. Chavez, Low cost matching network for ultrasonic transducers, *Physics Procedia*. 3 (2010) 1025–1031.
- [254] H. Huang, D. Paramo, Broadband electrical impedance matching for piezoelectric ultrasound transducers, *IEEE Transactions on Ultrasonics, Ferroelectrics and Frequency Control*. 58 (2011) 2699–2707.
- [255] V. Khmelev, R. Barsukov, S. Tsyganok, M. Khmelev, Adaptive phase lock system of ultrasonic electronic generators, in: *International Workshops and Tutorials on Electron Devices and Materials*, IEEE, 2006: pp. 229–231.
- [256] J. Luo, G. Du, J. Fang, The research on phase lock method of ultrasonic power supply with variable step length control, in: *2014 International Power Electronics and Application Conference and Exposition*, IEEE, 2014: pp. 400–405.
- [257] A. Tekile, I. Kim, J.-Y. Lee, 200 kHz sonication of mixed-algae suspension from a eutrophic lake: the effect on the caution vs. outbreak bloom alert levels, *Water*. 9 (2017) 915.
- [258] T. Kikuchi, T. Uchida, Calorimetric method for measuring high ultrasonic power using water as a heating material, *Journal of Physics: Conference Series*. 279 (2011) 012012.
- [259] R.A. Al-Juboori, T. Yusaf, L. Bowtell, V. Aravinthan, Energy characterisation of ultrasonic systems for industrial processes, *Ultrasonics*. 57 (2015) 18–30.
- [260] Water - heat capacity (specific heat), (n.d.). https://www.engineeringtoolbox.com/specific-heat-capacity-water-d_660.html (accessed 10 November 2017).
- [261] T. Uchida, T. Kikuchi, M. Yoshioka, Y. Matsuda, R. Horiuchi, Development of high ultrasonic power measurement technique by calorimetric method using water as heating elements for high ultrasonic power standard, *Acoustical Science and Technology*. 36 (2015) 445–448.
- [262] J. Klíma, a. Frias-Ferrer, J. González-García, J. Ludvík, V. Sáez, J. Iniesta, Optimisation of 20 kHz sonoreactor geometry on the basis of numerical simulation of local ultrasonic intensity and qualitative comparison with experimental results, *Ultrasonics Sonochemistry*. 14 (2007) 19–28.
- [263] A. Kumar, T. Kumaresan, A.B. Pandit, J.B. Joshi, Characterization of flow phenomena induced by ultrasonic horn, *Chemical Engineering Science*. 61 (2006) 7410–7420.
- [264] O. Dahlem, J. Reisse, V. Halloin, The radially vibrating horn: a scaling-up possibility for sonochemical reactions, *Chemical Engineering Science*. 54 (1999) 2829–2838.
- [265] Bandelin Electronic GmbH & Co. KG, High-power ultrasound. Sonoreactors, (2015).
- [266] B. Balasundaram, S.T.L. Harrison, Optimising orifice geometry for selective release of periplasmic products during cell disruption by hydrodynamic cavitation, *Biochemical Engineering Journal*. 54 (2011) 207–209.
- [267] K.K. Jyoti, a. B. Pandit, Hybrid cavitation methods for water disinfection, *Biochemical Engineering Journal*. 14 (2003) 9–17.
- [268] S. Arrojo, Y. Benito, a. Martínez Tarifa, A parametrical study of disinfection with hydrodynamic cavitation, *Ultrasonics Sonochemistry*. 15 (2008) 903–908.
- [269] M. Lüring, Y. Tolman, Effects of commercially available ultrasound on the zooplankton grazer *Daphnia* and consequent water greening in laboratory experiments, *Water*. 6 (2014) 3247–3263.
- [270] R.G. Cohen, S.G. Rodríguez gil, C.G. Vélez, The post-embryonic development of *Artemia persimilis* Piccinelli & Prosdocimi, *Hydrobiologia*. 391 (1998) 63–80.
- [271] B. Mittmann, P. Ungerer, M. Klann, A. Stollewerk, C. Wolff, Development and staging of the water flea *Daphnia magna* (Straus, 1820; Cladocera, Daphniidae) based on morphological landmarks, *EvoDevo*. 5 (2014) 12.
- [272] Aalco Metals Limited, Stainless steel tubular products, (2009).
- [273] M. Franke, P. Braeutigam, Z.-L. Wu, Y. Ren, B. Ondruschka, Enhancement of chloroform degradation by the combination of hydrodynamic and acoustic cavitation, *Ultrasonics Sonochemistry*. 18 (2011) 888–894.

- [274] E.M. Polk, Impedance matching circuits for piezoelectric transducers, Massachusetts Institute of Technology, 1978.
- [275] K.B. Bader, J.L. Raymond, J. Mobley, C.C. Church, D.F. Gaitan, Inertial cavitation threshold dependence on static pressure., *The Journal of the Acoustical Society of America*. 128 (2010) 2313.
- [276] J. Sponer, Dependence of the cavitation threshold on the ultrasonic frequency, *Czechoslovak Journal of Physics*. 40 (1990) 1123–1132.
- [277] I.R. Webb, S.J. Payne, C.-C. Coussios, The effect of temperature and viscoelasticity on cavitation dynamics during ultrasonic ablation, *The Journal of the Acoustical Society of America*. 130 (2011) 3458–3466.
- [278] E. Herbert, S. Balibar, F. Caupin, Cavitation pressure in water, *Physical Review E - Statistical, Nonlinear, and Soft Matter Physics*. 74 (2006).
- [279] T. Numakura, K. Kashiwagura, T. Makuta, Development and optimization of microbubble generator with a hollow cylindrical ultrasonic horn, *Journal of JSEM*. 14 (2014) s52–s56.
- [280] P.R. Gogate, A.B. Pandit, A review of imperative technologies for wastewater treatment I: oxidation technologies at ambient conditions, *Advances in Environmental Research*. 8 (2004) 501–551.
- [281] P.P. Sangave, A.C. Mukherjee, A.B. Pandit, Ballast Water Treatment Using Hydrodynamic Cavitation, 43 (2014).
- [282] E.F. Karamah, I. Sunarko, Disinfection of Bacteria Escherichia Coli using Hydrodynamic Cavitation, *International Journal of Technology*. 4 (2013) 209.
- [283] X. Jin, Z. Li, L. Xie, Y. Zhao, T. Wang, Synergistic effect of ultrasonic pre-treatment combined with UV irradiation for secondary effluent disinfection, *Ultrasonics Sonochemistry*. 20 (2013) 1384–1389.

Achievements

Publications (ballast water treatment - ultrasonics)

1. Osman, H., Lim, F., Lucas, M., 2017. Ultrasonic treatment of ballast water. *Water Research* (submitted).
2. Turangan, C., Lu, X., Tandiono, Kang, C. W., Osman, H., Lim, F. Development of compressible cavitation model for low power ultrasonic disinfection system in ballast water treatment process. *Proceedings of the 12th European Fluid Mechanics Conference (EFMC12)*. Vienna, Austria, 9–13 September 2018.
3. Chang-Wei, K., Tandiono, Turangan, C., Osman, H., Lim, F., Lucas, M., 2018. Numerical and experimental studies of cavitation generation for ballast water treatment. *Proceedings of the 37th International Conference on Ocean, Offshore, and Arctic Engineering (OMAE2018)*. Madrid, Spain, 17–22 June 2018.
4. Osman, H., Lim, F., Lucas, M., 2017. Vibration response of a high-power compact large-area ultrasonic resonator. *Proceedings of the 2017 IEEE International Ultrasonics Symposium (IUS)*. Washington, D.C., USA, 6–9 September 2017.
5. Osman, H., Lim, F., Lucas, M., 2017. Parametric study of multiple orifice resonators. *Proceedings of the 46th Ultrasonic Industry Association Symposium (UIA46)*. Dresden, Germany, 24–26 April 2017.
6. Osman, H., Lim, F., Lucas, M., Balasubramaniam, P., 2016. Development of an ultrasonic resonator for ballast water disinfection. *Physics Procedia*, 87, 99–104.

Publications (ballast water treatment – non-ultrasonics)

1. Kang, C.W., Osman, H., 2017. Ballast water management system (BWMS) performance validation – scaling methodology. *8th International Conference on Ballast Water Management*. Singapore, 24–25 April 2017.
2. Chew, H.H., Osman, H., Chua, C.Y., Balasubramaniam, P., 2016. Ballast water treatment with biofouling control. *Society of Naval Architects and Marine Engineers, Singapore (SNAMES) 36th Annual Journal*.

3. Li, H., Osman, H., Kang, C.W., Ba, T., 2017. Numerical and experimental investigation of UV disinfection for water treatment. *Applied Thermal Engineering*, 111, 280–291.
4. Ba, T., Li, H., Osman, H., Kang, C.W., 2016. Characteristic correlation study of UV disinfection performance for ballast water treatment. *69th Annual Meeting of the APS Division of Fluid Dynamics*. Portland, Oregon, USA, 20–22 November.
5. Chew, H.H., Osman, H., Chua, C.Y., Balasubramaniam, P., 2016. Application of ultra-low frequency field in ballast water disinfection. *Proceedings of the 6th GEF-UNDP-IMO GloBallast R&D Forum and Exhibition on Ballast Water Management*. Montreal, Canada, 16–18 March.

Patent application

Title: Ultrasonic device having large radiating area

Korean application number: 10-2017-0042158

US application number: 15/475,993

Competition

Finalist, Marine Innovation and Entrepreneurship Competition (MTEC 2017), Cocoon Networks, London, UK.

Additional research grant awarded

Project ID: SMI-2015-MA-06

Project Title: Development and implementation of a low power ultrasonic disinfection system for high-flow ballast water treatment through numerical and experimental studies of ultrasonic cavitation.

Project Duration: 36 months beginning Dec 2016

Grant award: \$638,000.00

Awarding body: Singapore Maritime Institute (SMI)

Role of the PhD candidate:

1. preparation of the research grant proposal;
2. designated as the project co-investigator representing Sembcorp Marine;
3. currently researching on the scale-up design of an ultrasonic treatment system.